

**A MODELLING INVESTIGATION INTO THE  
WATER EXCHANGE TIMESCALES IN  
ESTUARINE WATERS**

*A thesis submitted to Cardiff University*

*In candidature for the degree of*

*Doctor of Philosophy*

*By*

**Yuheng Ren**

*Division of Civil Engineering, Cardiff School of Engineering*

*Cardiff University*

2013

# Acknowledgements

I would like to express my sincere gratitude to my supervisors, Prof. Binliang Lin, Dr. Shunqi Pan, and Dr. William Rauen for their continuous support, guidance and encouragement. I am deeply indebted to my supervisor, Prof. Binliang Lin, for his endless patience and constructive criticism, and for enlarging my knowledge of hydrodynamic modelling and providing me academic freedom to pursue this research. I am greatly inspired by his attitude to novelty and high quality of research. I would like to thank my supervisor, Dr. Shunqi Pan, I am impressed by his precise research attitude. He gave me lots of valuable advice on my research and helped me refine my thesis writing. I would like to thank my supervisor, Dr. William Rauen, his broad knowledge of physics improved my understanding and interpretation of the experiment results.

It is my honor to have the opportunity to study at the Institute of Environment and Sustainability at the Cardiff University. I would like to thank my colleagues and dear friends there: Fei Wang, Haiyan Yang, Dr. Kuo Yan, Matthew Cowle, Rhodri Lucas and Athanasios Angeloudis. Thanks for their company and kind assistance along the way of my PhD study. I also would like to thank all the people there for their help and friendship.

I would like to thank Dr. Jian Sun at Tsinghua University, for providing me modelling data and giving lots of valuable advice on my research. With his help, my knowledge of numerical modelling methods was enlarged. I own thanks to the Water Department of Arup Group, Ltd in Cardiff for providing me the research scholarship and the internship opportunity. Many thanks are due to the people there for their friendship,

especially to Dr. Lei Yang, Mr. David Evans for helping me gain insight into civil engineering work and practical experience.

I am grateful for my previous postgraduate supervisor, Prof. Hongwu Tang at Hohai University, for leading me to the world of hydrodynamic and for his continuous encouragement.

Finally, I would like to express my deepest appreciation to my family. I cannot thank my parents and younger sister, Siyu, enough for their support and attention throughout my whole life. I cannot accomplish this thesis without their love every day.

# Abstract

Based on the concepts of water exchange timescales, a three-dimensional model has been refined to predict the age of water (AW). The model has been applied to two estuaries with very different characteristics. One estuary is a partially stratified micro-tidal estuary, i.e., the Pearl River Estuary (PRE), China and the other one is a well-mixed macro-tidal estuary, i.e., the Severn Estuary and Bristol Channel, UK (SEBC).

The focus of this study is to investigate the influence of density-induced circulation on the estuarine water exchange process. A comparison between the predictions made using the barotropic mode and the baroclinic mode has been undertaken in the above two estuaries. The results indicate that due to the partially stratified phenomenon, in the PRE lower AW values are observed at the water surface, with higher AW values occurring near the bed. In the wet season, a more obvious AW stratification can be observed. The density-induced circulation causes an increase in the water mixing rate and a decrease in the timescales by a ratio greater than 50%. The stratification of the AW distribution is also enhanced. However, in the homogenous phenomenon of the SEBC, the baroclinic forcing's impact on the water exchange process is very small.

A model investigation is then carried out to predict the spatio-temporal variation of AW distribution in response to other dynamic factors. A regression analysis reveals that the age of freshwater exponentially decreases with the growth of discharge. Scenario analyses show that the tidal influence becomes more pronounced when the discharge is relatively small, and the varying tidal range mainly impacts on the fluctuation range of the AW, instead of its depth-averaged value. Moreover, the



vertical variation in the AW is enhanced during neap tides due to less mixing. The age of seawater in the estuary is lowest near the estuary mouth and it increases further upstream.

In the SEBC, the impacts of proposed tidal stream turbines with two different array arrangements on the water exchange process are analysed to investigate changes in the water level, current speed and AW distributions. A physical model investigation into the water exchange processes in a small scale model of the SEBC is then undertaken to estimate the travel time between different locations, and the water and tracer fluxes through two selected cross sections.

# Contents

<b>Acknowledgements</b>	i
<b>Abstract</b>	iii
<b>Table of Contents</b>	v
<b>List of Figures</b>	x
<b>List of Tables</b>	xvii
<b>Nomenclature</b>	xix
<b>Abbreviation</b>	xxiii

<b>Chapter 1 Introduction.....</b>	<b>1</b>
1.1 BACKGROUND .....	2
1.2 OBJECTIVES OF THE STUDY .....	5
1.3 OUTLINE OF THE THESIS .....	6
<b>Chapter 2 Literature Review.....</b>	<b>8</b>
2.1 WATER EXCHANGE IN ESTUARINE SYSTEM.....	9
2.2 DENSITY-INDUCED CIRCULATION AND STRATIFICATION .....	12
2.2.1 Stratification classification.....	13
2.2.2 The stratification stability.....	15
2.3 WATER EXCHANGE TIMESCALES .....	19
2.3.1 Residence time and exposure time .....	20
2.3.2 Age of water (AW) .....	24
2.4 DESCRIPTIONS OF TWO ESTUARIES .....	26
2.4.1 The Pearl River Estuary (PRE) .....	27
2.4.2 Severn Estuary and Bristol Channel (SEBC) .....	32
SUMMARY .....	34

## **Chapter 3 Methodology.....36**

3.1. INTRODUCTION.....	37
3.2. HYDRODYNAMIC AND TRANSPORT MODULES .....	38
3.2.1 Shallow water equations.....	38
3.2.2 Transport equations for salinity .....	41
3.2.3 Transport equation for a scalar quantity .....	42
3.3 WATER EXCHANGE TIMESCALES .....	42
3.3.1 Age of water .....	43
3.3.2 Residence time, exposure time and return coefficient.....	47
3.3.3 Connectivity matrix.....	49
3.3.4 Local residence time and transit time.....	50
3.4 EXPERIMENTATION METHODS.....	50
3.4.1 Physical model of the Severn Estuary and Bristol Channel .....	50
3.4.2 Model setting up.....	52
3.4.3 Data acquisition and processing systems .....	54

## **Chapter 4 Water Age Distribution in the Pearl River**

### **Estuary.....63**

4.1 INTRODUCTION.....	64
4.2 MODEL SETUP .....	65
4.2.1 Mesh and algorithm.....	65
4.2.2 River discharge.....	66
4.2.3 Salinity .....	69
4.2.4 Wind.....	69
4.2.5 Sensitivity test .....	71
4.3 MODEL CALIBRATION AND VALIDATION .....	71
4.3.1. Water elevation.....	72
4.3.2. Currents .....	74

4.3.3. Salinity .....	76
4.4 DESIGN OF MODEL SCENARIOS .....	82
4.4.1 Real-time condition .....	82
4.4.2 Constant river discharge condition .....	83
4.4.3 Tidal currents .....	84
4.4.4 Density-induced circulation and wind .....	84
4.4.5 Tracer released position .....	84
4.5 RESULTS .....	85
4.5.1 AW distributions in the wet and dry seasons (case 1) .....	85
4.5.2 Residual currents (case 1) .....	88
4.6 DISCUSSION .....	90
4.6.1 Influence of the river discharge .....	90
4.6.2 Influence of tidal current .....	96
4.6.3 Influence of density-induced circulation .....	97
4.6.4 Influence of wind forcing .....	116
4.6.5 AW from open sea .....	119
SUMMARY .....	121

## **Chapter 5 Exposure Time and Residence Time in the Pearl**

<b>River Estuary .....</b>	<b>124</b>
5.1 INTRODUCTION .....	125
5.2 MODEL SCENARIOS .....	125
5.2.1 ARTM and AETM .....	125
5.2.2 Influence of river discharge .....	127
5.2.3 Influence of initially releasing water level .....	128
5.2.4 Influence of density-induced circulation .....	128
5.2.5 Water exchange between the segments .....	128
5.3 CONVERGENCE OF CALCULATION .....	128
5.4 RESULTS .....	129

5.5 DISCUSSION .....	130
5.5.1 Initially releasing region.....	130
5.5.2 Influence of the river discharge.....	132
5.5.3 Initial releasing water level .....	134
5.5.4 Influence of density-induced circulation.....	136
5.5.5 Water exchange process between segments .....	137
SUMMARY .....	140

## **Chapter 6 Water Exchange Timescales in the Severn Estuary and the Bristol Channel.....142**

6.1 INTRODUCTION.....	143
6.2 MODEL SETUP .....	144
6.2.1 Mesh and algorithm.....	145
6.2.2 Boundary conditions .....	145
6.2.3 Salinity .....	146
6.2.4 Tidal stream turbines' module .....	148
6.2.5 Sensitivity tests.....	149
6.3 MODEL CALIBRATION AND VALIDATION .....	150
6.3.1. Water level and tidal currents.....	151
6.3.2. Salinity .....	153
6.4 MODEL SCENARIOS .....	155
6.5 RESULTS AND DISCUSSION.....	155
6.5.1. Influence of density-induced circulation.....	155
6.5.2 Influence of tidal stream turbines.....	158
SUMMARY .....	167

## **Chapter 7 Laboratory Experiments of the Severn Estuary and the Bristol Channel.....169**

7.1 INTRODUCTION.....	170
-----------------------	-----

7.2. DESIGN OF EXPERIMENTS, RESULTS AND DISCUSSION.....	170
7.2.1 Design of experiments.....	170
7.2.2 Results and Discussion.....	172
SUMMARY.....	184

## **Chapter 8 Conclusions and Recommendations for Further**

<b>Research.....</b>	<b>186</b>
8.1. WATER EXCHANGE TIMESCALES IN TWO ESTUARIES .....	188
8.2. RECOMMENDATIONS FOR FURTHER RESEARCH .....	190

## **Appendix A: HYDRODYNAMIC AND TRANSPORT MODULES**

<b>OF MIKE 3.....</b>	<b>191</b>
-----------------------	------------

<b>Appendix B: NUMERICAL SOLUTION.....</b>	<b>201</b>
--	------------

## **Appendix C: THE TRADITIONAL CENTRAL REGIME**

<b>THEORY.....</b>	<b>210</b>
--------------------	------------

## **Appendix D: NUMERICAL MODEL PARAMETERS AND**

<b>SENSITIVITY TEST.....</b>	<b>215</b>
------------------------------	------------

<b>Reference.....</b>	<b>218</b>
-----------------------	------------

# List of Figures

Fig. 2.1. Classification of estuaries based on the stratification levels: (a) highly stratified; (b) partial mixed; (c) fully mixed.....	14
Fig .2.2. Illustration of a baroclinic fluid.....	16
Fig 2.3. Illustration of salty water gradient and water elevation gradient during the flood and the ebb.....	17
Fig. 2.4. The influence of barotropic and baroclinic terms on the vertical velocity (a) Ebb period, (Pandoe and Edge, 2004); (b)–(c) When the ebb changes to the flood; (d) Flood period.....	17
Fig. 2.5. Transport path of a water parcel released from the inlet of Humen inside the Pearl River Estuary as an example to present three timescales .....	21
Fig. 2.6. Mass of tracer remains in model domain, solid line is based on the definition of average residence time calculation; the dot line is based on the definition of average exposure time calculation.....	23
Fig. 2.7. Topography of the Pearl River Estuary and the adjacent coastal area. Left squares: eight major entrances; Left black line: sea boundary; Dash lines: the main stem of the PRE along west channel.....	27
Fig. 2.8. Topography of the Severn Estuary and Bristol Channel.....	33
Fig. 3.1. Illustration of the age model used in this study.....	37
Fig. 3.2. Cartesian co-ordinate in modelling.....	39
Fig. 3.3. Illustration of tracer concentration distribution function.....	44
Fig. 3.4. Illustration of mass budget equation for tracer concentration.....	44
Fig. 3.5. Schematic of calculation for tracer concentration and age concentration in water age model.....	46
Fig. 3.6. Photography of the physical model of Severn Estuary and Bristol Channel.....	51
Fig. 3.7. Domain covered by the physical model of Severn Estuary.....	52
Fig. 3.8. Bathymetry of the physical model of Severn Estuary and Bristol Channel showing the positions of sampling points.....	52
Fig. 3.9. Photography of the perforated pipe which supplies the water to the physical model, the weir and the baffle.....	53
Fig. 3.10. Calibration for water level readings at point A with best fitting liner formula.....	54

Fig. 3.11. Illustration of a down-looking ADV probe, sampling volume and acoustic pulses (figure reproduced from Sontek <a href="http://www.sontek.com">http://www.sontek.com</a> ).....	56
Fig. 3.12. Illustration of four positions of sensors in the beaker for the calibration of fluorometers.....	59
Fig. 3.13. Calibration curves used to correct tracer concentration readings, x: fluorometer readings (ppb); y: actual concentration (ppb).....	60
Fig. 4.1. Illustration of mesh for modelling the Pearl River Estuary.....	66
Fig. 4.2. River discharges for eight tributaries over one year.....	67
Fig. 4.3. Monthly averaged total discharge over a tidal cycle, $Q_f$ , and water volume between high and low water levels, $\Delta V$ .....	68
Fig. 4.4. Mean flow ratio $R_f$ from April 2006 to March 2007. ....	69
Fig. 4.5. Monthly mean wind velocity averaged over 10 years (1999-2008) in the study area.....	70
Fig. 4.6. Map of the Pearl River Estuary showing sampling stations.....	72
Fig. 4.7. Measured and predicted water elevations at stations S09, and S25, S28 in July and October 2006.....	74
Fig. 4.8. Measured and predicted water elevations at stations S05, S16 in July and October 2006.....	74
Fig. 4.9. Measured and predicted water currents at stations S05 and S16 on 8th and 9th Jul, 2006.....	75
Fig. 4.10. Measured and predicted water currents at stations S05 and S16 on 19th and 20th Oct, 2006.....	76
Fig. 4.11. Measured and predicted salinity at the surface and near the bottom at stations S03, S05, S08 and S16 on 9th and 10th Sept, 2007.....	77
Fig. 4.12. Measured and predicted salinity at the surface and near the bottom at stations S03, S05, S08 and S16 on 18th and 19th Sept, 2007.....	78
Fig. 4.13. Measured and predicted salinity in sampling stations in (a) July 2006 (b) October 2006 (c) March 2007. ....	79
Fig. 4.14. Salinity distributions for real-time condition (case 1): (a) surface, wet season; (b) bed, wet season; (c) surface, dry season; (d) bed, dry season.....	81
Fig. 4.15. Water age distributions for real-time condition (case 1): (a) surface, wet season; (b) bed, wet season; (c) surface, dry season; (d) bed, dry season; vertical distribution along the west channel in the (e) wet season; (f) dry season.....	87
Fig. 4.16. Vertical salinity distribution along the west channel in the (a) wet season; (b) dry season.....	88



Fig. 4.17. Residual current fields in the wet season for the real-time condition (case 1): (a) surface; (b) bed; (c) vertical distribution of longitudinal component $v$ along the west channel.....	90
Fig. 4.18. Time series of depth-averaged freshwater age at S16 and its yearly mean value for real-time condition (case 1).....	91
Fig. 4.19. Total discharge and depth-averaged age at four stations over a year for real-time condition (case 1).....	92
Fig. 4.20. Monthly depth-averaged age $T$ (days) in response to the total river discharge $Q$ ( $m^3/s$ ) at four stations for real-time condition (case 1) .....	93
Fig. 4.21. Monthly depth-averaged age (days) at 15 stations under constant discharges.....	94
Fig. 4.22. Monthly averaged (a) vertical difference in the age and (b) depth-averaged age of April 2006 for case 3 (constant mean discharge and tides), case 5 (only tides without discharge) and case 6 (only mean discharge without tides) at 15 sampling stations.....	95
Fig. 4.23. Water age horizontal distributions at spring tide in the wet season for case 1 (a) at surface, high water; (b) near bed, high water; (c) at surface, low water; (d) near bed, low water.....	98
Fig. 4.24. Water age horizontal distributions at spring tide in the dry season for case 1 (a) at surface, high water; (b) near bed, high water; (c) at surface, low water; (d) near bed, low water.....	99
Fig. 4.25. Water age vertical distributions of along-channel section for case 1 (a) spring high water in the wet season; (a) spring low water in the wet season; (c) spring high water in the dry season; (b) spring low water in the dry season.....	100
Fig. 4.26 Temporal variation of water elevation, salinity vertical difference, water age vertical difference, and depth-averaged vertical eddy viscosity at S08 and S16: (a)-(d) July 2006; (e)-(h) January 2007.....	103
Fig. 4.27. Time series of (a) water level; (b) depth-averaged water age; (c) water age vertical difference; (d) water age vertical difference in percentage at S16 under high, mean and low discharges in June 2006.....	105
Fig. 4.28. Water age distributions for the barotropic mode (case 7): (a) surface, wet season; (b) bed, wet season; (c) surface, dry season; (b)bed, dry season; vertical distribution along the west channel: (e) wet season; (f) dry season.....	110
Fig. 4.29. The relation between the monthly averaged total discharge and depth-averaged age at S16 for cases 1 and 7.....	111
Fig. 4.30. Typical vertical distributions of residual current, salinity level $s'$ , tracer $c'$ , age concentration $\alpha'$ , and age (negative velocity is upstream and position velocity is downstream, negative value of concentration represents that concentration is lower	

than vertical mean concentration) adapted from Shen and Lin, 2006.....	112
Fig. 4.31. Vertical profile of current (u, v), tracer, age concentration, age, salinity and density at S16 over the spring tide in the wet season with $\Delta t = 40$ min for the baroclinic mode (a-h) and for the barotropic mode (a1-f1).....	116
Fig. 4.32. Horizontal age distributions without the influence of wind (case 8): (a) surface, wet season; (b) bottom, wet season; (c) surface, dry season; (d) bottom, dry season.....	118
Fig. 4.33. The age distributions of seawater for the real-time condition (case 1): (a) surface, wet season; (b) bed, wet season; (c) surface, dry season; (d) bed, dry season.....	121
Fig. 5.1. Illustration of the estuary division.....	126
Fig. 5.2 Cumulative averaged exposure time, average residence time and their corresponding relative remnant functions under the real-time condition (case 1) by initially releasing at segment 1 at the high water on 1st April, 2006, and observing in the entire estuary.....	129
Fig. 5.3. Average exposure time for the entire estuary with different initialised regions and times (cases 1–4).....	131
Fig. 5.4. Average residence time for entire estuary with different initialised region and time (cases 1–4).....	131
Fig. 5.5. The return coefficient for the entire estuary with different initialised region and time (cases 1–4).....	131
Fig. 5.6. Average residence time $t_r$ (days) and average exposure time $t_e$ (days) of the entire estuary in response to the freshwater discharge, with empirical best fitting equations in forms of power law, $Q$ is the total discharge.....	133
Fig. 5.7. The average exposure time (days) of each segment and the entire estuary in response to the river discharge under constant discharge (cases 5-7).....	134
Fig. 5.8. Illustration of sensitivity of average exposure time to tracer releasing water level. $\gamma$ is the ratio of predicted timescales released at low water to that released at high water.....	135
Fig. 5.9. Comparison of water exchange timescales when released from each segment or the entire estuary with and without density-induced circulation (case 1, case 11) (ARTM: average residence time; AETM: average exposure time).....	136
Fig. 5.10. The connectivity ratios for each segment by releasing the tracer from (a) segment 1; (b) segment 2; (c) segment 3; (d) segment 4 with starting time in four seasons or under mean flow condition (cases 1-4, case 6).....	139
Fig. 6.1. Map of the Severn Estuary and Bristol Channel showing sampling stations; Circles: Tidal currents observing sites S1 and S2; Squares: Tidal elevation observing	

sites Newport, Hinkley, and Mumbles.....	144
Fig. 6.2. Mesh of the Severn Estuary and Bristol Channel (UTM-30).....	145
Fig. 6.3. Fig. 6.3. Positions of arrays of tidal stream turbines with spring mean ebb currents as background (UTM-30): (a) one array of tidal stream turbines; (b) four arrays of tidal stream turbines.....	148
Fig. 6.4. Definition of turbine angles: $d$ is the diameter of turbine; $\theta_{flow}$ is the current direction; $\theta_{alignment}$ is the angle between projection north and alignment; $\theta$ is the angle between alignment and flow.....	149
Fig. 6.5. Measured and predicted water elevations at stations (a) Hinkley, (b) Mumbles, and (c) Newport. ....	151
Fig. 6.6. Measured and predicted tidal currents at stations (a) S1 and (b) S2.....	151
Fig. 6.7. Predicted depth-averaged salinity distributions in February 2002 (UTM-30): (a) at high water at Swansea; (b) at low water Swansea. ....	153
Fig. 6.8. Observed salinity distributions in February 1978 (Stephens, 1986): (a) at high water at Swansea; (b) at low water at Swansea.....	154
Fig. 6.9. Monthly depth-averaged age distributions for real-time condition (case 1) in February 2002 (a) for the baroclinic mode; (b) for the barotropic mode (c) the difference of baroclinic mode to the barotropic mode.....	157
Fig. 6.10. Map of the Severn Estuary and Bristol Channel showing the 15 sampling points.....	158
Fig. 6.11. Changes in water levels across the estuary at spring high water at Barry (see Fig. 6.2) after including the first turbine array from (a) the current study; (b) the two-dimensional simulation by Ahmadian et al., (2012).....	160
Fig. 6.12. Changes in depth averaged velocities across the estuary at mean ebb at Barry (see Fig. 6.2) after including the first turbine array from (a) the current study; (b) the two-dimensional simulation by Ahmadian et al., (2012).....	162
Fig. 6.13. Age difference after including (a) the first turbine array (b) the second turbine array averaged over February 2002, the positive values present an increase in age values.....	164
Fig. 6.14. (a) Positions of two sampling points P1 and P2 in the background of the age difference of Fig. 6.13a; Time series of parameters in February 2002: (b) average water level at two points; (c) age values at two points excluding the turbine module; age difference due to the turbine module at (d) P1 and (e) P2.....	166
Fig. 7.1. Position of cross-section F-G-H.....	171
Fig. 7.2 Depth profile along cross-section B, looking from downstream.....	172

Fig. 7.3. Depth profile along cross-section F-G-H, looking from downstream.....	172
Fig. 7.4. Average water levels at seven points over a tidal period.....	173
Fig. 7.5. Vertical profiles of speed at key moments at point G: (a) High water; (b) Mean ebb water; (c) Low water; (c) Mean flood water.....	174
Fig. 7.6. Vertical profiles of velocity at point B at (a) High water; (b) Mean ebb water; (c) Mean flood water.....	175
Fig. 7.7. Time series of depth-averaged velocity at point G perpendicular to the cross-section F-G-H, positive value represents towards upstream while the negative value represents towards downstream.....	176
Fig. 7.8. Time series of depth-averaged velocity at point B perpendicular to the cross-section B, the positive value represents towards upstream while the negative value represents towards downstream.....	177
Fig. 7.9. Measured tracer concentration at points F, G, H with distance to the bed of 5 cm, being injected at point A.....	179
Fig. 7.10. Measured tracer concentration at points F, G, and H with distance to the bed of 5 cm, being injected at point C.....	180
Fig. 7.11. Measured tracer concentration at point G with distances to the bed of 1cm, 5 cm and 10 cm, being injected at point A.....	181
Fig. 7.12. Measured tracer concentration at point G with a distance to the bed of 5 cm, being injected at point A, B, C, D, and E.....	182
Fig. 7.13. Measured tracer concentration at point J with a distance to the bed of 5 cm, being injected at point A, B, C, and E, respectively.....	181
Fig. 7.14. Water flux through cross-section B over a tidal period; positive values represent velocity directed towards upstream.....	182
Fig. 7.15. Time series of tracer flux through cross-section B; positive values indicate towards upstream.....	183
Fig. 7.16. The water flux through the cross-section F-G-H over a tidal period; the positive values represent towards upstream while the negative values represent towards downstream.....	183
Fig. 7.17. Time series of tracer flux through the cross-section F-G-H, the positive values represent towards upstream while the negative values represent towards downstream.....	184
Fig. B.1. Bathymetry of the Pearl River Estuary (left); Illustration of the vertical 10-level sigma layers of along-channel section (left dash line) in the model (right).....	201
Fig. D.1. Sensitivity test of roughness height at S16 in Jun, 2006. Points: measured	

data; Line: predicted.....	216
Fig. D.2. Sensitivity test of roughness height at S16 in Oct, 2006. Points: measured data; Line: predicted data. ....	216

# List of Tables

Table 2.1 A summary of hydrodynamic characteristics of two estuaries applied in this study.....	27
Table 3.1. The prepare procedure of solutions with different concentrations.....	58
Table 3.2. Readings from three fluorometers of standard levels of solutions for calibration.....	60
Table 4.1. Measured monthly averaged river discharges of eight tributaries in 2006.....	66
Table 4.2. Monthly mean wind velocity averaged over 10 years (1999 – 2008) in study area.....	69
Table 4.3. A summary of the measured data for the Pearl River Estuary from 2006 to 2007.....	71
Table 4.4. The mean absolute errors (psu) and root-mean-square errors (psu) between the predicted and measured salinity values.....	77
Table 4.5. A summary of the forcing conditions used in the model simulations.....	81
Table 4.6. Depth-averaged AW (unit: days) at four stations along the west channel and the total discharge (unit: $m^3/s$ ) in each month over one year.....	91
Table 4.7. Empirical fitting equations between the total river discharge and the age at four stations and correlation R-squared values (Q: discharges; T: age).....	92
Table 4.8 The comparison of the monthly depth-averaged age at station S16 for case 1 and case 7 over one year and the difference between two cases.....	110
Table 5.1. A summary of model scenarios for the Pearl River Estuary... ..	126
Table 5.2. Average residence time (days), average exposure time (days) for the entire estuary with different releasing times and regions (Cases 1-4) .....	129
Table 5.3. Average exposure time (days) for the entire estuary by releasing at high water or low water (cases 5–10) .....	134
Table 5.4. Average exposure time by observing in each segment with the starting time at high water (a) on 1st Apr, 2006; (b) on 1st Jul, 2006; (c) on 1st Oct, 2006; (d) on 1st Jan, 2007.....	137
Table 6.1. A summary of the model scenarios for the Severn Estuary and Bristol Channel.....	155
Table 6.2. Surface and bed age values (days) at 15 sampling point.....	158
Table 7.1. Measurement arrangements.....	171

Table 7.2. Calculated mean travel time between points in each test.....	178
Table A.1 Empirical constants in the $k-\epsilon$ model.....	193
Table A.2 Astronomical arguments (Pugh, 1987).....	200
Table A.3 Nodal modulation terms (Pugh, 1987).....	200
Table D.1. A summary of the model set up attributes of Pearl River Estuary.....	216
Table D.2. A summary of the model set up attributes of the Severn Estuary and Bristol Channel.....	217

# Nomenclature

## Roman Symbols

$a(t, \vec{x})$	mean water age at time $t$ , location $\vec{x}$ and age $\tau$
$A$	horizontal eddy viscosity
$A_e$	effective area of turbine exposed to current
$A_i$	the volume of the cell
$b$	bottom control parameter
$b_i$	phase based on the motion of the moon and the sun relative to the earth
$B$	buoyancy production term
$c(t, \vec{x}, \tau)$	tracer concentration time $t$ , location $\vec{x}$ and age $\tau$
$C$	concentration of scalar quantity
$C(t, \vec{x})$	tracer concentration
$c_a, c_b, w_a$ and $w_b$	empirical factors
$c_d$	drag coefficient of air
$C_D$	drag coefficient
$c_s$	constant number
$c_\mu$	empirical constant
$C_L$	lift coefficient
$C_s$	concentration of scalar quantity at the source
$d$	still water depth
$d\theta$	normalised time step
$ds$	the integration variable along the boundary
$d\rho/dz$	vertical gradient of the water density
$D_h$	horizontal turbulent (eddy) diffusion coefficient
$D_v$	vertical turbulent (eddy) diffusion coefficient
$e_i$	correction for earth tides based on Love numbers
$\hat{E}$	evaporation rate
$E(\theta)$	normalised concentration
$f$	Coriolis parameter
$f_i$	nodal factor
$\vec{F}$	the flux vector function
$F_c$	horizontal diffusion term
$F_k, F_\varepsilon$	horizontal diffusion terms for $k$ and $\varepsilon$
$F_s$	horizontal diffusion term
$F_u, F_v$	horizontal stress term in $x, y$ directions



$g$	gravitational acceleration
$h$	total water depth
$h_{dry}, h_{flood}, h_{wet}$	Three parameters to define the cell is dry, flood or wet
$h_{\sigma}$	a fixed fraction of the total depth of the sigma layer
$H_i$	amplitude
$i$	constituent number
$k$	turbulent kinetic energy per unit mass
$k_s$	roughness height
$k_p$	linear decay rate of scalar quantity
$k_p$	linear decay rate of scalar quantity
$\vec{K}$	diffusivity tensor
$l$	characteristic length
$M$	Manning number
$M(t_0)$	mass of material in the interested region at an initial time $t_0$
$M(\tau)$	mass of material continually staying in the region after time $\tau$
$\vec{n}$	the unit outward normal vector along the boundary
$n_j$	the unit outward normal vector at the $j^{th}$ side
$N$	buoyancy frequency
$N_B$	Brunt-Väisälä frequency
$NS$	the number of sides of the cell
$N_{\sigma}$	a constant number of layers in the sigma domain
$r(\tau)$	remnant function for residence time
$s$	salinity level
$\bar{S}$	mean flow shear
$s_s$	salinity source
$s'$	depth varying parts of salinity
$S$	magnitude of the discharge due to point sources
$\vec{S}$	vector of source terms
$S_{ij}$	deformation rate
$t$	time
$t_0$	initial time
$T$	temperature
$T_m$	mean travel time
$T_i$	period of the constituent
$i$	concentration sample number
$i_0$	the species
$i_1$ to $i_5$	Doodson numbers

$Ri_g$	gradient Richardson number
$P$	shear production term
$\hat{P}$	precipitation rate
$P_a$	atmospheric pressure
$Q$	discharge
$Q_R$	river volume flux
$u, v$ and $w$	the velocity components in the x, y and z directions
$\bar{u}, \bar{v}$	depth-averaged velocities in x, y directions
$u'$	depth varying part of velocity
$\vec{u}$	velocity field
$\vec{u}_b$	flow velocity above the bottom.
$u_s, v_s$	velocity by which the water is discharged into the ambient water
$\vec{u}_w$	wind speed 10 m above the sea surface
$\vec{U}$	vector of conserved variables
$U_{\tau b}$	friction velocity associated with the bed stress
$U_{\tau s}$	friction velocity associated with the surface stress
$V$	current speed
$w_{10}$	wind velocity 10 m above the sea surface
$x, y$ and $z$	Cartesian co-ordinates
$z_0$	bed roughness length scale

## Greek Symbols

$\alpha(t, \vec{x})$	age concentration
$\alpha$	correction factor
$\Delta z_s$	distance from the surface
$\Delta z_b$	distance from the bottom
$\Delta \Gamma_j$	the length/area of the $j^{\text{th}}$ interfac
$\eta$	surface elevation
$\eta_{ACTUAL}$	actual elevation
$\eta_T$	equilibrium tidal potential
$\kappa$	von K árm án constant
$\Omega$	interested region
$\nu_t$	vertical eddy viscosity
$\varphi$	angular rate of revolution
$\phi(\tau)$	distribution function of residence time
$\rho$	density of water
$\rho_0$	reference density of water
$\rho_a$	density of air
$\rho_w$	density of water

$\sigma_c$	weighting factor between the equidistant distribution and the stretch distribution
$\sigma_i$	discrete $\sigma_i$ levels in the discretization in the sigma domain
$\sigma_k, \sigma_\varepsilon, c_{1\varepsilon}, c_{2\varepsilon}$ and $c_{3\varepsilon}$	empirical constants
$\sigma_T$	Prandtl number
$\theta$	normalised time
$\theta'$	angle between alignment and flow
$\theta_{alignment}$	angle between projection north and alignment
$\theta_{flow}$	current direction
$\theta_{return}$	return coefficient
$\tau_r$	average residence time
$\bar{\tau}_b$	bottom stress( $\tau_{bx}, \tau_{by}$ )
$\tau_{bx}, \tau_{by}$	x and y components of the bottom stresses
$\tau_e$	average exposure time
$\tau_{Err}^n$	relative error of the accumulative average residence time
$\tau_{sx}, \tau_{sy}$	x and y components of the surface wind
$\gamma_{i,j}$	the ratio of the time spent in subdomain $\Omega_j$ and the total time spent in the interested domain, by tracer initially released in subdomain $\Omega_i$ .
$\varepsilon$	dissipation rate of turbulent kinetic energy
$\Gamma_i$	boundary of the ith cell
$\xi$	$\xi = z/H$ , H is the total depth

# Abbreviate

AW	Age of Water
ATRM	Average Residence Time
AETM	Average Exposure Time
ET	Exposure Time
PRE	Pearl River Estuary
SEBC	Severn Estuary and Bristol Channel
RT	Residence Time
TKE	Turbulent Kinetic Energy

# **Chapter 1**

---

## **Introduction**

## 1.1 BACKGROUND

Many estuarine systems around the world are facing serious environmental problems, such as increased biomass of phytoplankton and dissolved oxygen depletion, especially those located near rapidly developing regions. The water exchange process plays a vital role in controlling estuarine water quality (Sheldon and Alber, 2002; Simons et al., 2006). When the water exchange ability in an area decreases, persisting accumulation of pollutants in the water body may occur, causing deterioration of hydro and eco-environment due to, for example, eutrophication, as well as the decrease of aquaculture yield potential (MacDonald, 2006). Adequately controlling the water exchange process could improve the estuarine water quality condition. An improved understanding of the water exchange process can provide solutions for environmental management of estuaries and adjacent water bodies.

The water exchange process depends heavily on the hydrodynamic characteristics, such as discharge, tides, wind, and density-induced circulation. Among them, the density-induced circulation is a fundamental factor that controls the stratification formation in estuarine waters. Density-induced circulation and stratification-induced poor vertical mixing can reduce water exchange ability, particularly near the bed. As a result, hypoxia phenomenon and oxygen-depleted “dead zones” would form. However, little research has been done to investigate the influence of density-induced circulation and stratification on the water exchange process in estuarine waters, resulting in an inadequate understanding of water exchange timescales, which are regarded as a useful methodology for quantifying the water exchange and mixing.

Therefore, this study intends to shed some light on this point in order to better understand the use of exchange timescales in estuarine water exchange process studies. In the present study, a three-dimensional age of water (AW) model is to be built based on the hydrodynamic model MIKE 3. Two independent timescales, i.e.,

exposure time and residence time, are traditionally used as the overall retention time to quantify the entire water body of an estuary or to investigate the water exchange mass between its different segments. The residence time is “the time it takes for any water parcel of the sample to leave the lagoon through its outlet to the sea” (Dronkers and Zimmerman, 1982). It also presents the time required to remove pollutants out of the area of interest, and it is a critical factor for assessing its water quality. Compared with residence time, the exposure time on the other hand, measures the total time a water parcel spends in an estuary including the time it leaves and re-enters the control domain. When the water exchange process in an estuary is complex due to the interactions of dynamical processes in multiple spatio-temporal dimensions, the AW, which is time- and location-dependent, has been identified as a fundamental water exchange timescale and is increasingly used in analysing the water exchange process and its spatial variations (Monsen et al., 2002; Delhez et al., 2004a; de Brauwere et al., 2011). Bolin and Rodhe (1973) introduced the concept of timescale ‘age’. Zimmerman (1976) defined the AW as the time elapsed since the water parcel departed from the region where the AW was prescribed to be zero. Deleersnijder et al. (2001) introduced the constituent-oriented age and residence time theory, which is a general theory based on an Eulerian approach, providing a set of equations for predicting the spatial and temporal AW distributions of every water constituent or group of constituents (Deleersnijder et al., 2001, 2002).

The developed AW model is examined with applications to two estuaries – with very different features – as case studies, namely the Pearl River Estuary (PRE) and the Severn Estuary and Bristol Channel (SEBC). The PRE is situated along the northern shelf of the South China Sea; it is a typical estuary experiencing tidal fluctuation and significant seasonally varying freshwater discharge (Dong et al., 2004). As a link between the limnetic environment through eight tributaries and the marine environment, the upstream–downstream physical structure in the PRE varies primarily in response to the interaction of discharge and tidal mixing. Density gradient drives a baroclinic forcing and creates a vertical circulation, leading to apparent

three-dimensional dynamical characteristics (Wong et al., 2003a, b). Furthermore, the Pearl River Delta has experienced rapid socio-economic changes and increased nutrient input over the past three decades. An estimated  $5.6 \times 10^8$  tons of domestic wastewater and  $5.5 \times 10^9$  tons of industrial effluent are discharged into the estuary annually (Chen and Ruan, 1994; Dai et al., 2006). The wastewater discharge has caused serious environmental problems in this area, including persistent hypoxia and nutrient-related algal blooms (Dai et al., 2006, 2008). The hydrodynamic process of the PRE has been studied using mathematical models and field observations, including salinity and temperature distributions, circulation and tidal phenomena, to examine the water environment (Wong et al., 2003a, b; Harrison et al., 2008). However, in such a spatially varying situation, it is difficult to separate the underlying dynamics' contributions to the transport properties. The predicted AW distributions are used to determine the spatial distribution of the dissolved substances' retention time and its temporal variation in response to dynamic conditions.

The SEBC constitutes a large, semi-enclosed body of water in the southwest of the UK with its length of approximately 200 *km*, covering an area of 5700 *km*<sup>2</sup> (Falconer et al., 2009). This area is well known for its large tidal range and its great tidal energy, having the second highest tidal range in the world of approximately 7–14 m and the peak tidal currents in excess of 2 m/s. Due to the macro-tidal regime and the strong tidal current, the hydrodynamic phenomenon in this estuary is well-mixed. This is very different from the partially stratified phenomenon in the PRE. By running the simulation for the baroclinic mode and the barotropic mode, respectively, the influence of density-induced circulation on estuarine water exchange process in two above estuaries is analysed based on predicted exchange timescales.

In addition, the great tidal energy has made the SEBC very attractive from a renewable energy point of view and a number of tidal renewable energy schemes have been proposed to be sited here, including tidal stream turbines with different array shapes (Ahmadian et al., 2012a, b). In the current study, a turbine module is



developed for inclusion within the AW model to simulate two different tidal turbine arrays in the SEBC. The impact of turbine arrays on the surrounding hydrodynamics and water exchange process is analysed based on spatial AW distributions. The modelling results can be used to optimise the position selection of turbines with aim of reduced environmental impact and high tidal energy extraction.

## **1.2 OBJECTIVES OF THE STUDY**

From the above introduction, the main aim of this study is to demonstrate the significance of proposed exchange timescales in quantifying estuarine water exchange process. The objectives of this study are centred on:

- 1) Developing a three-dimensional AW model based on the advanced hydrodynamic model MIKE 3. Calibrating and validating the model by the field data from the PRE and the SEBC.
- 2) Applying the model to estimate the AW distributions in a partially stratified micro-tidal estuary and a well-mixed macro-tidal estuary, i.e., the PRE and the SEBC, respectively. Analysing the AW distributions and their spatio-temporal variations and conducting a series of model scenario simulations. Comparing the density-induced influence on AW distributions in these two different estuaries.
- 3) Predicting the overall exchange timescales, i.e., the average residence time and the average exposure time, in the PRE. Investigating the water exchange process between different segments of the estuary by connectivity ratios.
- 4) Developing a turbine module for inclusion within the AW model to simulate the impacts of the proposed tidal stream turbines in the SEBC with two different turbine arrays on the surrounding hydrodynamics and water exchange process

based on AW distributions.

- 5) Undertaking a three-dimensional physical model investigation into the water exchange process in a scale model of the SEBC by measuring the average travel times between points, the water flux and the tracer flux through cross sections. The measurements include water elevation, flow velocity and tracer concentration curves.

### **1.3 OUTLINE OF THE THESIS**

This thesis consists of seven chapters. This is the first chapter to describe the background of the research, as well as the aims and objectives of the study.

Chapter 2 reviews the literatures related to the water exchange study in estuarine system, particularly in stratified estuaries and also introduces the water exchange timescales applied in the current study including their definitions and applications. Two estuaries, i.e., the PRE and the SEBC are described in Chapter 2.

Chapter 3 presents the governing equations of the developed AW model applied in this study, together with calculation methods for the timescales.

In Chapters 4 and 5, the AW model is utilised to predict the water exchange timescales in the PRE in response to the hydrodynamic conditions by conducting a series of model scenario simulations, and the results are discussed.

Chapter 6 presents the numerical modelling study of water exchange timescales conducted in the SEBC. The scenario analyses are performed, the impact of density-induced circulation is analysed and compared with the results in the PRE. The influence of proposed tidal stream turbines on the hydrodynamics and water exchange

process are investigated based on predicted AW distributions.

Chapter 7 describes a physical investigation into the water exchange process in the fiberglass model of the SEBC based on mean travel time between points and flux calculation.

Chapter 8 summarises the conclusions and recommendations on the future work.

## **Chapter 2**

---

### **Literature Review**

## **2.1 WATER EXCHANGE IN ESTUARINE SYSTEM**

Estuaries act as a link, connecting the land and the ocean which are easily contaminated by the upstream limnetic environment. Many estuaries in the world have experienced environmental problems over the past decades, especially those located near rapidly developing regions. Economic development and urbanisation have significantly increased nutrient inputs, and other discharged pollutants to the estuarine waters. This has brought severe adverse impacts on the estuarine environment, which have the potential to degrade water quality, and consequently have deleterious effects on aquatic organisms and human health through the food chain. This has increasingly caused concerns to the environmental management of estuaries and coastal seas (Fukumoto and Kobayashi, 2005; Kemp et al., 2005).

The published studies indicated that both the amount of discharged pollutant and the water exchange process have significant influences on the estuarine ecosystem. The estuarine water exchange process includes water transport between an estuary and its tributaries and adjacent coastal seas, which finally transports dissolved substances out of the estuary. The water exchange process plays a critical role in controlling the chemical and biological processes, and consequently greatly affects several other processes, including retention of autochthonous materials and ingress of planktonic larvae (Lowery, 1988; Sheldon and Alber, 2002; Hare et al., 2005). When the water exchange ability decreases, the persisting accumulation of pollutants in the water body may cause environmental problems, such as eutrophication and the decrease of aquaculture potential capability (MacDonald, 2006; Simons et al., 2006). Therefore, the exchange rate is an important factor to determine the fate of contaminated

substances.

Previous studies have mainly focussed on the contributions of different hydrodynamic parameters to the water exchange process. Yanagi and Hinata (2004) analysed the water exchange time scale between Tokyo Bay and the Pacific Ocean and indicated that the water exchange time mainly depended on the strength of the northerly monsoon during winter. Moreover, the water exchange time becomes longer when the warm water mass is blocked in the surface layer at the bay mouth. Based on a two-dimensional model of Yangtze Estuary and Hangzhou Bay, Kong et al. (2007) studied the characteristics of water and sediment exchange between these two water bodies, and indicated that the hydrodynamic mechanisms have significant influences on the water exchange, including tidal range, tidal current kinetic energy, tide-induced residual currents and the trace of water particles. Li et al. (2008) analysed the impact of the Xuanmen Dam project and other recent land reclamation projects on the water exchange in Yueqing Bay, Zhejiang, China. Increase of 6 days and 4.5 days in semi-exchange time were observed near the dam and at the bay end, respectively, and this was caused by the dam. Gong et al. (2009) indicated the important role of wind in regulating stratification, estuarine circulation, and transport timescale in estuaries based on the concept of water age in the tidal Rappahannock River – a western tributary of Chesapeake Bay, USA. The above studies indicated that these parameters, such as river discharge, tide, wind, density-induced circulation and variation of bed level, may have different influences in estuarine waters. However, little research has been done to investigate the influence of density-induced circulation and stratification on estuarine water exchange process based on the exchange timescales.

Studies linking the water exchange with environmental processes, e.g. larval transport,

nutrient budget, and sediment plumes have been undertaken to provide better information for environmental assessment. James and Sreedharan (1983) used the modified tidal prism theory to study the water exchange in the Beypore Estuary of the Chaliyar River on the Malabar Coast. The exchange ratios for different volume segments were computed to determine the permissible industrial pollutant budget. Pejrup et al. (1993) conducted a water exchange modelling study based on the conservation of saltwater and freshwater to predict the concentration of nutrients and nutrient net budget. Stoschek and Zimmermann (2006) used a three-dimensional numerical model to simulate the water exchange and sediment transport in the Weser River with the aim of minimising sedimentation in harbours, which may affect the water quality in the areas.

Investigations into the estuarine water exchange process have been conducted by numerical modelling (Ribbe et al., 2008; de Brauwere et al., 2011; de Brye et al., 2012) or based on field surveyed data (Lin et al., 1990; Yanagi and Hinata, 2004). Simple box models and two-dimensional models were used in some water exchange studies (James and Sreedharan, 1983; Kong et al., 2007; Yuk and Aoki, 2009). However, the water exchange process is driven by several complex hydrodynamic factors. The current field and associated circulations are usually spatially varying. Three-dimensional models which predict complicated dynamics of boundary layers more accurately could better estimate the estuarine hydrodynamics (Shen and Hass, 2004; Wang et al., 2004; Liu et al., 2008).

Water exchange time scales have been increasingly used in estuarine water exchange process research in recent years. Lin et al. (1990) investigated the water exchange in the Pearl River Estuary (PRE) by using three different numerical tools: estuary

seawater exchange ratio, flushing time and water exchange ratio. With an application to Kraka (Adriatic Sea), Legović (1991) presented a method of computing the exchange time of freshwater and seawater in the stratified estuary based on river inflow, depth of the halocline and salinity in the upper brackish water layer. Ribbe et al. (2008) assessed water renewal time scales for marine environments in a case study of Hervey Bay, Australia. Brye et al. (2012) studied the water age, residence time and exposure time in the Scheldt Estuary to characterise the water exchange dynamics in this estuary

## **2.2 DENSITY-INDUCED CIRCULATION AND STRATIFICATION**

Linking between the limnetic and marine environments, estuaries are always characterised by a variety of complex and complicated processes. Generally, the upstream–downstream physical structure inside the estuary varies mainly in response to the interaction of the freshwater discharge, friction and tidal mixing. Therefore, one typical and important estuarine phenomenon is the mixing zone between the light freshwater and heavy saline water which form the density gradients vertically in the water column and spatially in the area. The density gradients act a baroclinic forcing and create a circulation. The density-induced circulation was initially proposed by Pritchard's work in the James River (1952).

In estuaries with an intense saltwater intrusion and large density gradients, the density-induced circulation plays a significant role in water characteristics and controls the water exchange process where the density variable distribution couldn't



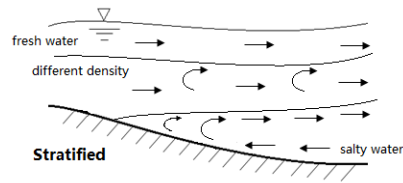
be ignored. Moreover, in stratified estuaries, the stratification forms layers that act as barriers to the vertical mixing which is also not negligible.

### 2.2.1 Stratification classification

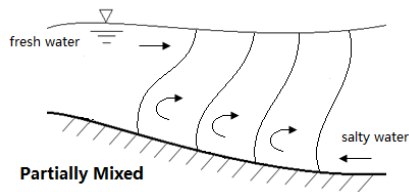
In general, density gradients are created by the freshwater discharge, and saline waters from the coastal shelf, in addition to heat input during high insolation periods. Among these features, the changes in salinity always play a dominant role, as the fresh river discharge mixes and dilutes with the saline seawater. Density gradients occur and drive the baroclinic forcing:  $\frac{g}{\rho_0} \int_z^\eta \frac{\partial \rho}{\partial x} dz$ ,  $\frac{g}{\rho_0} \int_z^\eta \frac{\partial \rho}{\partial y} dz$  (Equations 3.2 and 3.3), which varies with depth, and thus a two-layer structure is present in the estuary: the lighter freshwater in the surface layers and the heavier saline water in the lower layers. As a consequence, the freshwater is mainly transported from the surface, while the saline water flows upstream near the bed (which is opposite to the surface water in direction) and a density-induced circulation can be observed. In an estuary, this circulation together with strong advection transport by river discharge will enhance the vertical density difference of the estuary, and bring a stratified hydrodynamic phenomenon. If the estuary is quite large, Coriolis effects may also be evident. These factors in combination with morphology of the study area lead to varying degrees of stratification.

There is a corresponding classification of estuary based on the type of stratification occurring: highly stratified, partially stratified and well mixed – as shown in Fig. 2.1 (Dyer, 1973). In a highly stratified estuary, the freshwater flows over a deeper layer of dense seawater (Fig. 2.1a). This seawater layer extends from the coastal shelf to the inside of the estuary, reaching the upstream of the estuary. Such estuaries exist where

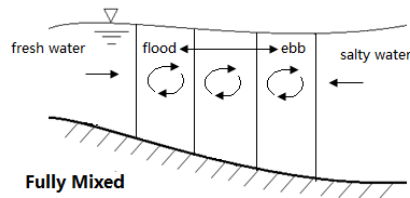
river discharge is large and dominates tidal motions.



(a)



(b)



(c)

Fig. 2.1. Classification of estuaries based on the stratification levels: (a) highly stratified; (b) partially mixed; (c) fully mixed.

Some estuaries are seasonally stratified, such as the PRE. Due to the large discharge in the wet season, this micro-tidal estuary is stratified. For a partially mixed estuary, the vertical mixing causes the seaward density to increase in both upper and lower layers (Fig. 2.1b). The bed salinity level is slightly higher than the surface. The stratification phenomenon is mainly regulated by the tidal cycles. The density

distribution is more stratified during ebb tides. For a fully mixed estuary vigorous mixing, caused by tidal currents or wind, produces the vertical density distribution more uniform (Fig. 2.1c).

### 2.2.2 The stratification stability

An incompressible flow with density increasing with depth can be seen as a stable stratified flow (Hansen and Rattray, 1965). The relative stability of the stratified flow can be described by the gradient Richardson number  $Ri_g$ :

$$Ri_g = N^2 / \bar{S}^2 \quad (2.1)$$

where  $\bar{S} = \sqrt{(\partial u / \partial z)^2 + (\partial v / \partial z)^2}$  represents the mean flow shear,  $u$  and  $v$  are mean velocity components.  $N$  is the buoyancy frequency, which is indicative of the water column stratification level (Pond and Pickard, 1983):

$$N^2 = -g / \rho (d\rho / dz) \quad (2.2)$$

where  $d\rho / dz$  represents the vertical gradient of the water density,  $g$  is the gravitational acceleration. If the  $Ri_g < 0.25$  or  $\log_{10}(Ri_g^{-1}) > 0.60$ , the flow is unstable and the turbulence mixing is enhanced, whereas when  $Ri_g > 0.25$  or  $\log_{10}(Ri_g^{-1}) < 0.60$ , the flow is stable and the mixing is inhibited. In other words, when  $Ri_g$  is large, the stratification is strong enough to prevent the shear instability.

It can be seen from Equation 2.1 that the stability of stratification is determined based on the relative importance of stratification and mixing. These two processes may have

temporal and spatial variations (e.g., wet and dry seasons, spring and neap tides).

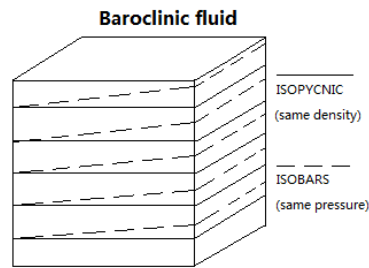


Fig .2.2. Illustration of a baroclinic fluid

Marshall et al. (2002) suggested that baroclinity is an important factor in maintaining stratification. For a baroclinic flow, its density distribution depends on pressure, temperature and salinity. Baroclinity is a measure of how misaligned the gradient of pressure is from the gradient of density in a fluid, which is proportional to the sine of the angle between the surfaces of constant pressure and density – as shown in Fig. 2.2 (Holton et al., 1992). The baroclinic flow forms the stratification and maintains its stability. When the stratification is strong enough to prevent the instability with large Richardson number, the stratification phenomenon is stable.

From the literature, it can be seen that several studies have been done to investigate the influence of the density-induced circulation and stratification phenomenon on the hydrodynamics. Zheng et al. (2002) built a three-dimensional nonlinear baroclinic numerical model to simulate the fresh and salt water mixing process in the Yangtze River Estuary. The results showed that the salinity distribution had the characteristics of a partial mixing pattern. Yuk and Aoki (2008) discussed the water transport and the vertical mixing under the density-stratified condition during the summer based on the field observations.

During the flood, the density gradient is in accordance with the water elevation gradient, thus the stratification may increase the flood current speed. During the ebb, these two gradients are opposite, thus the ebb current speed could be reduced (Fig. 2.3).

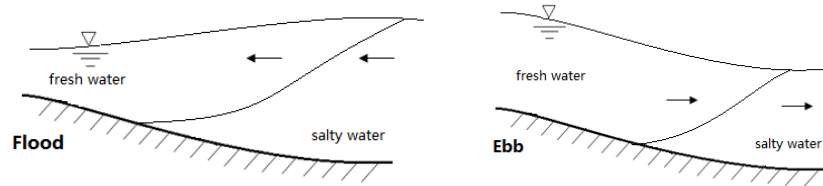


Fig 2.3. Illustration of salty water gradient and water elevation gradient during the flood and the ebb.

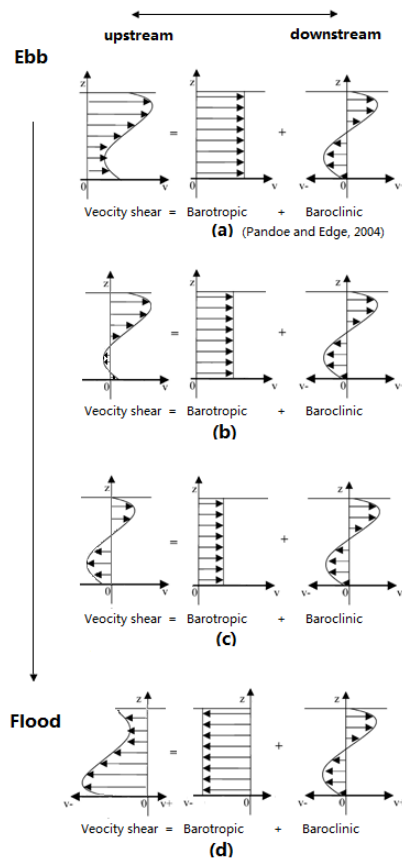


Fig. 2.4. The influence of barotropic and baroclinic terms on the vertical velocity (a) Ebb period, (Pandoe and Edge, 2004); (b) – (c) When the ebb changes to the flood; (d) Flood period.

Pandoe and Edge (2004) indicated that density-induced circulation may bring

different influences to current speed in the upper and lower layers over a tidal cycle (Fig. 2.4). The direction of the baroclinic current is downstream at the surface, while it is upstream near the bed. During the ebb, the baroclinic and barotropic terms could be additive producing high acceleration in the upper layers (Fig. 2.4a). However, the baroclinic current decreases the seaward ebb current speed in the lower layers. When the ebb changes to the flood, if the baroclinic current is more pronounced, the bottom water may flow upstream, which is opposite to the surface water in directions (Fig. 2.4b, c). During the flood, the contribution of baroclinic current is different from that during the ebb (Fig. 2.4d). It decreases the speed of surface current, while increasing the bottom current speed.

From the above research, it can be seen that in stratified estuaries, stratification and density-induced circulation play significant roles in estuarine hydrodynamics. Some studies further investigated their influences in practical applications with issues of concern, such as the concentration distributions of nutrients, hypoxia locations and sediment transport. Stratification is believed to be an essential condition for the formation of hypoxia on continental shelves (Rabalais and Gilbert, 2009). About half of the oxygen-depleted “dead zones” include regular summer stratification with predictable oxygen depletion. Wan et al. (2012) revealed that stratification contributes to the water hypoxia in the estuary. Wang et al. (2012) revealed that in the Yangtze River Estuary, China, the geographical displacement of the hypoxic zone was controlled by the seasonal changes in the regional water column stratification.

Moreover, Pandoe and Edge (2004) indicated that in the case of an idealised tidal inlet in stratified water, the inclusion of a baroclinic term can demonstrate the prevailing alongshore sediment transport. Primo et al. (2012) indicated that the vertical

distribution and migration pattern of ichthyoplankton assemblage in the Mondego Estuary are related to seasonal stratification and river flow, increasing amplitude during periods of less stratification and lower water currents. Williams et al. (2012), in a case study, revealed that the highest concentrations of larvae occurred at sites with a large vertical difference in salinity.

## **2.3 WATER EXCHANGE TIMESCALES**

As introduced in Section 2.1, the estuarine environmental problems due to the water exchange rate have received increasing attention in recent years and the methods of water exchange study are various. As auxiliary variables, water exchange timescales are increasingly applied to quantify the complex spatio-temporal structure of the transport process in estuarine waters, such as the age of water, residence time, exposure time, and travel time (Zimmerman, 1976; Takeoka, 1984; Deleersnijder et al., 2001; Monsen et al., 2002; Delhez et al., 2004a, b).

There are two advantages for applying water exchange timescales concepts in estuarine study. Firstly, it is clear that they are holistic as statistical methods which can take into account all of the results and processes. Secondly, the accurate predictions of a hydrodynamic model traditionally rely on the model calibration and verification by limited time series data recorded at fixed locations. The long-term transport process is difficult to assess. Characteristics of the transport processes for a dissolved substance in an estuary depend primarily on the low-frequency residual flow that is impacted by the interactions among density field, river flow, wind, and the non-linear rectification of the periodic tides. Therefore, due to the high variation

of dynamics for most estuaries, it is generally difficult to separate and quantify the influences of hydrodynamic mechanisms on the long-term transport process of a substance. The timescales can be used to understand the underlying dynamics contributing to the transport properties and provide a direct quantitative insight into the rate of functioning of the estuarine water exchange process. This turns out to be very valuable in an interdisciplinary environment from a management perspective (Delhez et al., 2004b; Shen et al., 2007).

Among various timescales, independent timescales, such as the exposure time and residence time, are traditionally used as the overall retention time to quantify the entire water body or investigate the water exchange mass between different segments. While for an estuary with spatial variations, the age of water has always been identified as a fundamental technique and used as an independent variable to quantify distribution of retention time in a three-dimensional space (Beckers et al., 2001; Monsen et al., 2002; Shen et al., 2004; Shen et al., 2007).

### **2.3.1 Residence time and exposure time**

A first-order water exchange timescale “residence time” (RT) is a measure of water-mass retention time within defined boundaries. It is defined as “the time it takes for any water parcel of the sample to leave the lagoon through its outlet to the sea” (Dronkers and Zimmerman, 1982). It also presents the time required to remove pollutants out of the system that is critical to the water quality. The RT is a parameter that represents the timescales of physical transport processes and is often compared with the timescales of biogeochemical processes. A short residence time is beneficial to the pollutant removal. However, with the excess pollutant loadings, the water



quality remains poor throughout an estuary in spite of a short residence time.

Bolin and Rodhe (1973) introduced the concept of ‘age’ of a water particle remaining in a water body. Zimmerman (1976) introduced the name of the RT as a complement of age, which is defined as the remainder of the lifetime of a particle considered. Takeoka (1984) introduced general properties of the RT in coastal sea and derived the average residence time for an ideal one-dimensional channel based on solving the advection-diffusion equation. For the RT, measurement stops as soon as the water parcel leaves the estuary for the first time. While the exposure time (ET), on the other hand, measures the total time a water parcel spends in the estuary including the time after it leaves and re-enters the control domain (Monsen et al., 2002; Delhez and Deleersnijder, 2006). The ET is especially relevant in macro-tidal estuaries, such as the Seven Estuary, UK, because the water is prone to leave the estuary at ebb, and re-enter at flood, many times before leaving forever.

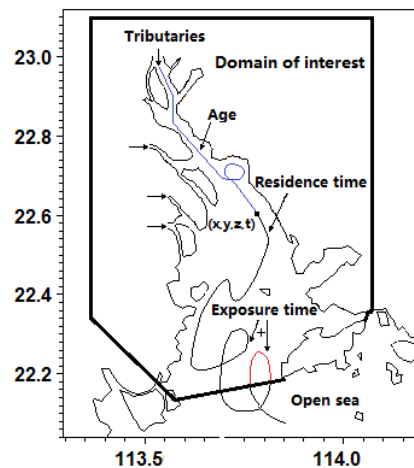


Fig. 2.5. Transport path of a water parcel released from the inlet of Humen inside the Pearl River Estuary as an example to present three timescales.

There are primarily three numerical modelling methods to calculate the RT or ET in

recent studies. The first method is based on the Lagrangian particle-tracking simulation (Tartinville et al., 1997; Luther and Haitjema, 1998; Miller and Luther, 2008). Liu et al. (2011) calculated the AW and RT of the Danshuei River estuarine system by a Lagrangian particle-tracking simulation. Oliveira et al. (2006) and Dias et al. (2009) used a three-dimensional hydrodynamic model in conjunction with a two-dimensional particle-tracking model, VELApart, to compute RT for passive tracers in a lagoon in Portugal. Burwell et al. (2000) used three-dimensional Lagrangian models to calculate the RT in Tampa Bay, Florida. However, this method requires a large number of particles for a reliable solution to be obtained (Spivakovskaya et al., 2007).

The second method is based on the constituent-oriented age and residence time theory based on the Eulerian approach (Delhez et al., 1999; Deleersnijder et al., 2001). de Brye et al. (2012) computed the RT and ET at each grid point and time step by solving an advection–diffusion–reaction equation backward in time.

The third method is estimating the average exposure time (AETM) and the average residence time (ARTM) based on Eulerian approach by using a passive conservative tracer as a surrogate (Arega et al., 2008; de Brauwere et al., 2011). At some instant of time  $t_0$ , the tracer can be uniformly introduced with a concentration of 1 g/L in the interested domain. The total masses  $M_{(t_0+t)}$  remaining in the domain with and without the re-enter portion can be seen in Fig. 2.6. The ARTM and AETM of an estuary, or a segment of the estuary, could be calculated by releasing the tracer from its own area. The water exchange between segments could also be investigated based on connectivity ratios calculated by AETM.

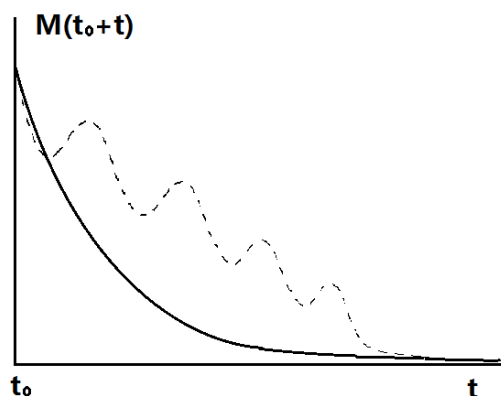


Fig. 2.6. Mass of tracer remains in model domain. The solid line is based on the definition of average residence time calculation; the dot line is based on the definition of average exposure time calculation.

In recent years, several successful applications on RT and ET have been demonstrated to understand the estuarine or riverine water exchange process. Shen et al. (2004) calculated the RT in the tidal York River through a series of three-dimensional numerical model experiments with respect to the sources of substance released from an upstream boundary under different hydrological conditions. The RT and the ET in the Scheldt Estuary was computed by de Brye et al. (2012) to better understand and characterise the dynamics in this estuary.

As overall retention time of substances, the RT and ET are always predicted to compare with biogeochemical processes in aquatic sciences (Josefson and Rasmussen, 2000; Abdelrhman, 2005). They are believed to be key parameters for the occurrence of algal blooms, as they require that phytoplankton cells are maintained in favourable conditions for long enough (Lucas et al., 1999a, b; Muylaert et al., 2000). Delesalle and Sournia (1992) established a direct linear relationship between phytoplankton biomass in coral reef lagoons and the RT. Crump et al. (2004) related the shifts in the bacterioplankton community composition along the salinity gradient of the Parker

River estuary.

### **2.3.2 Age of water (AW)**

Although timescales such as the RT and the ET have often been used to estimate the overall retention time for a water body, the steady-state approach does not account for spatial and temporal variations in an estuary. The water exchange process in estuaries is usually influenced by complex hydrodynamic processes and irregular topographic features, and the retention time in deep channels and shallow areas varies substantially. Thus the water exchange time for a dissolved substance at a given location can be quantified based on the concept of age of water (AW). The AW is time and position dependent and it can represent the transport of individual water parcels in a spatially varied situation. It is defined as the time elapsed since the water parcel departs from the region where the AW is prescribed to be zero. This zero AW region could be tailored to address any particular aspect of the dynamics by defining from one- to three-dimensional, i.e., a point, a curve, a surface or a volume, depending on the study requirements.

The AW values can be calculated by the field observations or predicted by the numerical simulations. Observational techniques, including the isotope-tracer decaying method and the lag time method, are widely used to measure mean water age (Adkins and Boyle, 1997; Hansell et al., 2004). However, these methods may underestimate the real AW values without considering the diffusion (Deleersnijder et al., 2001; Delhez et al., 2003; Delhez and Deleersnijder, 2008).

Numerical simulation includes advection and diffusion processes in addition to

realistic topography and forcing conditions. There are two numerical methods for calculating AW: the particle-tracking model based on the Lagrangian approach and the model based on the Eulerian approach. Chen (2007) presented a laterally averaged two-dimensional trajectory model for narrow rivers and estuaries to calculate transport timescales in the Alafia River Estuary. The results indicated that the models computed in the Lagrangian formalism appeared to be much more accurate in the representation of advection and have the advantage of obtaining the pathway of water parcels. They are suitable for simulating the transit time between point sources of pollution.

Neither the field observation method nor the Lagrangian numerical method includes the diffusion process of water particles. Therefore, the computational cost by Lagrangian formalism is high because a large amount of particles must be released to simulate the random walk due to diffusion. However, in principle, the diffusion process results in the complexity of the AW spatial structure. Without the diffusion, the water particles inside a parcel are isolated from the outside environment and therefore have the same age. In fact, diffusion induces the exchange of particles inside and outside of the water parcel and consequently results in the coexistence of water particles with different ages in a water parcel. In practice, the size of the grid points in modelling cannot be infinitely small, and commonly, water parcels of different ages are found at one grid point together (Liu et al., 2012).

Deleersnijder et al. (2001) introduced the constituent-oriented age and residence time theory to simulating the age of technetium-99 released from the La Hague nuclear fuel reprocessing plant in the English Channel. It is a general theory by Eulerian formalism for calculating the age of every water constituent at any time and position

(Delhez et al., 1999; Deleersnijder et al., 2001), or group of constituents (Deleersnijder et al., 2002). de Byre et al. (2012) computed tidally averaged AW distribution of renewing water and its M2 amplitude in the Scheldt Estuary. The renewing water in the estuary was split into three types for a better understanding of the fate of dissolved pollutants. Though this Eulerian method could not provide information on the pathway of the target water mass, the predicted AW distribution could reveal the spatio-temporal distribution of the dissolved substances' retention time.

## **2.4 DESCRIPTIONS OF TWO ESTUARIES**

Two estuaries with different dynamic characters – the PRE, China, and the Severn Estuary and Bristol Channel, UK (SEBC) – were investigated as cases in the current study. The PRE is the largest estuary in Southern China. It has a micro-tidal environment with a mean tidal range of 0.8–1.7m. The SEBC is located between southeast Wales and southwest England and has the internationally notable large tidal range of 7–14 m. The PRE has an inverted funnel shape covering an area of approximately  $2500 \text{ km}^2$  with a length of approximately 70 km and a large sea boundary opening to the south. The SEBC has a length of approximately 200 km and an area of approximately  $5700 \text{ km}^2$  with a sea boundary opening to the west. The PRE receives seasonally varying freshwater discharge from eight upstream tributaries. In the wet season, the total discharge reaches  $2 \times 10^4 \text{ m}^3/\text{s}$  and the estuary is stratified. In the dry season, the estuary phenomenon becomes partially mixed with the decreased discharge. In the SEBC, the freshwater discharge from the River Severn is approximately  $100 \text{ m}^3/\text{s}$ , which is very small in comparison with the seawater

entering the estuary (Xia et al., 2010a). Thus, the estuary presents a nearly homogenous phenomenon for salinity, temperature and phytoplankton distributions. A summary of the two estuaries hydrodynamic characteristics is listed in Table 2.1.

**Table 2.1 A summary of hydrodynamic characteristics of two estuaries applied in this study**

		The Pearl River Estuary	Severn Estuary & Bristol Channel
Area	(km <sup>2</sup> )	2500	5700
Length	(km)	70	200
Width	(km)	4 – 60	0.13 – 72
Tidal range	(m)	0.8 – 1.7	7 – 14
Total River Discharge	(m <sup>3</sup> /s)	$4 \times 10^3 - 2 \times 10^4$	Appr. 100
Density		seasonally stratified	well mixed

#### 2.4.1 The Pearl River Estuary (PRE)

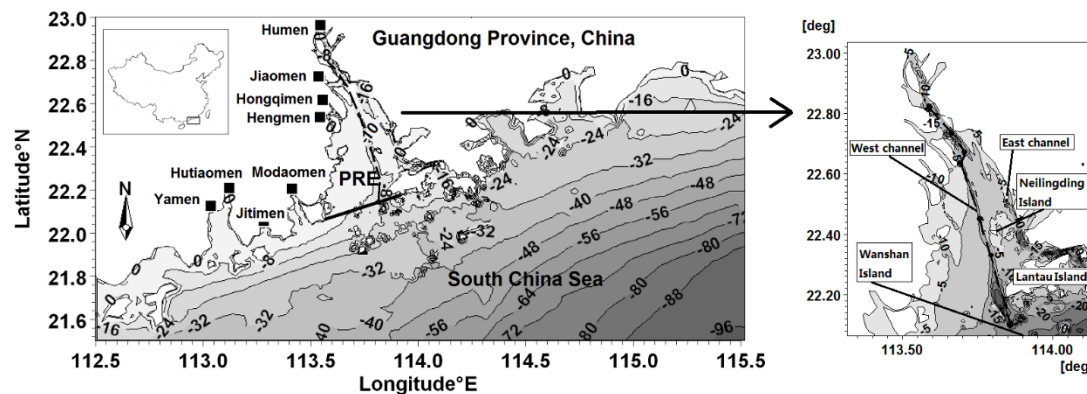


Fig. 2.7. Topography of the Pearl River Estuary and the adjacent coastal area. Left squares: eight major entrances; Left black line: sea boundary; Dash lines: the main stem of the PRE along west channel.

Fig. 2.7 shows the map of the PRE bounded by the black line. This region is one of the fastest developing and densely urbanised regions in Asia. The PRE delta has been at the forefront of the economic expansion with its proximity to Hong Kong and Macao as the key factors in promoting economic growth. This delta is also rich in agricultural resources and aquaculture, as well as providing a unique environment for tourism.

It can be seen from Fig. 2.7 that the PRE is an inverted funnel type with a narrow neck in the north and a wide mouth opening to the south – gradually widening towards the mouth of the estuary. The width in the E–W direction varies from 4 km near Humen at the northern end, and 60 km between Macau and the Lantau Islands at the southern end (Mao et al., 2004; Larson et al., 2005; Ji et al., 2011). The water depth varies from 2 m to 30 m with the average depth being approximately 4.8 m. There are two longitudinal deep channels along the estuary, namely the west channel and the east channel (see Fig.2.7), both being approximately 1 km wide (Dong et al., 2004). The water depth of the east channel varies from approximately 5 m to 32 m with a mean value of approximately 17 m. The west channel is slightly shallower than that in east with a mean water depth of approximately 12 m. These two deep channels provide convenient passages for the sea water to enter into the middle reach of the estuary. A longitudinal section along the west channel is approximately along the main axis of the estuary starting from Humen and ending at the estuary mouth. This channel was selected for the hydrodynamic investigation in the current study (see Fig. 2.7).

The PRE receives a seasonal varying river discharge from the Pearl River. The Pearl River has the second largest mean annual runoff in China after the Yangtze River. The Pearl River consists of three main rivers originating from different directions, namely the West River, North River and East River, with a catchment area of  $4.5 \times 10^5 \text{ km}^2$  (Dong et al., 2004; Larson et al., 2005). The catchment has a sub-tropical climate, with a long summer period and a short winter period, and the annual mean rainfall is 1470 mm (Dai et al., 2008). The three rivers branch into a network of small rivers and later merge into eight tributaries – four in the west



(Medaomen, Jitimen, Hutiaomen, and Yamen) and four in the east (Humen, Jiaomen, Hongqimen and Hengmen). Then the water from the eight tributaries is discharged to three different coastal areas with estuarine character – known as the PRE, Modaomen, and Huang Maohai. The latter two are much smaller than the former in area. Four eastern tributaries are directly connected within the PRE. Among eight tributaries, the discharge passing through Modaomen is the largest. The second largest discharge is through Humen. There is no noticeable difference of annual river discharges over the past years, but there are significant seasonal variations. The annual mean discharge is approximately  $5.4 \times 10^3 \text{ m}^3/\text{s}$ , while around 70 – 80% of the river discharge occurs during the wet season (from April to September (Dong et al., 2004). The highest total discharge observed in the wet season is approximately  $2 \times 10^4 \text{ m}^3/\text{s}$ , while the lowest discharge is observed in the dry season is approximately  $4 \times 10^3 \text{ m}^3/\text{s}$  (Wong. et al., 2003a, b; Dong et al., 2004). The total amount of the discharge is around  $3.36 \times 10^{11} \text{ m}^3/\text{yr}$  and the amount that directly enters into the PRE is  $1.742 \times 10^{11} \text{ m}^3/\text{yr}$  – which occupies 53.4% – and other parts enter into the Modaomen area and Huangmao Sea (Kot and Hu, 1995; Harrison et al., 2008).

Although the PRE is a micro-tidal estuary with a small tidal range, the tidal flow induced mixing plays a significant role in determining the salinity and temperature distribution, especially during the spring tides in the dry season (from October to March), see Wong et al. (2003a). The mean tidal range across the estuary is between 0.8 m and 1.7 m. Due to the narrower and shallower inverted funnel shaped estuary layout, the average tidal range is smallest at the sea boundary. The mean tidal range outside the boundary is 0.85 m to 0.95 m (Zhao, 1990). When the tidal wave is progressing upstream, the tidal energy is concentrated and the tidal range is amplified,

reaching the maximum at the estuary head near Humen (Mao et al., 2004). In summary, the mean tidal range is about 0.8 m near the Wanshan Islands, 0.9 m around Neilingding Island and 1.7 m in Humen and the maximum value observed near Humen is approximately 3.58 m (Zhao, 1990; Lin and Liang, 1996). All eight tributaries are influenced by the tides. Because of the large discharge during the wet season, the influence of tide currents on the tributaries becomes smaller (Zheng, et al., 2010). Along the cross-estuary section, there is also a significant lateral difference in tidal range with larger values in the east (Xu, 1985; Zhao, 1990). Tide asymmetry is also found in the estuary, showing stronger flood currents in Humen and Yamen, and longer ebb duration at the entrances of all tributaries (Zheng, et al., 2010). This temporal difference is largest in Hengmen and decreases towards the east.

Wind also plays an essential role in controlling the dynamics in the PRE, especially at the surface. This area experiences alternating monsoons every year, northeasterly winds dominate during the dry season and southwesterly winds during the wet season (Zhao, 1990; Dong et al., 2004). During the summer, the overly large discharge and the seaward advection of the surface plume driven by the wind enhances the vertical stratification in the estuary.

In this region, a number of forcing mechanisms – including the bottom topography, tide and coastal current, wind and freshwater discharge – operate in concert to control the circulation and water properties (Wong et al., 2003a). The estuarine dynamics always have apparent three-dimensional characteristics.

The flow patterns inside the PRE are observed to have two circulations: longitudinal gravitational circulation and horizontal counter-clockwise circulation. In wet seasons,

it presents a typical salt wedge induced longitudinal circulation: freshwater outflows from the upstream tributaries set up a strong density gradient and results in a south-westward flowing coastal current. The stratification can extend into the coastal waters outside of the estuary because of the larger river discharge and the south-westward monsoon winds. When river outflow dominates the western channel, a salt water intrusion often occurs via the eastern channel in the estuary. Thus the horizontal distribution of the mean current inside the estuary depicts a counter-clockwise circulation: stronger flood currents on the eastern side and stronger ebb currents on the western side (Mao et al., 2004). These two circulations are fundamental factors that control the water quality condition (Wong et al., 2003a, b). They are seasonally varying. In the dry season, the water is partially mixed and homogeneous water columns are observed. The circulations become weak. The tide plays a more significant role in the estuarine hydrodynamics.

The PRE is stratified in the wet season, and partially mixed in the dry season. Its density is mainly determined by the salinity level. In the wet season, the salinity level varies from 1 psu to 34.5 psu. In the dry season, the salinity level varies from 3 psu to 32 psu (Dong et al., 2004). In the wet season, due to the two circulations described previously, the salinity is observed to be higher on the eastern side than the western side (Yang et al., 1995).

The Pearl River delta region has experienced rapid socio-economic changes in the past three decades, which result in a considerable increase of the nutrient input. The increased wastewater discharge has caused several environmental problems, such as persistent hypoxia and nutrient-related algal blooms (Dai et al., 2006; Dai et al., 2008). Agricultural activities have also resulted in a rise of pollution from fertilisers and

pesticides (Neller and Lam, 1998). The bloom events were observed lasting 1–2 weeks which was indicated with associated nutrient discharge and enhanced phytoplankton production (Dai et al., 2008). During the wet season, the stratification prevents the vertical exchange of water and may lead to inferior water quality in the bottom layer (Larson et al., 2005).

#### **2.4.2 Severn Estuary and Bristol Channel (SEBC)**

The SEBC constitutes a large, semi-enclosed body of water in the southwest part of the UK. It is located around 240 km west of London between southeast Wales and southwest England. The length of the SEBC is approximately 200 km, covering an area of approximately 5700  $km^2$  (Falconer et al., 2009). This area has a macro-tidal regime, strong tidal currents, and high turbidity due to the exposure to short period wind waves. From the topography of the SEBC – as shown in Fig. 2.8, the gradient of seabed elevation is relatively steep, with the water depth decreasing from approximately 60 m near the open seaward boundary to approximately 10 m near Gloucester. Moreover, the estuary becomes narrower upstream, from approximately 72 km at the open seaward boundary to approximately 130 m near upstream end Gloucester. Inside the estuary, there is a large area of intertidal mudflats (Falconer et al., 2009).

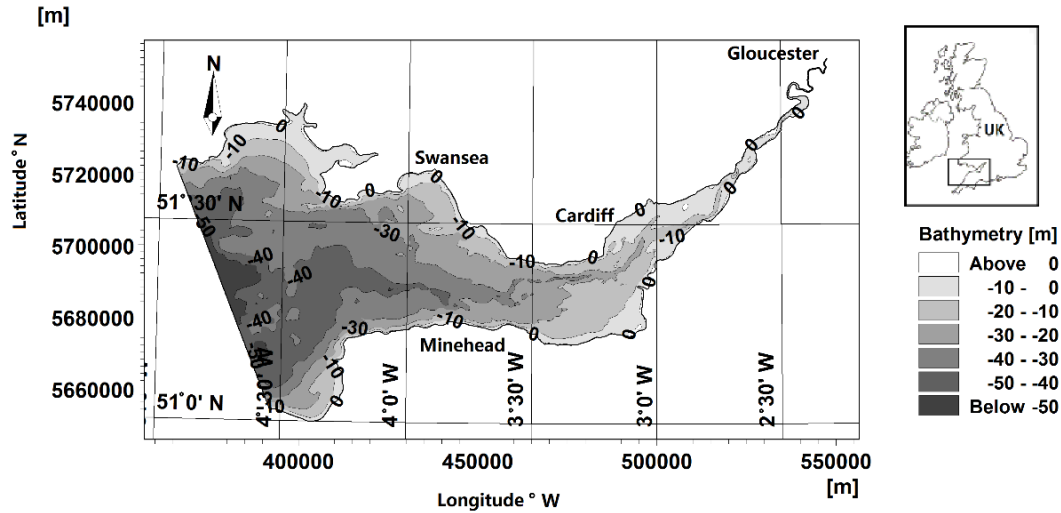


Fig. 2.8. Topography of the Severn Estuary and Bristol Channel.

The SEBC has the second highest tidal range in the world, with the spring and neap tidal ranges exceeding 14 m and 7 m at Avonmouth, respectively. There is a weir at the head of the estuary at Gloucester which defines the tidal limit of the estuary (Ahmadian, et al., 2012a).

The hydrodynamic processes in the SEBC have been extensively studied using numerical models (Owen, 1980; Uncles and Jordan, 1994; Barber and Scott, 2000). The spring tidal currents in the estuary are well in excess of 2 m/s (Falconer et al., 2009). Fast tidal currents produce strong horizontal and vertical mixing, and large bed stresses. These lead to a pronounced horizontal dispersion, nearly homogenous salinity, temperature and phytoplankton distributions.

The large tidal range in the SEBC also provides an excellent opportunity for the vast amount of tidal energy to be extracted (Kirby and Shaw, 2005; Xia et al., 2010a, b, Ahmadian et al., 2012a, b), in order to overcome the over-dependence on traditional energy sources and face an increasing demand of renewable energy resources in the

recent decades. Tidal power has great potential for future electricity generation, since tides are predictable when compared to wind energy, or solar power. (Falconer et al., 2009).

Various proposals have been made regarding the construction of a tidal barrage across the estuary and the development of tidal stream turbines to enable tidal energy to be generated, while the development of turbines may influence the surrounding hydrodynamics and cause some damage to the environment and marine habitat. Though this influence is not easily mitigated, through modelling, the position selection and turbine array design could be optimised based on AW distributions with the aim of reduced environmental impact and high tidal energy extraction.

## **SUMMARY**

In summary, in order to efficiently manage the estuarine environment a good understanding of the water exchange process is necessary. Density-induced circulation is a fundamental factor that influences the estuarine water exchange process. It enhances the upper layer currents during ebb tides and lower layer currents during flood tides. It also acts as a barrier to the water mixing between high and low density layers which could lead to anoxia and affect the primary production. However, only limited research has been carried out to investigate the influence of density-induced circulation and stratification on the estuarine water exchange process. This study intends to improve the understanding of the water exchange process in estuaries based on the concept of age of water. The influence of river discharge and tides, as well as the density-induced circulation, will be investigated.

A three-dimensional water age numerical model will be refined based on MIKE 3 and applied to two estuaries with very different features, the Pearl River Estuary and the Severn Estuary, as case studies. The water exchange process in these two estuaries, a micro-tidal estuary and a macro-tidal estuary, will be analysed based on predicted three exchange timescales, water age, the exposure time and the residence time. For the Severn Estuary, a tidal stream turbine module will be developed for inclusion within the water age model. The influence of turbines on the surrounding hydrodynamics and water exchange process can be investigated based on simulated spatial water age distributions. This could help to optimise the position selection of turbines with the aim of lowest environmental impact and highest tidal energy extraction. Furthermore, a physical model of the Severn Estuary will be investigated to verify the numerical modelling results.

## **Chapter 3**

---

### **Methodology**



### 3.1. INTRODUCTION

Most modern three-dimensional estuarine models were set up based on Navier-Stokes equations, complemented with equations for turbulence, and solute and mass transport. These models use either structured or unstructured grids, and solve the governing equations with the finite difference, finite element and finite volume methods (Liu et al., 2008). In the current study, a three-dimensional water age model was built based on the state-of-the-art hydrodynamic and solute transport model, namely MIKE 3. The chapter describes the governing equations and details of model development and implementation, with a specific focus on the hydrodynamic calculation.

The MIKE 3 Flexible Mesh (FM) is a comprehensive surface water model developed by the Danish Hydraulic Institute. It has been used in a wide variety of applications concerning three-dimensional studies of hydrodynamics and solute transport processes in the water environment: estuaries, bays, coastal areas and related phenomena in rivers and lakes (Zhang, 2006; Kheiashy et al., 2010). Based on two modules of MIKE 3: a hydrodynamic module (HD) for computing water levels, currents and salinity stratification, and a transport module (TR) for predicting tracer transport, a three-dimensional water age model for predicting water age distribution (Fig. 3.1).

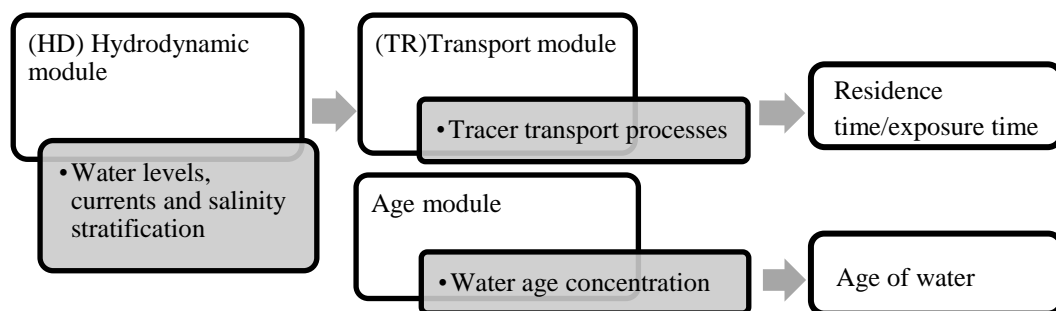


Fig. 3.1. Illustration of the age model used in this study.

To simulate the influence of the proposed tidal stream turbines on hydrodynamics in the Severn Estuary and Bristol Channel, a turbine module was added.

## **3.2. HYDRODYNAMIC AND TRANSPORT MODULES**

The HD module solves the three-dimensional Reynolds averaged Navier-Stokes equations (Reynolds, 1895). In addition, the module also takes into account evaporation and precipitation on the water surface, and salinity distribution. The salinity distribution is governed by the conservation and transport laws for mass and solute. The module also includes a choice of turbulence closure models. Whilst the detailed description of the module can be found elsewhere, for the completeness of the thesis, governing equations used in the module are briefly presented in the following sections.

### **3.2.1 Shallow water equations**

To describe the three-dimensional incompressible water flow, the Reynolds averaged Navier-Stokes equations can be used assuming a Boussinesq and hydrostatic pressure distribution. The equations are solved using a vertical sigma-transformation, details are introduced in Appendix A.

The continuity equation can be written as

$$\frac{\partial u}{\partial x} + \frac{\partial v}{\partial y} + \frac{\partial w}{\partial z} = 0 \quad (3.1)$$

and the two horizontal momentum equations for the x- and y- component, respectively (Schlichting, 1979):

$$\frac{\partial u}{\partial t} + \frac{\partial u^2}{\partial x} + \frac{\partial vu}{\partial y} + \frac{\partial wu}{\partial z} = fv - g \frac{\partial \eta}{\partial t} - \frac{1}{\rho_0} \frac{\partial P_a}{\partial x} - \frac{g}{\rho_0} \int_z^\eta \frac{\partial \rho}{\partial x} dz - \frac{1}{\rho_0 h} \left( \frac{\partial s_{xx}}{\partial x} + \frac{\partial s_{xy}}{\partial y} \right) + F_u + \frac{\partial}{\partial z} \left( \nu_t \frac{\partial u}{\partial z} \right) + u_s S \quad (3.2)$$

$$\frac{\partial v}{\partial t} + \frac{\partial v^2}{\partial x} + \frac{\partial uv}{\partial y} + \frac{\partial wv}{\partial z} = -fu - g \frac{\partial \eta}{\partial t} - \frac{1}{\rho_0} \frac{\partial P_a}{\partial x} - \frac{g}{\rho_0} \int_z^\eta \frac{\partial \rho}{\partial x} dz - \frac{1}{\rho_0 h} \left( \frac{\partial s_{xx}}{\partial x} + \frac{\partial s_{xy}}{\partial y} \right) + F_v + \frac{\partial}{\partial z} \left( \nu_t \frac{\partial v}{\partial z} \right) + v_s S \quad (3.3)$$

where  $t$  is the time;  $x$ ,  $y$  and  $z$  are the Cartesian co-ordinates (see Fig. 3.2);  $\eta$  is the surface elevation;  $d$  is the still water depth;  $h = \eta + d$  is the total water depth;  $u$ ,  $v$  and  $w$  are the velocity components in the  $x$ ,  $y$  and  $z$  directions, respectively;  $f = 2\varphi \sin\theta$  is the Coriolis parameter ( $\varphi$  is the angular rate of revolution and  $\theta$  is the geographic latitude);  $g$  is the gravitational acceleration;  $P_a$  is the atmospheric pressure;  $\rho_0$  is the reference density of water;  $\rho$  is the density of water;  $s_{xx}$ ,  $s_{xy}$ ,  $s_{yx}$ ,  $s_{yy}$  are components of the radiation stress tensor;  $\nu_t$  is the vertical eddy viscosity;  $S$  is the magnitude of the discharge due to point sources and  $(u_s, v_s)$  is the velocity by which the water is discharged into the ambient water.

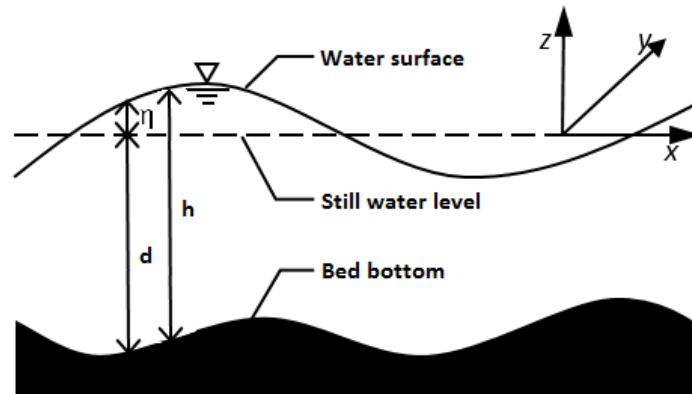


Fig. 3.2. Cartesian co-ordinate in modelling.

The horizontal stress terms are described using a gradient-stress relation, which is simplified to

$$F_u = \frac{\partial}{\partial x} \left( 2A \frac{\partial u}{\partial x} \right) + \frac{\partial}{\partial y} \left( A \left( \frac{\partial u}{\partial y} + \frac{\partial v}{\partial x} \right) \right) \quad (3.4)$$

$$F_v = \frac{\partial}{\partial x} \left( A \left( \frac{\partial u}{\partial y} + \frac{\partial v}{\partial x} \right) \right) + \frac{\partial}{\partial y} \left( 2A \frac{\partial v}{\partial y} \right) \quad (3.5)$$

where  $A$  is the horizontal eddy viscosity.

The surface and bottom boundary condition for  $u$ ,  $v$  and  $w$  are

At  $z = \eta$ :

$$\frac{\partial \eta}{\partial t} + u \frac{\partial \eta}{\partial x} + v \frac{\partial \eta}{\partial y} - w = 0, \quad \left( \frac{\partial u}{\partial z}, \frac{\partial v}{\partial z} \right) = \frac{1}{\rho_0 v_t} (\tau_{sx}, \tau_{sy}) \quad (3.6)$$

At  $z = -d$ :

$$u \frac{\partial d}{\partial x} + v \frac{\partial d}{\partial y} + w = 0, \quad \left( \frac{\partial u}{\partial z}, \frac{\partial v}{\partial z} \right) = \frac{1}{\rho_0 v_t} (\tau_{bx}, \tau_{by}) \quad (3.7)$$

where  $(\tau_{sx}, \tau_{sy})$ ,  $(\tau_{bx}, \tau_{by})$  are the  $x$  and  $y$  components of the surface wind and bottom stresses, respectively.

The total water depth  $h$  can be obtained from the kinematic boundary condition at the surface Equation (3.1), once the velocity field is known from momentum equations (Equations 3.2 and 3.3). However, a more robust continuity equation is obtained by vertical integration of the local continuity equation by considering the surface conditions of precipitation and evaporation as

$$\frac{\partial h}{\partial t} + \frac{\partial h \bar{u}}{\partial x} + \frac{\partial h \bar{v}}{\partial y} = hS + \hat{P} - \hat{E} \quad (3.8)$$

where  $\hat{P}$  and  $\hat{E}$  are precipitation and evaporation rates, respectively, and  $\bar{u}$ ,  $\bar{v}$  are the depth-averaged velocities, given as

$$h \bar{u} = \int_{-d}^{\eta} u dz, \quad h \bar{v} = \int_{-d}^{\eta} v dz \quad (3.9)$$

The fluid is assumed to be incompressible. Hence the density ( $\rho$ ), does not depend on the pressure, but depends on both the temperature ( $T$ ) and the salinity level ( $s$ ), with the equation of state as (UNESCO, 1981):

$$\rho = \rho(T, s) \quad (3.10)$$

### 3.2.2 Transport equations for salinity

The transport of salinity ( $s$ ) is described by the general transport-diffusion equations as:

$$\frac{\partial s}{\partial t} + \frac{\partial us}{\partial x} + \frac{\partial vs}{\partial y} + \frac{\partial ws}{\partial z} = F_s + \frac{\partial}{\partial z} \left( D_v \frac{\partial s}{\partial z} \right) + s_s S \quad (3.11)$$

where  $D_v$  is the vertical turbulent (eddy) diffusion coefficient,  $s_s$  is salinity source,  $F_s$  is the horizontal diffusion term defined by

$$F_s = \left[ \frac{\partial}{\partial x} \left( D_h \frac{\partial}{\partial x} \right) + \frac{\partial}{\partial y} \left( D_h \frac{\partial}{\partial y} \right) \right] s \quad (3.12)$$

where  $D_h$  is the horizontal diffusion coefficient. The diffusion coefficient can be related to the eddy viscosity.

$$D_h = \frac{A}{\sigma_T}, D_v = \frac{v_t}{\sigma_T} \quad (3.13)$$

where  $\sigma_T$  is the Prandtl number, which is assumed to be a constant in many applications (Rodi, 1984).

The surface and bottom boundary conditions for the salinity are

at both  $z = \eta$  and  $z = -d$

$$\frac{\partial s}{\partial z} = 0 \quad (3.14)$$

### 3.2.3 Transport equation for a scalar quantity

The conservation equation for a scalar quantity is given by

$$\frac{\partial C}{\partial t} + \frac{\partial uC}{\partial x} + \frac{\partial vC}{\partial y} + \frac{\partial wC}{\partial z} = F_c + \frac{\partial}{\partial z} \left( D_v \frac{\partial C}{\partial z} \right) - k_p C + C_s S \quad (3.15)$$

where  $C$  is the concentration of scalar quantity,  $k_p$  is the linear decay rate of scalar quantity,  $C_s$  is the concentration of scalar quantity at the source and  $D_v$  is the vertical diffusion coefficient.  $F_c$  is the horizontal diffusion term defined by

$$F_c = \left[ \frac{\partial}{\partial x} \left( D_h \frac{\partial C}{\partial x} \right) + \frac{\partial}{\partial y} \left( D_h \frac{\partial C}{\partial y} \right) \right] C \quad (3.16)$$

where  $D_h$  is the horizontal diffusion coefficient.

Other details of the hydrodynamic and transport modules of MIKE 3, including the numerical solutions and discretization scheme, are given in Appendixes A and B, respectively. The model equations are discretized based on an implicit, finite difference scheme on a staggered grid and solved non-iteratively by use of the alternating directions implicit technique.

## 3.3 WATER EXCHANGE TIMESCALES

MIKE 3 has been widely used in water management projects, for example, a sustainable water use and management project in Okanagan Basin, Canada, a large-scale river basin management and planning project in entire central and northern Greece and the restoration of damaged mixed hardwood wetland project in upper Myakka River in Southwest Florida, USA (<http://www.mikebydhi.com>). In the

current study a water age module has been included in MIKE 3 through the Eco-Lab facility to analyse the water exchange spatial-temporal ability in estuaries.

### 3.3.1 Age of water

As introduced in Chapter 2, the age of water (AW) is the time elapsed since the tracer parcel under consideration exited the region where its AW is prescribed to be zero (Zimmerman, 1976). Thus the retention time for a dissolved substance at a given location can be quantified. This allows for the estimation of AW to be presented as a spatial variable and it reveals detailed transit time information for solute transport in a complex estuary. The governing equations used for coding the AW model are discussed and given in this section.

The diffusion process induces the exchange of particles inside and outside of a water parcel and consequently results in the coexistence of water particles with different ages in a water parcel. In practice, the size of the grid points in modelling cannot be infinitely small, and commonly, water parcels of different ages are found at one grid point together (Liu et al., 2012). Therefore, the tracer concentration  $c(t, \vec{x}, \tau)$  is a function of time  $t$ , location  $\vec{x}$  and age  $\tau$  (Deleersnijder et al., 2001). The tracer concentration  $C(t, \vec{x})$  is related to the corresponding concentration distribution function (shown in Fig. 3.3) by the integral

$$C(t, \vec{x}) = \int_0^{\infty} c(t, \vec{x}, \tau) d\tau \quad (3.17)$$

The mean AW  $a(t, \vec{x})$  at time  $t$  and location  $\vec{x}$  is given by

$$a(t, \vec{x}) = \frac{\int_0^{\infty} \tau c(t, \vec{x}, \tau) d\tau}{\int_0^{\infty} c(t, \vec{x}, \tau) d\tau} \quad (3.18)$$

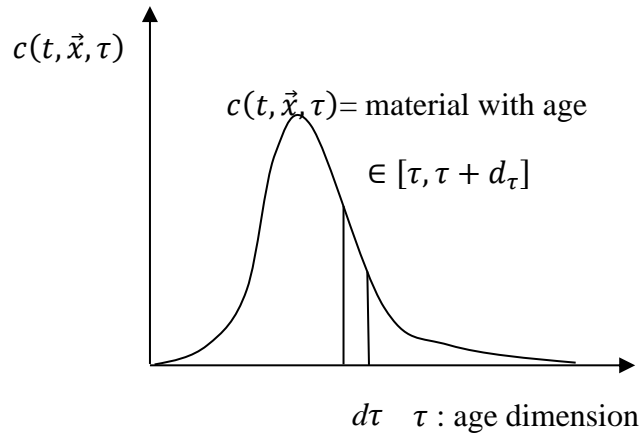


Fig. 3.3. Illustration of tracer concentration distribution function.

If the age concentration  $\alpha(t, \vec{x})$  is defined as

$$\alpha(t, \vec{x}) = \int_0^{\infty} \tau c(t, \vec{x}, \tau) d\tau \quad (3.19)$$

then the mean AW  $a(t, \vec{x})$  could be written as

$$a(t, \vec{x}) = \frac{\alpha(t, \vec{x})}{c(t, \vec{x})} \quad (3.20)$$

Assuming that there are no other sources and sinks within the estuary, the mass budget of  $c(t, \vec{x}, \tau)$  in space and time is shown below (Fig. 3.4)

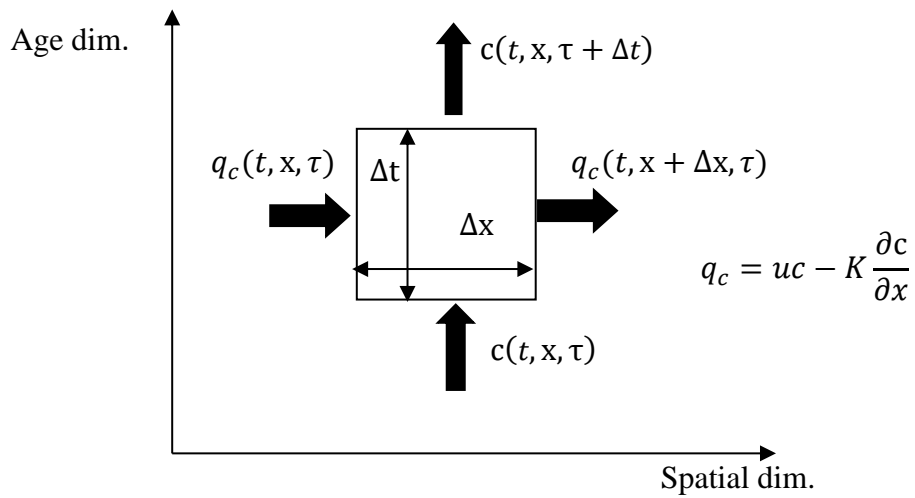


Fig. 3.4. Illustration of mass budget equation for tracer concentration.



In the five-dimensional space, the consistency check of tracer concentration  $c(t, \vec{x}, \tau)$  could be written as

$$\frac{\partial c}{\partial t} + \nabla \cdot (\vec{u}c - \vec{K} \cdot \nabla c) = -\frac{\partial c}{\partial \tau} \quad (3.21)$$

where  $\vec{u}$  is the velocity field, and  $\vec{K}$  is the diffusivity tensor.

After integrating both sides of Equation 3.21 with respect to  $\tau$  over  $[\infty, 0]$ , the transport equation for calculating the concentration  $C(t, \vec{x})$  can be written as Equation 3.22 (Deleersnijder et al., 2001; Delhez and Deleersnijder, 2002).

$$\frac{\partial C(t, \vec{x})}{\partial t} + \nabla \cdot (\vec{v}C(t, \vec{x}) - \vec{K} \cdot \nabla C(t, \vec{x})) = 0 \quad (3.22)$$

since

$$\int_0^\infty \frac{\partial c}{\partial \tau} d\tau = c|_0^\infty = 0 \quad (3.23)$$

The integral of this derivative multiplied by  $\tau$  is also known for the calculation of age concentration  $\alpha(t, \vec{x})$  shown in Equation 3.24 (Deleersnijder et al., 2001; Beckers et al., 2001):

$$\frac{\partial \alpha(t, \vec{x})}{\partial t} + \nabla \cdot (\vec{v}\alpha(t, \vec{x}) - \vec{K} \cdot \nabla \alpha(t, \vec{x})) = C(t, \vec{x}) \quad (3.24)$$

since

$$\int_0^\infty \tau \frac{\partial c}{\partial \tau} d\tau = \tau c|_0^\infty - \int_0^\infty c d\tau = 0 - C(t, \vec{x}) \quad (3.25)$$

By predicting the age concentration  $\alpha(t, \vec{x})$  and tracer concentration  $c(t, \vec{x})$ , the spatially varying AW  $a(t, \vec{x})$  distribution in the estuary can be calculated using

Equation 3.20. Thus, the calculation of AW at each grid point and time step requires solving two advection-diffusion-reaction equations: Equations 3.22 and 3.24. In this study, these two equations were set up in the Age model based on the EcoLab of MIKE 3.

The transport equations 3.22 and 3.24 can also be written in the non-conservative form:

$$\frac{\partial c}{\partial t} + u \frac{\partial c}{\partial x} + v \frac{\partial c}{\partial y} + w \frac{\partial c}{\partial z} = D_x \frac{\partial^2 c}{\partial x^2} + D_y \frac{\partial^2 c}{\partial y^2} + D_z \frac{\partial^2 c}{\partial z^2} + S_c + P_c \quad (3.26)$$

$$\frac{\partial \alpha}{\partial t} + u \frac{\partial \alpha}{\partial x} + v \frac{\partial \alpha}{\partial y} + w \frac{\partial \alpha}{\partial z} = D_x \frac{\partial^2 \alpha}{\partial x^2} + D_y \frac{\partial^2 \alpha}{\partial y^2} + D_z \frac{\partial^2 \alpha}{\partial z^2} + S_\alpha + P_\alpha \quad (3.27)$$

where  $u$ ,  $v$ ,  $w$  are flow velocity components, in the  $x$ ,  $y$ ,  $z$  direction respectively.  $D_x$ ,  $D_y$ , and  $D_z$  are dispersion coefficients.  $S_c$  and  $P_c$  are source and sink terms related to tracer concentration  $c(t, \vec{x})$ .  $S_\alpha$  and  $P_\alpha$  are source and sink terms related to age concentration  $\alpha(t, \vec{x})$ . According to Equations 3.22 and 3.24,  $P_c$  and  $P_\alpha$  are specified as 0 and  $c(t, \vec{x})$ , respectively. A schematic of calculation procedure for tracer concentration and age concentration is shown in Fig. 3.5.

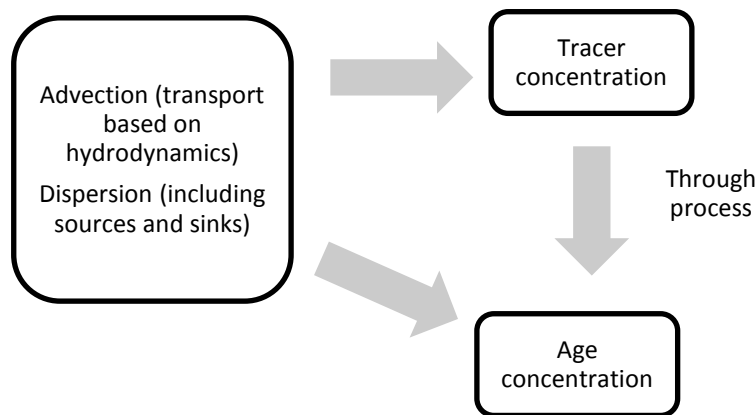


Fig. 3.5. Schematic of calculation for tracer concentration and age concentration in water age model

### 3.3.2 Residence time, exposure time and return coefficient

Based on the experimentally determined residence time and exposure time distribution curves, the local flushing ability and transport process in the PRE were clearly presented. Based on the return coefficient, the importance of return flow to the estuary was further investigated. The water exchange between the estuary's different segments was also studied by connectivity ratio.

The residence time of a material is the time taken for it to reach the outlet of the interested region for the first time (Zimmerman, 1976). Different from the residence time, the calculation of exposure time allows the material to exit the interested region and re-enter at a later time. The residence time or exposure time has been estimated by tracking Lagrangian particles (Luther and Haitjema, 1998; Miller and Luther, 2008; Tartinville et al., 1997). However, this method requires a large number of particles for a reliable solution to be obtained (Spivakovskaya et al., 2007). Takeoka (1984) introduced a remnant function  $r(\tau)$  to calculate the residence time. Defining the total mass of material in the interested region at an initial time  $t_0$  as  $M(t_0)$ , and  $M(\tau)$  is the mass of material continually staying in the region after time  $\tau$  ( $\tau > t_0$ ). Thus  $M(\tau)$  is the mass of material whose residence time is greater than  $\tau$ .

From the above, the distribution function of residence time can be defined as

$$\phi(\tau) = -\frac{1}{M_0} \frac{dM(\tau)}{d\tau} \quad (3.28)$$

It can further be assumed that

$$\lim_{\tau \rightarrow \infty} M(\tau) = 0 \quad (3.29)$$

with the average residence time,  $\tau_r$ , being defined as

$$\tau_r = \int_{t_0}^{\infty} \tau \phi(\tau) d\tau \quad (3.30)$$

Integrating the above equation by parts gives

$$\tau_r = \int_{t_0}^{\infty} \frac{M(\tau)}{M_0} d\tau = \int_{t_0}^{\infty} r(\tau) d\tau \quad (3.31)$$

where  $r(\tau) = \frac{M(\tau)}{M_0} \in [0, 1]$  is called remnant factor.

For exposure time  $\tau_e$ ,  $M(\tau)$  includes the fraction of material that leaves and re-enters this region. Thus,  $\tau_e$  is usually larger than  $\tau_r$ . The exposure time has also been widely used in coastal and estuarine environment assessment studies (Monsen et al., 2002; Delhez, 2006; de Brauwere et al., 2011).

In the current model, the initial concentration of material in the interested region  $\Omega$  is set to be 1 g/L while it is 0 g/L elsewhere (Gourgue et al., 2007), i.e.

$$c(t_0, \vec{x}) = \begin{cases} 1 \text{ g/L} & (x, y, z) \in \Omega \\ 0 \text{ g/L} & (x, y, z) \notin \Omega \end{cases} \quad (3.32)$$

For each scenario, the model runs until the relative error of the accumulative average residence time  $\tau_{Err}^n$  is less than  $\tau_{cr}$  which is set to be 0.001 (Yuan et al., 2007).  $\tau_{Err}^n$  is defined as follows

$$\tau_{Err}^n = \frac{\tau_r^{(n+1)T} - \tau_r^{nT}}{\tau_r^{(n+1)T}} \quad (3.33)$$

where  $T$  is the period of a tidal cycle.

To represent the difference between the residence time and exposure time, a return

coefficient introduced by Arega et al. (2008) and de Brauwere et al (2011) was used in the current study. A measure was derived of the proportion of the exposure time that was due to returning water.

$$\theta_{return} = \frac{\tau_e - \tau_r}{\tau_e} \quad (3.34)$$

where  $\theta_{return}$  is the return coefficient describing the contribution of returning water to the timescales.

### 3.3.3 Connectivity matrix

In order to investigate the water exchange between subdomains, the interested domain can be divided into several boxes. The estuarine exposure time is then decomposed into the exposure time of subdomains, resulting in a connectivity matrix by using an additional time diagnostic. It is a measure of how long a water parcel initially present in subdomain  $\Omega_i$  ( $c_i(t_0, \vec{x}) = 1$  g/L) and spends in subdomain  $\Omega_{j, j \in \{1, \dots, n\}}$  ( $c_j(t_0, \vec{x}) = 0$ ).

$$\tau_{i,j} = \int_{t_0}^{\infty} \frac{M_{i,j}(\tau)}{M_{i0}} d\tau = \frac{\int_{t_0}^{\infty} \int_{\Omega_j} c_i(t, \vec{x}) d\vec{x} d\tau}{\int_{\Omega_i} c_i(t_0, \vec{x}) d\vec{x}} = \frac{\int_{t_0}^{\infty} \int_{\Omega_j} c_i(t, \vec{x}) d\vec{x} d\tau}{\int_{\Omega_i} d\vec{x}} \quad (3.35)$$

This measure would then allow the identification of connections between subdomains by time spent journeys of water parcels released at different subdomains (de Brauwere et al., 2011).

The dimensionless quantity defined by equation 3.29 can be used to express the ratio of the time spent in subdomain  $\Omega_j$  and the total time spent in the interested domain by tracer initially released in subdomain  $\Omega_i$ . It represents the connections among the subdomains. It indicates the water exchange ability and expresses the mostly exposed locations from each subdomain.

$$\gamma_{i,j} = \frac{\tau_{i,j}}{\tau_i} = \frac{\tau_{i,j}}{\sum_{j=1}^n \tau_{i,j}} \quad (3.36)$$

According to the definition, it could be known that  $\sum_{j=1}^n \gamma_{i,j} = 1$ .

### 3.3.4 Local residence time and transit time

The normalised concentration,  $E(\theta)$ , is defined as

$$\int_0^\infty E(\theta) d\theta = 1 \quad (3.37)$$

where  $d\theta$  is the normalised time step, defined as  $\theta = t/T$ , where  $T$  is the mean residence time, given by

$$T = \frac{\sum c_i t_i \Delta t_i}{\sum c_i \Delta t_i} \quad (3.38)$$

where the summation index “ $i$ ” is the concentration sample number.

## 3.4 EXPERIMENTATION METHODS

### 3.4.1 Physical model of the Severn Estuary and Bristol Channel

A physical fiberglass model of the Severn Estuary and Bristol Channel has been built in the tidal tank in the Hydraulics Laboratory in the School of Engineering, Cardiff University (see Fig. 3.6). An oscillating overflow weir was used to generate tides of varying or constant amplitude and period. This is a distorted model which has different scales in the horizontal and vertical directions, with the horizontal and vertical scale ratios being 1:25000 and 1:125, respectively. The physical model is 5.743 m  $\times$  3.938 m.

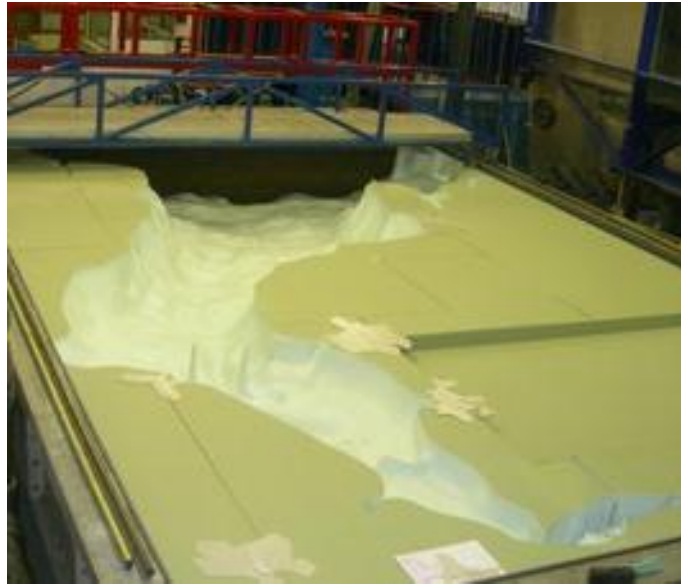


Fig. 3.6. Photograph of the physical model of Severn Estuary and Bristol Channel.

Fig. 3.7 shows a map of the Severn Estuary with the model covered area being in the rectangular box. Point A ( $W4.3755^{\circ}$ ,  $N50.9978^{\circ}$ ) and point B ( $W4.7995^{\circ}$ ,  $N51.6508^{\circ}$ ) are the north and the south end points of the seaward boundary.

The upstream section of the River Sever, from the First Severn Bridge to its tidal limit Haw Bridge has been rotated anti-clockwise to fit into the tidal basin in the laboratory. The layout of this physical model in the tidal basin with bathymetry data is shown in Fig. 3.8. In this study, 11 sampling points were selected. The representations of sampling points are introduced later in Section 7.2.1.

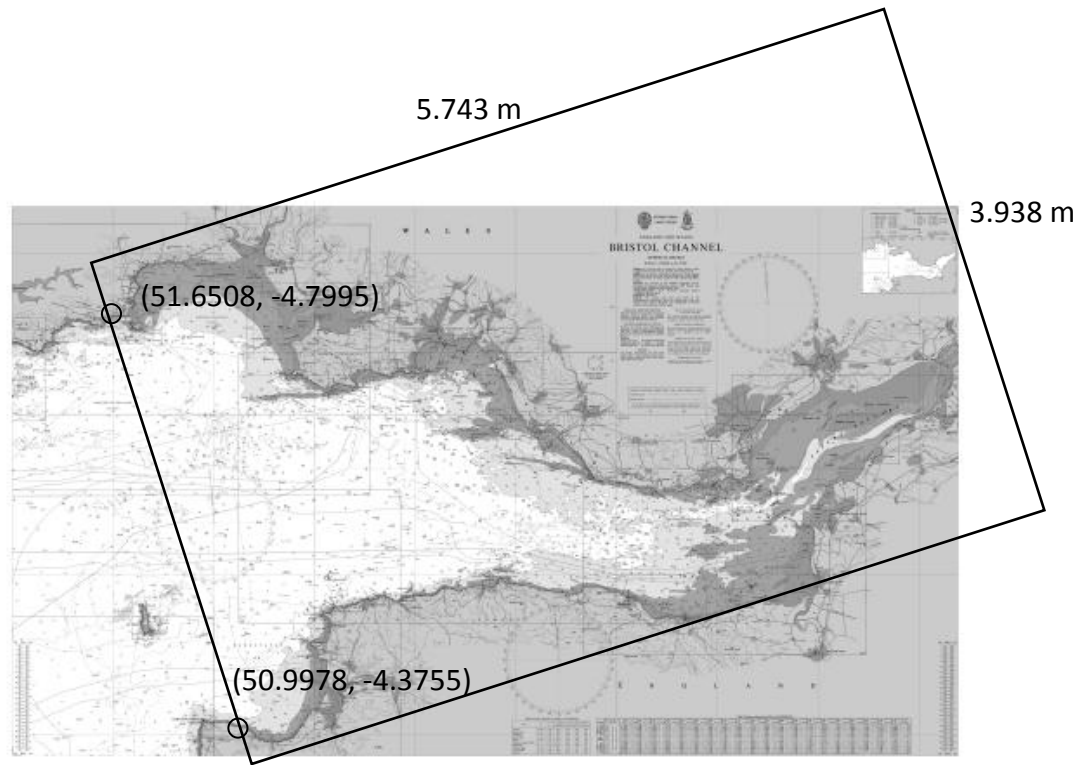


Fig. 3.7. Domain covered by the physical model of Severn Estuary.

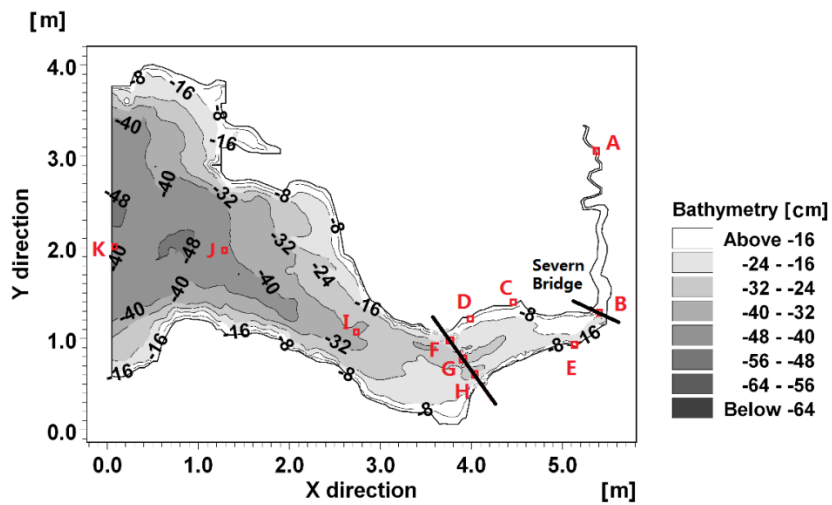


Fig. 3.8. Bathymetry of physical model of Severn Estuary and Bristol Channel, showing the positions of sampling points.

### 3.4.2 Model setting up

In the experiments, the water was supplied from pipes connected to the main re-circulation tank. The water entered into the basin via a large perforated pipe between the baffle and a movable weir at the downstream of the model (see Fig. 3.9). The



baffle between the pipe and the basin prevented large eddies in the pumped water from entering the basin. The perforated pipe and the baffle were used to ensure that the longitudinal velocity at the inlet is approximately distributed uniformly. The water levels along the downstream boundary follows the movements of the weir. The weir can be raised or lowered via the control of a computer program. In the distorted model, the tidal range and period are selected according to the Froude in law of scaling. As introduced above, the scale ratio for horizontal  $L_{rh}= 25000$  while the scale ration for vertical  $L_{rv}= 125$ . Then the scale ratio for velocity  $v_r$  is :

$$v_r = \frac{v_m}{v_p} = \frac{\sqrt{2gh_m}}{\sqrt{2gh_p}} = \sqrt{L_{rv}} \quad (3.39)$$

And the scale ratio for time T is

$$T_r = \frac{T_m}{T_p} = \frac{L_{rh}}{\sqrt{L_{rv}}} \quad (3.40)$$

In the current study, the tidal range was 80 cm and tidal period was 40 s.



Fig. 3.9. Photography showing the perforated pipe which supplies the water to physical model, weir and baffle.

### 3.4.3 Data acquisition and processing systems

#### 3.4.3.1 Water level measurements

In the current study, water level data at monitoring points were collected by three wave probes. Each device consists of two parallel stainless steel wires. The electrical conductivity between two wires varies depending on the immersed height of the probes. The data acquisition and processing systems were described as below.

##### *3.4.3.1.1 Preparation and data acquisition*

An automated multi-probe water level monitoring system was used for wave probes. The probes were positioned at aimed points, ensuring the middle portion of the probes submerged into the water over tidal cycles. Before reading the data, each probe was calibrated at five standard water levels (i.e., 10 cm, 30 cm, 40 cm, 50 cm and 70 cm). Fig. 3.10 shows a calibration for water level at point A. By calibrating the probe at standard water levels, the liner formula was obtained which can be used to transfer the readings to real water levels. The calibration can be checked in-situ by measuring with a pointer gauge.

The readings were recorded by computer software for a sampling time of 160 s, i.e., 4 tidal periods, starting when the hydrodynamics in the model presented tidal symmetric.

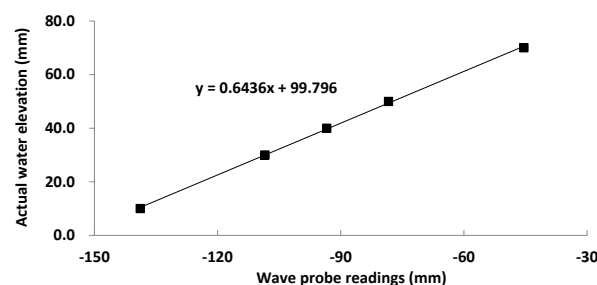


Fig. 3.10. Calibration for water level readings at point A with best fitting liner formula.

#### *3.4.3.1.2 Data processing*

The output file from the water level acquisition software was a text file (\*.txt) with data columns of the time and readings. By the formulae for calibration, real water levels can be obtained. Then the water levels over one tidal period were averaged over four tidal cycles.

#### *3.4.3.2 Velocity measurements*

##### *3.4.3.2.1 Preparation of ADV probes*

ADV probes are high-resolution three-dimensional instruments which have been widely used to study rapid velocity fluctuations in the laboratory or real circumstance. The principle of ADV is the emission of acoustic pulses via the central beam of the probe at a known frequency. From the echo received, the frequency shift caused by the movements of suspended particulate scatters with the sampled flow can be measured. Then the velocity of flow in three directions can be obtained.

In the current study, two ADV probes manufactured by Nortek-AS were used, one is downward-looking, and the other one is upward-looking. Each one has three focused beams. The sampled volume where reflected the pulse corresponds roughly to a cylinder, with diameter and height of 6 mm and 9 mm, respectively, and lying at approximately 5 cm from the probe tip (Nortek-AS, 1997a). A schematic representation of an ADV probe illustrating the emitted and reflected acoustic pulses is shown in Fig. 3.11.

The ADV probes were attached to the movable racks. Their positions were set manually responded to the measurement requirements. Their coordinate system orientations followed that definition for the physical model and their depths were guided by millimetre scales affixed to the supporting racks.

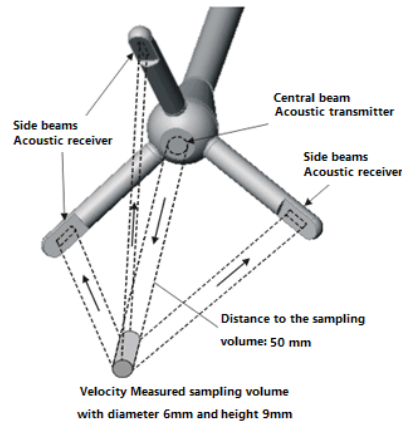


Fig. 3.11. Illustration of a down-looking ADV probe, sampling volume and acoustic pulses (figure reproduced from Sontek <http://www.sontek.com>).

#### 3.4.3.2.2 Data acquisition

The time series of measured velocity were recorded by an acquisition software in a control computer, including the speed and direction (Nortek-AS, 1997b). This ADV operation system required the definition of a number of parameters, such as temperature and salinity. In the current study, the water temperature and salinity were set to 20 °C and 0 psu, respectively. The allowed measured speed range was set to 10 cm/s. The sampling rate adopted was 25 Hz (up to 200 Hz of sampling frequency). The temporal length acquired in each sampling point was three minutes, which corresponded to 4,500 instantaneous velocity values.

To obtain valid measurements of good quality, the value of the signal-to-noise ratio (SNR) of the ADV measurements had to be maintained above 15 dB, and the correlation parameter (COR) should be maintained greater than 70%. This required the frequent addition of further seeding materials to the measured water body, better at the low water level to minimise the material losses. The SNR values were also monitored by the ADV probes and recorded during measurements. Once the SNR was below 15 dB, the measured velocity presented large fluctuations frequently which made measurements invalid.

#### 3.4.3.2.3 Data processing

The output file from the ADV data acquisition software was a binary file (\*.adv) with data columns of the time, speed in three directions, the correlation parameter (COR) and SNR value. Then the software WinADV was applied to process the data and be saved as an excel file (\*.xlsx). Samples with low COR or low SNR were removed from the velocity time series, where the restrictions were set as: the average SNR  $\geq 15$  dB and the average COR  $> 70\%$ .

#### 3.4.3.3 Tracer concentration measurements

A series of tracer experiments were conducted using the fluorescent dye rhodamine. In each experiment, a pre-prepared tracer solution was injected using a syringe at one point, and two pre-calibrated Turner Design's Cyclops-7 submersible fluorometers were used to measure simultaneous concentration of the dye at monitoring points.

The tracer experiments were carried out with the tank filled with the freshwater, not the seeded water used after the velocity measurements, in order to mitigate potential tracer losses due to absorption. Due to the limitation of measured equipment, when the monitoring points were more than two, identical experiments with the different injecting points were undertaken.

##### *3.4.3.3.1 Preparation of tracer solutions*

Rhodamine, also known as Tetraethylrhodamine, is a common fluorescent dye used in water tracing tests with the advantages of relatively low cost and high detectability (Smart and Laidlaw, 1977). In our laboratory, the dye rhodamine was available as 20% Rhodamine WT concentrate. With the aim that the maximum values of measured tracer curves were better between 100 ppb and 150 ppb, the solution for each injection was designed to be 20 ml of 400 ppm solution, i.e., 8 mg of tracer mass. Therefore, the rhodamine was diluted to 400 ppm and stored in an amber glass kept at the room temperature. The dilution procedure was carried out using the equipment and facilities

in the Soil Mechanics Laboratory, Cardiff University, observing conventional laboratory and safety practices.

Before the injection and the measurements, the fluorometers required the setting up and calibration. firstly. Following the instructions given by the manufacturer, two standard samples were required to be prepared for the setting up of the fluorometers: one was the pure water (0 ppb), and the other one was 200 ppb of rhodamine. For the calibration, more standard solutions with different concentration levels are required. Therefore, the 400 ppm solution was further diluted into the 200 ppb solution and other different concentration levels. The prepare procedure is shown in Table 3.1. In each dilution, the volume of base solution was calculated to obtain 2 L of the solution with the prescribed concentration.

**Table 3.1. The prepare procedure of solutions with different concentrations**

Steps	Base solution		Added pure water	Aimed solution	
	Volume	Concentration	Volume	Volume	Concentration
<b>Step 1</b>	0.001 L	400 ppm	1.999 L	2 L	200 ppb
<b>Step 2</b>	1.500 L	200 ppb	0.500 L	2 L	150 ppb
<b>Step 3</b>	1.333 L	150 ppb	0.667 L	2 L	100 ppb
<b>Step 4</b>	1.000 L	100 ppb	1.000 L	2 L	50 ppb
<b>Step 5</b>	0.800 L	50 ppb	1.200 L	2 L	20 ppb

#### *3.4.3.3.2 Preparation of digital fluorometers*

Digital fluorometers are normally used to measure and convert the fluorescence intensity of sample readings into tracer concentration. Generally, a fluorometer uses a photomultiplier to measure the amount of light emitted by the analysed sample at the emission wave length for the fluorescent tracer used, after excitation by an internal light source (Turner Designs, 1998).

Following the processes of control software, the fluorometers were set up by the pure water (0 ppb) and 200 ppb of rhodamine. As seen in Fig. 3.12, the sampling water was

placed in a glass beaker on a non-reflective black surface and the sensor was placed with four different distances above the bottom, respectively (the minimum requirement is greater than 3 inches, i.e., 7.62 cm). Besides the sensor is required to have more than 2 inches, i.e., 5.08 cm, clearance between the circumference of the sensor and the inside surface of the beaker. Thus the sensor is placed in the centre of the container. After the setting up, other standard concentration solutions were used to calibrate the fluorometers. Table 3.2 presents the records of actual concentrations and the readings from three fluorometers for each calibration.

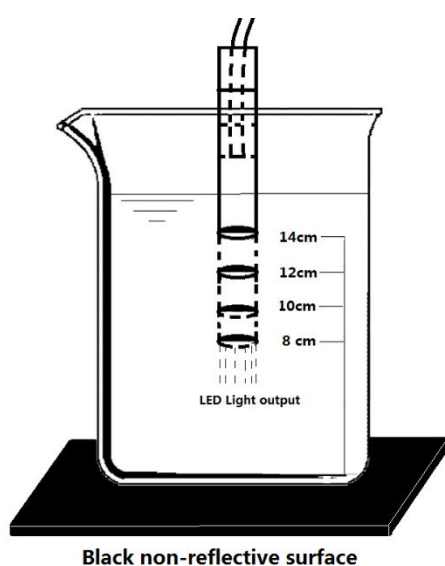


Fig. 3.12. Illustration of four positions of sensors in beaker for calibration of fluorometers.

Three curves for calibration were plotted in Fig. 3.13 for three fluorometers according to Table 3.2. A regression analysis was carried out between the readings and the actual concentration of solutions with the best fitting linear formulae. The formulae were then used to correct the readings from measurements. The calibration was undertaken before each new round of experiments after the 400 ppm solution was freshly prepared.

**Table 3.2. Readings from three fluorometers of standard levels of solutions for calibration**

no.	Fluorameter Position of sensor	Concentration (ppb)											
		Actual	Reading	Actual	Reading	Actual	Reading	Actual	Reading	Actual	Reading	Actual	Reading
1	Central-14cm	200	194.00	150	144.90	100	94.58	50	42.66	20	16.16	0	-0.03
	Central-12cm	200	193.00	150	144.92	100	94.12	50	42.88	20	16.80	0	0.00
	Central-10cm	200	189.80	150	144.90	100	93.19	50	42.36	20	16.13	0	0.00
	Central-8cm	200	190.20	150	144.93	100	93.20	50	42.26	20	16.28	0	0.00
	Average	200	191.75	150	144.91	100	93.96	50	42.54	20	16.34	0	-0.01
2	Central-14cm	200	188.50	150	142.20	100	94.85	50	42.51	20	16.30	0	0.00
	Central-12cm	200	191.60	150	142.21	100	100.20	50	42.95	20	16.41	0	0.00
	Central-10cm	200	187.10	150	142.20	100	94.69	50	42.21	20	16.22	0	0.00
	Central-8cm	200	188.20	150	142.17	100	94.69	50	42.20	20	16.33	0	-0.01
	Average	200	188.85	150	142.20	100	96.11	50	42.47	20	16.32	0	0.00
3	Central-14cm	200	188.00	150	143.30	100	94.07	50	43.65	20	16.67	0	0.00
	Central-12cm	200	187.50	150	143.31	100	95.29	50	43.69	20	16.82	0	0.00
	Central-10cm	200	186.30	150	143.27	100	94.53	50	43.36	20	16.68	0	0.00
	Central-8cm	200	187.60	150	143.32	100	94.58	50	43.50	20	16.74	0	-0.01
	Average	200	187.35	150	143.30	100	94.62	50	43.55	20	16.73	0	0.00

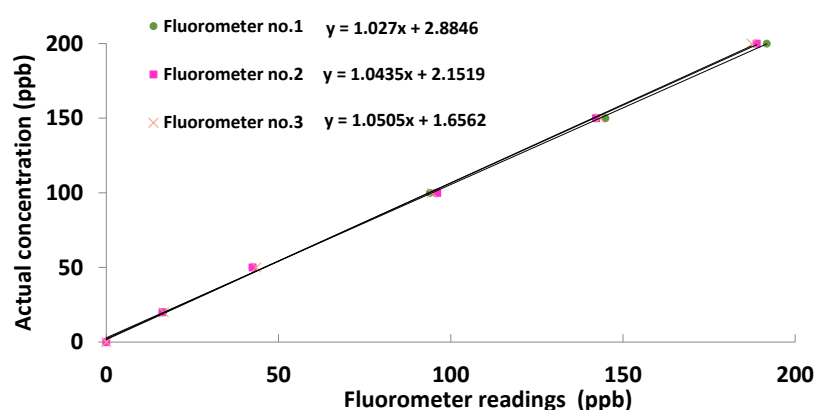


Fig. 3.13. Calibration curves used to correct tracer concentration readings, x: fluorometer readings (ppb); y: actual concentration (ppb).

#### 3.4.3.3.3 Injection of the tracer

Before the tracer injection in each test, the physical model was firstly run for approximately two hours with the tides created by the movable sluice gates, in order to allow the dye injected in the last test could be completely dissolved into a constant



average background concentration. If the background concentration reached close to 10 ppb, the whole water system including the tank would be renewed by the pure water to avoid the influence of background concentration on measurements.

In each test, 20 ml of 400 ppm rhodamine, i.e., 8 mg of tracer mass was injected using a syringe at high water at the injecting point. The injection was done manually within 3 seconds as uniformly as possible, to avoid causing significant disturbances to the surrounding flow.

#### *3.4.3.3.4 Data acquisition*

For gaining the information of tracer mass through the designated cross-sections, at each point tracer concentrations were measured at different depths. The fluorometers can detect materials as far as 3 inches, i.e., 7.62 cm, from the sensor head. An exception to this is using a flow through cap when taking measurements. The water samples were continuously pumped from monitoring locations through thin pipes, directed into the inflow port of the shape cap which connected the sensor head. A peristaltic pump with low flow rate was applied to avoid interfering with water level or current speed surround the pumping point in the model. The pumping point was also required to be positioned below the low water surface. After the analysis of the sensor, the sampled water flowed out of the cap and was discarded. The travel time along the pipes was calculated for each test associated with the length of pipes and the pumped flow rate. This temporal delay was later discounted from the actual sample readings.

The fluorometers were set to record at high water by pressing the button on the datalogger, 200 seconds, i.e., 5 tidal cycles, before the dye solution injection which was also at high water. In the current study, the sampling rate adopted was 1 Hz, which corresponded to 1 measurement per second. The maximum memory space was 9,999 data points for each test.

#### *3.4.3.3.5 Data processing*

The output file tracer experiment was in the form of a log file in ASCII format. This file contained the time series of the measured tracer concentrations. The first step of data processing was deducting the travel time through the pipes and discounting the background concentration. Secondly, some abnormal spikes occurred in the records caused by improper calibration or malfunction of the fluorometers were identified. Processed by the FORTRAN routines, the high and low spikes were taken away from the readings. After taking account of the above aspects, the tracer concentration curves were obtained and the travel time between points was assessed, providing information for the water exchange process.

## **Chapter 4**

---

# **Water Age Distribution in the Pearl River Estuary**

## 4.1 INTRODUCTION

The Pearl River Estuary, China (PRE), situated along the northern shelf of the South China Sea, is a typical estuary experiencing tidal fluctuations and significant seasonally varying freshwater discharge as described in Chapter 2 (Dong et al., 2004). As a link between the limnetic environment through eight tributaries and the marine environment, the estuary's upstream–downstream physical structure varies primarily in response to the interaction of the river discharge and the tidal mixing. The density gradient drives a baroclinic forcing and creates a vertical circulation leading to apparent three-dimensional dynamical characteristics (Wong et al., 2003a, b). Furthermore, the estuary's delta region has experienced rapid socio-economic changes in the past three decades that has brought increased nutrient inputs. The hydrodynamics of the PRE have been studied using mathematical models and field observations, including salinity and temperature distributions, circulation, and tidal phenomena, to examine the water environment (Wong et al., 2003a, b; Harrison et al., 2008). However, in such a situation with spatial variations, it is difficult to separate the underlying dynamics contributing to the transport properties. It is desirable to examine the spatial distribution of the dissolved substances' retention time and its temporal variation.

In this chapter, the timescales' concepts are applied in the PRE to investigate its water exchange process in three-dimensional space and its temporal variation. A three-dimensional age of water (AW) model is built based on the advanced hydrodynamic model MIKE 3, which has been verified against survey data in the PRE.

The definitions of water exchange timescales has been introduced in Section 2.3. The study area, i.e., the PRE was described in Section 2.4. In the current chapter, section 4.2 describes the setup of the AW model. Section 4.3 presents the verification results for model hydrodynamic parameters. The design of model scenarios is introduced in Section 4.4. Section 4.5 outlines the predicted AW distributions and Section 4.6 describes a discussion of these results. The main summaries drawn are explained.

## **4.2 MODEL SETUP**

### **4.2.1 Mesh and algorithm**

Bottom topography is an important factor that affects the flow properties in numerical modelling. Hence, an accurate representation of bottom topography by the model grid is critical to successful estuarine and coastal modelling. An unstructured grid provides a degree of flexibility in the representation of complex geometries and enables smooth representations of boundaries. Small elements may be used in areas where more detail is desired, and larger elements used where less detail is needed, leading to an optimised resolution for a given amount of computational time. In this study, the fine flexible triangle mesh was used for accurately modelling the complex shorelines and unconnected islands in the PRE. The computational time of MIKE 3 could be slow if the mesh around these islands is very fine. To save the computational time, the islands are reshaped by fewer vertices. After the simplification, it took approximately 5-7 days to run a 1 year simulation.

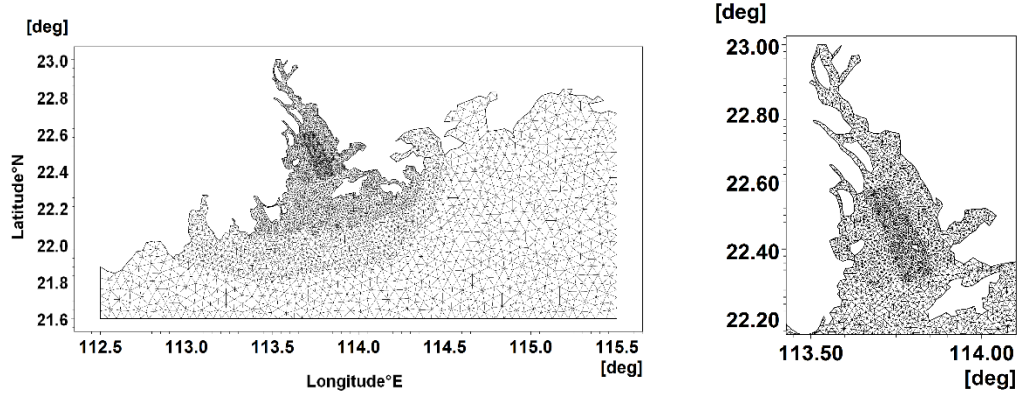


Fig. 4.1. Illustration of mesh for modelling the Pearl River Estuary.

There were 8511 elements in each horizontal plane and the model grid size varied from approximately 300 m (inside the PRE) to 4 km (over the continental shelf). In the vertical direction, 10 sigma layers were deployed with thicknesses equally distributed across the water depth, which enabled the stratification phenomenon in the deep channels can be properly simulated. It used finite-volume algorithms to solve the three-dimensional Navier-Stokes equations.

#### 4.2.2 River discharge

The monthly mean discharges from eight tributaries in the year 2006 are listed in Table 4.1. In the simulation, the monthly mean values were defined at the middle of each month and the hourly discharges were applied in simulations which were interpolated from the monthly averaged flow by the Cubic Spline Interpolation method. Fig. 4.2 shows the discharge for each tributary over one year. The year 2006 was selected because the river discharge for this 2006 was similar to the mean value over all years.

**Table 4.1. Measured monthly average river discharges of eight tributaries in 2006 (m<sup>3</sup>/s)**

Discharge	Humen	Jiaomen	Hongqimen	Hengmen	Modaomen	Jitimen	Hutiaomen	Yamen
January	621.3	581.0	215.0	376.2	950.5	201.5	208.2	201.5
February	673.1	629.5	232.9	407.5	1029.7	218.3	225.6	218.3
March	880.2	823.1	304.5	532.9	1346.5	285.5	295.0	285.5
April	1605.1	1501.0	555.3	971.8	2455.4	520.6	537.9	520.6
May	2692.5	2517.9	931.5	1630.0	4118.8	873.2	902.4	873.2
June	3676.3	3437.8	1271.0	2225.0	5623.8	1192.0	1232.0	1192.0
July	3831.6	3583.1	1325.0	2319.0	5861.4	1242.0	1284.0	1242.0
August	3262.1	3050.5	1128.0	1974.0	4990.1	1058.0	1093.0	1058.0
September	2330.1	2178.9	806.1	1410.0	3564.4	755.7	780.9	755.7
October	1346.3	1258.9	465.7	815.0	2059.4	436.6	451.2	436.6
November	1009.7	944.2	349.3	611.3	1544.6	327.5	338.4	327.5
December	932.0	871.6	322.4	564.3	1425.7	302.3	312.4	302.3
Maximum(high)	3831.6	3583.1	1325.0	2319.0	5861.4	1242.0	1284.0	1242.0
Minimum(low)	621.3	581.0	215.0	376.2	950.5	201.5	208.2	201.5
Mean	1905.0	1781.5	658.9	1153.1	2914.2	617.8	638.4	617.8

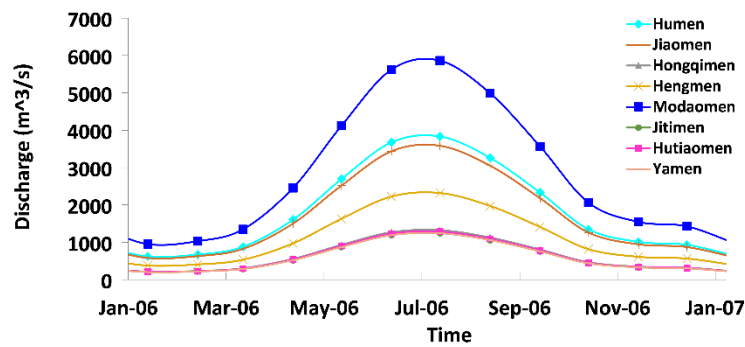


Fig. 4.2. River discharges for eight tributaries over one year.

For the entire estuary, a mean flow ratio  $R_f$  was defined herein (Equation 4.1) to measure the contribution from the tides and the freshwater discharge (Lane, 2004; Yuan et al, 2007).

$$R_f = \frac{Q_f}{\Delta V} \quad (4.1)$$

where  $Q_f$ , the accumulative freshwater discharge over a tidal cycle, and  $\Delta V$ , the total water volume between the high and low water levels. The monthly averaged total

discharge from eight tributaries  $Q_f$  and water volume  $\Delta V$  from April 2006 to March 2007 are plotted in Fig. 4.3 with the relative  $R_f$  shown in Fig. 4.4. In general, flow ratios which were less than 0.1 indicate a well-mixed condition (Lane, 2004). It can be seen from Fig. 4.4 that the value of  $R_f$  was between 0.02 and 0.1 for most months which represent a partially mixed condition for the estuary. During the wet season - June, July and August - the  $R_f$  value was greater than 0.1, which indicated the estuary was stratified and the contribution of discharge to water exchange ability was more significant.

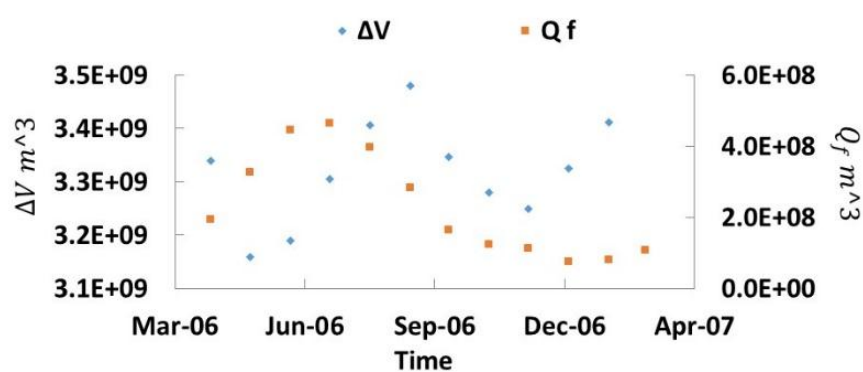


Fig. 4.3. Monthly averaged total discharge over a tidal cycle,  $Q_f$ , and water volume between high and low water levels,  $\Delta V$ .

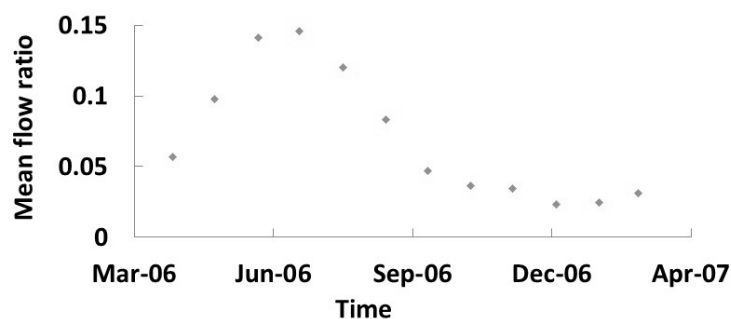


Fig. 4.4. Mean flow ratio  $R_f$  from April 2006 to March 2007.



### **4.2.3 Salinity**

Because the sea boundaries have been extended far away from the estuary downstream (Fig. 2.7), the influence of the specification of the open boundary conditions on the interior tracer concentration or salinity was considered relatively small. The west and south open boundary conditions for salinity were specified using a Neumann boundary condition. When the flow at the open boundary changed from outflow to inflow, the inflow salinity value was set using the Neumann boundary condition. For the east boundary, a prescribed constant salinity value of 35 psu was used in the incoming water. The salinity value of the river discharges was set at 0 psu and the initial value over the entire model area was specified as 35 psu. The temperature was not considered due to its relatively small influence on the estuary density variation when compared with salinity (Dong et al., 2004). The PRE is stratified in the wet season, and partially mixed in the dry season. Its density is mainly determined by the salinity level. In the wet season, the salinity level varies from 1 psu to 34.5 psu, and the temperature varies only between 21 °C and 31.1 °C. Low temperature (below 27.1 °C) occurs only in the deep water area outside the estuary mouth. In the dry season, the salinity level varies from 3 psu to 32 psu, and the corresponding temperature varies only from 18 °C to 19.1 °C (Dong et al., 2004).

### **4.2.4 Wind**

As introduced in Section 2.4, this area receives seasonal variable monsoon. The wind forcing plays a prevailing role in hydrodynamics, especially at the surface. The wind velocity data applied in this model are obtained from QSCAT/NCEP blended wind data (<http://rda.ucar.edu/datasets/ds744.4/>), which are derived from a space and time

blend of QSCAT-DIRTH scatter meter observations and NCEP analyses. It is a global data set with the wind components being a resolution of  $0.5 \times 0.5$  degree. The monthly wind speed and direction averaged from 10 years (1999–2008) were applied in models, as shown in Table 4.2 and Fig. 4.5.

**Table 4.2. Monthly mean wind velocity averaged over 10 years (1999–2008) and over the PRE**

Multi-year Average Wind				
	Speed (m/s)	Direction (degree)	u_mean (m/s)	v_mean (m/s)
Jan-06	7.074	42.6	-4.787	-5.209
Feb-06	6.614	47.2	-4.853	-4.493
Mar-06	5.123	65.9	-4.675	-2.095
Apr-06	3.325	74.9	-3.210	-0.868
May-06	2.271	93.1	-2.268	0.122
Jun-06	3.562	181.4	0.089	3.561
Jul-06	3.193	179.9	-0.003	3.193
Aug-06	1.859	152.6	-0.855	1.650
Sep-06	2.358	55.7	-1.948	-1.328
Oct-06	6.273	61.0	-5.488	-3.038
Nov-06	7.380	41.8	-4.922	-5.498
Dec-06	7.586	42.1	-5.085	-5.630

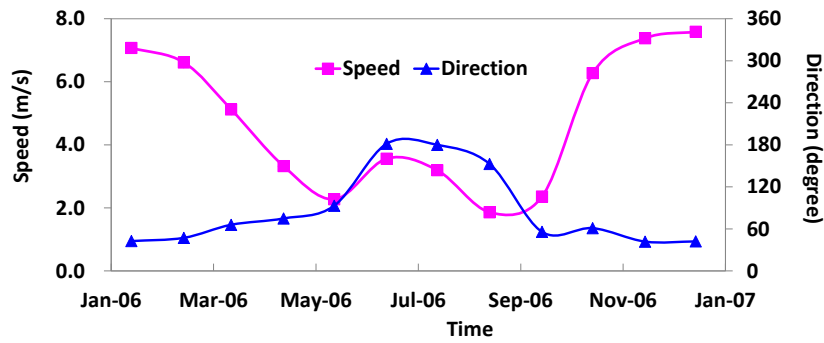


Fig. 4.5. Monthly mean wind velocity averaged over 10 years (1999–2008) in study area.

It can be seen that in the dry season, the estuary receives the northeastern wind with the speed being in excess of 7 m/s, while in the wet season the southwestern wind prevails this area with speed approximately 3 m/s. The main characteristics of monsoon wind from QSCAT/NCEP blended wind data generally agree well with previous research (Zhao, 1990; Wong et al., 2003a; Dong et al., 2004).

#### **4.2.5 Sensitivity test**

The program was selected after comparisons and tests of various programs, considering the adequate modelling of bed roughness height and turbulence. The time step was selected to 30 s. A bottom roughness height of 0.3 m was set which generally reproduced the observed data well. For the eddy viscosity, the Smagorinsky coefficient was specified horizontally and the vertical eddy viscosity was determined using a  $k - \epsilon$  model (Rasmussen et al., 1999). The model parameters used in the sensitivity test, including the roughness height, horizontal and vertical eddy viscosity, and boundary conditions can be found in Appendix D.

### **4.3 MODEL CALIBRATION AND VALIDATION**

A data set of field survey, conducted at 28 sampling stations during the period from 2006 to 2007 (Fig. 4.6), was used to validate the model. The model predictions were compared with the measured data and presented here. The data covered three typical conditions: the wet season with a high volume of freshwater discharge (July 2006), the average season with a mean volume of discharge (October 2006 and September 2007), and the dry season with a low volume of discharge (March 2007). More details of the measured data are given in Table 4.3.

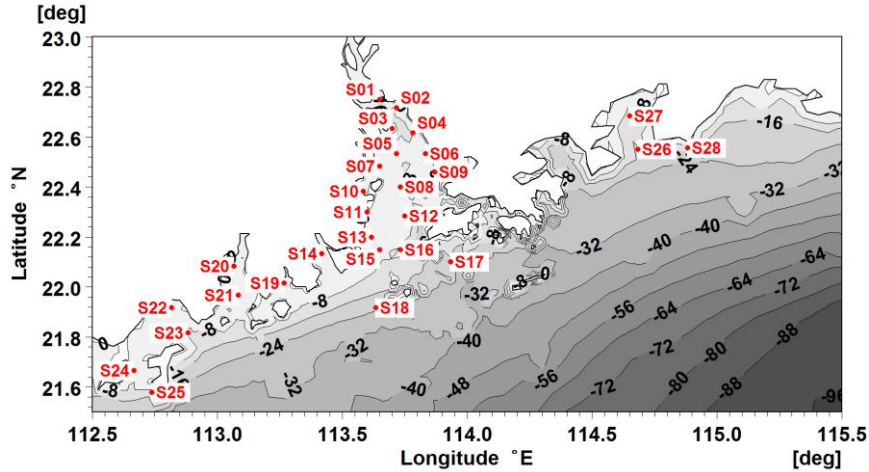


Fig. 4.6. Map of the Pearl River Estuary showing sampling stations.

**Table 4.3. A summary of the measured data for the Pearl River Estuary from 2006 to 2007**

Time	Description	Water elevation	Water current	Salinity
		One data per hour	Surface, middle and bed values (speed, direction); One data per hour	Surface and bed values, one data every two hours
08/07/2006–09/07/2006	Spring tide in the wet season	S05, S16	S05, S16	One data in one month
08/07/2006–10/07/2006	Spring tide in the wet season	S09, S25, S28		Surface and bed values, one data in one month
19/10/2006–20/10/2006	Neap tide in the mean – inflow season	S05, S16	S05, S16	
19/10/2006–21/10/2006	Neap tide in the mean-inflow season	S09, S25, S28		
09/09/2007–10/09/2007	Spring tide in the average season			S03, S05, S09, S16
18/09/2007–19/09/2007	Neap tide in the average season			S03, S05, S09, S16
07/2006	Wet season			S01–S08, S10–S24, S26, S27
10/2006	Average season			S17, S18, S26, S27
03/2007	Dry season			S01–S08, S10–S24, S26, S27

#### 4.3.1. Water elevation

Fig. 4.7 shows comparisons of the measured and predicted water surface elevations at stations S09, S25 and S28 (water depth: 12.9 m, 21.3m, and 7.0 m, respectively) in July and October 2006. The data from 8<sup>th</sup> to 10<sup>th</sup> Jul, 2006 represented the spring tide in the wet season. The mean absolute errors at S25 and S28 were 0.097 m and 0.071

m, respectively, with the corresponding root-mean-square errors being 0.115 m and 0.084 m, respectively. The predicted water elevations generally agreed well with the measured data, except the prediction at station S09 was relatively high at the high water. As shown in Fig. 4.6, station S09 is located on the east side of the middle estuary, where the complex topography may influence the prediction of the hydrodynamics. It can be seen from Fig. 4.7 that the predictions of water elevations for the neap tide in the average season fit well with the measured data.

Fig. 4.8 shows the comparison between the measured and computed surface elevations at stations S05 and S16 (water depth: 5.02 m and 8.09 m) in July and October 2006, respectively. At station S05, the predicted water level was 0.5m higher than the measured data at high tides. The predicted water elevations generally agreed well with the measured data at S16.

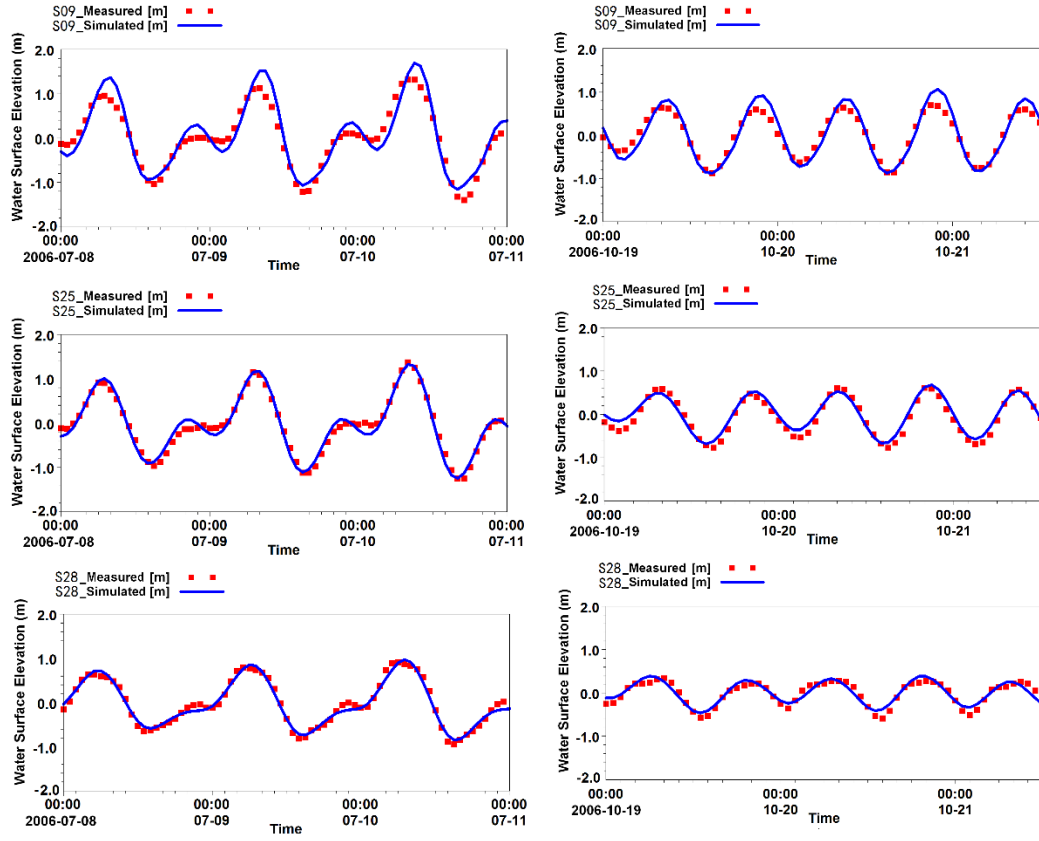


Fig. 4.7. Measured and predicted water elevations at stations S09, S25, S28 in July and October 2006.

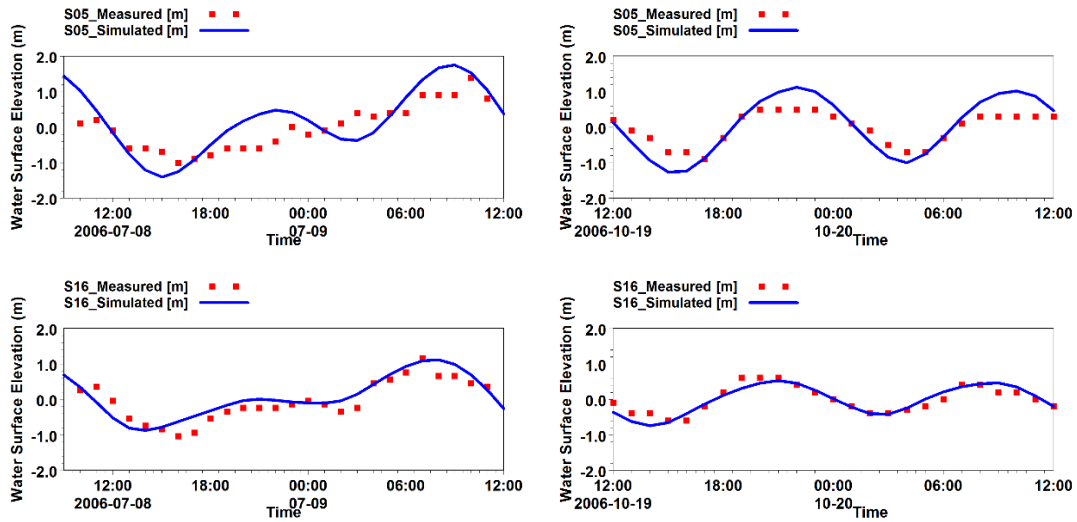


Fig. 4.8. Measured and predicted water elevations at stations S05, S16 in July and October 2006.

### 4.3.2. Currents

Fig. 4.9 and 4.10 present the comparisons of the depth-averaged current speed and direction at S05 and S16 in July and October 2006, respectively. The agreement of

tidal current was generally satisfactory except a small phase difference. For July 2006, the mean absolute difference of speed at stations S05 and S16 were 0.145 m/s and 0.149 m/s, respectively. The root-mean-square errors were 0.186 m/s and 0.172 m/s, respectively. For October 2006, the mean absolute difference of speed at stations S05 and S16 were 0.132 m/s and 0.171 m/s, respectively. The root-mean-square errors were 0.067 m/s and 0.086 m/s, respectively. It could be concluded that the model can reflect the real variation of the hydrodynamics status of the PRE.

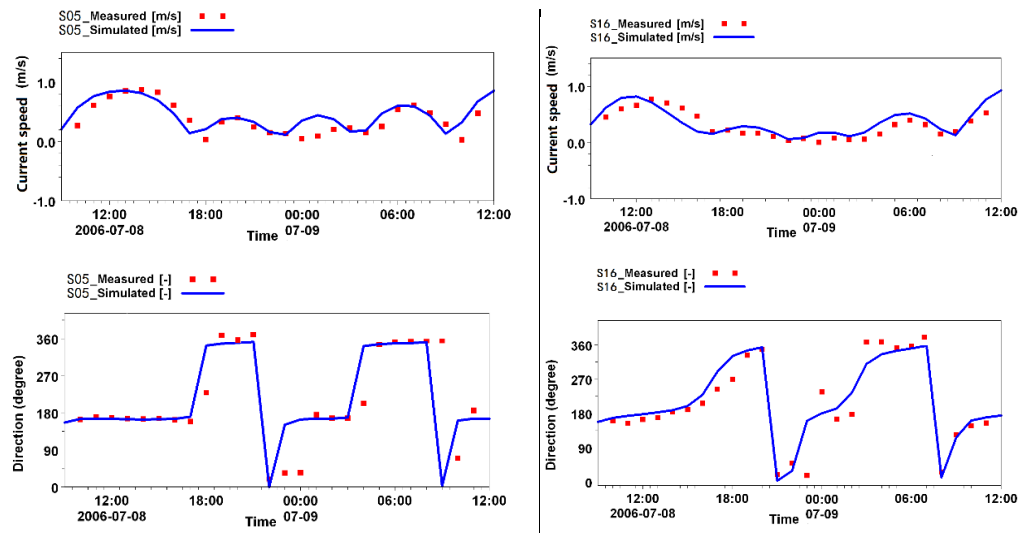


Fig. 4.9. Measured and predicted water currents at stations S05 and S16 on 8<sup>th</sup> and 9<sup>th</sup> Jul, 2006.

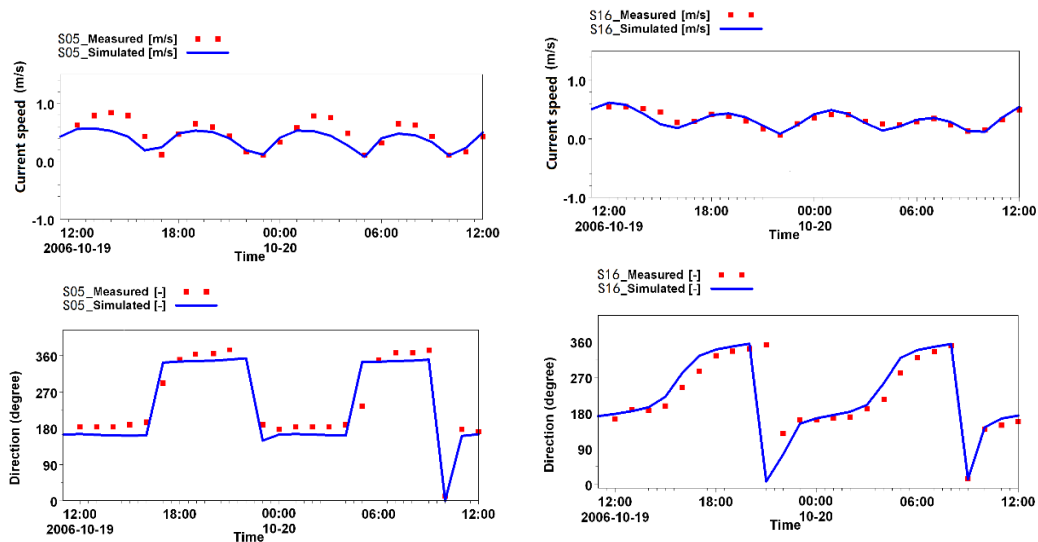


Fig. 4.10. Measured and predicted water currents at stations S05, S16 on 19<sup>th</sup> and 20<sup>th</sup> Oct, 2006.

### 4.3.3. Salinity

In the PRE, the salinity distribution controls the density stratification and, hence, influences the physical processes in the estuary. In this study, the surface and bed salinity at four stations along the west channel (S03, S05, S08 and S16), measured every two hours for both the spring tide and the neap tide in September 2007 (the average season) were used for calibration. Fig. 4.11 and Fig. 4.12 present the comparisons of the predicted and the measured salinity for the spring tide and the neap tide, respectively. It can be observed from Fig. 4.11 that the predicted salinity levels at S03 for the spring tide were higher than the measured data. As shown in Fig. 4.12, the predicted salinity showed higher values at the surface and lower values near the bed at stations S05 and S08. It illustrated that in the real circumstance, the freshwater of the upper estuary flowed downstream more quickly in the surface layers under the strong salinity stratification. The mean absolute errors and root-mean-square errors between the predicted and measured salinity at four stations for the spring tide were shown in Table 4.4.



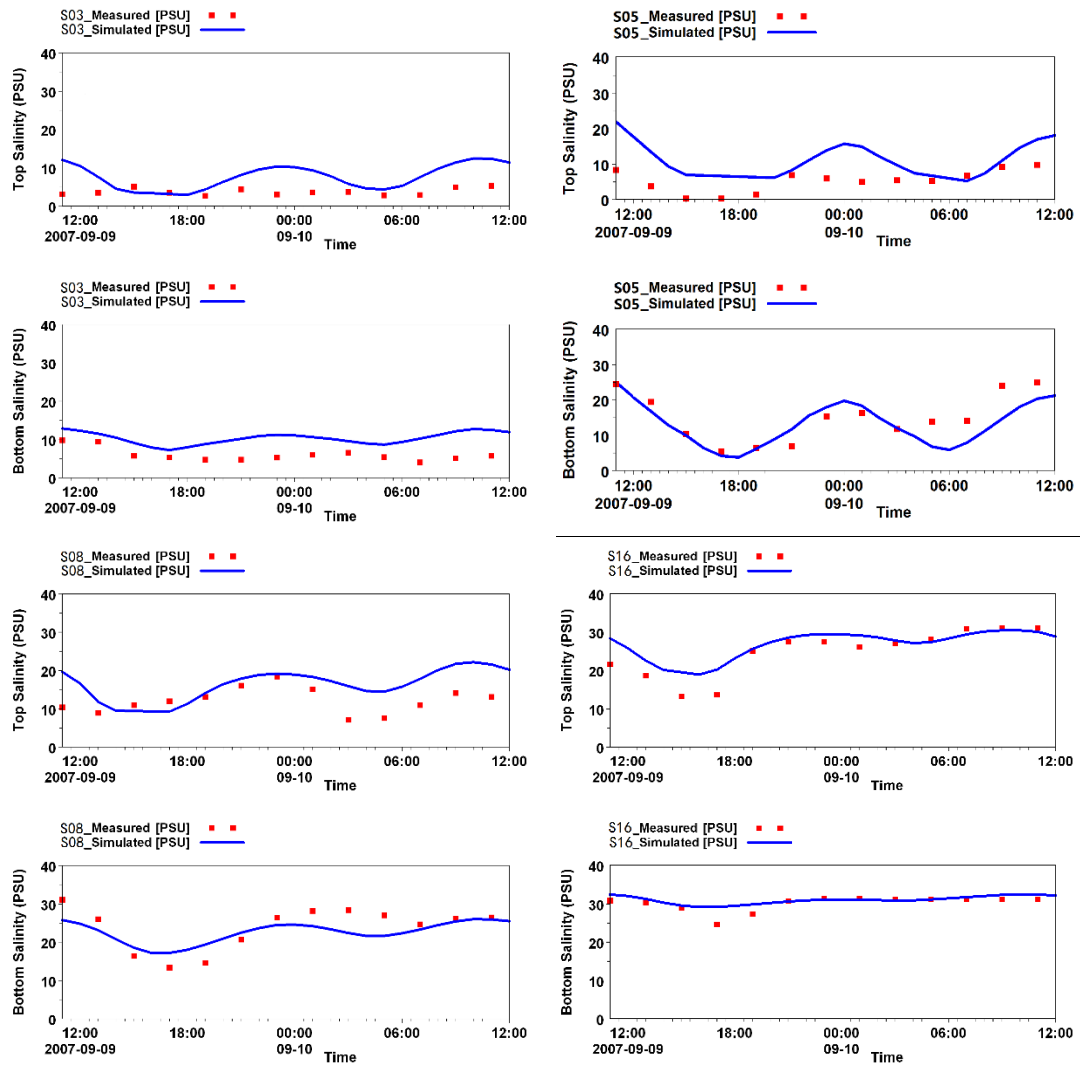
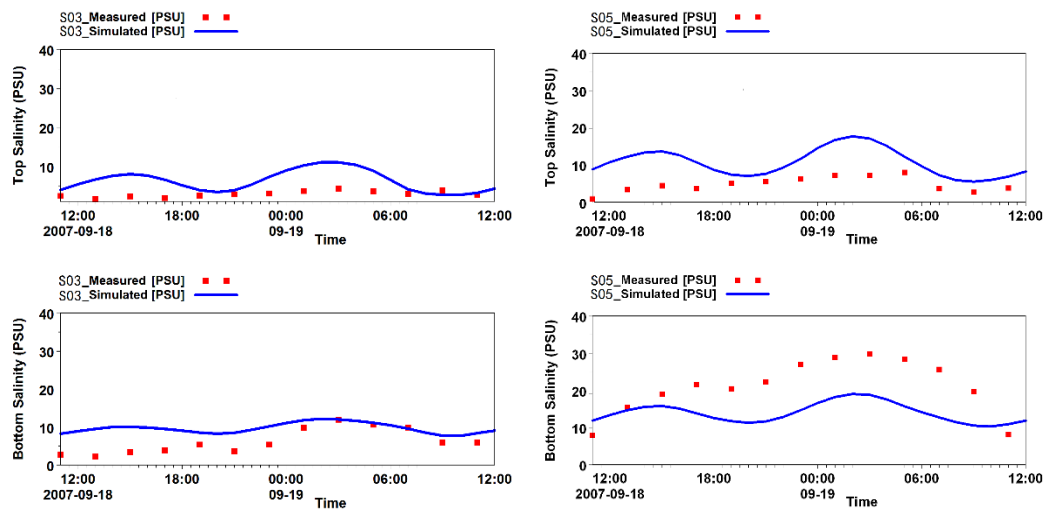


Fig. 4.11. Measured and predicted salinity at the surface and near the bottom at stations S03, S05, S08 and S16 on 9th and 10th Sept 2007.



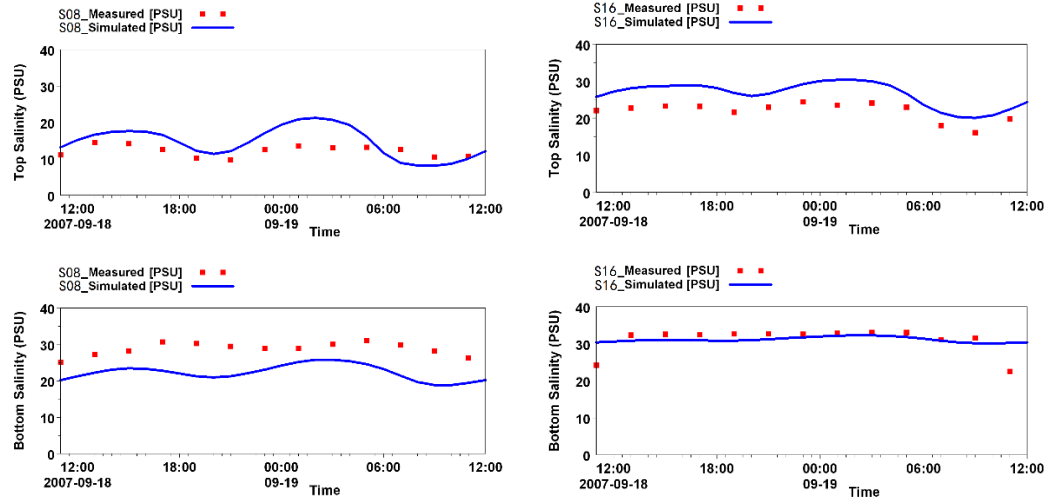
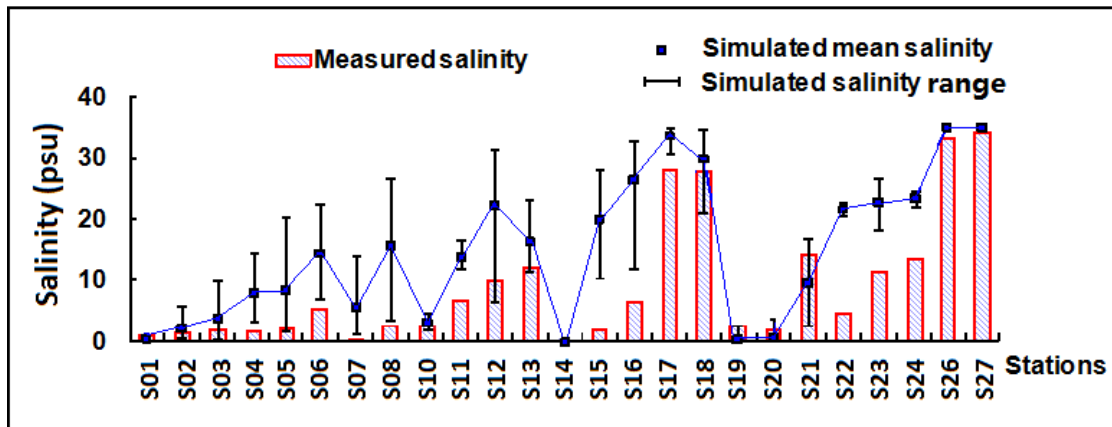


Fig. 4.12. Measured and predicted salinity at the surface and near the bottom at stations S03, S05, S08 and S16 on 18<sup>th</sup> and 19<sup>th</sup> Sept, 2007.

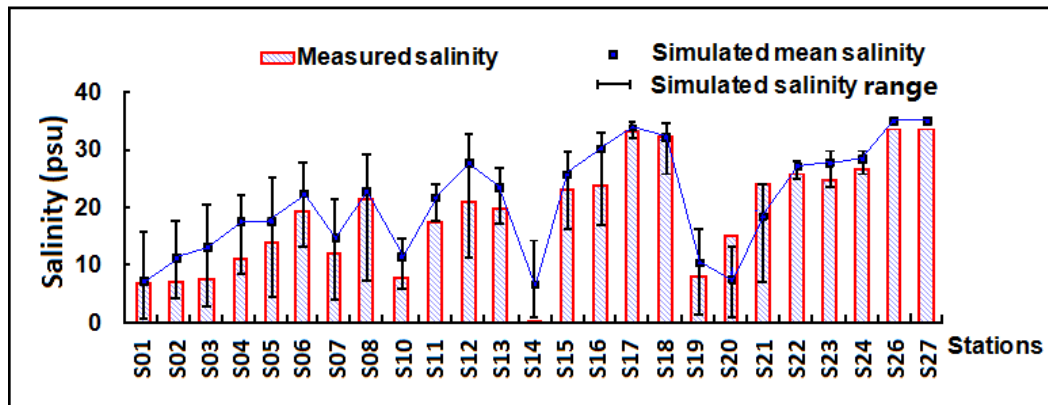
**Table 4.4. The mean absolute errors (psu) and root-mean-square errors (psu) between the predicted and measured salinity values**

On 9th, 10th Sep, 2007 (the spring tide of the average season)								
	S03		S05		S08		S16	
	Surface	Bed	Surface	Bed	Surface	Bed	Surface	Bed
<b>Mean absolute error (psu)</b>	4.22	5.57	5.64	3.62	4.76	3.19	2.71	1.10
<b>Root-mean-square error (psu)</b>	4.94	5.95	6.64	4.82	5.67	3.66	3.57	1.65

Fig. 4.13 shows the predicted salinity ranges and measured data at sampling stations over three different typical months. Only one salinity measurement was made at each station per month and the timing is different for different stations. Due to the scarcity of the observed data, the measured data is compared with monthly range of predicted data. From Fig. 4.13 it can be observed that the measured salinity values increased towards the sea boundary. Among these three months, the salinity values in the wet season (July 2006) were lowest while those in the dry season (March 2007) were greatest. This can be contributed to the large seasonal variation of freshwater discharge. In October 2006 and March 2007, the predicted salinity fit the measured data generally well.

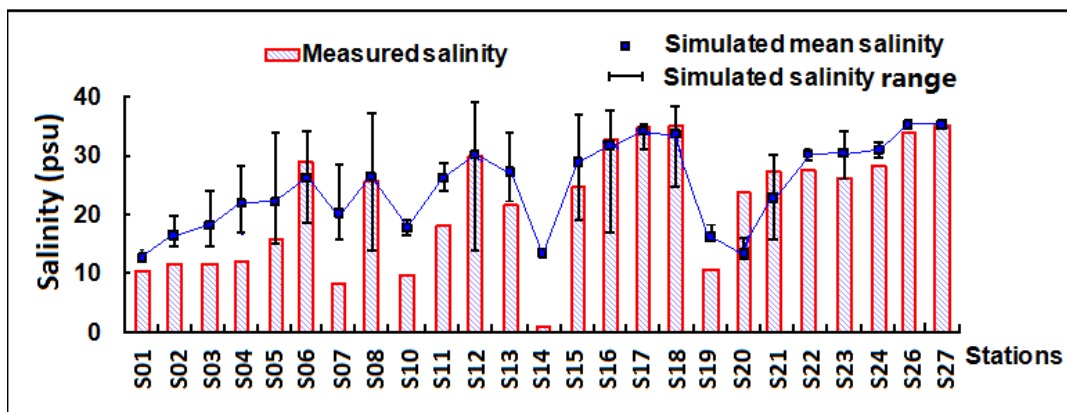


(a)



D

(b)



(c)

Fig. 4.13. Measured and predicted salinity in sampling stations in (a) July 2006 (b) October 2006 (c) March 2007.

However, in July 2006 the predicted salinity showed higher values at the stations in the upper estuary and stations S22, S23, and S24. There were two possible reasons for the errors in the upper estuary. Firstly, the water patterns in the upper estuary were strongly influenced by the local complex bathymetry between two deep channels. Secondly, the interpolated hourly discharge can bring errors to the predicted hydrodynamic situation in the upper estuary. From Fig. 4.13a, the measured salinity values at stations S22, S23 and S24 were lower than predicted values. These three stations are inside of the Guanghai bay, the salinity values were primarily influenced by the Dalongdongxi sluice.

Fig. 4.14 presents the predicted surface and bed salinity distributions averaged over three months during the wet and dry seasons, respectively. It is cautioned that the bottom distribution is for that in the lowest sigma layer (shallower inside the estuary but deeper in the coastal waters). The salinity was least in front of the tributaries' inlets and increased towards the open sea. During the wet season (see Fig. 4.14a), the surface salinity values were between 0 psu and 30 psu inside the estuary with diluted water filled the surface in the west region. The contour lines were nearly parallel and oriented from northeast to southwest. The mean salinity was approximately 5 psu with higher values in the east. The near bed salinity (Fig. 4.14b) presented two inward tongue patterns with high salinity values through the deep channels. The salinity was greater than 30 psu in the lower estuary.

In the dry season, the bed salinity distribution did not change much compared with the wet season (Fig. 4.14d). However, the surface salinity was generally larger than the wet season, being approximately 20 psu near the Nei Lingding Island (Fig. 4.14c). The lateral salinity difference became smaller. The predicted salinity fields agreed

well with the previous field measurements by Larson et al. (2005) and Dong et al. (2004). Therefore, the model predictions correctly reflected the hydrodynamic variation of the salinity trend throughout the tidal cycles.

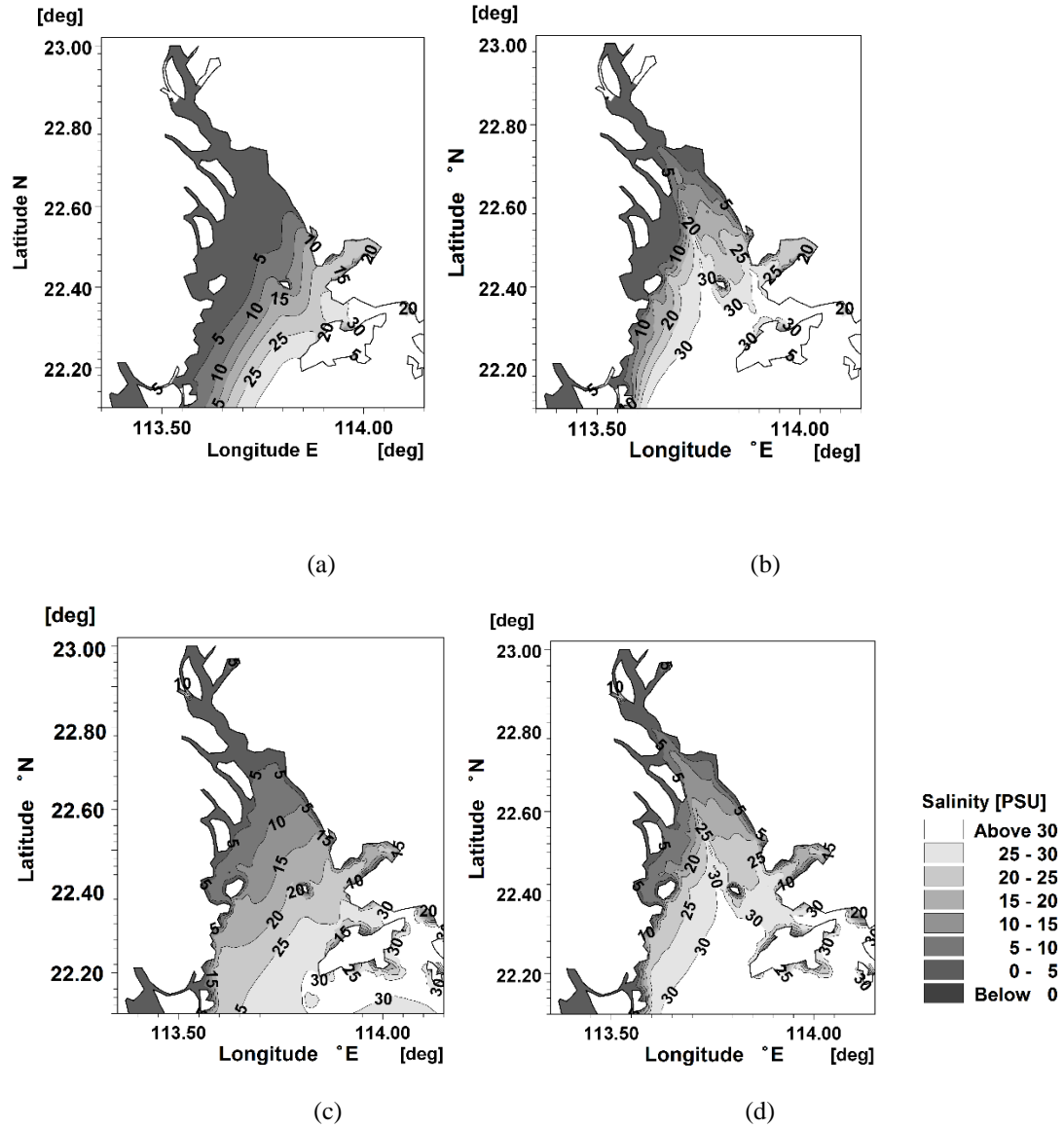


Fig. 4.14. Salinity distributions for real-time condition (case 1): (a) surface, wet season; (b) bed, wet season; (c) surface, dry season; (d) bed, dry season.

Above all, the model was able to capture the tidal propagation and quantify the mixing and transport processes in the PRE reasonably well. Using the model for studying the AW distribution is sufficiently justified.

## 4.4 DESIGN OF MODEL SCENARIOS

The real-time hydrodynamics for the model setup were given in Section 4.2. To predict the AW distributions, a passive tracer of concentration 1 g/L and age concentration of 0 was continuously released, along with freshwater from inlets of tributaries or tides along the open boundaries according to the AW calculated aims. To predict the age of the freshwater, the initial tracer concentration in the modelling domain was set to 0 g/L. At three sea open boundaries, the tracer concentration  $C(t, \vec{x})$  and age concentration  $\alpha(t, \vec{x})$  were set according to the Neumann boundary condition. Because the sea boundaries have been extended far away from the estuary mouth as shown in Fig. 2.7, the influence of the boundary condition specification on the interior tracer concentration was negligible for all cases. By investigating the AW variations through 12 model experiments under different hydrodynamic conditions, it is possible to diagnose the contributions of underlying dynamic processes. A summary of the forcing conditions used in the simulations is listed in Table 4.5.

**Table 4.5. A summary of the forcing conditions used in the model simulations**

Simulations	River discharge	Tides	Wind	Salinity	Tracer released position
Case1	Continuous discharge	Eight tidal constituents	With wind	Baroclinic	Eight tributaries
Case2	High discharge	Eight tidal constituents	No wind	Barotropic	Eight tributaries
Case3	Mean discharge	Eight tidal constituents	No wind	Barotropic	Eight tributaries
Case4	Low discharge	Eight tidal constituents	No wind	Barotropic	Eight tributaries
Case5	No discharge	Eight tidal constituents	No wind	Barotropic	Eight tributaries
Case6	Mean discharge	No tides	No wind	Barotropic	Eight tributaries
Case7	Continuous discharge	Eight tidal constituents	With wind	Barotropic	Eight tributaries
Case8	Continuous discharge	Eight tidal constituents	No wind	Baroclinic	Eight tributaries
Case9	Continuous discharge	Eight tidal constituents	With wind	Baroclinic	Open sea boundaries

### 4.4.1 Real-time condition

Case 1 was an experiment running under real-time hydrodynamic conditions. Along

the sea boundaries, half-hourly observed tidal levels, which were integrated from eight tidal constituents, were applied. This scenario was initially conducted for 3 months before predictions, with the aim to reduce the effects of the initial conditions. Therefore, case 1 was conducted for 12 months in total, from January 2006 to March 2007.

#### **4.4.2 Constant river discharge condition**

The highest, mean and the lowest discharge from eight tributaries in 2006 were selected to be representative of the high, mean, and low constant discharge hydrologic conditions (see Table 4.1). Cases 2 to 4 were conducted under these three constant river discharge conditions, separately, without wind forcing and salinity variation. The comparisons among these scenarios could reveal the influence of discharge on the AW values. Under high discharge, it needs 2 months spin-up period to reach a relative equilibrium for the AW distribution, while it needs 3 months and 5 months for the mean discharge and low discharge conditions, respectively. Therefore, each scenario was run for 6 months, starting from 1<sup>st</sup> Jan, 2006. The results of three scenarios, averaged over June 2006, were used for comparison.

Case 5 was conducted under only tidal currents without discharge, density variation or wind forcing. By comparison with the constant discharge cases (cases 2–4), the contribution of the river discharge on water transport property can be observed directly.

#### **4.4.3 Tidal currents**

In case 6, only mean discharge was applied in the modelling without tidal currents, density variation or wind forcing. By comparison with the mean discharge condition with tides (case 3), the impact of tidal currents on the AW distributions can be observed.

#### **4.4.4 Density-induced circulation and wind**

For cases 7 and 8, the model configurations were the same as the real-time condition (case 1), except without the density-induced circulation or wind forcing, respectively. Case 7 was executed for the barotropic mode; the density phenomenon is considered as homogenous in the modelling domain. In case 8, the model did not include the seasonally varying monsoons. By comparison with the real-time condition (case 1), the contributions of these two mechanisms: density-induced circulation and wind can be observed.

#### **4.4.5 Tracer released position**

Renewal water is defined as the water initially being outside the interested domain, which will progressively replace the original water. The renewing water for the PRE in the current study could be split into two types: the sea water originating from the coastal shelf and the freshwater discharge originating from the upstream eight tributaries. Case 9 was designed to predict the age of seawater by releasing the tracer with tidal currents in floods.



## 4.5 RESULTS

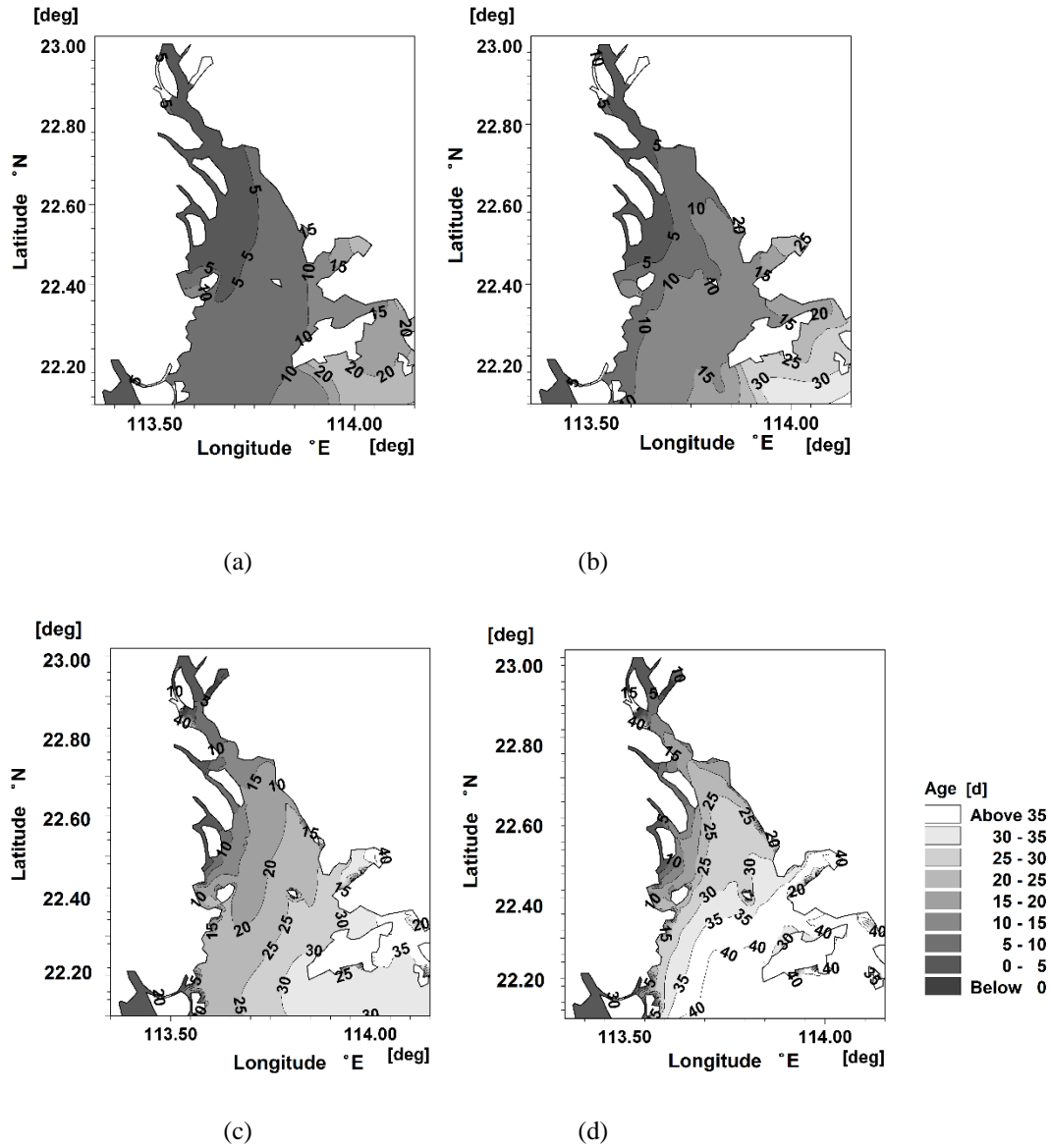
### 4.5.1 AW distributions in the wet and dry seasons (case 1)

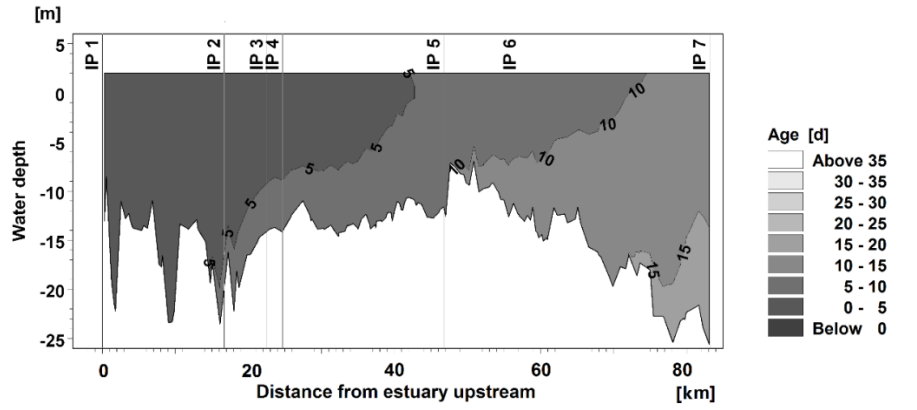
The AW varies with time and space depending on the stratification–mixing process which is strongly regulated by discharge, tidal current and other forcing conditions. The AW distribution varies over tidal cycles. Therefore, the age of freshwater averaged over two three-month periods: June–August 2006; December 2006–February 2007 were used to present the horizontal and vertical AW distributions in the wet and dry seasons under the real-time condition (case 1), respectively (Fig. 4.15).

The freshwater age was least in the upstream and increased towards downstream. Because the inlets of eastern tributaries are located on the west bank of the PRE and the Coriolis force steers the freshwater toward the western side of the estuary. Moreover, the water depth along the western coastal line is shallower than the eastern side (see Fig. 2.7). Thus the freshwater was transported much quickly out of the estuary associated with the ebb flow on the west side, resulting in a decrease of the AW values. However, the salty seawater is more dominant in the east through the deep channels. It can be seen in Fig. 4.15, during both the wet and dry seasons, the contour lines of surface AW were oriented from the northeast to the southwest with lower values on the west.

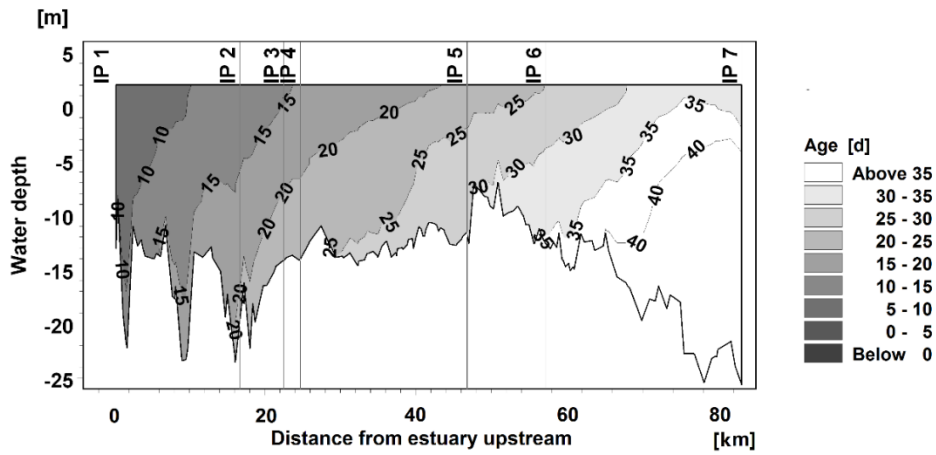
During the wet season (Fig. 4.15a), the surface AW value was less than 10 days in a large part of the estuary. The value was between 10 days and 20 days on the east side of the lower estuary. The bed AW value was larger (Fig. 4.15b), ranging from 5 days

to 20 days. The 10-day contour line oriented from northeast to southwest, crossing the middle estuary. The AW in the lower portion of estuary and the east region varied from 10 days to 20 days. Fig. 4.15e showed that the vertical AW distribution presented a two-layer structure. Along the bed the 5-day and 10-day contour lines intruded to approximately 16 km and 47 km from the upstream end, respectively. In the lower estuary, the AW value reached greater than 15 days near the bed, approximately 5 days greater than the surface.





(e)



(f)

Fig. 4.15. Water age distributions for real-time condition (case 1): (a) surface, wet season; (b) bed, wet season; (c) surface, dry season; (d) bed, dry season; vertical distribution along the west channel in the (e) wet season; (f) dry season.

During the dry season the AW distribution was quite different from the wet season. The AW values became larger than the wet season in both the surface and bed layers. At the surface, the mean AW was approximately 25 days (Fig. 4.15c). At the bed the AW varied from 15 days to greater than 40 days with a landward tongue shaped contour line of 25 days being formed along the estuary (Fig. 4.15d). As shown in the vertical AW distribution shown in Fig. 4.15f, the AW became less stratified in the dry

season than the wet season. The AW value was less than 10 days at the upstream end and greater than 40 days near the estuary mouth.

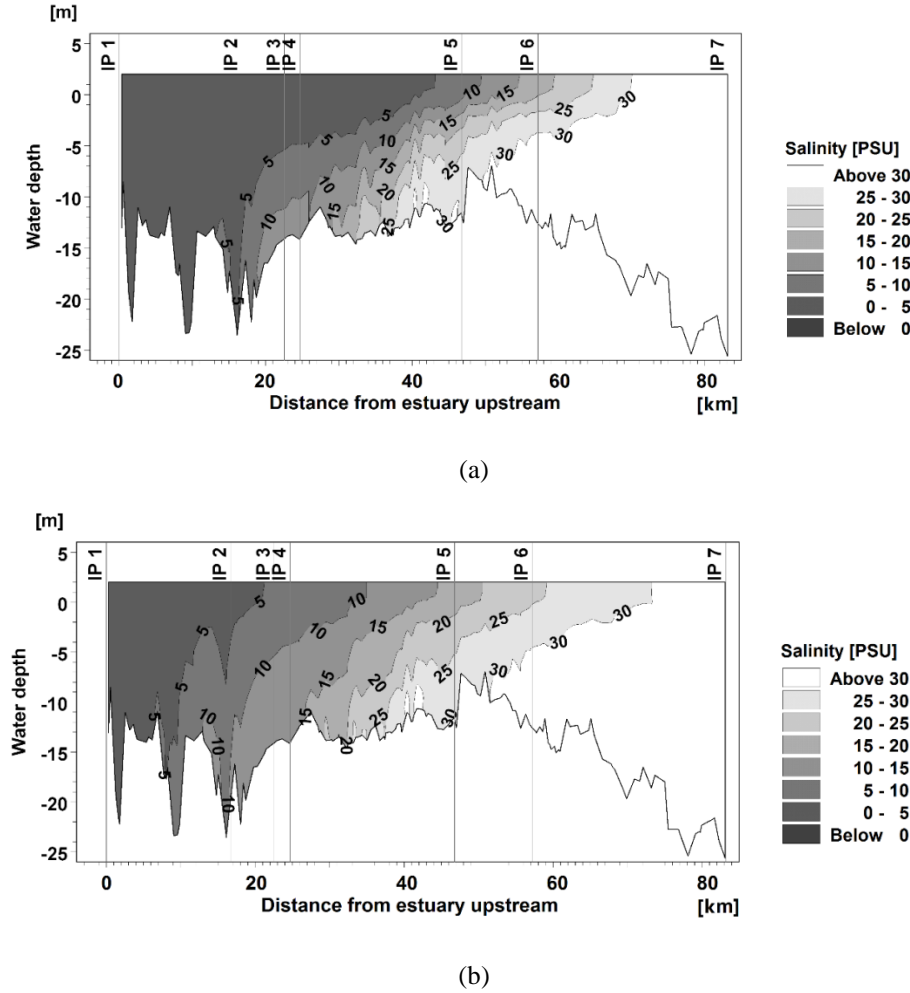


Fig. 4.16. Vertical salinity distribution along the west channel in the (a) wet season; (b) dry season.

#### 4.5.2 Residual currents (case 1)

The AW distributions reflected the water exchange process of the estuary. Its distributions followed the residual current pattern. Take residual current field during the wet season for example, which was also averaged over three months: June–August 2006, as shown in Fig. 4.17. The residual velocity field was calculated by

$$\bar{\vec{v}} = \frac{1}{T} \int_{T_1}^{T_2} \vec{v} dt \quad (4.2)$$

where  $\vec{v}(x, y, z, t) = (u, v, w)$  is the velocity at points.  $T_1$  and  $T_2$  represent 1<sup>st</sup> Jun, 2006 and 31<sup>st</sup> Aug, 2006, respectively.

The AW distributions reflected the spatial pattern of dissolved substances' retention time in the estuary. Its distribution was strongly related to the residual current pattern. Fig. 4.17 shows the predicted horizontal and vertical residual current fields in the wet season. The large volume of the river discharge induced seaward southwestern currents at the surface, leading to a large salinity gradient. The water was transported out of the estuary along the west channel in the upper layers more quickly with flow speed between 0.8 m/s and 1.0 m/s (Fig. 4.17a). Near the bed, the salty water intrusion was largely observed through two deep channels with landward speed ranging from 0.1 m/s to 0.2 m/s (Fig. 4.17b). The velocity direction changed from landward in the lower estuary to the west on the west side of the middle estuary. Fig. 4.17c presents the vertical distribution of the longitudinal residual velocity component  $v$ , where the positive values represent directions towards upstream while the negative values represent directions towards downstream. It can be observed that along the main axis, the surface water speed in the longitudinal direction reached 0.2–0.3 m/s towards downstream, while the water near the bed flowed landward with speeds less than 0.1 m/s. In the middle layers, the landward speed can reach 0.1–0.2 m/s. Due to this gravitational circulation, the AW distribution displayed lower values in the surface layers and inward tongue shaped patterns with higher values in the bed layers, which also resembled the salinity stratification (Fig. 4.14, Fig. 4.16).

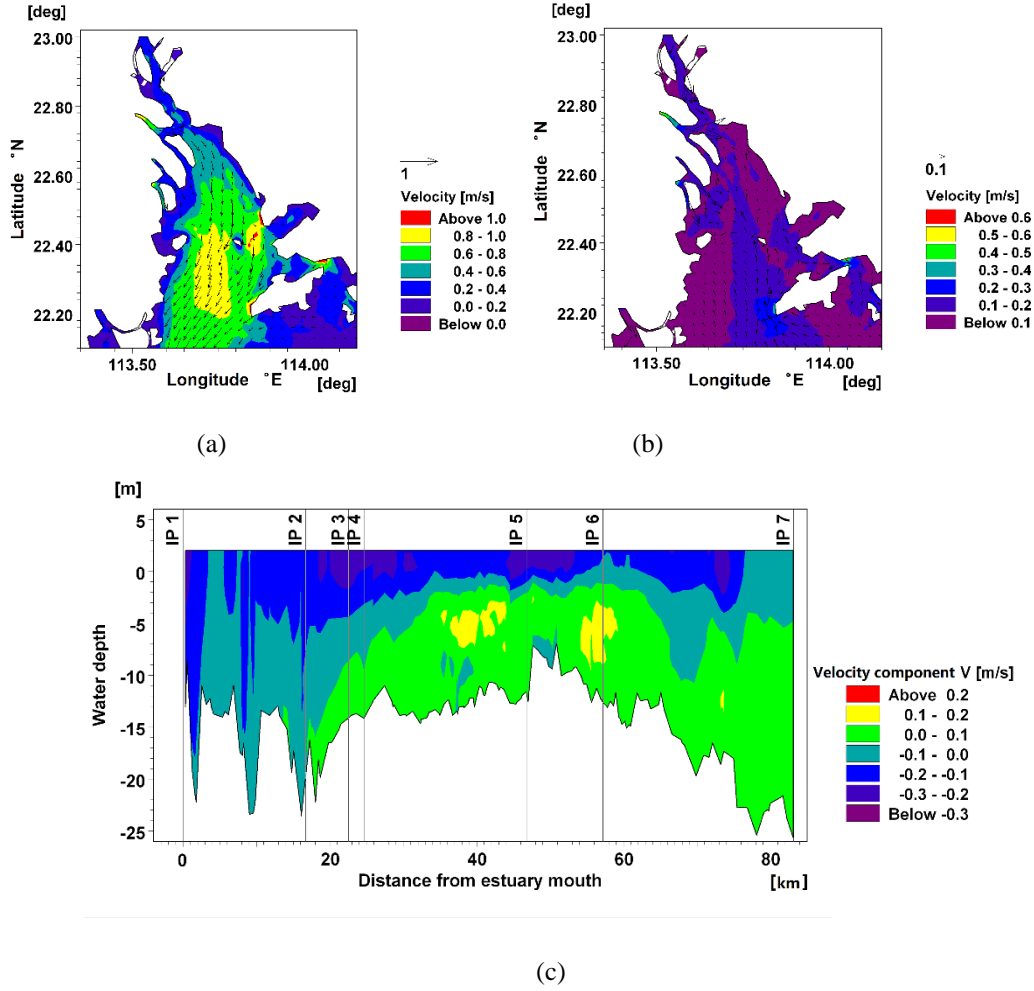


Fig. 4.17. Residual current fields in the wet season for the real-time condition (case 1): (a) surface; (b) bed; (c) vertical distribution of longitudinal component  $v$  along the west channel.

## 4.6 DISCUSSION

### 4.6.1 Influence of the river discharge

#### 4.6.1.1. Real-time condition (case 1)

Fig. 4.18 shows the time series of depth-averaged AW at station S16 during the period from April 2006 to March 2007 for the real-time condition (case 1). This was after a three-month transient period allowing water discharged from the upstream to reach the downstream boundary as the hot start. It can be seen that the AW varied from 8

days to 36 days with an average AW of 18 days. The variation was due to the varying river discharge and other dynamic conditions in the modelling period. The AW decreased from April to July with the growth of discharge. Following the wet season, the AW turned to grow and reached the peak of 36 days (maximum) in January 2007. The fluctuation over tidal cycles was primarily attributed to the tidal currents.

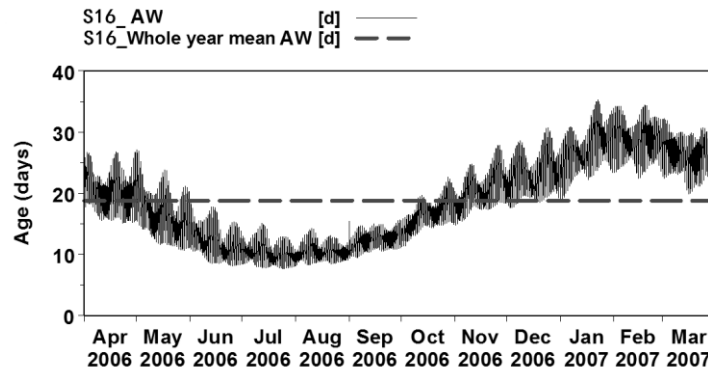


Fig. 4.18. Time series of depth-averaged freshwater age at S16 and its yearly mean value for real-time condition (case 1).

Four sampling stations, S03, S05, S08 and S16 (see Fig. 4.6), were selected to characterize the AW values along the main longitudinal axis of the estuary. Fig. 4.19 plots the monthly total river discharge from the eight tributaries and the depth averaged AW at the four stations for the real-time scenario (case 1). It can be observed that the AW values were negatively proportional to the amount of river discharge. For example, the AW at S16 was 23.17 days in January (dry season), when the total discharge was  $3.4 \times 10^3 \text{ m}^3/\text{s}$ . When the discharge increased to  $2.07 \times 10^4 \text{ m}^3/\text{s}$  in July (wet season), the AW value at S16 fell to 8.98 days. Among the four stations, the AW values at S16 were greatest, with the averaged value over the entire year being 15.18 days. The AW values at S03 were the smallest, ranging from 6.4 days to 19.5 days with a mean value of 11.39 days. Therefore, the AW value was

related to the distance from the point position to the upstream. The station with a shorter distance to a tributary inlet has a lower AW value. In addition, the differences in the AW values among the four stations were larger in the dry season. For example, the difference between S03 and S16 was 7.35 days in February and decreased to 2.57 days in July. Therefore, the longitudinal variation of the AW values inside the PRE was enhanced during the dry season.

**Table 4.6. Depth-averaged AW (unit: days) at four stations along the west channel and the total discharge (unit:  $m^3/s$ ) in each month over one year**

	Total discharge	S03	S05	S08	S16
January	3355.2	17.67408	18.5554	21.69734	23.17614
February	3634.9	19.46064	21.60011	26.42407	26.81167
March	4753.2	16.18923	17.00505	20.15466	21.52731
April	8667.7	11.21516	11.76617	13.37115	14.8684
May	14539.5	8.176113	8.568947	9.391516	10.81142
June	19849.9	6.865884	7.230401	7.594917	8.984201
July	20688.1	6.410665	6.971165	7.531666	8.983303
August	17613.7	7.035321	7.718389	8.401458	9.856057
September	12581.8	7.283976	7.280786	8.03836	9.222816
October	7269.7	10.32422	10.52313	11.37542	12.49745
November	5452.5	12.21794	12.64275	14.6647	16.34131
December	5033	13.83413	14.50925	17.2754	19.08234

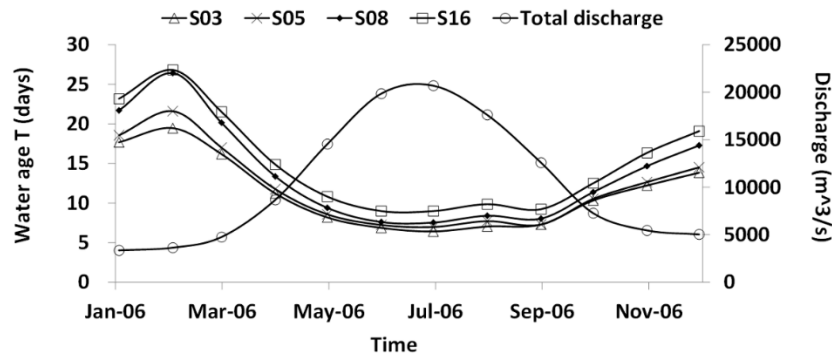


Fig. 4.19. Total discharge and depth-averaged age at four stations over a year for real-time condition (case 1).

The AW values at the four stations are plotted against the river discharge in Fig. 4.20.



It can be observed that the AW values monotonically decreased as the discharge increased. When the discharge amount was below  $5.0 \times 10^3 \text{ m}^3/\text{s}$ , the AW value declined more substantially. Empirical formulae derived by fitting the data are listed in Table 4.7. The power law formulae generally fit the predicted results well, with correlation R-squared values greater than 0.91.

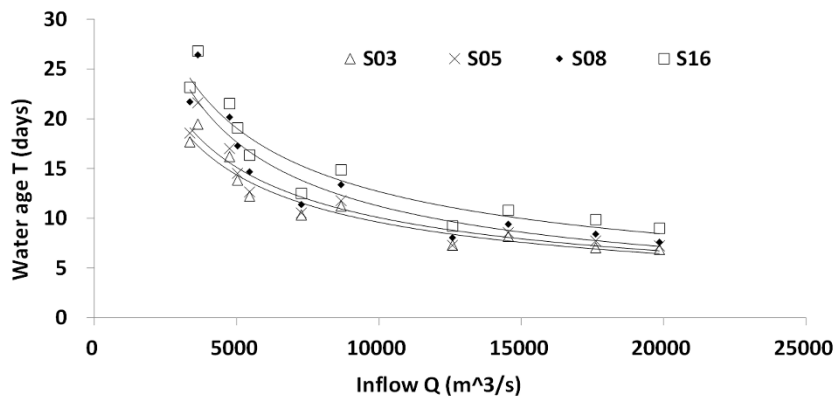


Fig. 4.20. Monthly depth-averaged age  $T$  (days) in response to the total river discharge  $Q$  ( $\text{m}^3/\text{s}$ ) at four stations for real-time condition (case 1).

**Table 4.7. Empirical fitting equations between the total river discharge and the age at four stations and correlation R-squared values (Q: discharges; T: age)**

Stations	Empirical equations	R-squared values
S03	$T = 2041.6Q^{-0.582}$	0.943
S05	$T = 2246.9Q^{-0.587}$	0.915
S08	$T = 4648.7Q^{-0.654}$	0.915
S16	$T = 2867.0Q^{-0.589}$	0.910

#### 4.6.1.2. High, mean and low constant discharge (cases 2-4)

An increase in the river discharge can bring stronger advection and stratification in an estuary. To further investigate the impact of the river discharge on the AW distributions, three additional model experiments under constant high, mean and low discharges (cases 2–4) were conducted.

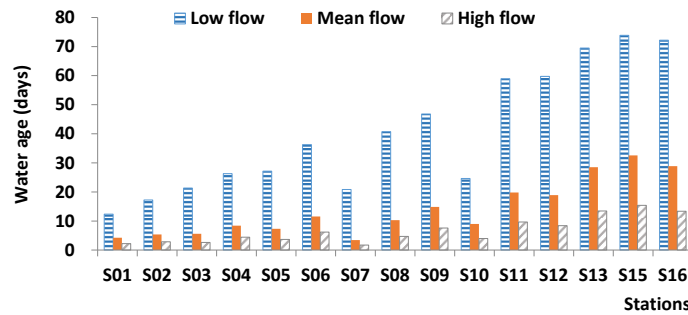


Fig. 4.21. Monthly depth-averaged age (days) at 15 stations under constant discharges.

Fig. 4.21 plots the monthly depth-averaged AW at 15 stations inside the estuary after a five-month spin-up period in response to the total discharge for cases 2 to 4. From the map of stations' locations (see Fig. 4.6), stations S01–S07 are in the upper portion of the estuary, while stations S08–S13, S15, and S16 are in the lower portion. Under the high discharge, the residual current speed was more pronounced, as expected, hence the lower AW values were observed. It took 4.73 days and 13.37 days for one water parcel to be transported to S08 near the Nei Lingding Island and S16 near the estuary mouth, respectively. With the decline in the discharge, the AW generally increased under the mean and low discharge conditions, especially in the upper portion of the estuary. It took 28.89 days and 72.17 days for one water parcel to be transported out of the estuary under the mean and low discharge conditions, respectively.

These results further suggest that the AW is a function of discharge. The discharge is one of the dominant factors in controlling the transport and mixing processes in the estuary.

#### 4.6.1.3. Without discharge (case 5)

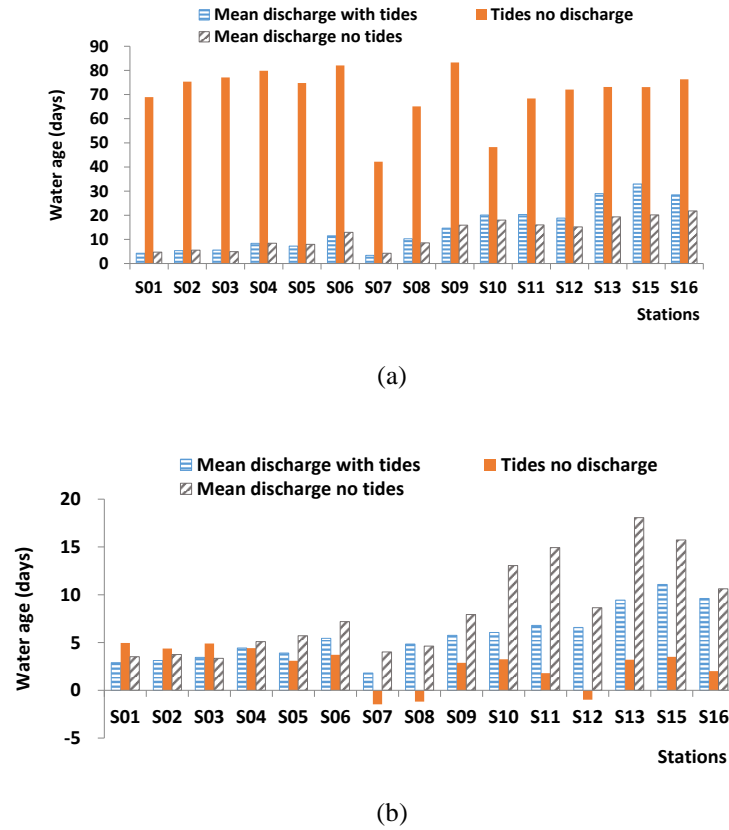


Fig. 4.22. Monthly averaged (a) vertical difference in the age and (b) depth-averaged age of April 2006 for case 3 (constant mean discharge and tides), case 5 (only tides without discharge) and case 6 (only mean discharge without tides) at 15 sampling stations.

Fig. 4.22 plots the depth-averaged AW and the AW vertical difference  $\Delta a$  at 15 stations for case 3 (mean discharge and tides), case 5 (tides without discharge) and case 6 (only mean discharge). By comparing with case 3, the AW values greatly increased at all stations for case 5, from 40 days to 80 days (Fig. 4.22a). The AW vertical difference  $\Delta a$  (Fig. 4.22b) showed that the stratification decreased at most stations without discharge, except station S01-S03 in the upper estuary. At stations S07, S08 and S12, the bottom AW was even smaller than the surface AW. Take S16, for example: the vertical AW difference dropped from 9.61 days to 2.01 days when discounting the impact of discharge.

The results indicated that the river discharge enhanced the water exchange process which brought a great decrease in the AW values. Moreover, the discharge increased the stratification in most areas of the estuary, except in the upper estuary where the vertical mixing induced by the discharge could be more pronounced.

#### **4.6.2 Influence of tidal current**

##### 4.6.2.1. Mean discharge without tides (case 6)

Case 6 was conducted under a constant mean discharge without the influence of tidal currents. In comparison with the results in case 3, the AW values decreased at most stations for case 6, as shown in Fig. 4.22a. However, the AW vertical difference  $\Delta a$  significantly increased, especially at the stations in the lower estuary. At stations S10, S11 and S13, the  $\Delta a$  even increased to about twice their original values (Fig. 4.22b)

In other words, the freshwater discharge plays an important role in reducing the presence of pollutants inside the estuary. Moreover, the tidal mixing by tides eroded the stratification structure, more significantly at stations in the lower estuary. The influence of tides is opposite to the river discharge. Although the PRE is located along a micro-tidal coast, tidal current plays a critical role in affecting hydrodynamic processes.

##### 4.6.2.2. High water and low water (case 1)

In an estuary, the stratification–mixing process is regulated by the tides; hence the AW varied temporally in response to the tidal heights over a spring and neap tidal cycle. From the literature it is known that the maximum stratification occurs at the end

of the neap tide. The minimum salinity difference and minimum stratification occurred at the end of the spring flood (Wong et al., 2003a). In this study, two spring tides in the wet and dry seasons resulting from the real-time condition (case 1) were selected to investigate the AW variation between high water and the low water (Fig. 4.23, Fig. 4.24).

From Fig. 4.23 it can be seen that during the wet season, at the surface, the AW values varied from 0 day to 15 days in most areas of the estuary at both high and low waters, a seaward tongue occurred on the west side at low water with values being less than 5 days (Fig. 4.23a). Near the bed, the AW distributions were nearly identical for high and low waters with the average AW value being approximately 10 days (Fig. 4.23b, d). It indicates that, in the wet season, the tidal influence is relatively small under the large volume of river discharge.

In the dry season, the surface AW distributions were significantly different between high and low waters (Fig. 4.24). At high water, the freshwater was confined along the western coastal line at the surface (Fig. 4.24a). The surface AW alignment was from the northeast to the southwest with the 25-day contour line crossed the middle estuary. At low water, the AW values were generally lower across the estuary with the seaward tongue of AW less than 15 days in the upper estuary, and seaward tongue of approximately 20 days in the middle estuary (Fig. 4.24c). The AW value near the Lantau Island was greater than 35 days at high water and it fell to approximately 25 days at low water. As shown in Fig. 4.24b and d, there was no obvious difference between the bed AW distributions in response to the water elevation variation.

From Figs. 4.25a and b, it can be seen that in the wet season the vertical AW

distribution had relatively little change in response to the tidal height. The surface AW was less than 5 days in the first 35 km upstream at high water, while at low water the 5-day contour extended approximately 10 km downstream. The surface AW near the estuary mouth decreased from 15 days at high water to 10 days at low water. During the dry season, the AW distribution was nearly homogenous vertically at high water (Fig. 4.25c), while it showed the stratified structure at low water (Fig. 4.25d).

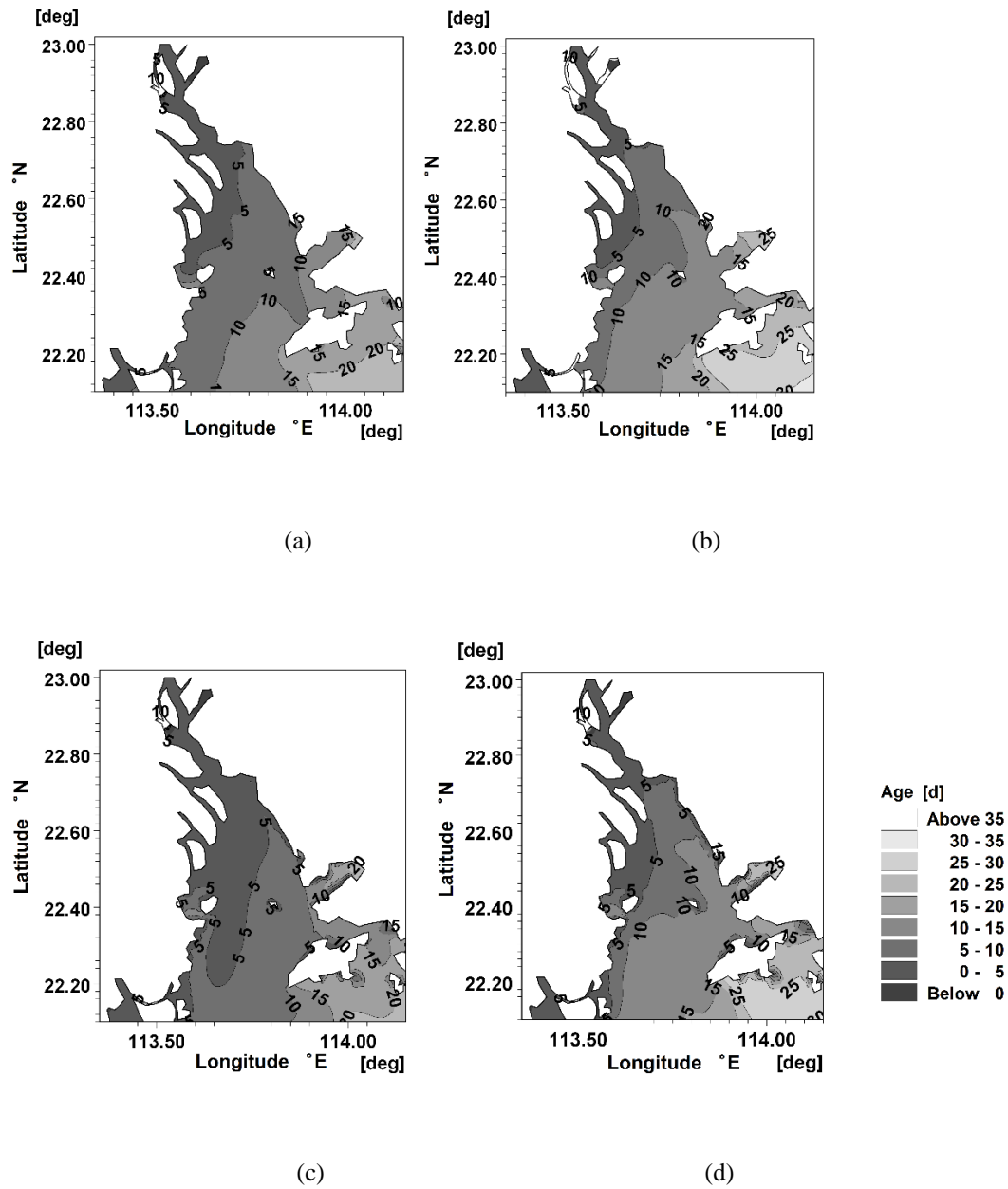


Fig. 4.23. Water age horizontal distributions at spring tide in the wet season for real-time condition (case 1) (a) at surface, high water; (b) near bed, high water; (c) at surface, low water; (d) near bed, low water.

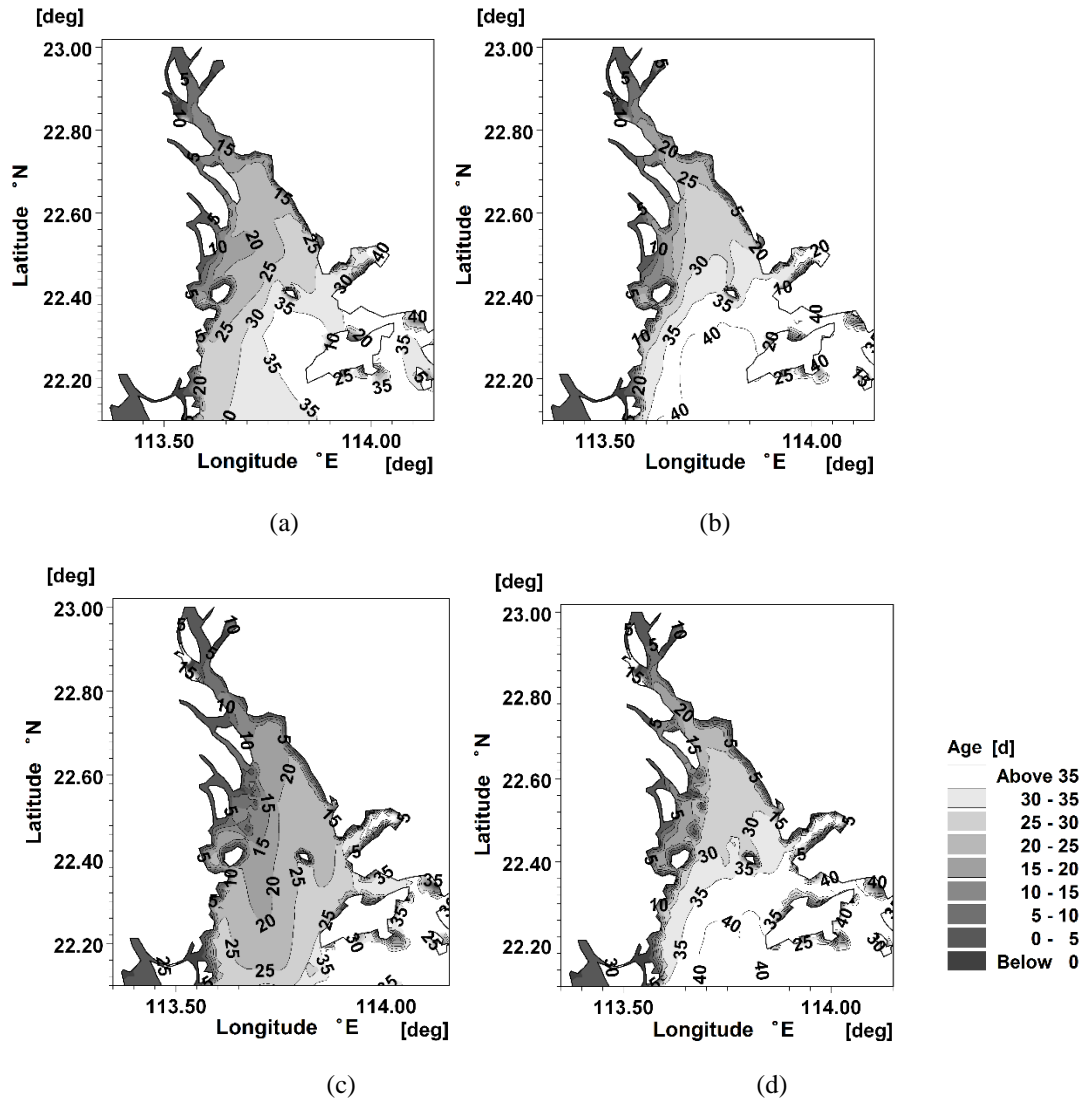
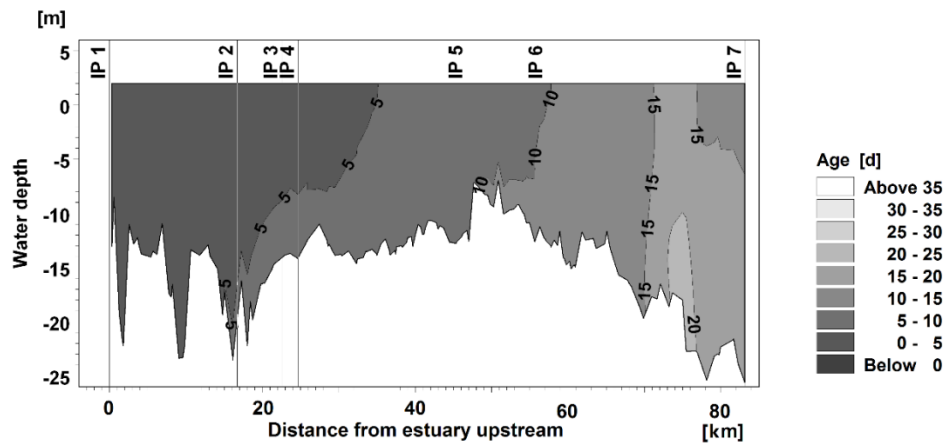
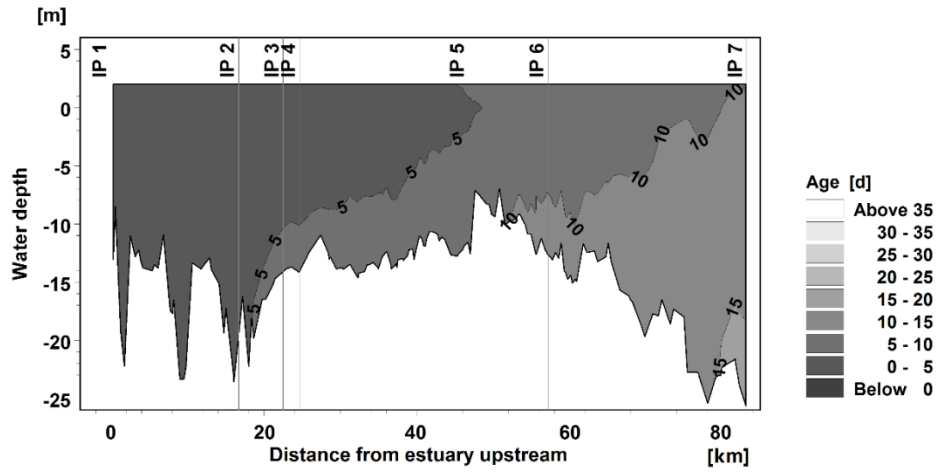


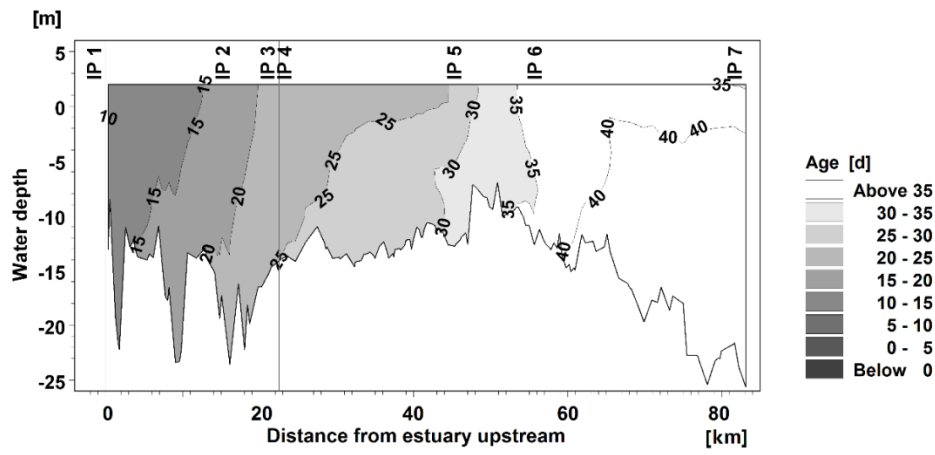
Fig. 4.24. Water age horizontal distributions at spring tide in the dry season for real-time condition (case 1) (a) at surface, high water; (b) near bed, high water; (c) at surface, low water; (d) near bed, low water.



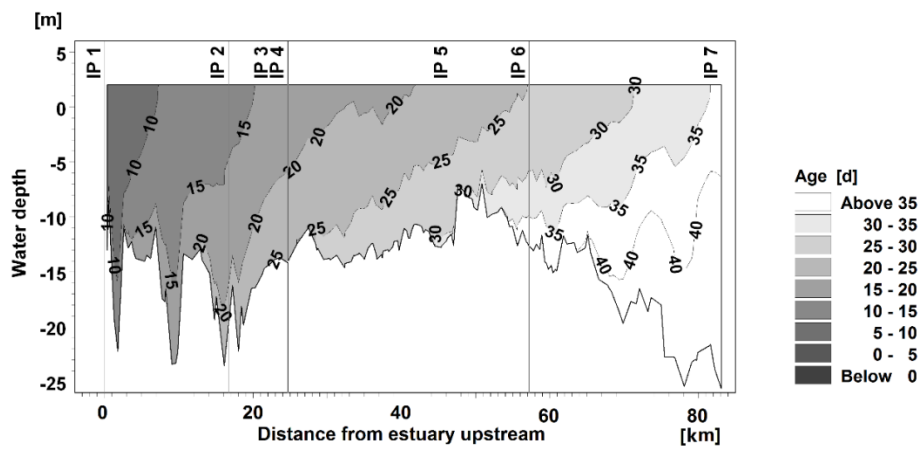
(a)



(b)



(c)



(d)

Fig. 4.25. Water age vertical distributions of along-channel section for real-time condition (case 1) (a) spring high water in the wet season; (a) spring low water in the wet season; (c) spring high water in the dry season; (b) spring low water in the dry season.



In summary, the results indicated that, compared with the wet season, the tidal influence was enhanced in the dry season due to the decrease in river discharge. Moreover, in the ebb tides the upper layer freshwater moved seaward faster than the denser bottom water. In the flood tides, the strong flow prevented the development of stratification and accelerated its breakdown (Simpson et al. 1990).

#### *4.6.2.3. Spring and neap tides (case 1)*

To better understand the influence of tides, Fig. 4.26 presents the time series of the hydrodynamic parameters (water elevation, salinity, vertical eddy viscosity) and AW values at stations S08 and S16 over two months: July 2006 and January 2007, representing the wet season and the dry season, respectively. The S08 represents the station, near Nei Lingding Island, in the middle estuary and S16 represents the station near the estuary mouth.

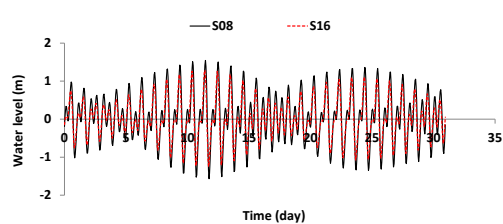
The time series of salinity vertical difference  $\Delta s$  showed that the tidally averaged  $\Delta s$  increased during neap tides (Fig. 4.26b, f). For example, in the wet season the maximum salinity stratification level, and consequently the maximum  $\Delta s$  at S08, was observed at the end of the neap ebb, being 25.6 psu. The minimum stratification and the minimum  $\Delta s$  (approximately 16 psu) were observed after the spring flood. It implied that the salinity stratification was enhanced during neap tides.

The results indicated that the salinity difference between high and low waters increased during spring tides with the increase in the tidal range (Fig. 4.26b, f). Take station S16 in the dry season, for example (Fig. 4.26f):  $\Delta s$  varied by nearly 10.87 psu over the course of a tidal cycle during spring tides, with its value being 11.80 psu at

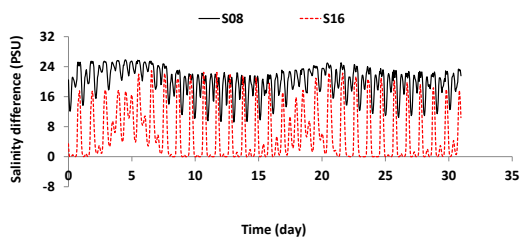
high water and 0.92 psu at low water, while the  $\Delta s$  remained nearly constant (approximately 7 psu) throughout the tidal cycle, during neap tides, with very small fluctuation.

It can be seen from Fig. 4.26c and 4.26g that the temporal variation of the AW vertical difference  $\Delta a$  was consistent with the salinity stratification. As the salinity stratification increased, during neap tides, the gravitational circulation became stronger. More dissolved substances were transported out of the estuary, leading to a relatively short AW at the surface. Then the AW surface–bed difference  $\Delta a$  was enhanced in the neap tide. In the wet season, the maximum  $\Delta a$  was observed at the end of the neap ebb tide, being approximately 7.59 days and 7.21 days for S16 and S08, respectively (Fig. 4.26c). The  $\Delta a$  between high water and low water increased from approximately 1.60 days in the neap tide to 3.51 days in the spring tide. During the dry season (see Fig. 4.26g), the  $\Delta a$  values generally increased in the neap tide. The  $\Delta a$  value between high and low waters increased in the spring tide. Take S16 for instance:  $\Delta a$  values between high and low waters decreased dramatically from 13.59 days to 1.64 days. It indicated that the tidal influence increased during the dry season when the discharge was relatively small.

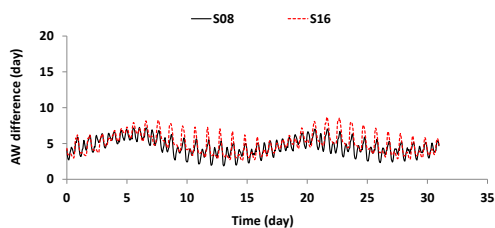
By comparing S08 and S16, it can be seen that the spring–neap tidal difference was more pronounced at S16, which was located in the lower estuary where tidal currents played a more significant role.



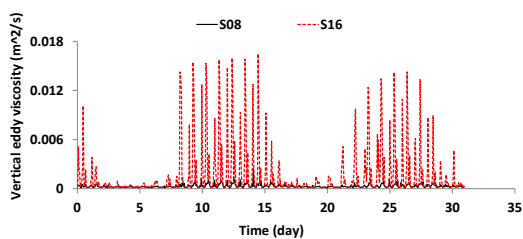
(a)



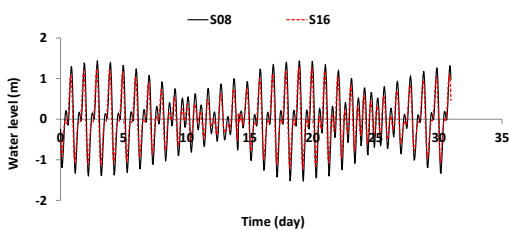
(b)



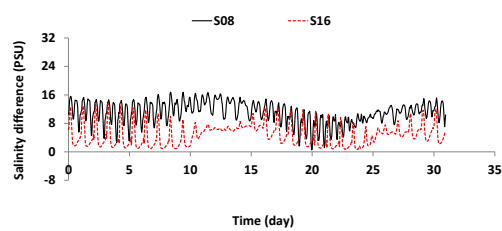
(c)



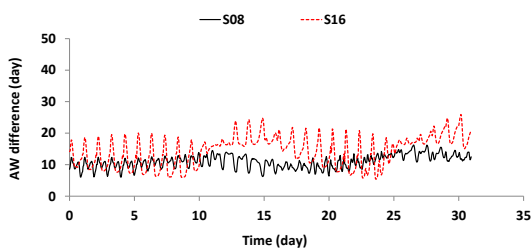
(d)



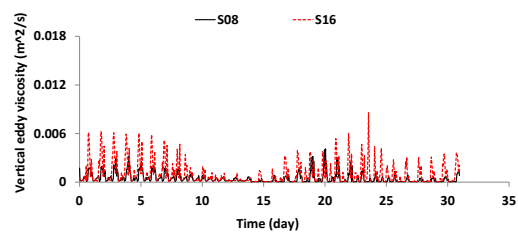
(e)



(f)



(g)



(h)

Fig. 4.26 Temporal variation of water elevation, salinity vertical difference, water age vertical difference, and depth-averaged vertical eddy viscosity at S08 and S16: (a)–(d) July 2006; (e)–(h) January 2007.

In summary, the AW vertical structure was consistent with the salinity stratification. The AW stratification was stronger during neap tides when the tidal mixing was weaker. It has a similar conclusion from Section 4.6.2.2: the tidal mixing could erode the stratification structure. Moreover, the variation of stratification structure between high and low waters is more pronounced during spring tides with the larger tidal range.

As aforementioned, the decrease of stratification at the spring tide can be explained by the increase of tidal force and stronger tide induced mixing. The vertical mixing of water between the upper and lower layers was enhanced, leading to the reduction in the vertical salinity and AW differences. This point was further confirmed by examining the depth-averaged vertical eddy viscosity  $\nu_t$  which represented the mixing strength (see Fig. 4.26d, h). In the wet season (Fig. 4.26d), the value of  $\nu_t$  at S16 was approximately  $0 \text{ m}^2/\text{s}$  in neap tides and increased to approximately  $0.016 \text{ m}^2/\text{s}$  in spring tides. The time series of  $\nu_t$  in the dry season showed a similar phenomenon (Fig. 4.26h). The maximum value of  $\nu_t$  at S16 exceeded  $0.016 \text{ m}^2/\text{s}$  during spring tides which represent the stronger tidal mixing.

#### *4.6.2.4. High, mean and low constant discharge (cases 2–4)*

Here, the predictions from three model experiments under high, mean and low discharges (cases 2–4) were used to further investigate tides' influence. Fig. 4.27 shows the time series of water level, depth-averaged AW and the vertical AW difference  $\Delta a$ , at station S16, over the 6th month under high, mean and low discharges, respectively.

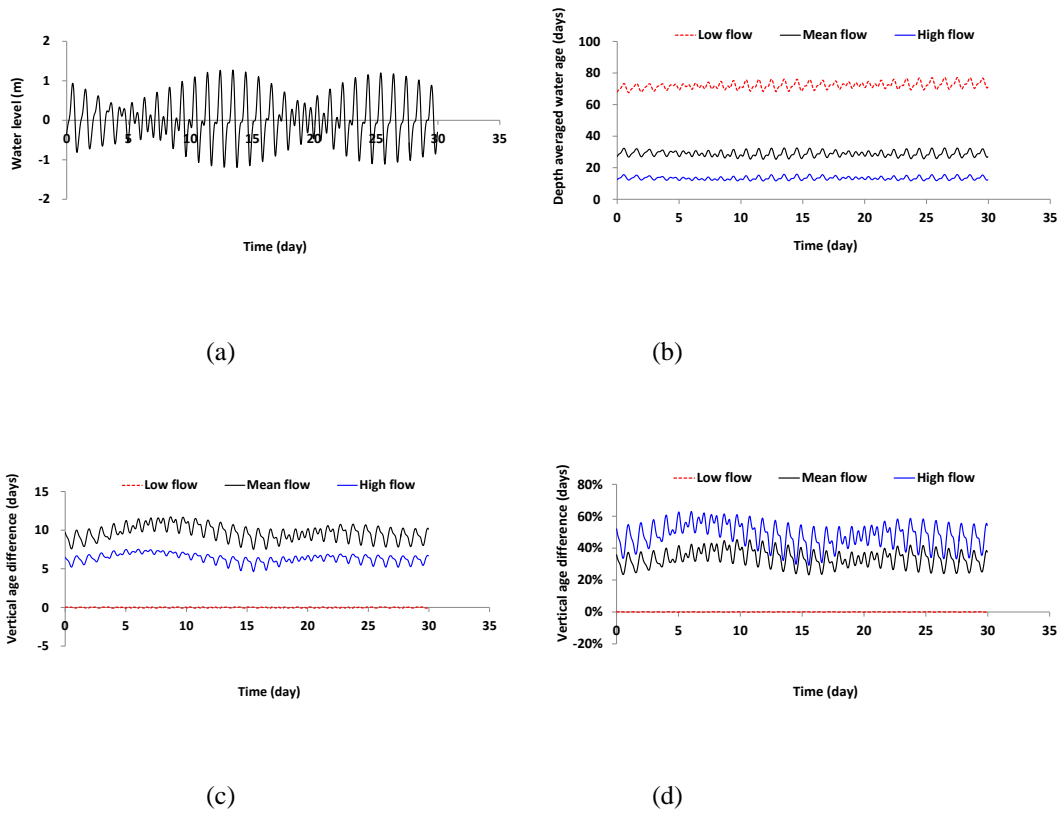


Fig. 4.27. Time series of (a) water level; (b) depth-averaged water age; (c) water age vertical difference; (d) water age vertical difference in percentage at S16 under high, mean and low discharges in June 2006.

It can be seen from Fig. 4.27b that under the low discharge the AW had large values, fluctuating between 67.6 days and 77.1 days. The maximum fluctuation was 9.5 days over the month. While the AW values under the high discharge ranged from 11.6 days to 15.9 days with temporal variation being approximately 4.3 days. The results indicated that the tidal influence became more significant when the discharge was relatively small.

From the time series of the AW under the average flow, the temporal AW difference between the high and low waters increased during spring tides, while the tidally depth-averaged AW within one month remained nearly constant over spring–neap periodic tides. From the time series of the relative AW vertical difference shown in

Fig. 4.27c, it can be observed that the AW stratification was enhanced during neap tides. The results suggested that a spring–neap tide has less influence on the tidally depth-averaged AW but impacts the tidally temporal AW difference and the AW vertical structure.

In addition, it can be seen that among the predictions under constant discharges, the AW vertical difference  $\Delta a$  was the smallest under the low discharge, being approximately 0 days. With the increase of discharge, the AW vertical difference  $\Delta a$  increased, i.e., the stratification was enhanced. The  $\Delta a$  under mean and high discharges were approximately 9.7 days (33.8% of depth-averaged AW) and 6.4 days (48.4% of depth-averaged AW), respectively. The results suggested that the tidal mixing eroded the stratification structure more easily under relatively small discharge. In other words, the AW stratification was primarily attributed to the river discharge.

In conclusion, by exhibiting the time series of the AW values under constant discharges and AW distributions in the wet and dry seasons, it was observed the tidal influence was more pronounced in the dry season when the discharge was relatively small. In addition, the AW values and vertical distribution were regulated by the tides and showed difference over high–low and spring–neap tides. Over a high–low water, the ebb flow brought a lower AW values and stronger AW vertical difference at the low water. While over a spring–neap tide, the stronger AW stratification was observed during neap tides. Because the increased tidal mixing during spring tides could erode the stratification structure which has been proven by the time series of vertical eddy viscosity. However, the spring–neap tides could only impact the AW vertical structure, while it has little impact on the tidally depth-averaged AW values.

### 4.6.3 Influence of density-induced circulation

#### 4.6.3.1. Comparison between the baroclinic mode (case 1) and the barotropic mode (case 7)

In the PRE, the combined effects of the river discharge and tides produced a two-layer, stratified structure during the wet season (Fig. 4.17a), while the estuary was observed partially mixed in the dry season (Fig. 4.17b). The density-induced circulation with the outflow freshwater in the upper layers and inflow salty water occurring in the lower layers was shown in Fig. 4.17c. By running the model for both the baroclinic mode (case 1) and the barotropic mode (case 7), the contribution of density-induced circulation to the water exchange processes could be investigated. In case 1, the pressure at one position could be written as follows:

$$p(x, y, z, t) = p_a(x, y, t) + \rho_0 g [\eta(x, y, t) - z] + \rho_0 g \int_z^\eta \frac{\rho'(z')}{\rho_0} dz' \quad (4.3)$$

where  $\rho' = \rho - \rho_0$ ;  $\rho$  is the density of water;  $\rho_0$  is the reference density of water, which was set to  $1.025 \times 10^3 \text{ kg/m}^3$  in the modelling;  $p_a(x, y, t)$  is one standard atmosphere pressure;  $\rho_0 g \eta(x, y, t)$  is the barotropic forcing term at this position due to the tide amplitude variation;  $\rho_0 g \int_z^\eta \frac{\rho'(z')}{\rho_0} dz'$  is the baroclinic term induced by density gradients, if the  $\eta \ll z$ , then this term could be written as  $\rho_0 g \int_z^0 \frac{\rho'(z')}{\rho_0} dz'$ . The AW model applied in the current study was based on the solution of three-dimensional incompressible Reynolds-average Navier-Stokes equations, subject to the assumptions of Boussinesq and hydrostatic pressure. Because the fluid is assumed to be incompressible, hence the density  $\rho$  does not depend on the pressure,

it is a function of only salinity and temperature. For the barotropic mode, both temperature and salinity will be constant and the density will not be updated during the simulation. The baroclinic component driven by the density gradient will be ignored.

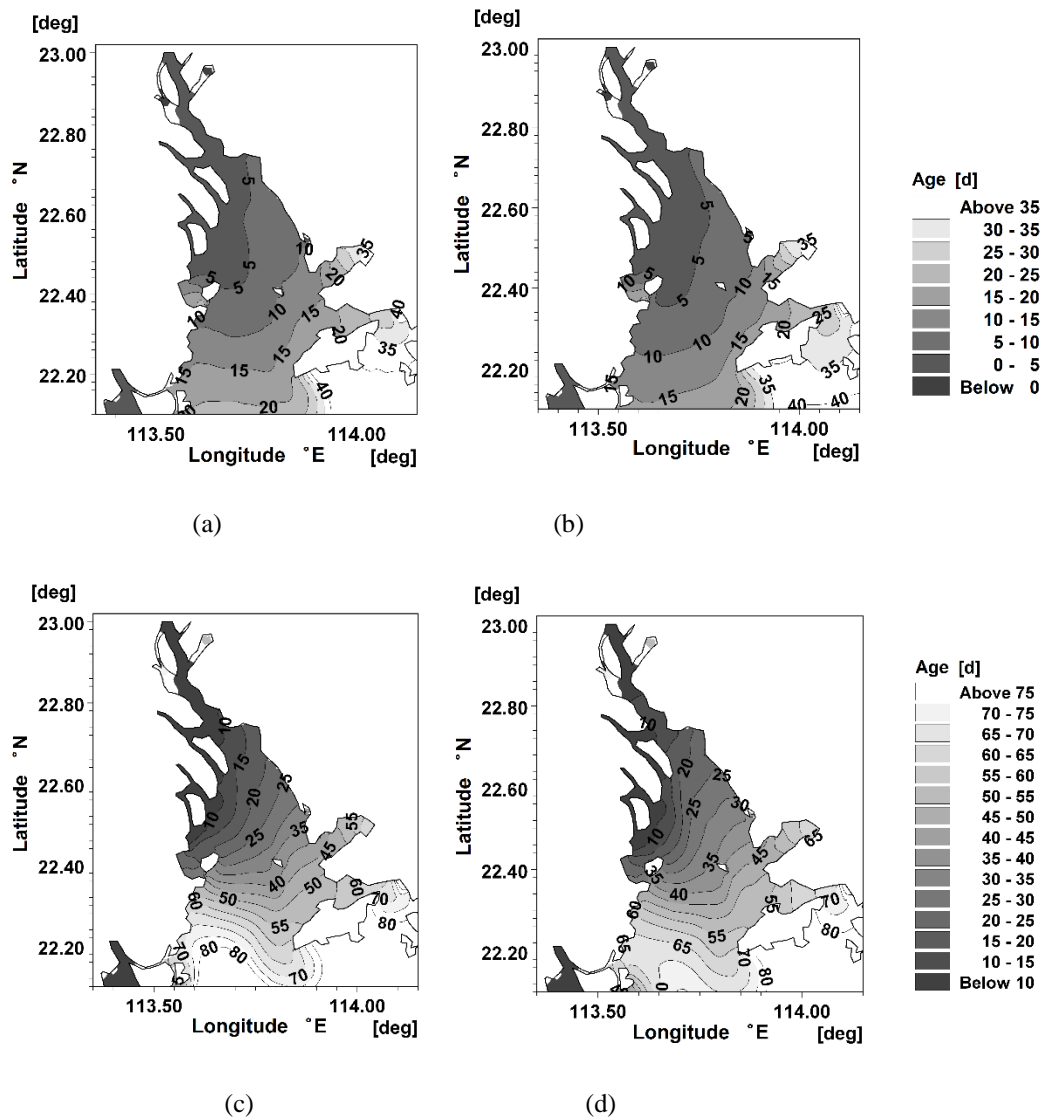
Fig. 4.28 shows the predicted AW distributions for the barotropic mode (case 7) in the wet season and dry season, respectively. By comparison with the predicted AW results for the baroclinic mode (case 1) in Fig. 4.15, in the wet season the surface AW increased from less than 10 days to between 10 and 20 days in the lower estuary (Fig. 4.28a). The bed AW value decreased from between 5 and 10 days to less than 5 days in the upper estuary while increasing from approximately 15 days to 25 days near the estuary mouth (Fig. 4.28b). In the dry season, the AW surface and bed distributions for the barotropic mode are similar, and they are very different for the baroclinic results. It can be seen that the surface seaward low AW tongue and the bed landward high AW tongue patterns disappeared, without the density-induced circulation, and the AW values were greatly increased. For instance, the surface AW value near the estuary mouth increased from approximately 30 days to greater than 70 days.

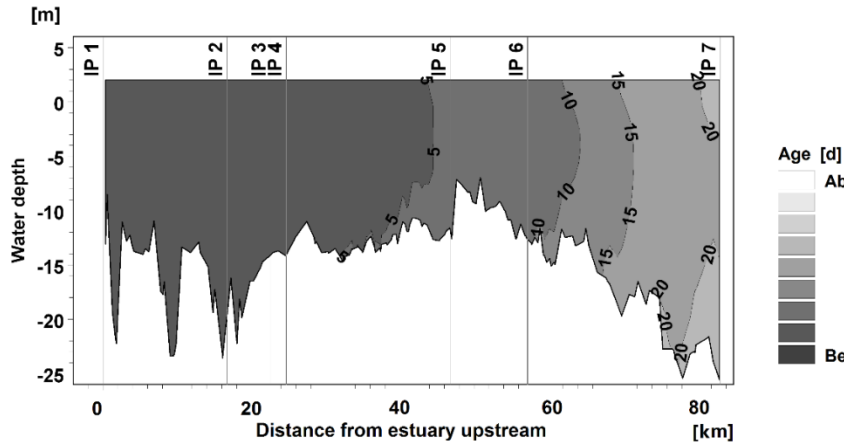
As shown from the vertical AW profile for the baroclinic mode (Fig. 4.159e, f), the AW distributions were more uniform without density-induced circulation. Even in the wet season, under the large volume of river discharge, the surface-bed AW difference was nearly zero along the longitudinal cross-section. For the first 40 km upstream, the AW was less than 5 days all along the water depth. The results indicated the importance of baroclinic forcing in producing the stratification.

Fig. 4.29 shows the relationship between the total discharge and the monthly

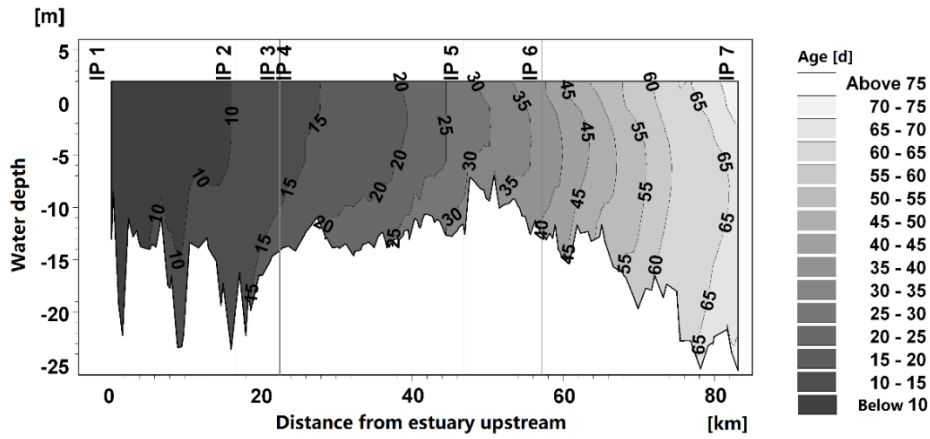


depth-averaged AW at S16 for the baroclinic and barotropic modes. It can be observed that the AW values were lower in all months for the baroclinic mode, see also Table 4.8. The results indicated that the density-induced circulation caused a decrease in the exchange timescales by more than 50%. With the impacts of density-induced circulation, the AW values in January and July were 50.74 days and 9.38 days lower, respectively, i.e., 68.64% and 51.07%.





(e)



(f)

Fig. 4.28. Water age distributions for the barotropic mode (case 7): (a) at surface, wet season; (b) near bed, wet season; (c) at surface, dry season; (b) near bed, dry season; vertical distribution along the west channel: (e) wet season; (f) dry season.

Similar results have been obtained by other researchers. The influence of density-induced circulation is more important in a micro-tidal estuary than in a macro-tidal estuary (Wang et al., 2004; Shen and Lin, 2006). The vertical age distribution resembles the stratification pattern of the salinity in the regions where stratification persists. The age difference between the surface and bottom is larger during neap tide than during spring tide.

**Table 4.8** The comparison of the monthly depth-averaged age at station S16 for case 1 and case 7 over one year and the difference between two cases.

Month	Total discharge	Baroclinic	Barotropic	Difference	Difference percentage
January	3355.2	23.18	73.91	50.74	68.64%
February	3634.9	26.81	83.01	56.2	67.70%
March	4753.2	21.53	86.8	65.28	75.20%
April	8667.7	13.7	41.06	27.35	66.63%
May	14539.5	10.71	26.33	15.62	59.31%
June	19849.9	8.98	18.2	9.22	50.64%
July	20688.1	8.98	18.36	9.38	51.07%
August	17613.7	9.86	21.59	11.74	54.35%
September	12581.8	9.22	28.64	19.42	67.80%
October	7269.7	12.5	40.94	28.44	69.47%
November	5452.5	16.34	57.43	41.09	71.55%
December	5033	19.08	65.09	46.01	70.68%

This is similar to the James River Estuary, a micro-tidal partially mixed estuary, where the influence of density-induced circulation on age distribution can be more than 45 days under the mean flow condition (Shen and Lin, 2006). As the PRE is a micro-tidal estuary, the results showed that the density-induced circulation played a significant role in regulating the transport process in the PRE.

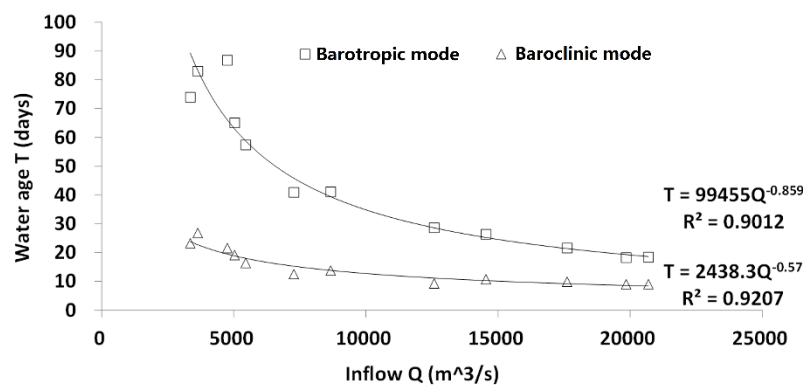


**Fig. 4.29.** The relation between monthly averaged total discharge and depth-averaged age at S16 for case 1 and case 7.

#### 4.6.3.2. *The Traditional Central Regime Theory*

As introduced in Section 4.5, the AW distribution resembled the salinity distribution. In the wet season, when the salinity stratification was intensified, the AW stratification was also enhanced. By the Traditional Central Regime theory, the relationship between the AW vertical profile and salinity profile can be explained. Thus, the AW vertical difference  $\Delta a$  was proven related to the strength of the estuarine circulation (Hansen and Rattray, 1965; Shen and Lin., 2006).

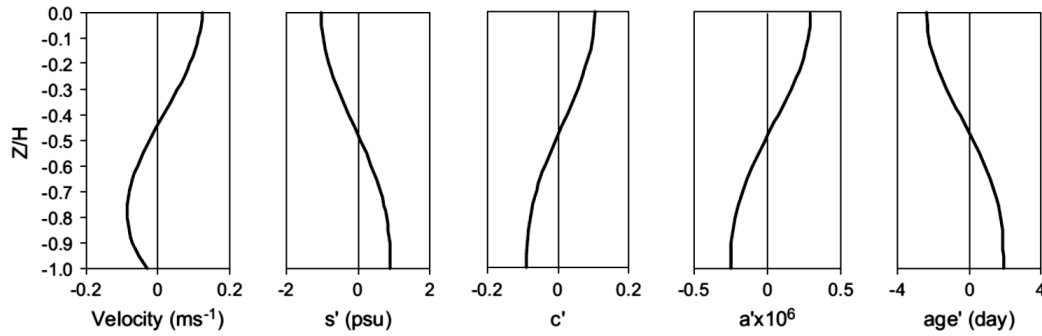


Fig. 4.30. Typical vertical distributions of residual current, salinity level  $s'$ , tracer concentration  $c'$ , age concentration  $\alpha'$ , and age (negative velocity is in the upstream direction, positive velocity is in the downstream direction, negative concentration corresponds to a concentration lower than vertical mean concentration) adapted from Shen and Lin, 2006.

The Traditional Central Regime theory was introduced in Appendix C. Fig. 4.30 is adapted from Shen and Lin, 2006, which illustrated the relationship among vertical variation distributions of the residual current, salinity  $s'$ , tracer  $c'$ , age concentration  $\alpha'$ , and AW. It can be observed that the residual current flows downstream at the surface and flows upstream near the bed. As the freshwater discharge has lower salinity, the salinity vertical profile is opposite to the residual

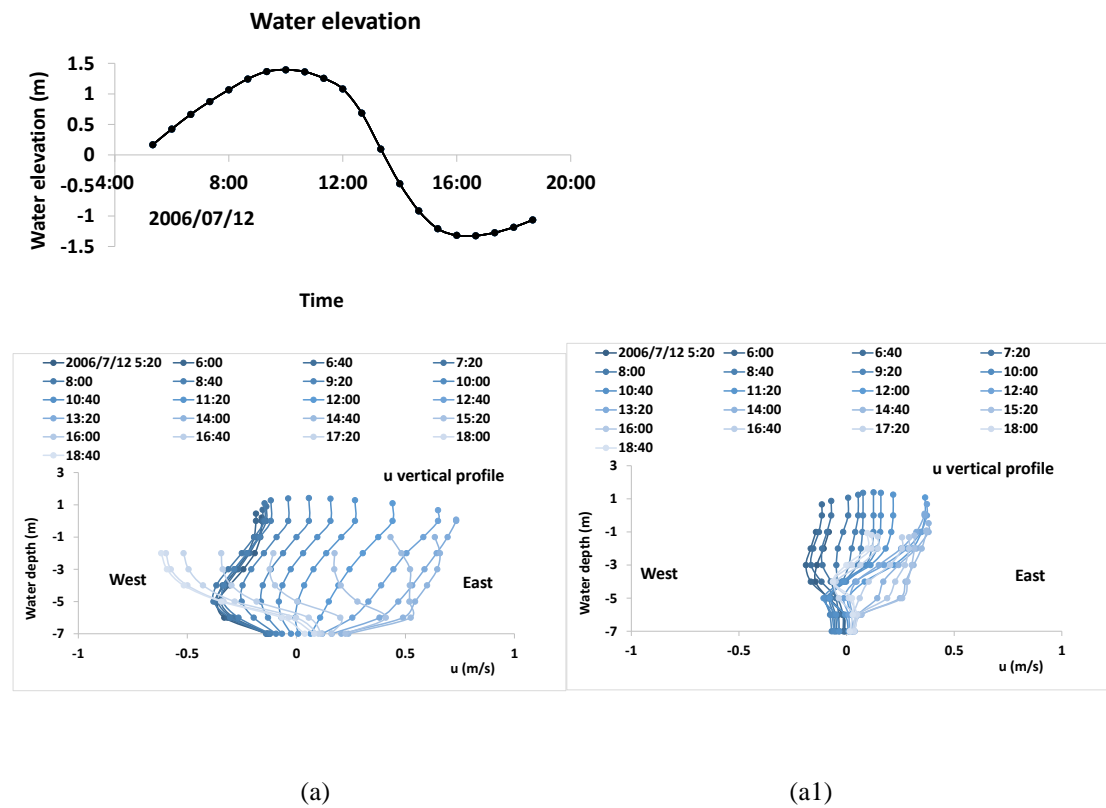
current. Note that the gradient of  $c'$  is in the opposite direction of  $s'$  since the source of the tracer is discharged from the head of an estuary and vanishes near the mouth of an estuary. Thus the high concentration appears near the surface with low concentration being near the bed, which is similar to the residual current profile.

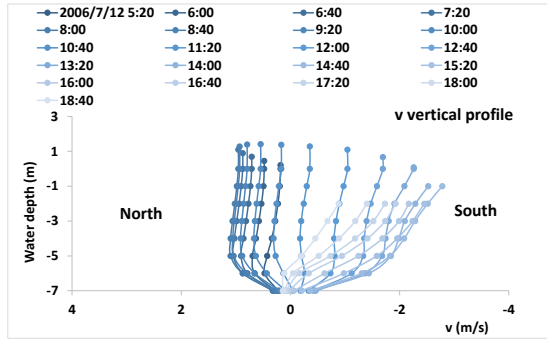
Fig. 4.31 shows the vertical profiles of current ( $u$ ,  $v$ ), tracer, age concentration,  $AW$ , salinity and density at S16 over a spring tidal cycle in the wet season for the baroclinic mode (case 1) and the barotropic mode (case 7), respectively. From the vertical profile of component  $u$  for the baroclinic mode, it is known that, at S16, the lateral flow was directed to the east during the flood and changed towards the west in the ebb (Fig. 4.31a). The speed of  $u$  was larger, especially at the surface, which was greater than 0.7 m/s to the east in the flood and more than 0.5 m/s towards the west in the ebb. For the barotropic mode, the component  $u$  ranged from 0.2 m/s to 0.4 m/s (Fig. 4.32a1). It indicated that without the density-induced circulation, the counter clock horizontal circulation was weaker.

From the profile of velocity longitudinal component  $v$ , it can be seen that the speed of  $v$  was larger in the upper layers for the barotropic mode than the baroclinic mode (Fig. 4.31b, Fig. 4.31b1), while the two-dimensional velocity for the barotropic mode showed more homogenous vertically (Fig. 4.31c1). For the baroclinic mode, the surface speed was higher than the bed speed during the flood, while it was opposite during the ebb. Since the tracer was discharged from the head of an estuary by freshwater, the gradient of the tracer concentration  $c$  (Fig. 4.31d) was in the opposite direction of  $s$  and  $\rho$  (Fig. 4.31g, h). Fig. 4.31g shows that the lower salinity was located at the surface and the higher salinity was near the bottom. The salinity vertical

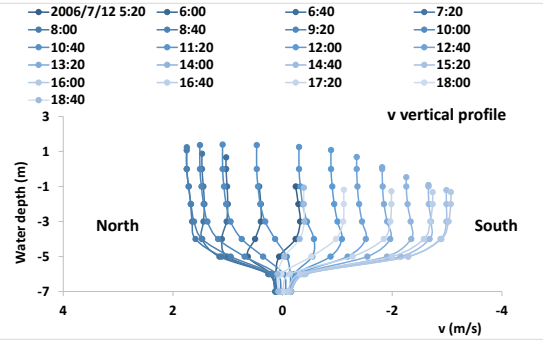
difference increased as the stratification level increased during the ebbs.

Through the Traditional Central Regime theory, the similarity of vertical AW and salinity profiles can be explained. From Fig. 4.31f, it can be seen that, for the baroclinic mode, the lower AW was in the surface layers and the higher AW was in the bed layers. At low water, the bed AW reached 30 days, which was 25 days more than the surface AW. However, as shown in Fig. 4.31f1, the AW was more uniformly distributed vertically, with the value being approximately 10 days for the barotropic mode. Therefore, the AW stratification was related to the strength of the estuarine circulation; the stratification level decreased when the density-induced circulation was not included in simulation.

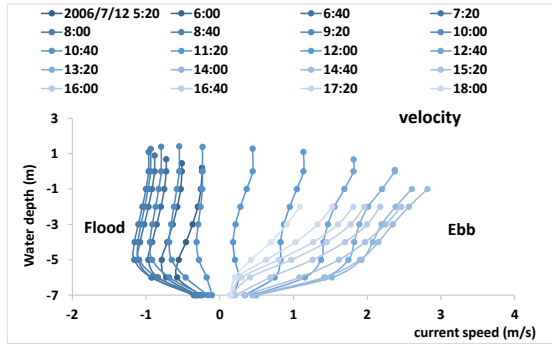




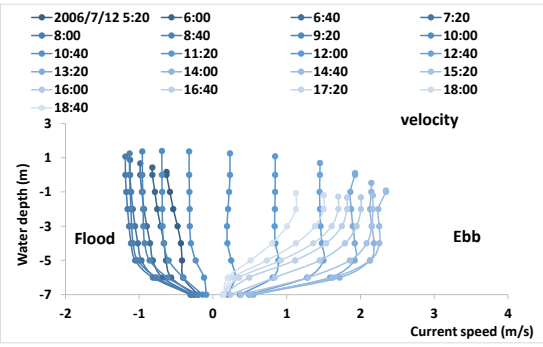
(b)



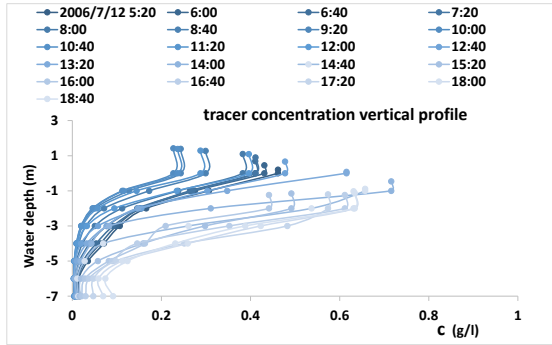
(b1)



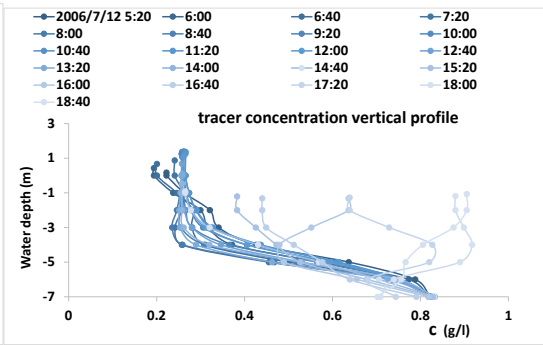
(c)



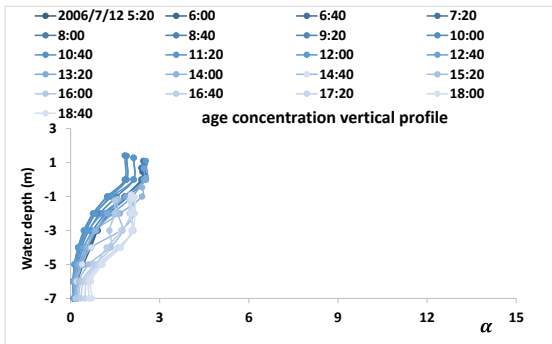
(c1)



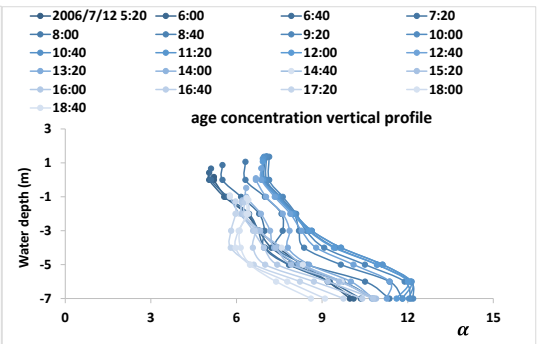
(d)



(d1)



(e)



(e1)

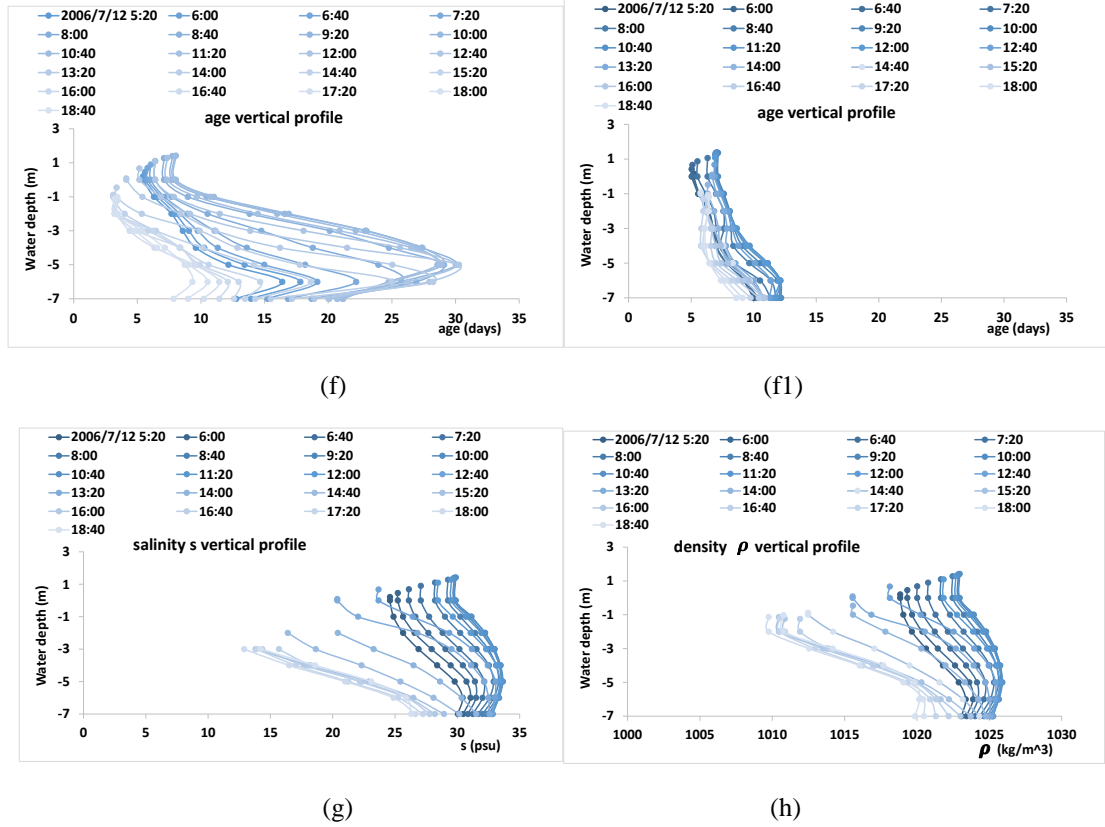


Fig. 4.31. Vertical profile of current ( $u$ ,  $v$ ), tracer, age concentration, age, salinity and density at S16 over the spring tide in the wet season with  $\Delta t = 40$  min for the baroclinic mode ( $a-h$ ) and for the barotropic mode ( $a1-f1$ ).

#### 4.6.4 Influence of wind forcing

The influence of wind on hydrodynamics in an estuarine system has been recognised by many researchers (Wang, 1979; Scully et al., 2005). It is expected that both the magnitude and direction of the wind forcing will affect the estuarine vertical mixing and stratification, thus affecting the water exchange process. In a shallow estuary, the residence time can vary by more than a factor of three in response to variations in wind induced flushing (Geyer, 1997).

As introduced in Section 4.2.4, the PRE receives the southwestern wind with speed of approximately 3 m/s in the wet season, while northeastern wind with speed being



approximately 7 m/s in the dry season. To investigate the influence of wind on the hydrodynamic processes, case 8 was conducted without wind forcing. Fig. 4.32 illustrates that the predicted horizontal AW distributions for case 8. By comparing the predictions with wind forcing (case 1) in Fig. 4.15, the contribution of wind-induced transport on the AW distributions could be observed.

When applying the southwestern wind in the wet season, it appeared the AW surface values generally increased by approximately 2.5 days (10 - 50%) across the estuary. It suggested that the upstream wind slowed the transport process of the surface water, while on the east side of the lower estuary, the age of the surface water decreased by 5 days (approximately 20%), from 25 days to 20 days. It suggested that due to the clockwise residual current field induced by the southwestern wind, the water on the east side was transported out of the estuary more rapidly. Near the bed, the AW values generally decreased by 5 days across the estuary. The results indicated that wind enhanced the vertical mixing and had the tendency to reduce the vertical stratification.

With the presence of the northeastern wind in the dry season, the AW values generally decreased by 5 days (approximately 30%) across the estuary at the surface, while there was no great difference for the bed AW values and the patterns. This indicated that under lower river discharge in the dry season, the northeastern wind enhanced the surface water exchange ability and thus the surface AW values decreased.

The results indicate that the wind has a significant influence on the AW distribution, especially for the surface water. With the wind forcing, the surface AW values increased in the wet season with southwestern monsoon, while the bed AW values decreased. In the dry season, the northeastern wind only enhances the surface water

exchange process. It implied that the influence from the wind varies with the season and its direction. In the wet season the wind could cause an increase in the vertical mixing inside the estuary, leading to a stratification area and an increased surface transport time.

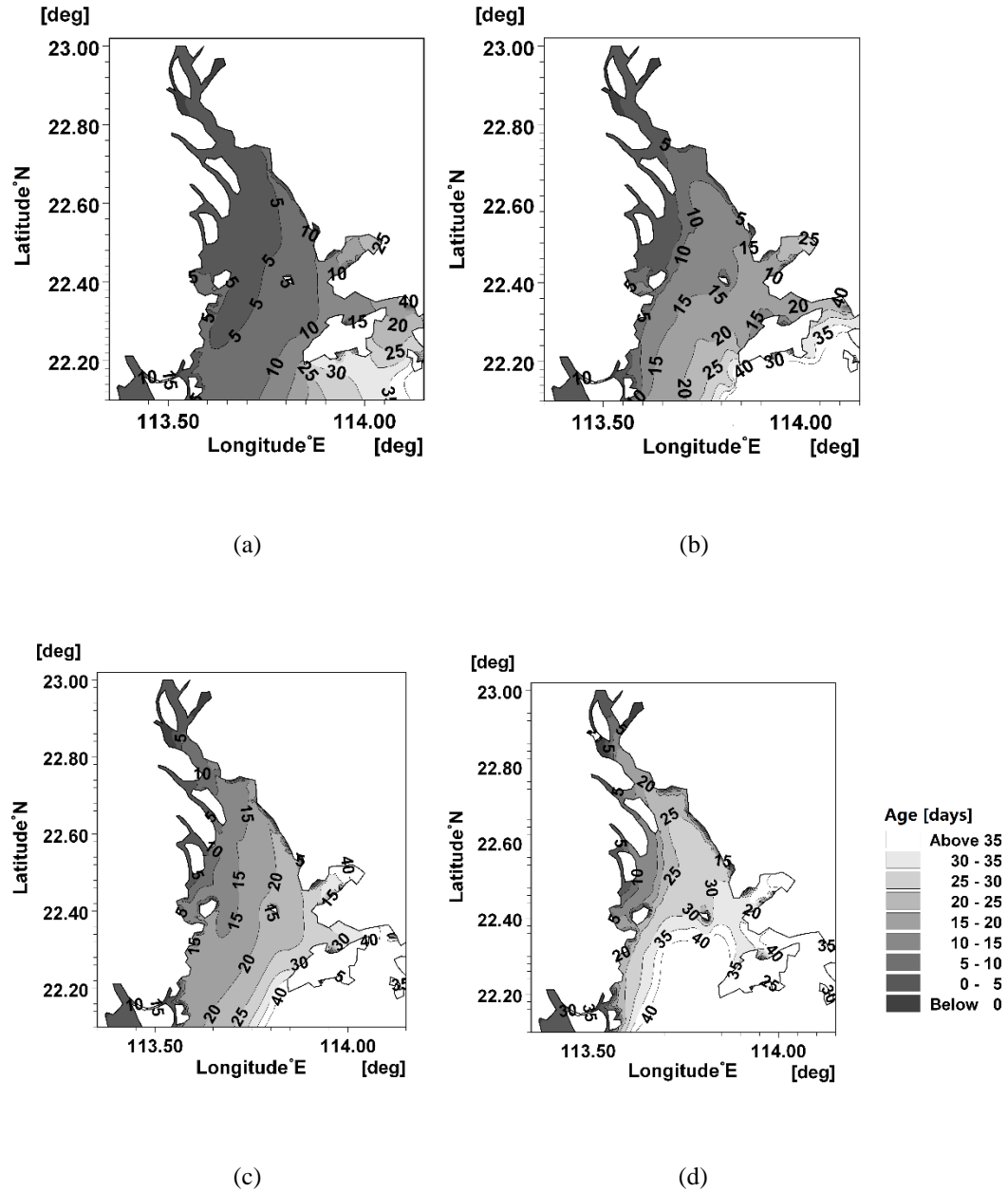


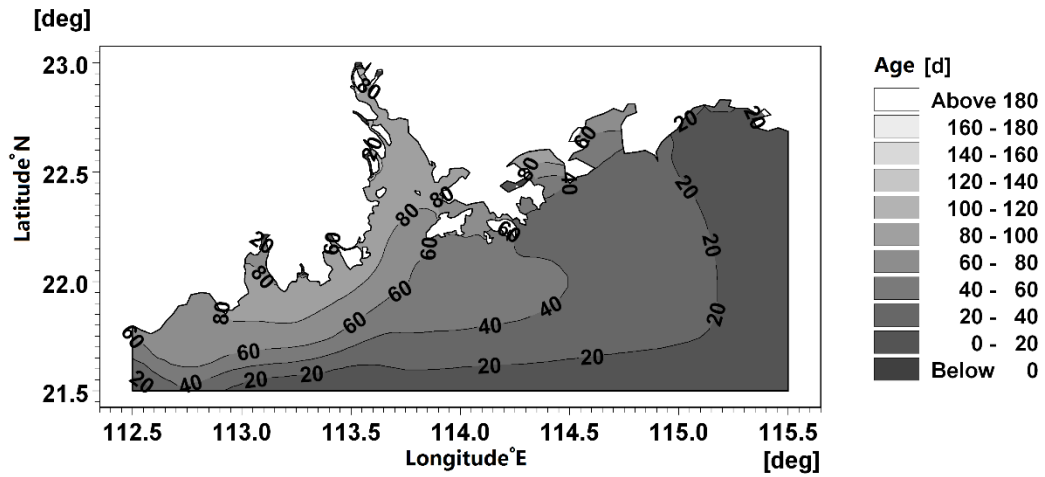
Fig. 4.32. Horizontal age distributions without the influence of wind (case 8): (a) at surface, wet season; (b) near bed, wet season; (c) at surface, dry season; (d) near bed, dry season.

#### 4.6.5 AW from open sea

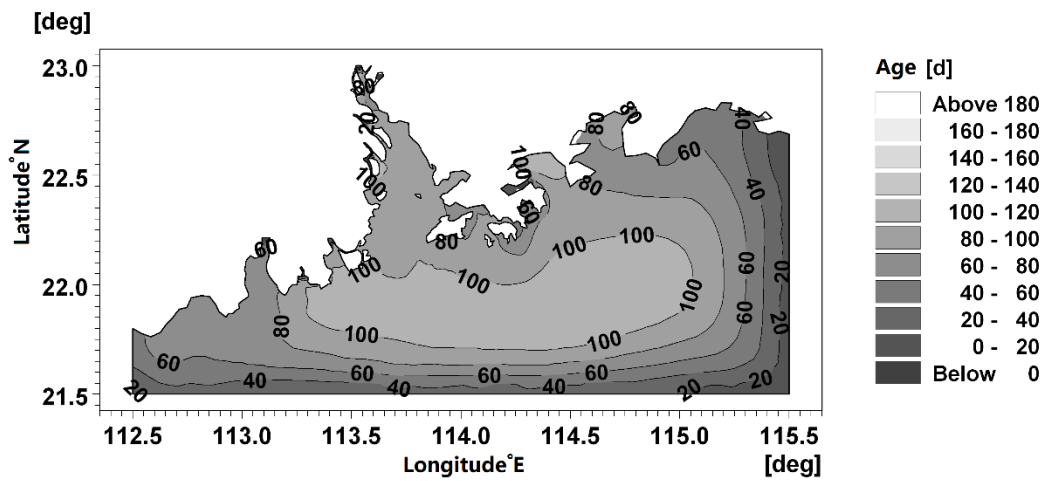
In this study, the renewing water to the PRE could be split primarily into two types: the water originating from the sea and the river discharge originating from the upstream tributaries. Case 9 was designed to simulate the AW of seawater. A tracer of concentration 1 g/L was released with the seawater at three sea boundaries. The initial tracer concentration and age concentration in the study area (Nei Lingding) was set to 0. The boundary conditions of age concentration were set as Neumann boundary condition.

Fig. 4.33 shows the horizontal AW distributions of seawater in the entire study domain during the wet and dry seasons, respectively. During the wet season (Fig. 4.38a, b), the AW inside the estuary varied from 80 days to 100 days at both the surface and the bottom. The surface AW reached the peak value in the upper estuary, while the greatest value for the bed AW was observed in the east outside the estuary mouth, being greater than 100 days. During the dry season, the AW of seawater was greater, ranging from 120 days to 160 days inside the estuary. The greatest AW was greater than 180 days, which was located at the east outside the estuary near the sea bed.

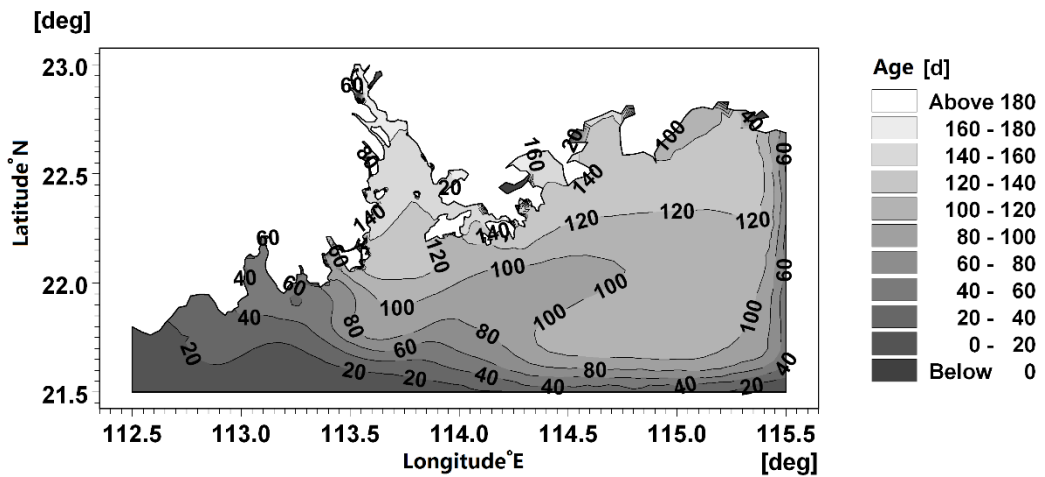
It can be seen from Fig. 4.15 that the AW was lowest near the estuary mouth and increased landward. The AW of seawater was observed much higher than that of river discharge. These results indicated that, between the two types of renewing water, the freshwater discharge replaced the original water inside the estuary more quickly.



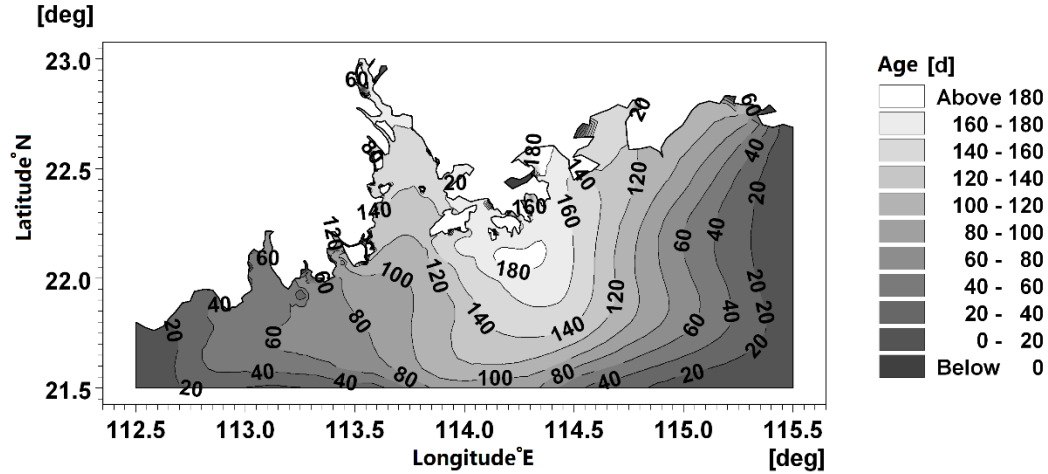
(a)



(b)



(c)



(d)

Fig. 4.33. The age distributions of seawater for the real-time condition (case 9): (a) at surface, wet season; (b) near bed, wet season; (c) at surface, dry season; (d) near bed, dry season.

## SUMMARY

The characteristics of the AW distributions inside the PRE and the relationship between the AW values and its hydrodynamic conditions were investigated. The main findings are:

- 1) The AW values increase from the northwestern part to the southern part of the PRE. Vertically, lower AW values always appear at the surface and the higher values are near the bed for both the wet and the dry seasons, leading to a landward tongue shaped AW profile towards the bed, which is caused by the vertical circulation. The age differences between the surface and bed water are approximately 5 days and 10 days in the wet and dry seasons, respectively, and a more obvious stratification of AW is in the wet season.
- 2) Due to the seasonal variation of the freshwater discharge, the values of AW in the

PRE are generally smaller in the wet season than in the dry season. The mean AW is approximately 10 days in the wet season and 25 days in the dry season. This indicates that the water inside the estuary is transported out of the estuary more quickly in the wet season under the higher river discharge. A regression analysis reveals that the AW values exponentially decrease with an increasing discharge.

- 3) Although the PRE is a micro-tidal estuary, the tidal influence is still significant when the discharge is relatively small, such as in the dry season. The difference between the high and low water AWs is larger in the spring tide due to the increased tidal range, while the tidally averaged mean AW remains nearly constant over a spring-neap tidal cycle. The AW difference between the surface and bed water is relatively large during neap tides when the impact of the tidal mixing process is weak.
- 4) From the scenario analysis it is found that by neglecting the baroclinic pressure gradient due to the density gradient, the AW value increases and the stratification becomes weaker. The depth-averaged AW can be doubled for the barotropic mode. It reflects the importance of density-induced circulation in shortening the retention time. Stratification is related to the strength of the estuarine circulation. The AW stratification level decreases when the density-induced circulation is not considered.
- 5) The monsoon wind has a significant influence on the AW distribution. In the wet season, with the southwestern wind forcing, the surface AW of the estuary increases, while the bed AW decreases in both seasons. It implies that the wind increases the vertical mixing inside the estuary and reduces the AW stratification

in the wet season. However, in the dry season, the northeastern monsoon enhances the surface water exchange process.

- 6) The water renewal inside the PRE can be divided into two types: the freshwater and the seawater. The seawater age values are lowest near the estuary mouth and increase upstream, ranging from 80 days to 100 days in the wet season, and between 120 days to 160 days in the dry season.

## **Chapter 5**

---

# **Exposure Time and Residence Time in the Pearl River Estuary**



## **5.1 INTRODUCTION**

In this chapter the overall retention timescales, including the average exposure time (AETM) and average residence time (ARTM) of the Pearl River Estuary (PRE), are evaluated for a better understanding of its hydrodynamic and solute transport processes. The water exchange capability between subdomains of the estuary is also investigated.

The details of model scenarios are given in Section 5.2, including the description of the segments' division. Section 5.3 presents the model predicted results. Then the summary drawn from this investigation is given.

## **5.2 MODEL SCENARIOS**

### **5.2.1 ARTM and AETM**

A summary list of the model scenarios is shown in Table 5.1. Each scenario run was undertaken twice, one with the density-induced circulation and one without. Three parameters are critical for calculating the timescales: the releasing time, location of releasing region and location of observation region. The estuary was divided into 4 segments from the upstream to the downstream with similar areas, see Fig. 5.1. In each simulation, 5 different tracer releasing locations were defined, including releasing from each segment and from the entire estuary.

**Table 5.1. A summary of model scenarios for the Pearl River Estuary**

Simulations	River discharge	Salinity	Tracer released time
Case1	Continuous discharge	Baroclinic	High water on 1 <sup>st</sup> Apr, 2006
Case2	Continuous discharge	Baroclinic	High water on 1 <sup>st</sup> Jul, 2006
Case3	Continuous discharge	Baroclinic	High water on 1 <sup>st</sup> Oct, 2006
Case4	Continuous discharge	Baroclinic	High water on 1 <sup>st</sup> Jan, 2007
Case5	High discharge	Baroclinic	High water on 1 <sup>st</sup> Apr, 2006
Case6	Mean discharge	Baroclinic	High water on 1 <sup>st</sup> Apr, 2006
Case7	Low discharge	Baroclinic	High water on 1 <sup>st</sup> Apr, 2006
Case8	High discharge	Baroclinic	Low water on 1 <sup>st</sup> Apr, 2006
Case9	Mean discharge	Baroclinic	Low water on 1 <sup>st</sup> Apr, 2006
Case10	Low discharge	Baroclinic	Low water on 1 <sup>st</sup> Apr, 2006
Case11	Continuous discharge	Barotropic	High water on 1 <sup>st</sup> Apr, 2006

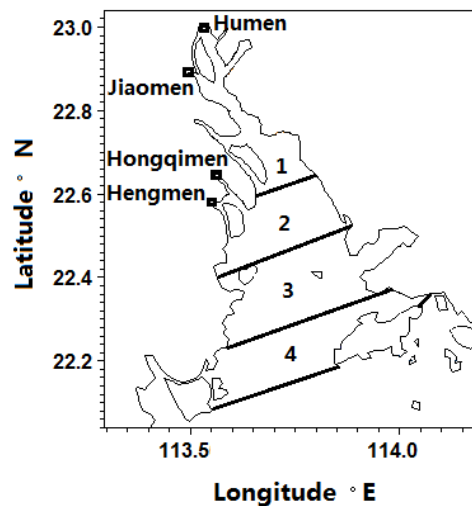


Fig. 5.1. Illustration of sub-division of study area.

The calculations of the ARTM and AETM were based on the remnant function concept introduced by Takeoka (1984). For case 1, after a three-month hot start, a conservative tracer of 1 g/L was released over the entire estuary. The total tracer amount in the estuarine water at  $t_0$  was defined as  $M_0$  and the tracer amount remaining in the estuary at time  $t$  was defined as  $M(t)$ . Therefore,  $M(t)$  was the amount of tracer whose residence time was longer than time  $t$ . Based on the definition of the ARTM, when the water has flowed out of the estuary boundary, the tracer concentration becomes 0 g/L immediately. No tracer could re-enter the estuary. While

for the calculation of AETM,  $M(t)$  includes the re-entered tracer mass with the flood tides, which is closer to the reality. The difference between the AETM and the ARTM was presented using a return coefficient (between 0 and 1) which provided the information about the fraction of water that re-entered the estuary after leaving it for the first time.

### **5.2.2 Influence of river discharge**

In case 1, the tracer was released at the high water on 1<sup>st</sup> Apr, 2006. Three more scenario runs were then conducted by releasing the tracer at the high water on 1<sup>st</sup> July, 1<sup>st</sup> Oct, 2006 and 1<sup>st</sup> Jan, 2007 (cases 2–4). The river discharge varied significantly in different seasons, with July and January representing the wet season and dry season, respectively, and January and October representing the average season. By comparing cases 1–4, the influence of river discharge on the water exchange process was analysed based on the predicted timescales.

### **5.2.3 Influence of initial release**

In order to analyse the sensitivity of water exchange timescales to the timing of tracer releasing, six scenario runs were simulated by releasing the tracer at high water and low water under constant high, mean and low river discharges (cases 5–10).

### **5.2.4 Influence of density-induced circulation**

Case 11 was carried out with a barotropic mode, i.e., the density was considered homogenous in the model domain. All other model parameters were the same as case

1 (baroclinic mode). By comparing the results with case 1, the influence of density-induced circulation was assessed.

### 5.2.5 Water exchange between segments

Based on the “connectivity ratio” defined by de Brauwere et al. (2011), the water exchange capability between segments of the model domain can be analysed based on connectivity ratios. As the tracer was allowed to leave and re-enter the subdomains, the AETM value was estimated between subdomains.

## 5.3 CONVERGENCE OF CALCULATION

For each simulation, the model was run until the relative errors  $t_{err}^n$  were less than a convergence. For AERM the criterion  $t_{err}^n$  was  $5 \times 10^{-5}$ , defined as

$$t_{err}^n = \frac{t_e^{(n+1)T} - t_e^{nT}}{t_e^{(n+1)T}} \quad (5.1)$$

where  $t_e$  is the AETM value, and  $T$  is the period of a tidal cycle.

## 5.4 RESULTS

Fig. 5.2 shows the model predicted AETM, ARTM in the PRE and their corresponding remnant functions  $r(t)$  by releasing tracer from segment 1, located in the upper estuary. It can be observed that although the remnant function for the exposure time oscillated over tidal cycles, its value decreased rapidly with time. Without re-entered tracers, the remnant function for the residence time decreased

more rapidly and dropped to approximately zero at 500 hours, i.e., 20.83 days, which was 16.67 days shorter than the exposure time. The cumulative exposure time and residence time converged exponentially to their average values, i.e., 11.88 days and 7.57 days, respectively. Similar convergence patterns were also found in other test cases.

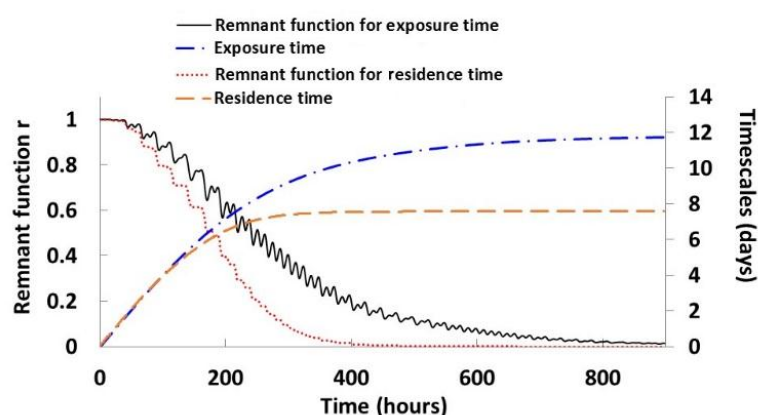


Fig. 5.2 Cumulative average exposure time, average residence time and their corresponding relative remnant functions under real-time condition (case 1) by initial release at segment 1 at high water on 1<sup>st</sup> April, 2006.

## 5.5 DISCUSSION

### 5.5.1 Region of initial release

**Table 5.2. Average residence time (days), average exposure time (days) for entire estuary with different releasing times and regions (Cases 1-4)**

Case No	Releasing time	Initial release region									
		Segment 1:		Segment 2:		Segment 3:		Segment 4:		The estuary	
		ARTM	AETM	ARTM	AETM	ARTM	ARTM	ARTM	AETM	ARTM	AETM
1	High water on 1st Apr,	7.57	11.88	3.66	7.82	1.58	6.03	0.35	4.01	2.04	7.08
2	High water on 1st Jul, 2006	5.11	6.76	3.72	5.45	2.53	4.68	1.40	3.90	2.71	4.98
3	High water on 1st Oct,	6.25	11.40	4.18	8.22	2.55	6.25	1.13	4.69	2.78	7.14
4	High water on 1st Jan, 2007	9.88	18.50	4.83	11.20	2.59	8.18	1.29	5.81	3.41	10.20

The predicted AETM and ARTM for the entire estuary in response to different initial

releasing regions and time are listed in Table 5.2 and plotted in Fig. 5.3 and Fig. 5.4.

It can be seen that the timescales were the longest when the tracer was released at segment 1. Starting at the high water on 1<sup>st</sup> April, 2006 (case 1), the AETM and ARTM were 11.88 days and 7.57 days, respectively. While the exchange timescales released from segment 4 were the lowest, i.e. the AETM was 4.01 days and the ARTM was only 0.35 days. Thus the timescales are sensitive to the distance between the initial releasing region and the downstream boundary. The tracer released in the upper estuary remained inside the estuary for a considerably longer time than released in the lower estuary. For the case of releasing in segment 1 the AETM and ARTM were 7.87 days and 7.22 days longer than that in segment 4.

In all of the cases, the AETM values were generally higher than the ARTM, as expected, due to the inclusion of re-entered tracer. Fig. 5.5 shows the return coefficients for each case, which expresses the importance of returning water. Among the four segments, the greatest return coefficient (0.64–0.91) was observed at segment 4 due to its closest distance to downstream boundary, i.e. more than half of the original water in this segment has re-entered the estuary at least once before escaping permanently. In contrast, the segment 1 had the lowest return coefficient (0.24–0.47). It suggested that the return coefficient was greater in the lower estuary where the effect of return flow was more pronounced.

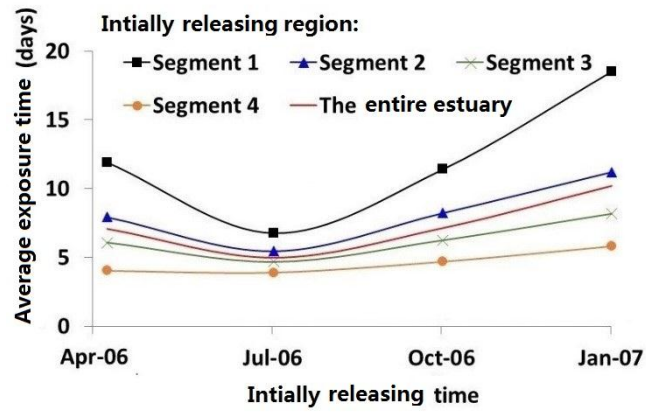


Fig. 5.3. Average exposure time for entire estuary with different initialised regions and times (cases 1–4).

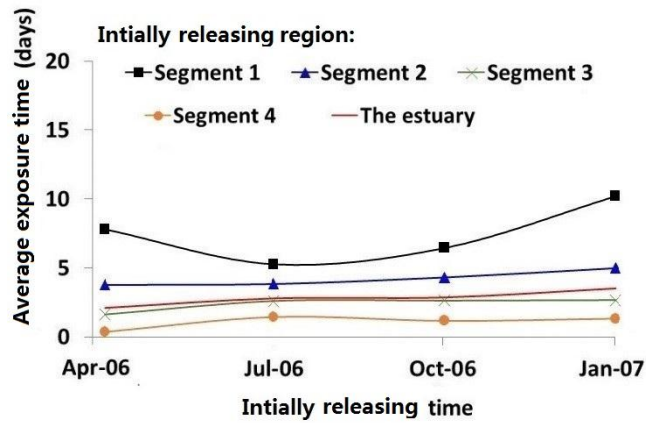


Fig. 5.4. Average residence time for entire estuary with different releasing regions and timing (cases 1–4).

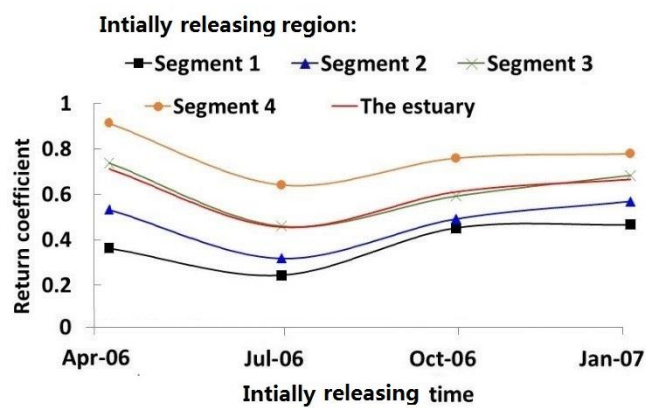


Fig. 5.5. Return coefficient for entire estuary with different releasing regions and timing (cases 1–4).

### 5.5.2 Influence of river discharge

It can be seen from Fig. 5.3 and Fig. 5.4 that for the four initial releasing times, the tracer released in July generally took the shortest time to reach the downstream boundary. By releasing from the segment 1, the AETM was 6.76 days and 18.50 days by releasing in July and January, respectively. The difference of 11.74 days was due to the river discharge. However, if the tracer was released from segment 4, this difference became 1.91 days. The results suggested that the river discharge played a more important role in the upper estuary because the tidal influence became more significant towards the estuary mouth.

In Fig. 5.6, the water exchange timescales for the estuary are plotted against the total discharge from eight tributaries. It can be seen that the AETM value decreased with an increasing discharge. When the discharge was increased from  $1793.5 \text{ m}^3/\text{s}$  (dry season discharge) to  $11058.7 \text{ m}^3/\text{s}$  (wet season discharge), the AETM was reduced by more than 50%, from 10.20 days to 4.98 days. A least-square regression analysis was conducted with empirical best fitting equations in the form of power law. The equation for the AETM fit well with correlation R-squared values greater than 0.93, which indicates that the AETM is a function of the freshwater discharge and decreases exponentially with the increase in discharge. However, a less well correlation between the ARTM and the discharge was observed. It is understandable that without including the re-entered tracer mass, the tides' influence on the exchange timescales' values was particularly important, so the variation in response to the seasonal discharge became less relevant.

It can be observed from Fig. 5.5 that the return coefficient varied in response to the



seasonal varying discharge. For releasing from segment 1, the return coefficient fell from 0.36 in the dry season to 0.24 in the wet season. For initial releasing region of the entire estuary, it also dropped from 0.71 to 0.46. Thus the influence of return flow on the water exchange timescales was altered by the river discharge. During the wet season, the fraction of returning water in flood flows was lower with a relatively large river discharge.

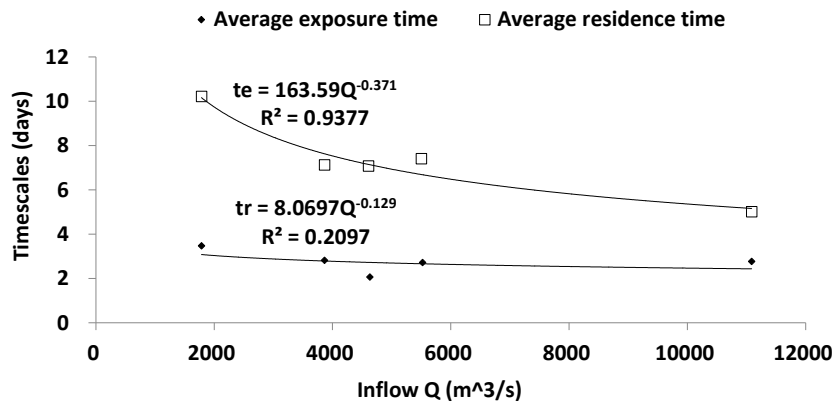


Fig. 5.6. Average residence time  $t_r$  (days) and average exposure time  $t_e$  (days) for entire estuary in response to freshwater discharge, with empirical best fitting equations in forms of power law.  $Q$  is the total discharge.

Cases 5–7 were conducted under constant high, mean and low discharges by releasing the tracer at high water on 1<sup>st</sup> April, 2006. Fig. 5.7 presents the AETM for each segment and the entire estuary in response to the river discharge from the results of cases 5–7. The results further indicates that the timescales decreased with the growth in discharge and the discharge influence was more pronounced for reasing tracer in segment 1 in the upper estuary.

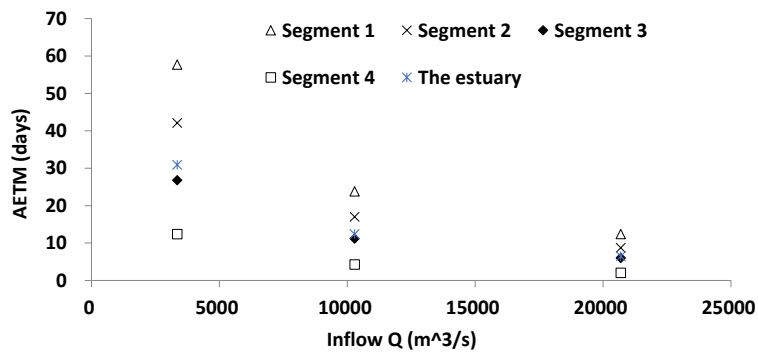


Fig. 5.7. Average exposure time (days) for each segment and entire estuary in response to river discharge under constant discharge (cases 5–7).

### 5.5.3 Initial releasing water level

**Table 5.3. Average exposure time (days) for the entire estuary by releasing at high water or low water (cases 5–10)**

Case no.	River discharge	Released water level	Average exposure time				
			Segment 1	Segment 2	Segment 3	Segment 4	The PRE
5	High discharge	High water	12.40	8.75	6.01	2.03	6.45
6	Mean discharge	High water	13.00	10.00	8.39	4.65	8.27
7	Low discharge	High water	23.80	17.00	11.20	4.27	12.40
8	High discharge	Low water	24.90	19.50	15.50	9.22	15.80
9	Mean discharge	Low water	57.70	42.10	26.80	10.10	30.90
10	Low discharge	Low water	59.80	48.20	36.00	23.10	38.10

Cases 5-10 were simulated to test the sensitivity of the timescales to the initial releasing water level. A constant discharge was applied in the upstream. The predicted AETM for the PRE are listed in Table 5.3. Under constant discharge conditions, the predicted timescales were significantly shorter by releasing at high water than at low water. For example, under a large discharge the AETM for the entire estuary was 6.45 days by releasing at high water, while it increased to 15.8 days by releasing at low water. It indicates that the tracer releasing water level is also important. After releasing at high water, the ebb currents in the first tidal cycle would brought a large volume of tracer mass out of the estuary.

For investigating the sensitivity of timescales in response to the releasing water level, a dimensionless parameter was defined, i.e., the ratio of a predicted timescale released at low water to that released at high water, i.e.(Yuan et al., 2007)

$$\gamma = \frac{AETM_{High}}{AETM_{Low}} \quad (5.2)$$

where  $AETM_{High}$  represents the timescale obtained by releasing the tracer at high water. While  $AETM_{Low}$  represents the timescale obtained by releasing the tracer at low water. Fig. 5.8 presents the ratio  $\gamma$  calculated using AETM predictions from cases 5–10. The results shows that the ratio  $\gamma$  was always between 0 and 1, i.e. the predicted timescales were always greater when released at the low water than high water. By releasing from different segments, the lower  $\gamma$  values were observed for releasing in segment 4 in the lower estuary, varying from 0.4 to 0.6, while the  $\gamma$  values for segment 1 in the upper estuary were always higher than 0.9. It indicated the influence of released water level was more prevailing in the lower estuary.

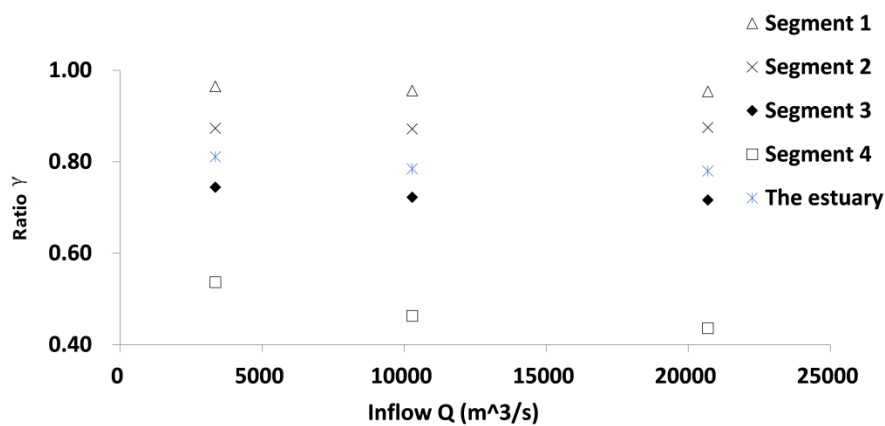


Fig. 5.8. Illustration of sensitivity of average exposure time to water level of tracer release .  $\gamma$  is ratio of predicted timescales released at low water to that released at high water.

### 5.5.4 Influence of density-induced circulation

In case 11, the case in which the tracer was released at high water on 1<sup>st</sup> Apr, 2006 was simulated based on the barotropic mode, with the density-induced circulation being ignored.

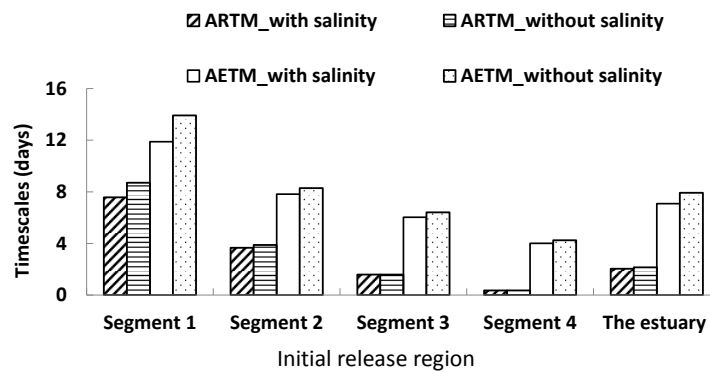


Fig. 5.9. Comparison of water exchange timescales when released from each segment or entire estuary with and without density-induced circulation (case 1, case 11) (ARTM: average residence time; AETM: average exposure time).

Fig. 5.9 shows the AETM and ARTM predictions based on the baroclinic mode and barotropic mode, i.e., cases 1 and 11. It can be seen that the timescales were lower for the baroclinic mode. For the releasing region of segment 1 in the upper estuary, the ARTM and AETM values were reduced by 12.99% and 14.66%, respectively, by including the density-induced circulation. This influence was less for downstream segments. It indicates that the density-induced circulation could enhance the transport processes and reduce the residence time, and the influence was more pronounced in the upper estuary.

### 5.5.5 Water exchange process between segments

As aforementioned, the PRE was divided into 4 segments in the present study, see Fig. 5.10. The water exchange capability between the segments was investigated here based on connectivity ratios. Table 5.4 shows the predicted AETM with different observing segments and releasing regions at high water for four seasons, i.e., cases 1–4.

Taking Table 5.4(a) as an example, the tracer released from segment 1 spent approximately 4.01 days in its original segment. Forced by the river discharge and tides, the tracer was transported downstream through the other three segments. In average, it delayed 3.50 days and 2.56 days at segments 2 and 3, respectively. Its delaying time was lowest at segment 4, being 1.80 days.

**Table 5.4. Average exposure time by observing in each segment with the starting time at high water (a) on 1<sup>st</sup> Apr, 2006; (b) on 1<sup>st</sup> Jul, 2006; (c) on 1<sup>st</sup> Oct, 2006; (d) on 1<sup>st</sup> Jan, 2007**

Observing region	Initial releasing region			
	Segment 1:	Segment 2:	Segment 3:	Segment 4:
Segment 1:	4.01	0.73	0.34	0.18
Segment 2:	3.50	2.76	1.22	0.64
Segment 3:	2.56	2.59	2.29	1.28
Segment 4:	1.80	1.96	2.16	1.89

(a)

Observing region	Initial releasing region			
	Segment 1:	Segment 2:	Segment 3:	Segment 4:
Segment 1:	2.19	0.27	0.08	0.04
Segment 2:	1.95	2.24	0.81	0.41
Segment 3:	1.54	1.79	2.12	1.34
Segment 4:	1.08	1.25	1.66	2.11

(b)

Observing region	Initial releasing region			
	Segment 1:	Segment 2:	Segment 3:	Segment 4:
Segment 1:	4.51	1.12	0.42	0.04
Segment 2:	3.15	3.31	1.37	0.37

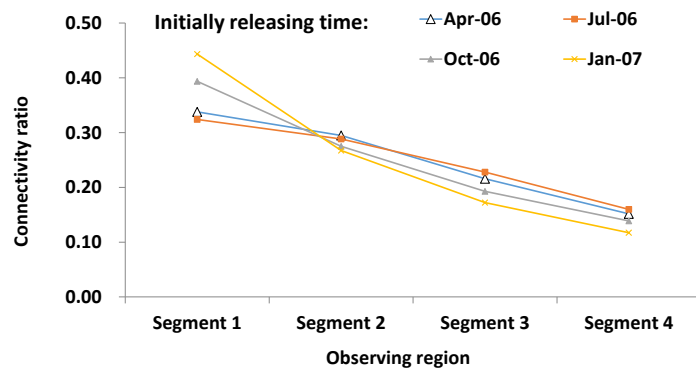
<b>Segment 3:</b>	2.21	2.31	2.43	1.21
<b>Segment 4:</b>	1.59	1.55	1.92	1.90

(c)

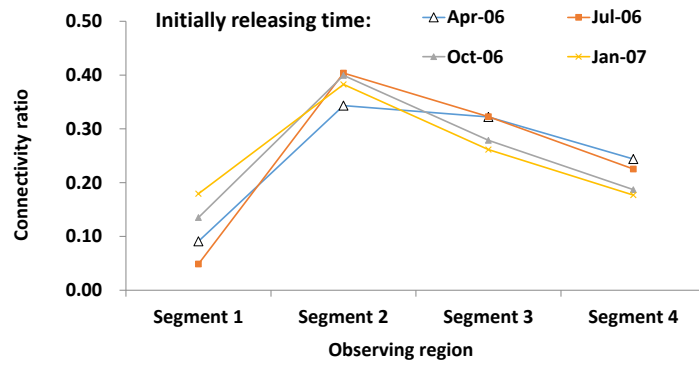
Observing region	Initial releasing region			
	Segment 1:	Segment 2:	Segment 3:	Segment 4:
<b>Segment 1:</b>	8.29	2.03	0.92	0.53
<b>Segment 2:</b>	5.00	4.33	2.13	1.23
<b>Segment 3:</b>	3.22	2.96	2.81	1.87
<b>Segment 4:</b>	2.19	2.00	2.13	2.08

(d)

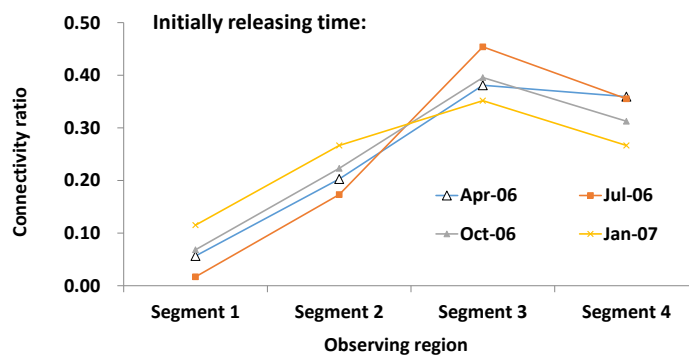
Fig. 5.10 plots the connectivity ratios between segments based on the results listed in Table 5.4. It can be observed the tracer spent most of its journey time in the original released segment, then in the segments downstream. For example, when the tracer was released from segment 2 in July, it spent nearly 3.31 days, i.e., 40% of its entire journey time in this original region (Figs. 5.10b). By releasing in October, the tracer from segments 1–3 stayed in their own releasing segments for nearly 40% of their travel times (Figs. 5.10a, b, c). The tracer from segment 1 even spent half of its journey in its own region (Fig. 5.10d). The results indicate that some tracers entered the upstream of the released segment associated with floods. However, their delay times were very short.



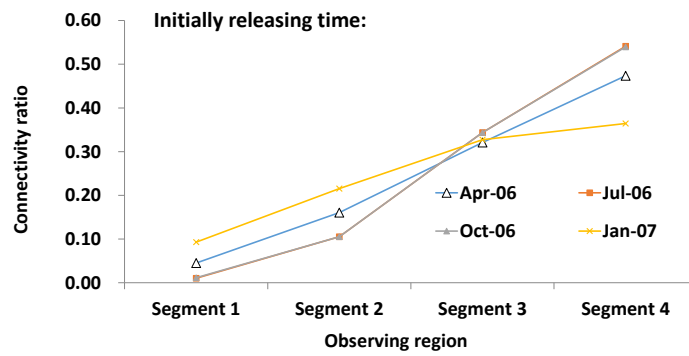
(a)



(b)



(c)



(d)

Fig. 5.10. Connectivity ratios for each segment by releasing the tracer from (a) segment 1; (b) segment 2; (c) segment 3; (d) segment 4 with starting time in four seasons (cases 1–4).

## SUMMARY

In this chapter, the influences of tracer releasing location on the AETM and ARTM

have been investigated. The main findings are:

- 1) The timescales are mainly determined by the distance from the tracer releasing position to the sea boundaries. The tracer initially released in the upper estuary would remain inside the estuary for a considerably longer time than those released in the lower estuary. The AETM and ARTM for releasing in segment 1 are 7.87 days and 7.22 days longer than those in segment 4, respectively.
- 2) By including the re-entered portion of tracer, the predicted AETM values are greater than the ARTM values for all of the test cases. The return coefficient becomes larger in the lower estuary where the return flow is more pronounced.
- 3) The AETM values decrease exponentially with an increase in discharge. The influence of discharge is more pronounced in the upper estuary. A similar conclusion has also been obtained in Chapter 4, where the water age values decrease exponentially with an increasing river discharge. However, a relatively weak relationship is observed between the discharge and the ARTM value, which is mainly influenced by the return flow. The return flow influence becomes weak under a relatively high discharge.
- 4) Under constant discharges, the water exchange timescales are lower when a tracer is released at high water than at low water. The influence of releasing water level is more significant in the lower estuary, where the currents transport a large volume of tracer out of the region during the first ebb tide.
- 5) By comparing the predictions made based on the baroclinic mode and barotropic



mode, it has been found that the density-induced circulation could enhance the transport processes and shorten the water exchange time, especially in the upper estuary. The same conclusion has also been found when the water age is investigated.

- 6) Based on the connectivity ratios, the water exchange processes at different subdomains have been investigated. The tracer particles are observed to spend more time in the initially released subdomain than in the downstream areas. If released in January, the tracer in segment 1 can spend half of its journey time in this segment.

## **Chapter 6**

---

# **Water Exchange Timescales in the Severn Estuary and the Bristol Channel**

## 6.1 INTRODUCTION

As introduced in Chapter 4, the horizontal and vertical distributions of age of water (AW) provide spatio-temporal retention time patterns of dissolved substances in the Pearl River Estuary (PRE). The density-induced circulation plays a significant role in controlling the water exchange process in a micro-tidal estuary. For the barotropic mode, the predicted AW values may be significantly greater than the real value due to the lack of density-induced circulation. While the strength of this circulation may be altered by other dynamic conditions, such as discharge and tides. It is therefore desirable to examine the AW distributions in a macro-tidal estuary.

Moreover, with the rapid development in marine renewable energy, devices such as tidal stream turbines are increasingly developed to harness the tidal stream energy (Falconer et al., 2009; Xia, et al., 2010a, b, c; Ahmadian et al., 2012a, b). The tidal range in the Seven Estuary and Bristol Channel (SEBC) is one of the highest worldwide and the peak tidal currents are well in excess of 2 m/s. The development of tidal turbines will change the current speed, and consequently have an impact on the surrounding environment and marine habitat. In the current study, the AW model is applied to the SEBC. Based on the predicted AW distributions, the water exchange in this macro-tidal estuary is investigated and the impact of density-induced circulation is analysed by conducting the simulations for the barotropic mode and baroclinic mode. Furthermore, the AW model is refined to include a turbine module to

investigate the impact of tidal stream turbines on the surrounding water exchange process.

Details of the turbine module are described in Section 6.2. The verification results for the hydrodynamic and salinity sub-models are presented in Section 6.3. Section 6.4 illustrates the model scenarios. Section 6.5 shows the model predicted AW distribution and the influence of density-induced circulation and tidal stream turbines on the water exchange process. Finally, the main findings drawn from the investigation in the SEBC are summarised.

## 6.2 MODEL SETUP

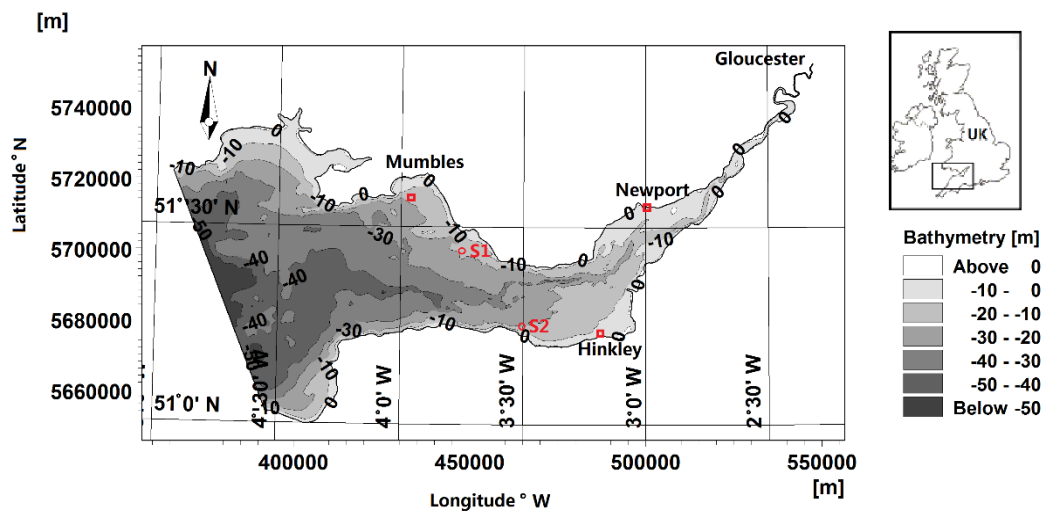


Fig. 6.1. Map of the Severn Estuary and Bristol Channel showing sampling stations

circles: tidal currents observing sites S1 and S2;

squares: tidal elevation observing sites: Newport, Hinkley, and Mumbles.

The MIKE 3 model with the implementation of water age module was applied to the

SEBC. The computational domain is shown in Fig. 6.1, together with the bathymetry.

The total model area is about 5700 km<sup>2</sup> which covers the entire estuary.

### 6.2.1 Model Mesh

There are 11681 elements in each horizontal plane and the mesh size varies from approximately 200 m in the upstream region to 1.5 km in the outer Bristol Channel near the sea boundary, as shown in Fig. 6.2. As an unstructured triangular mesh is used, the computational domain fits well the complex land boundary. In the vertical direction, 10 sigma layers are used. The layer thickness is equally distributed across the water depth.

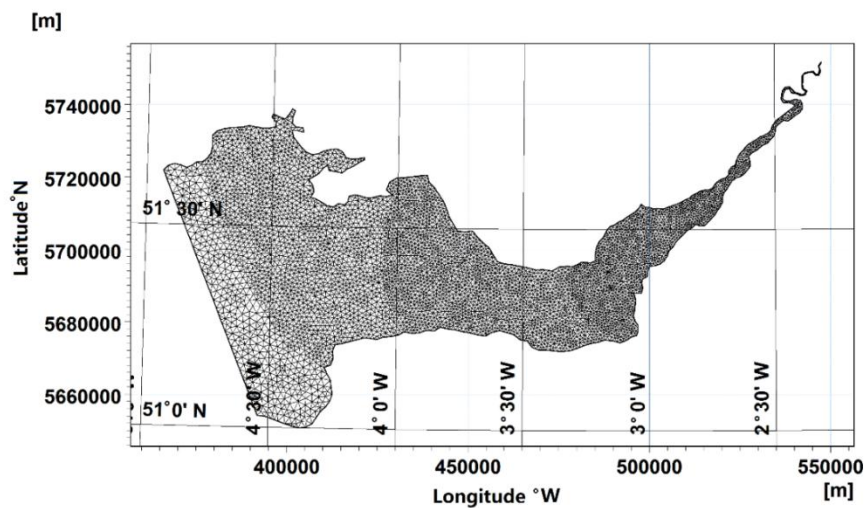


Fig. 6.2. Mesh of the Severn Estuary and Bristol Channel model (UTM-30).

### 6.2.2 Boundary conditions

The upstream boundary was set at the River Severn tidal limit, located close to

Gloucester. Only the river discharge from the River Severn was considered in the simulations, which is the most significant amongst all of the rivers in terms of discharge into the basin from England and Wales. The discharge from the River Severn was set to  $100 \text{ m}^3/\text{s}$ . The western boundary, i.e. the open sea boundary, was set between Hartland point in England and Stackpole Head in Wales, with the temporally varying water level being specified along this boundary. The water level values for this boundary were derived from the global tidal model prediction of the MIKE model, which includes the major diurnal (K1, O1, P1 and Q1) and semidiurnal tidal constituents (M2, S2, N2 and K2).

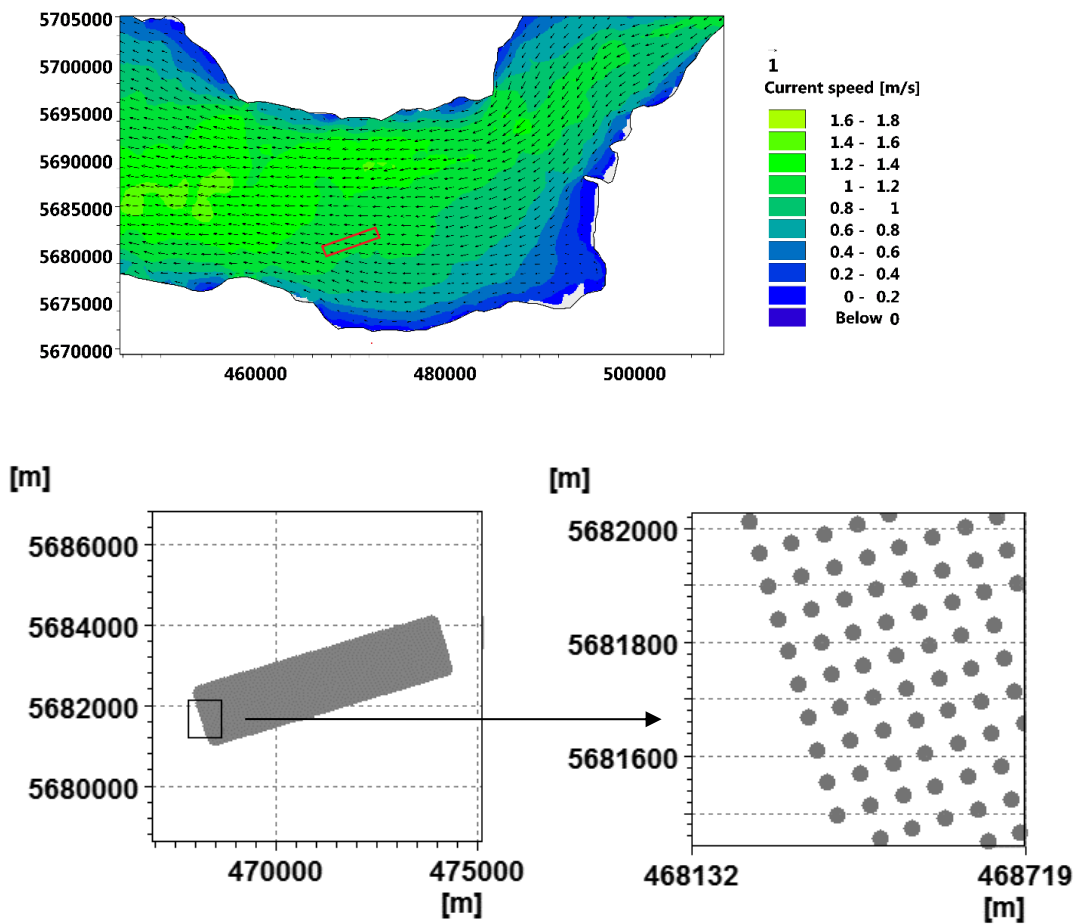
### **6.2.3 Salinity**

The salinity values were set to 0 psu and 35 psu at the river and the sea boundaries, respectively. The initial salinity over the entire computational domain was specified as 0 psu. The effect of temperature variation was not considered in the simulation.

### **6.2.4 Tidal stream turbines' module**

The requirements for selecting a suitable position to deploy tidal stream turbines are manifold, including high currents and a minimum depth at low spring tide, distance from the navigation channels, proximity to the national grid connections and support infrastructure (Ahmadian et al., 2012a). In the current study, two locations for tidal stream turbines were considered, see Fig. 6.3. The first one was sited at the same

location suggested by Ahmadian et al. (2012a) (Fig. 6.3a) with an array of 2000 stream turbines with a diameter of 10 m. The second site was selected by considering the relatively high currents and a suitable depth based on the prediction from the current study (Fig. 6.3b). For both arrays, the distance between two turbines was set to 50 m as illustrated in Fig. 6.3. The influence of two proposal turbine arrays on the water exchange process was investigated based on the AW concept using the three-dimensional model. The model took into account the change of flow area occupied by the tidal stream turbines.



(a)

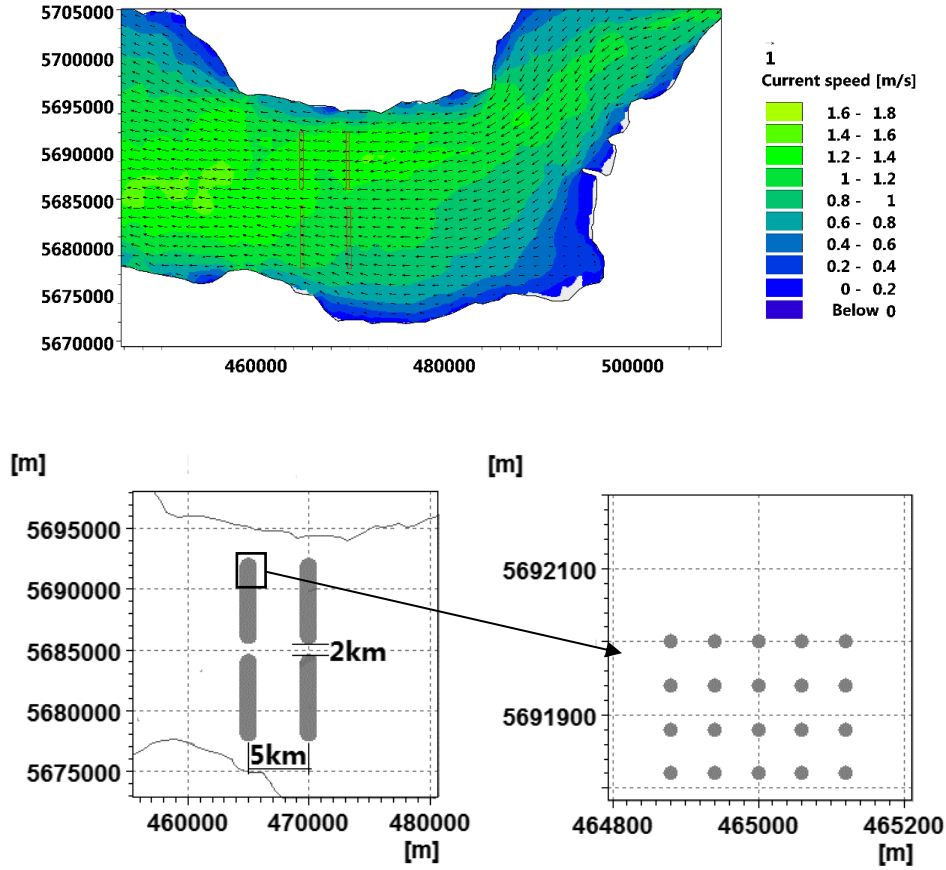


Fig. 6.3. Positions of arrays of tidal stream turbines with spring mean ebb currents as background

(UTM-30):

(a) one array of tidal stream turbines;

(b) four arrays of tidal stream turbines.

The effect of the turbine arrays on the flow field was modelled by calculating the currents and drag and lift forces (see Fig. 6.4). The effective drag force,  $F_D$  and  $F_L$ , are determined from

$$F_D = \frac{1}{2} \rho_w \alpha C_D A_e V^2 \quad (6.1)$$

$$F_L = \frac{1}{2} \rho_w \alpha C_L A_e V^2 \quad (6.2)$$



where  $\rho_w$  is the density of water,  $\alpha$  is a correction factor,  $C_D$  is the drag coefficient,  $C_L$  is the lift coefficient,  $A_e$  is the effective area of turbine exposed to current and  $V$  is the current speed

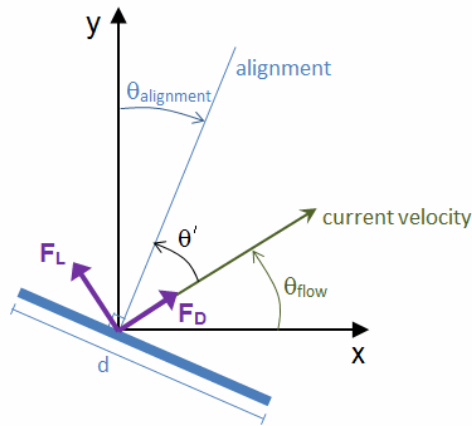


Fig. 6.4. Definition of turbine angles:  $d$  is diameter of turbine;  $\theta_{flow}$  is current direction;  $\theta_{alignment}$  is angle between projection north and alignment;  $\theta'$  is angle between alignment and flow.

In the current study, the lift force was considered as zero and the resistance imposed by the turbine blades was specified by a constant drag coefficient of 1.0.

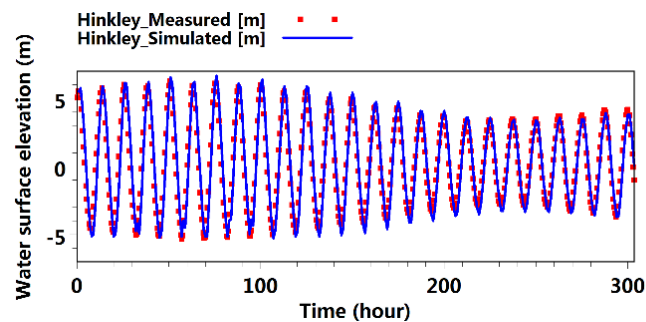
### 6.2.5 Sensitivity tests

A bottom roughness height of 0.1 m was used which was found to well reproduce the observed data in general. For the eddy viscosity, the Smagorinsky coefficient was specified horizontally and the vertical eddy viscosity was determined using a k-epsilon model. A constant time step of 5 s was used for all simulations. The main parameters of the model are given in Appendix D.

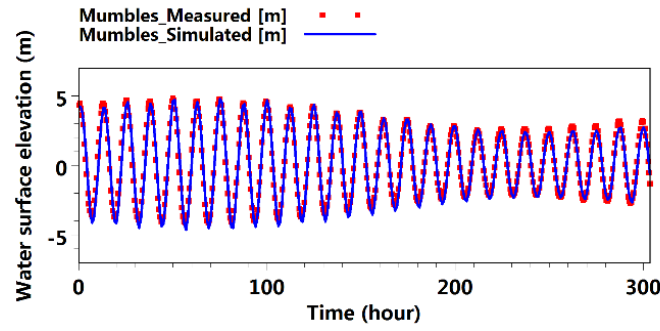
## 6.3 MODEL CALIBRATION AND VALIDATION

### 6.3.1. Water level and tidal currents

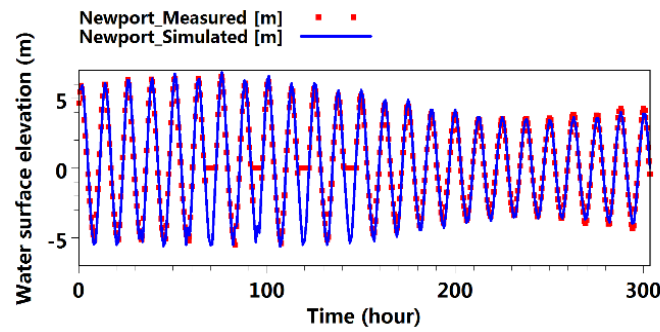
The measured data from the Admiralty Chart data and data collected by Stapleton et al. (2007) were used for model calibration. The model simulation started on 1<sup>st</sup> Jun, 2001 and ended on 1<sup>st</sup> Mar, 2002. Numerical model predicted and measured water elevations, depth-averaged current speeds are shown in Fig. 6.5 and Fig. 6.6, respectively. The positions of sampling points can be seen in Fig. 6.1. With the available measured data, the comparisons were made from 5:30pm on 20<sup>th</sup> Jul, 2001, for about 300 hours. It can be seen from Fig.6.5 that in general a good agreement between the model predicted and measured water levels has been achieved for the three sampling locations. Fig. 6.6 shows the predicted current directions at S1 and S2 agree well with the measured data. While discrepancies can be seen between the predicted current speed and the measured data at several points of time, with the prediction being approximately 20% lower than the data.



(a)

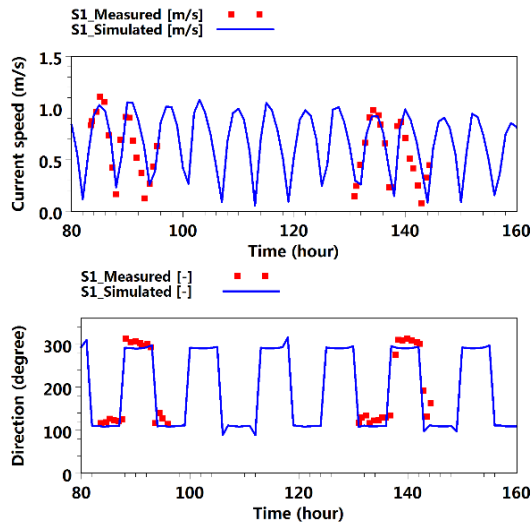


(b)

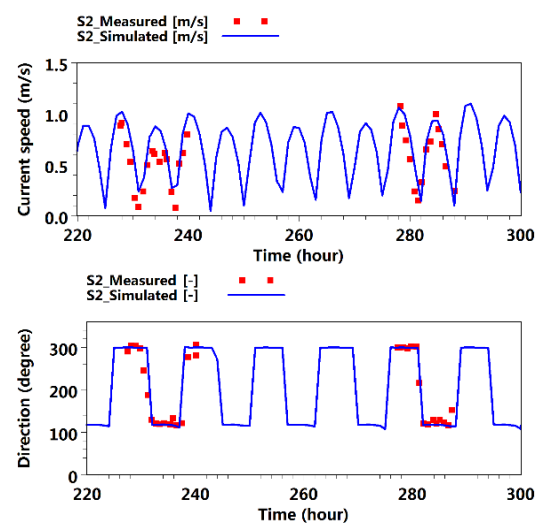


(c)

Fig. 6.5. Measured and predicted water elevations at stations (a) Hinkley, (b) Mumbles, and (c) Newport.



(a)



(b)

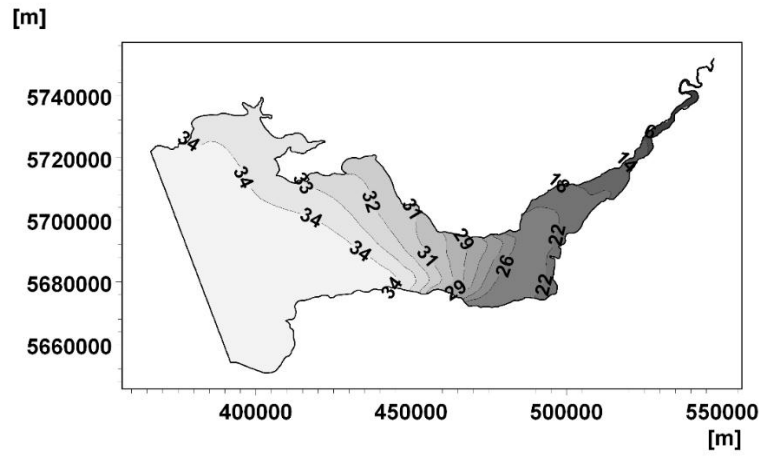
Fig. 6.6. Measured and predicted tidal currents at stations (a) S1 and (b) S2.

### 6.3.2. Salinity

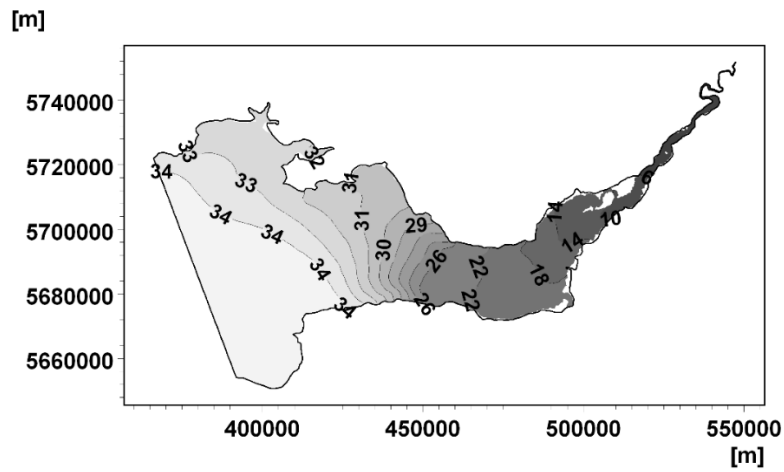
Fig. 6.7 illustrates the predicted salinity distributions in February 2002 at high and

low waters at Swansea, respectively. At high water, the salinity decreased gradually from approximately 35 psu along the open sea boundary to approximately 20 psu in the upstream end, with the isohalines being nearly parallel in Bristol Channel, from northwest to the southeast (Fig. 6.7a). The salinity difference between the north side and the south side decreased in the upper estuary. At low water, some areas along the coastal lines became dry (Fig. 6.7b). With the effects of ebb flow, , the low water salinity concentration the Severn Estuary was lower by 2.0 – 8.0 psu than the high water.

By comparing the model results with the observed salinity patterns reported in Stephens (1986) (Fig. 6.8), it can be seen that the predicted salinity values were slightly lower on the south side of the lower Bristol Channel. The main reasons are thought to be: firstly due to the fact that only the fresh water input from the River Severn was included in the model. The actual total fresh river inputs would be higher if discharges of other rivers were fully included. In addition, the salinity condition at the sea boundary was set at 35 psu constantly which may also vary. Generally, the predicted salinity patterns match the field data well at both high and low tide levels in the SEBC. The salinity variation between high and low tides was also largely consistent with the observation.

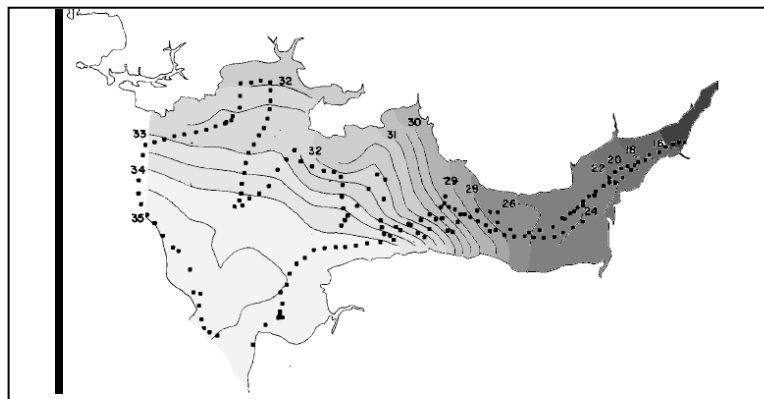


(a)

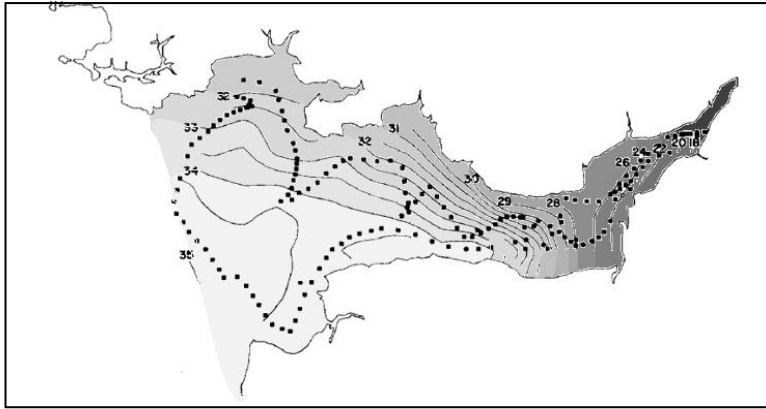


(b)

Fig. 6.7. Predicted depth-averaged salinity distributions in February 2002 (UTM-30): (a) at high water at Swansea; (b) at low water at Swansea.



(a)



(b)

Fig. 6.8. Measured salinity distributions in February 1978 (Stephens, 1986): (a) at high water at Swansea; (b) at low water at Swansea.

## 6.4 MODEL SCENARIOS

After model validation under natural conditions in the SEBC, the model was then used to investigate the water exchange process in the estuary based on the model predicted AW distributions. The model results were analysed to examine the influences of density-induced circulation and the proposed turbines on the flow field. To predict the AW distributions, a passive tracer of concentration 1 g/L and zero age concentration was continuously released along with the freshwater from the upstream boundary. The initial concentration of tracer inside the model domain was set to 0 g/L. Along the downstream sea boundary, the tracer concentration and age concentration were set according to the Neumann boundary condition. By investigating the AW variations through four model scenarios as listed in Table 6.1, a better understanding of the contribution of density-induced circulation and the impacts of proposed turbines on the water exchange process could be obtained. Cases 1 and 2 were

conducted, without the turbines, for the baroclinic mode and barotropic mode, respectively. Cases 3 and 4 were conducted to investigate the baroclinic model influence on the first turbine array and the second turbine array, respectively.

**Table 6.1. A summary of the model scenarios for the Severn Estuary and Bristol Channel**

<b>Simulations</b>	<b>Salinity</b>	<b>Tidal stream turbines</b>
<b>Case1</b>	Baroclinic	No turbines
<b>Case2</b>	Barotropic	No turbines
<b>Case3</b>	Baroclinic	With first turbine array
<b>Case4</b>	Baroclinic	With second turbine array

## **6.5 RESULTS AND DISCUSSION**

### **6.5.1. Influence of density-induced circulation**

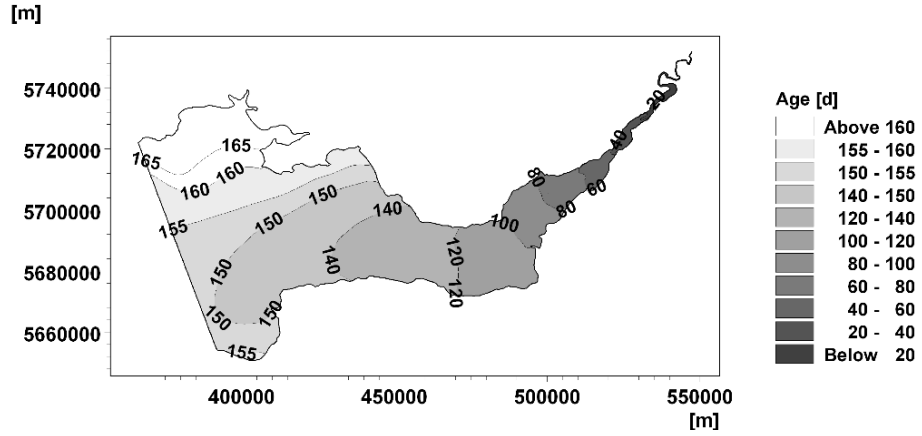
In order to reach quasi equilibrium status, the simulation duration was set to 9 months, from 1<sup>st</sup> Jun, 2001 to 1<sup>st</sup> Mar, 2002. Fig. 6.9 shows the distributions of freshwater age averaged over February 2002, the last month of simulation, for the baroclinic mode and the barotropic mode (cases 1 and 2), as well as the difference between them.

For the baroclinic mode, the AW values decreased towards upstream, from approximately 155 days in the downstream to approximately 40 days near the Severn Bridge (Fig. 6.9a) over the 9-month simulation. The greatest AW value was over 165 days, observed on the north side of the Bristol Channel, which was approximately 20 days greater than the south side. For the barotropic mode, the AW distribution was similar to that for the baroclinic mode (Fig. 6.9b). The difference between the two AW distributions, as shown in Fig. 6.9c, shows that in general the AW values have

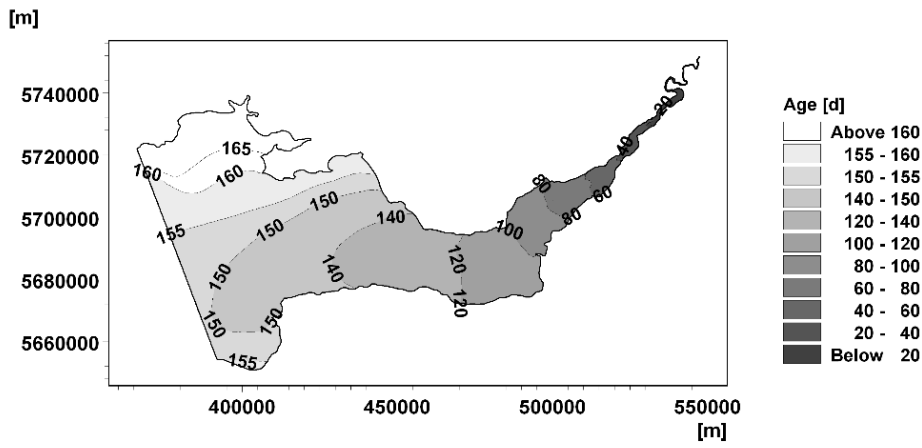
increased for less than 1 day across the estuary by including the density-induced circulation. Along the main stem of the estuary, the AW values were observed to increase by 0.2–0.4 days, and the greatest difference was greater than 2 days at the northern bank of the Bristol Channel. However, along both banks of the middle estuary, the AW values were found to decrease slightly, by approximately 0.2 days. This indicates that due to the homogenous salinity distribution in the SEBC, the contribution of density-induced circulation to the water exchange process is insignificant. On the northern bank of the lower estuary, the water exchange ability slightly decreased with the density-induced circulation, evidenced by the increase in the AW value by approximately 1.2%.

To further study the density impacts, AW values at 15 sampling points shown in Table 6.2 were investigated. These sampling points were selected to characterise the AW values along the main axis (points 1–5), the south land boundary (points 6 – 10) and the north land boundary (points 11 – 15) (see Fig. 6.10). The AW values generally increased 0.1%–0.65% with the density-induced circulation, which indicates a decrease in water exchange ability. Along these three axes, the reduction in water change ability was observed greater along the main axis, being approximately 0.31 days in average, i.e., 0.29%. Comparing with the PRE, the influence of baroclinic forcing is much weaker in the SEBC. It indicates that the influence of density-induced circulation on the hydrodynamics and water exchange process is relatively small in a macro-tidal estuary.

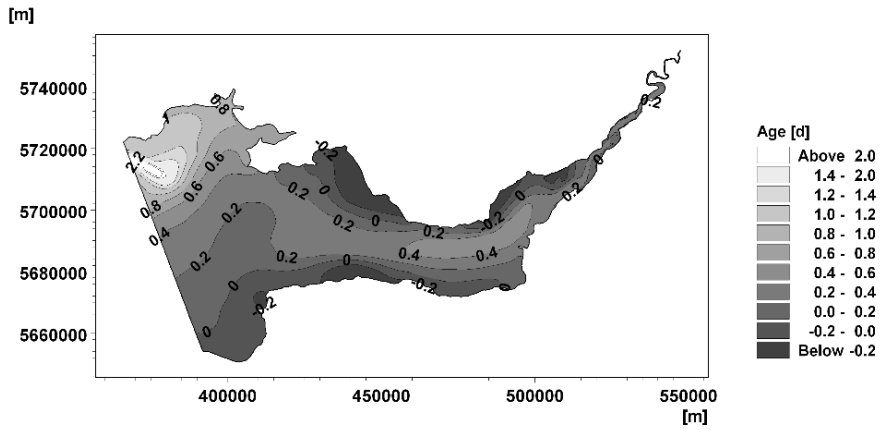




(a)



(b)



(c)

Fig. 6.9. Monthly depth-averaged age distributions for real-time condition (case 1) in February 2002 (a) baroclinic mode; (b) barotropic mode (c) difference between baroclinic mode and barotropic mode.

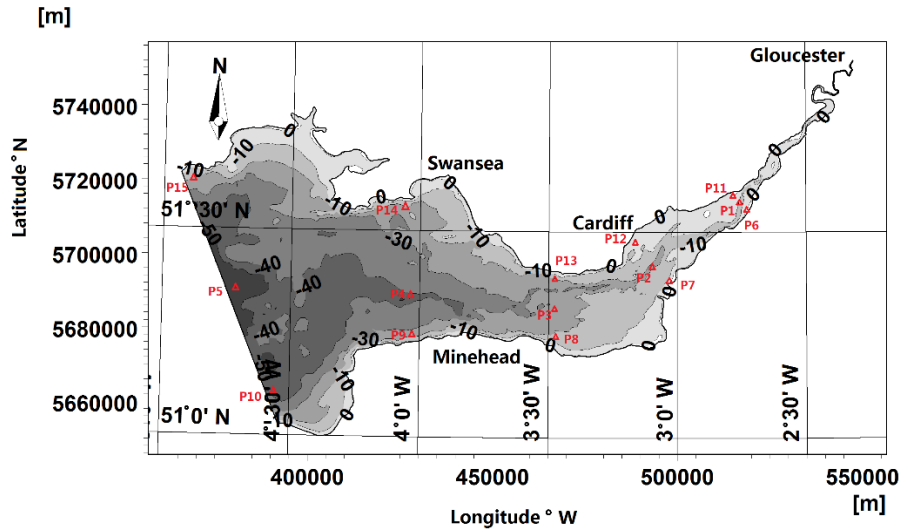


Fig. 6.10. Map of the Severn Estuary and Bristol Channel showing 15 sampling points.

Table 6.2. Surface and bed age values (days) at 15 sampling points

Points	Age		Difference between cases				
	Baroclinic mode without turbines (case 1)	Barotropic mode without turbines (case 2)	Baroclinic mode with first turbine array (case 3)	Baroclinic – Barotropic		Baroclinic mode with first turbine array – without turbines	
P1	53.76	53.63	53.75	0.13	0.22%	-0.01	-0.02%
P2	90.36	89.87	90.35	0.49	0.53%	-0.01	-0.01%
P3	123.29	122.94	123.30	0.35	0.28%	0.01	0.00%
P4	142.61	142.29	142.61	0.32	0.22%	0.00	0.00%
P5	153.20	152.93	153.21	0.27	0.18%	0.01	0.01%
P6	54.72	54.56	54.71	0.16	0.29%	-0.01	-0.02%
P7	91.04	90.69	91.04	0.35	0.39%	0.00	0.00%
P8	121.84	121.87	121.84	-0.03	-0.02%	0.00	0.00%
P9	141.27	141.45	141.28	-0.18	-0.13%	0.01	0.00%
P10	153.62	153.73	153.62	-0.11	-0.08%	0.00	0.00%
P11	52.96	52.82	52.94	0.14	0.27%	-0.02	-0.04%
P12	84.96	85.22	84.96	-0.26	-0.31%	0.00	0.00%
P13	124.87	124.74	124.87	0.13	0.10%	0.00	0.00%
P14	155.72	155.79	155.73	-0.07	-0.04%	0.01	0.01%
P15	170.67	169.57	170.68	1.10	0.65%	0.01	0.01%

### 6.5.2 Influence of tidal stream turbines

The AW model was then used to predict the hydrodynamic processes with the turbine module included. The change in the water level, the maximum ebb tidal current and

the AW distribution were analysed, with the results being compared with the two-dimensional model predictions made by Ahmadian et al. (2012a).

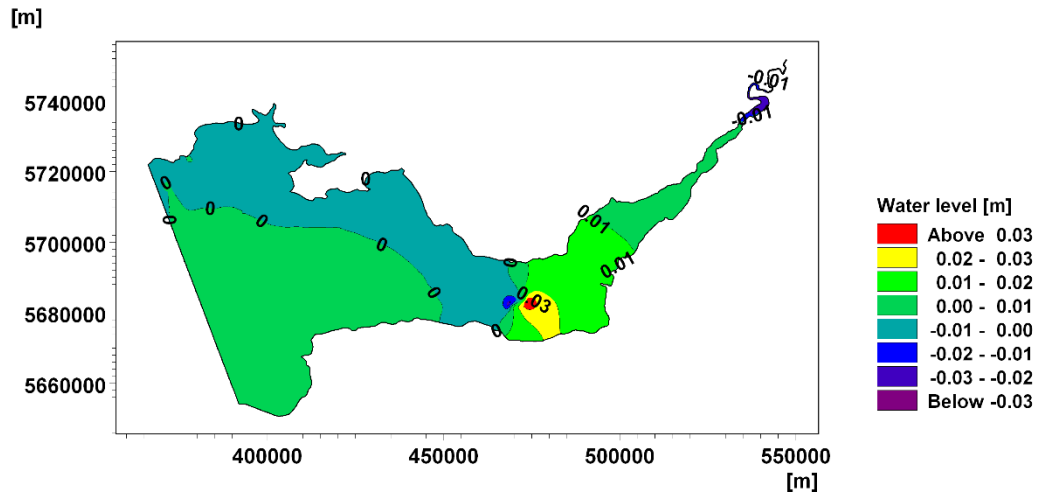
#### 6.5.2.1. Prediction of water level difference

Fig. 6.11a illustrates the difference in water level distributions between the cases with and without the turbine array at the spring high tide at Barry (see also Fig. 6.2), with the prediction presented in Ahmadian et al. (2012a) being shown Fig. 6.11b.

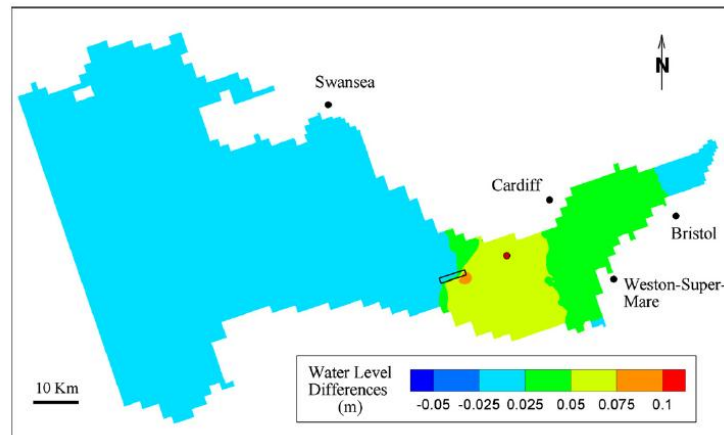
After including the tidal stream turbines, the water level varied in both the upstream and downstream areas of the turbine array, especially in the vicinity of the turbines (Fig. 6.11a). For the 5 km upstream reach from the turbines, the water level increased for more than 3 cm. This growth extended to 20 km upstream from the turbines, varying from 1 to 2 cm. However, in the upstream near the Gloucester, the water level decreased for more than 2 cm, in contrast to the increase in the downstream of the turbines. For an area with a length of approximately 5 km downstream of the turbines, the water level decreased by 1–2 cm and on the northern bank of the Bristol Channel it decreased by less than 1 cm.

As seen from Fig. 6.11b that the water level distributions predicted by Ahmadian et al. (2012a) are similar to the results from the current study, i.e., the water level increased in the upper estuary and decreased in the lower estuary. However, their predicted the water level increase in the upstream area of the turbine array was approximately 3

times of the current study results. Considering the depth of the turbine site was greater than 20 m, the turbines did not make a significant change in the water level. Nevertheless, the turbines affected the velocity distribution, especially in the vicinity of the turbines.



(a)



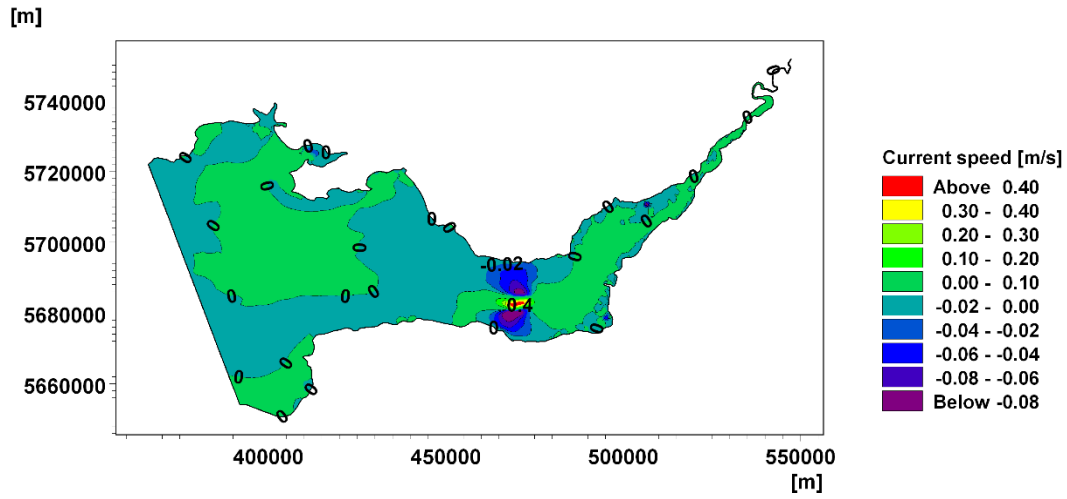
(b)

Fig. 6.11. Changes in water levels across the estuary at spring high water at Barry (see Fig. 6.2) after including the first turbine array from (a) current study; (b) two-dimensional model prediction by Ahmadian et al., (2012).

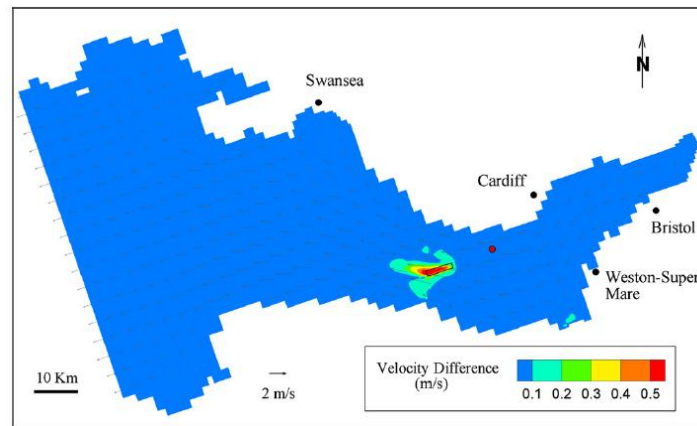
#### 6.5.2.2. Prediction of velocity difference

Fig. 6.12 illustrates the velocity difference between the cases with and without the turbine array at mean ebb tide at Barry (see Fig. 6.2), and their comparisons with the prediction presented in Ahmadian et al. (2012a). The positive values represent a decrease of the current speed after including the turbines. In the location very close to the turbines, the velocity was reduced by approximately 0.4 m/s (Fig. 6.12a). On both sides of the turbines, the velocity increased by less than 0.1 m/s. In the upstream region, as the River Severn became increasingly narrow, the change due to the turbines was nearly zero.

From the two-dimensional model prediction, the velocity reduced greater than 0.5 m/s near the turbines. In other parts of the estuary, the change in velocity speed was less than 0.1 m/s (Fig. 6.12b). By comparing the two modelling results, the velocity changes induced by the turbines were observed similar in distribution, while the magnitude being variable. The current study also predicted the decrease in speed on both sides of the turbines. This was probably due to the different setup of drag forces to flow induced by the turbines in the two models.



(a)



(b)

Fig. 6.12. Changes in depth averaged velocities across the estuary at mean ebb at Barry (see Fig. 6.2) after including the first turbine array from (a) current study; (b) two-dimensional model prediction by Ahmadian et al., (2012).

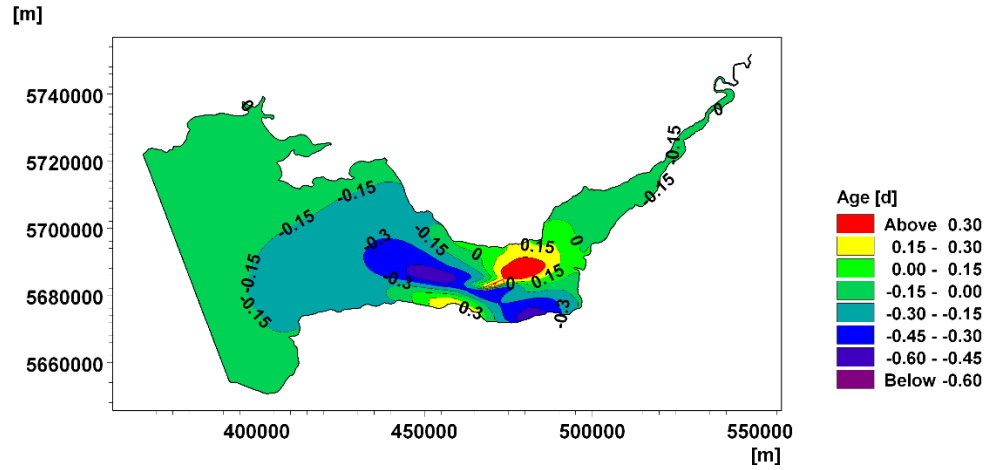
### 6.5.2.3. Prediction of AW distributions

Fig. 6.13 plots the AW difference between two types of turbine arrays. For the first turbine array, the AW values were largely affected by the turbines, with a decrease of less than 0.6 days in most areas of the estuary (Fig. 6.13a). In the lower Bristol Channel, the AW values were reduced by approximately less than 0.15 days. In the middle Bristol Channel, the AW values fell by 0.15–0.3 days. The greatest reduction

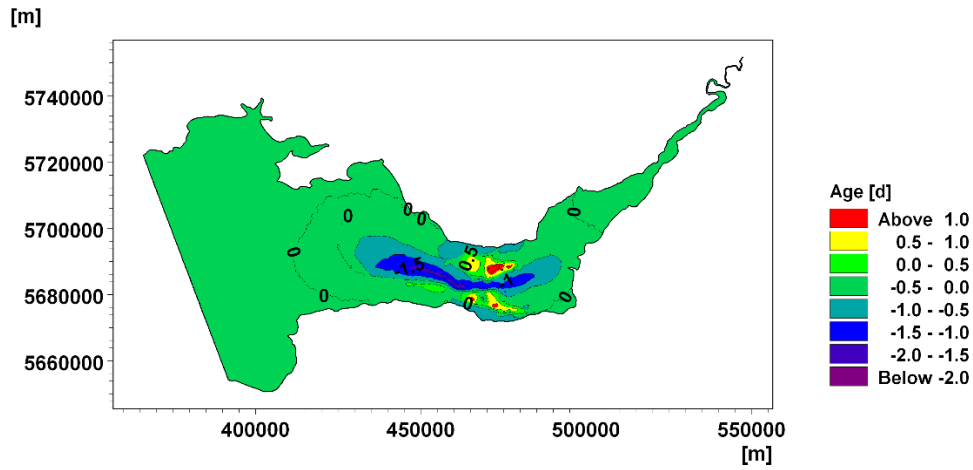
was in the downstream area of the turbines, being over 0.6 days. However, in the upstream area of the turbines, the AW increased by greater than 0.3 days.

It can be seen from Fig. 6.11 and Fig. 6.12 that the increase the reduction in current speed around the turbines result in a longer travel time for the tracer located in the upstream area of the turbines, leading to an increase in the AW values there. However, the increase in water current on both sides of the turbines brought a reduction in AW values, i.e., an increase in water exchange process, on both sides in the downstream area.

The above conclusion was further proven by the results from the simulation by applying the second turbine array (Fig. 6.13b). The AW values in the upstream area of the turbines increased by up to 1.0 day. While due to the increased currents on both sides of the turbines, a decrease in AW values was observed, varying from 0 to 2.0 days. Compared with Fig. 6.13a, the change in AW values became larger, which indicates that the second turbine array could bring more significant influence on the estuarine hydrodynamics. The water exchange in the upstream area of the turbines became weaker, while it was enhanced on both sides of the turbines, especially along the main axis, in the 2 km width area between the two rows, representing by a decrease in AW value of 1.5–2.0 days.



(a)



(b)

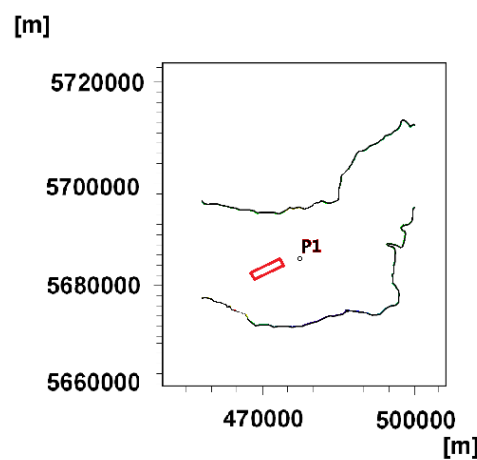
Fig. 6.13. Age difference after including (a) the first turbine array (b) the second turbine array averaged over February 2002, the positive values present an increase in age values.

In the estuarine environment, the influence of turbines may be altered by other hydrodynamic factors, such as tides. Fig. 6.14 plots the time series of AW values at points P1 (upstream) and P2 (downstream) over February 2002 without the turbines, and the changes in their values due to the first turbine array. It can be seen that the AW values fluctuated with tides (Fig. 6.14c). It difference between the high tide and low tide could be greater than 15 days. The tidally averaged AW values were under a

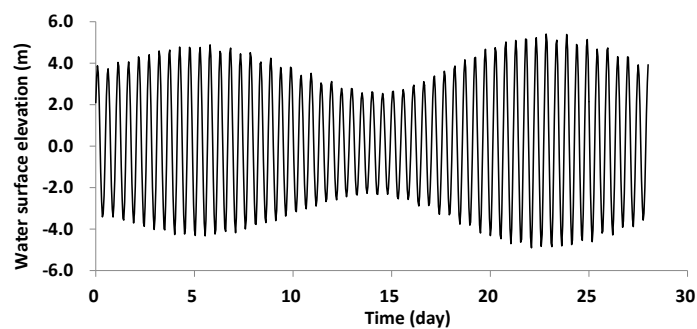


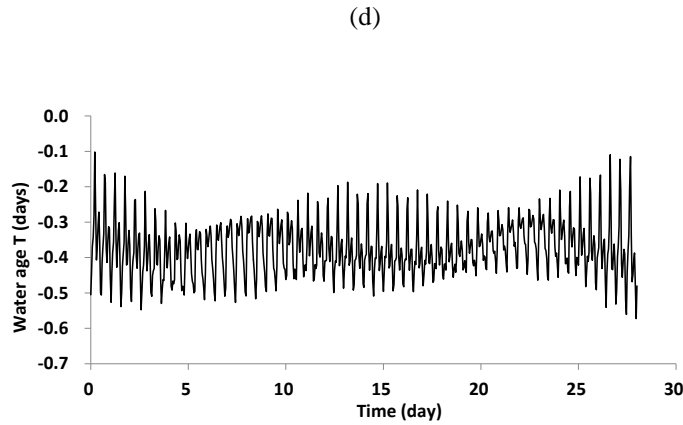
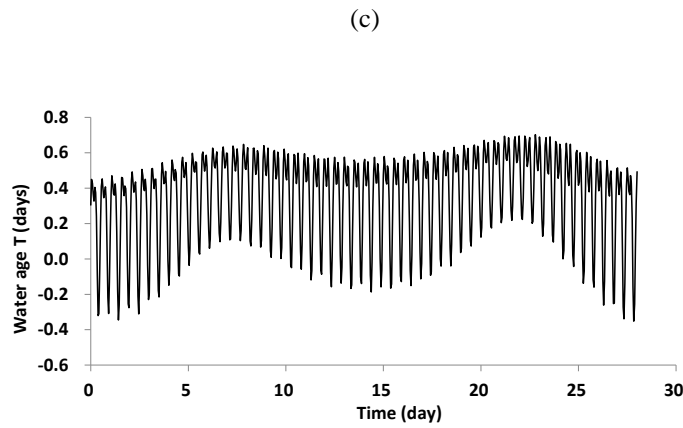
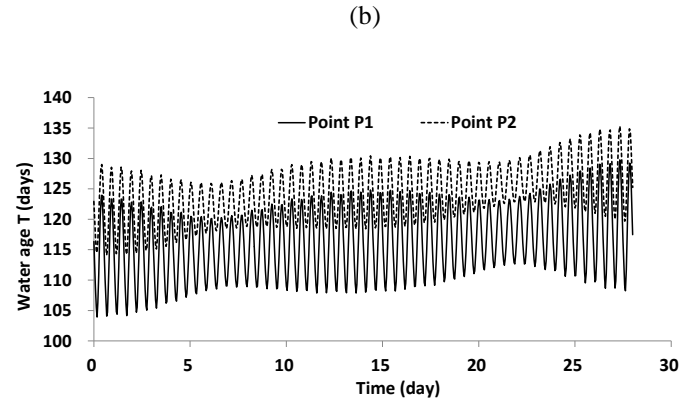
relatively stable condition with slight oscillations. The tidally averaged AW value at P1 was approximately 122 days, being 10 days higher than that at P2.

Fig. 6.14d and 6.14e present the time series of AW variation at P1 and P2 induced the turbine module. It can be seen that the influence of turbines was regulated by tides. At the upstream point P1, the change in AW values varied from -0.35 to 0.71 days, with an average value being 0.36 days. It increases during the flood phase of the spring tides, with the maximum being greater than 0.4 days. The AW value at the downstream point P2 decreases 0.10- 0.57 days after the instalment of the tidal stream turbine.



(a)





(e)

Fig. 6.14. (a) Positions of two sampling points P1 and P2 in background of age difference of Fig. 6.13a; Time series of parameters in February 2002: (b) average water level at two points; (c) age values at two points excluding the turbine module; age difference due to install turbines at (d) P1 and (e) P2.

Due to the first turbine array, the water exchange process in the upstream of the turbines became weaker during the flood tide, especially at high water during spring

tides, represented by an increase in AW values. However, the upstream water exchange process became stronger during the ebb. In the downstream of the turbines, an increase in the water exchange process was observed.

## **SUMMARY**

The main aim of the study presented in this chapter is to investigate the water exchange process in the Severn Estuary and Bristol Channel based on the age of water (AW) concept. Numerical model simulations are conducted for the barotropic mode and the baroclinic mode to assess the impact of the density-induced circulation on the water exchange process. Moreover, a tidal stream turbine module has been developed. The model has been applied to two types of turbine arrays, one is adapted from the two-dimensional research report by Ahmadian et al. (2012), and the other one is selected according to the high tidal currents and a suitable water depth. The influence of proposed turbines on the surrounding hydrodynamic and water exchange process is assessed. The main conclusions are:

- 1) For the baroclinic mode, the AW values increase from the downstream (approximately 155 days) towards the upstream (approximately 40 days near the Severn Bridge). Comparing with the results for the barotropic mode, the AW values increase by less than 1 day (less than 2.5%) after including the density-induced circulation across the estuary. However, on both sides of the estuary, the AW values decrease approximately by 0.2 days (less than 0.5%). It

indicates that due to the homogenous density distribution in the SEBC, the baroclinic forcing contribution to the water exchange process in this macro-tidal estuary is very limited.

- 2) The influence of the first turbine array on the high water level and peak ebb current speed across the estuary has been investigated. The results show that with turbines the high water level increases for over 3 cm in a large part of the estuary, especially in the upstream area of the turbines. Considering the mean water depth of approximately 20 m across the estuary, the change in the water level due to the turbines is small. The peak tidal ebb current speed in the vicinity of turbines array decreases by approximately 0.4 m/s. On both sides of a turbine, the speed increases by less than 0.1 m/s.
- 3) The influence of the two turbine arrays on the surrounding water exchange process has been analysed based on the changes in AW distributions. For the first turbine array, the water exchange process becomes weaker in the upstream of the turbines during the flood tide. However, it is enhanced during the ebb tide with a decrease of AW values of 0.35 days. The water exchange process in the downstream area of the turbines is strengthened during both the flood and the ebb tides, with a decrease of AW values being 0.3–0.45 days. This is related to the higher water level in the upstream and the quicker water currents on both sides of the turbines.

## **Chapter 7**

---

### **Laboratory Experiments of the Severn Estuary and the Bristol Channel**

## **7.1 INTRODUCTION**

To further investigate the exchange timescales into water exchange process in estuarine waters, in this chapter a physical model investigation is undertaken in a fibreglass model of the Severn Estuary and the Bristol Channel (SEBC). Due to the limitations of experimental facility, the physical model is conducted without considering stratification. The measurements include water levels by wave probes, flow velocities by Acoustic Doppler Velocimeters (ADV), and tracer concentrations by digital fluorometers. The mean travel time between selected sampling points and the time series of water and tracer fluxes through two selected cross-sections are estimated, providing information for investigating the water exchange process in the model domain.

This chapter describes the design of experiments, and analyses the measured hydrodynamic data and the water exchange process in the model domain. Finally, the laboratory experiment is summarised.

## **7.2 DESIGN OF EXPERIMENTS, RESULTS AND DISCUSSION**

### **7.2.1 Design of experiments**

Details of the experimental arrangements are given in Table 7.1. Each test was conducted twice or even three times to gain more accurate results.

The locations of sampling points are shown in Fig. 3.7. Point A was located at the upstream end of the estuary; point B was situated near the Seven Bridge; points C and D represented the locations near two cities: Newport and Cardiff, respectively; The cross-section F-G-H was from Penarth, on the north side, to Weston-Super-Mare on

the south side, along three islands: Sully Island, Flat Holm Island and Steep Holm Island (see Fig. 7.1); Points I, J, K were located along the main axis of the Bristol Channel. The vertical profiles of two cross-sections in the physical model, Section B and Section F-G-H, were presented in Fig. 7.2 and Fig. 7.3, respectively.

**Table 7.1. Measurement arrangements**

Water elevation	Flow velocity	Tracer concentration	
Measured points	Measured points with distance to bed (cm) and water depth (cm)	Injected points	Measured points with distance to bed (cm)
A B C G I J K	B_3, 4, 15, 16 cm	A	F_5 cm
			G_1, 5, 10 cm
			H_5 cm
			J_5 cm
	G_1, 2, 3, 4, 5, 6, 8, 16, 17, 18, 19, 20 cm	B	G_5cm
			J_5cm
		C	F_5cm
			G_5cm
			H_5cm
			J_5cm
	H_1, 5 cm	D	G_5cm
		E	G_5cm
			J_5cm

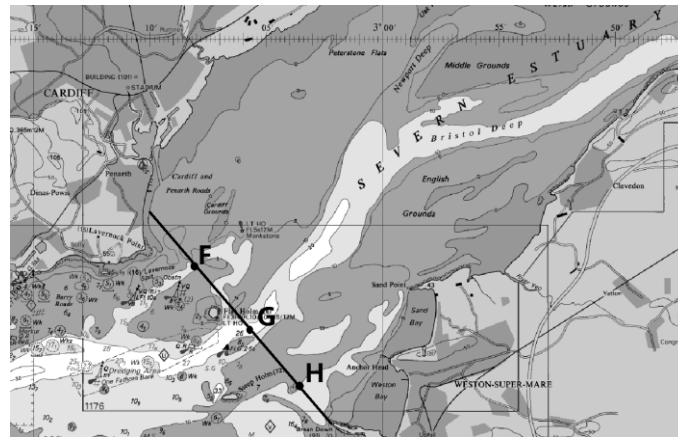


**Fig. 7.1. Position of cross-section F-G-H.**

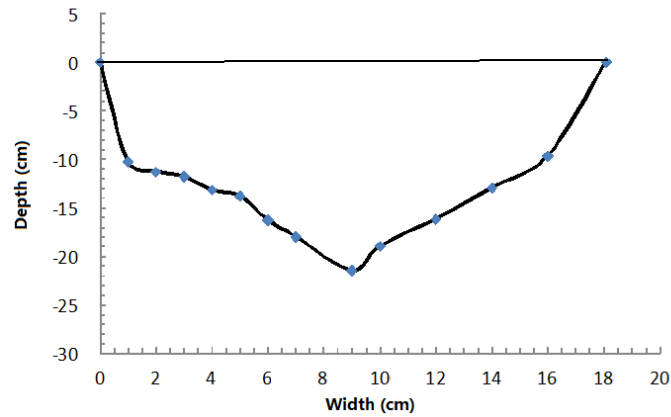


Fig. 7.2 Depth profile along cross-section B, looking from downstream.

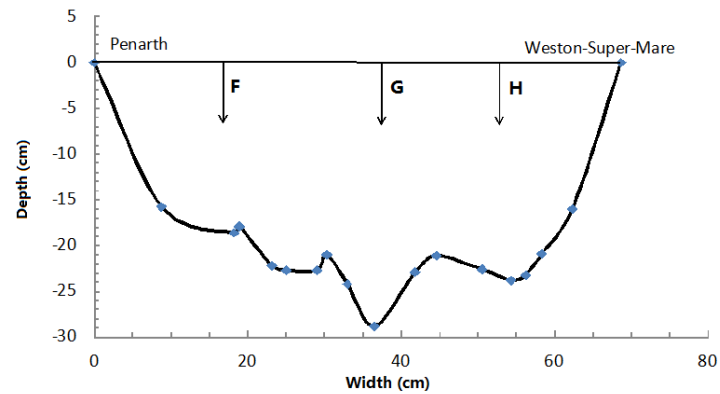


Fig. 7.3. Depth profile along cross-section F-G-H, looking from downstream.

## 7.2.2 Results and Discussion

### 7.2.2.1 Water levels

Time series of measured water levels over one tidal cycle at 7 points are plotted in Fig. 7.4. It can be seen that the tidal range at Point K, near the downstream boundary, was approximately 80 cm corresponding to the movements of the weir, while the tidal range reached approximately 106 cm at Point A, located at the upstream end. It indicates that as the estuary became narrower towards upstream, the tidal energy was concentrated and the tidal range amplified.



Among the seven points, six of them kept wet over the whole tidal period, while Point A became dry when the water level was lower than -10.44 cm. The water levels showed some fluctuations during the flood tide, at the upper estuary points, A, B and C. The fluctuations were attributed to the reflection of tidal waves from the upstream boundary.

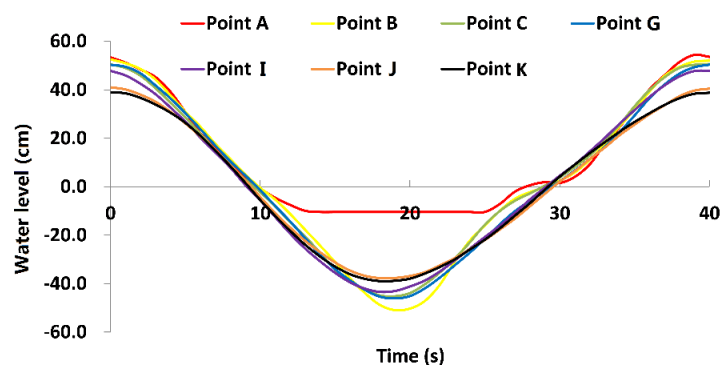


Fig. 7.4. Average water levels at seven points over a tidal period.

## 7.2.2.2 Flow velocity

### *7.2.2.2.1 Velocity vertical profiles at key moments*

Fig. 7.5 and Fig. 7.6 illustrate the vertical profiles of flow speed at points G and B, respectively. The speed values were averaged over four tidal periods. It can be seen that, at high water or low water, the speeds at point G were less than 3 cm/s along the water depth with very little difference along the depth (Fig. 7.5a, c).

At mean ebb water, the largest speed was observed in the middle and bottom layers, being approximately 7 cm/s, while the surface speed was 5–6 cm/s (Fig. 7.5b). At mean flood water, the vertical speed profiles are nearly logarithmic. The largest speed was greater than 9 cm/s observed at the surface, while the bottom speed was approximately 3–5 cm/s (Fig. 7.5d). The vertical velocity profile at the mean ebb

water was not logarithmic, and the velocity values at the middle layers were slightly higher than the surface velocity. However, the vertical velocity profile at the mean flood water was close to logarithmic.

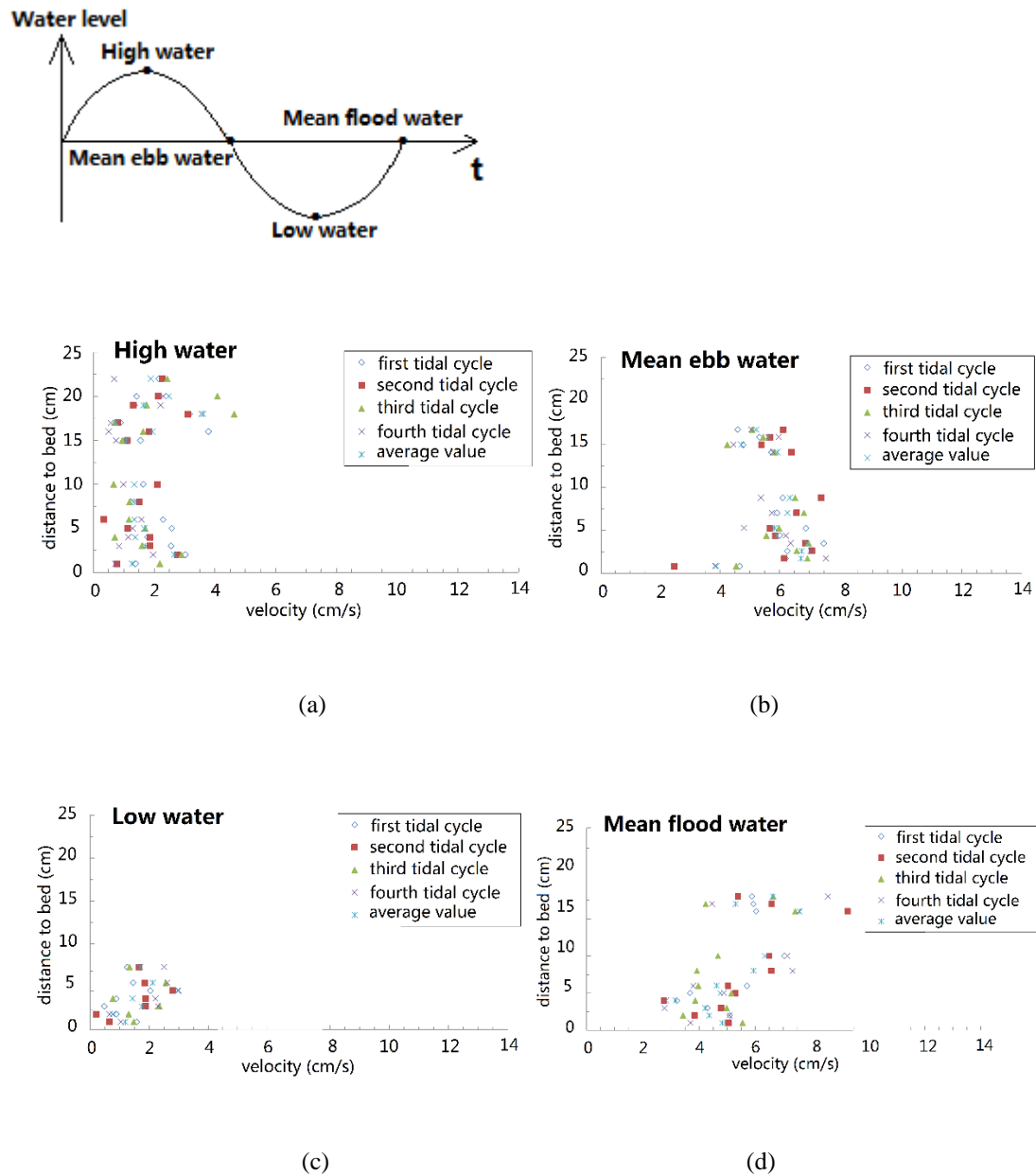


Fig. 7.5. Vertical profiles of speed at key moments at point G: (a) High water; (b) Mean ebb water; (c) Low water; (d) Mean flood water.

Point B was located near the Severn Bridge and was the rotated point for the physical model. Therefore, the hydrodynamics near this point was complex because of the

rapid change in flow directions. Due to the narrow width along cross-section B, the velocity at the low water was less accurate. It can be seen from Fig. 7.6 that the speed at high water was less than 6 cm/s, and it increased to a maximum of 13 cm/s at mean ebb water. At mean flood water, the speed was observed to be approximately 12 cm/s at the surface, while it was reduced to less than 5 cm/s near the bed.

Similar to point G, the larger velocity at point B was observed in the middle layers at mean ebb water. Over a tidal cycle, the largest vertical difference was observed at mean flood water. The flood speed was observed higher at point B than at point G, whilst it was the opposite during the ebb.

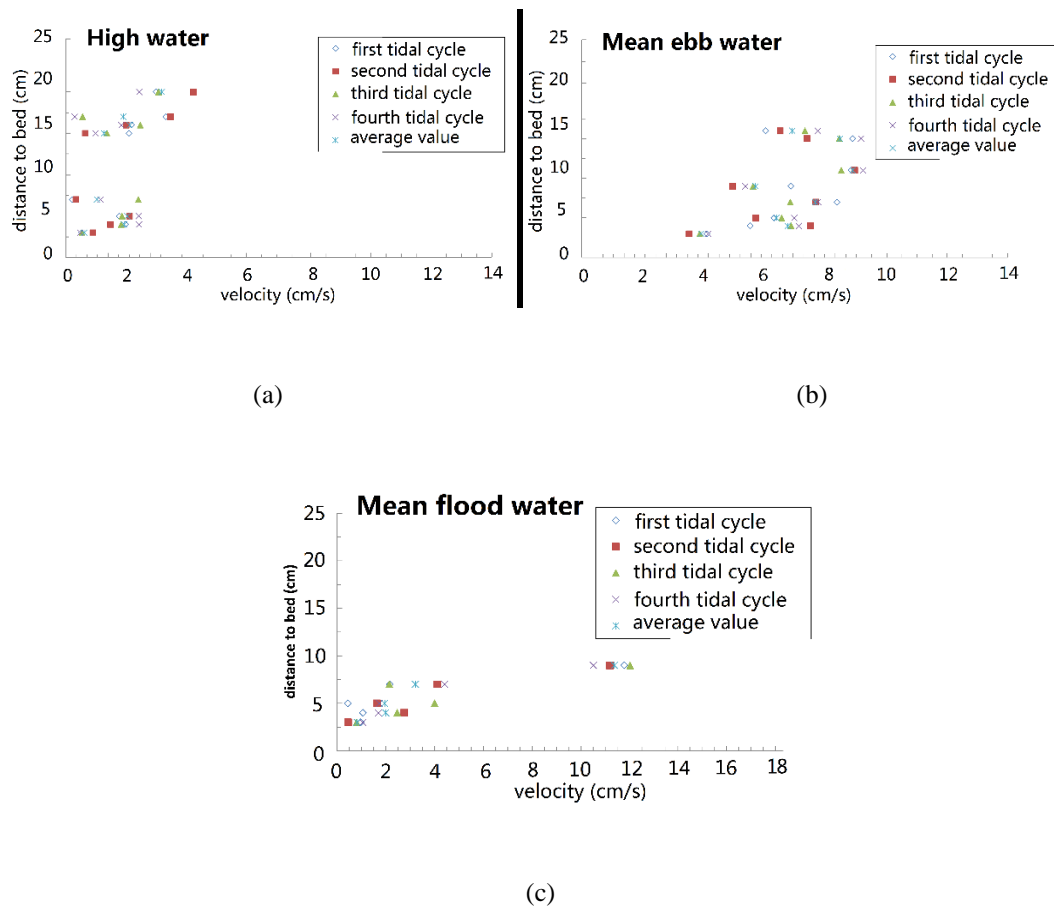


Fig. 7.6. Vertical profiles of velocity at point B at (a) High water; (b) Mean ebb water; (c) Mean flood water.

#### 7.2.2.2.2 Time series of velocity over a tide

Fig. 7.7 and Fig. 7.8 present the time series of depth-averaged velocity over a tide period, i.e., 40 seconds, at points G and B, respectively, together with the local water levels. The results were averaged over 4 tidal cycles.  $V$  was the speed component perpendicular to the cross-section, calculated by Equation 7.1.

$$V = u * \cos\alpha + v * \sin\alpha \quad (7.1)$$

where  $\alpha$  is the angle between cross-section F-G-H and the longitudinal axis  $y$ .  $u$ ,  $v$  were the velocity components in the  $x$ ,  $y$  directions, respectively. The positive value indicates towards upstream. Compared with point G, the velocity value at point B fluctuated more strongly, especially during the flood tide. The depth-averaged velocity at point B, perpendicular to its cross-section, varied between 0 and 2 cm/s during the flood, which was lower than the flood velocity perpendicular to cross-section F-G-H at point G, varying between 0 to over 6 cm/s, while stronger ebb currents were observed at point B, with the maximum being approximately 6 cm/s. The time series of velocity were used later, for the calculation of water and tracer fluxes through the cross-section.

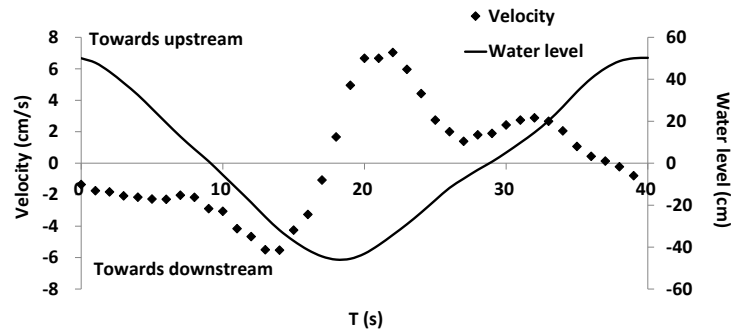


Fig. 7.7. Time series of depth-averaged velocity at point G perpendicular to cross-section F-G-H, positive value represents directed towards upstream while negative value represents directed towards downstream.

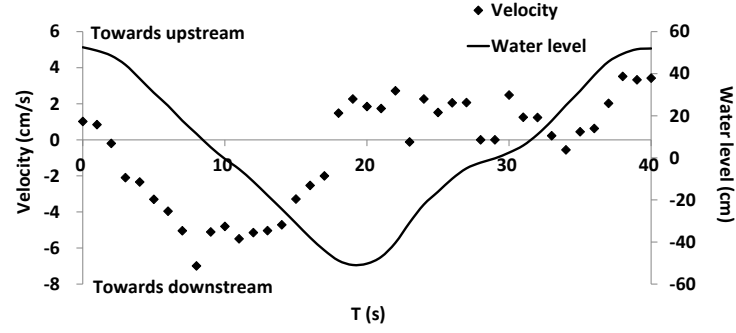


Fig. 7.8. Time series of depth-averaged velocity at point B perpendicular to cross-section B, positive value represents directed toward upstream while negative value represents directed toward downstream.

### 7.2.2.3 Tracer concentration

#### *7.2.2.3.1 Mean travel time between points*

Based on the measured tracer curves by digital fluorometers, mean travel time  $T_m$  between points in each test was calculated by Equation 7.2 and listed in Table 7.2.

$$T_m = \frac{\sum C_i t_i \Delta t}{\sum \Delta t} \quad (7.2)$$

where  $\Delta t$  is time step;  $i$  is the number of time step;  $C_i$  is the measured tracer concentration at  $t_i$ . Based on Equation 3.40, the mean travel time was up-scaled and compared with age distributions shown in Table 7.2, it was found that the up-scaled travel time was almost half of the age at sampling locations. This is thought to be due to the large scale difference between the physical and prototype models. In the future, the physical model needs be updated to allow it to be better scaled.

**Table 7.2. Calculated mean travel time between injecting and receiving points**

Injected points	Measured points with the distance to bed(cm)	Mean travel time T (min)
<b>A</b>	F_5 cm	21.71
	G_1 cm	21.95
	G_5 cm	25.17
	G_10 cm	23.06
	H_5 cm	20.55
	J_5 cm	40.03
<b>B</b>	G_5cm	20.65
	J_5cm	45.61
<b>C</b>	F_5cm	23.49
	G_5cm	25.17
	H_5cm	29.40
	J_5cm	42.07
<b>D</b>	G_5cm	29.89
<b>E</b>	G_5cm	27.17
	J_5cm	55.76

#### 7.2.2.3.2 Same injecting points

Fig. 7.9 and Fig. 7.10 present the real-time tracer concentration curves at F (on the north side), G (along the main axis) and H (on the south side) with distance to bed of 5cm, injected at points A and C, respectively. The maximum value of tracer curves at point F was approximately 38 ppb, being 13 ppb higher than point G, and more than twice of point H (Fig. 7.9). The results indicates that the tracer particles injected at point A were transported downstream, mainly along the north side of the cross-section, while the first arrival times for the tracer particles at the three points were similar.

It can be seen from Fig. 7.10 that by injecting at point C, near the city of Newport on the north side of the estuary, the curves were significantly different from the results with injected point at A (Fig. 7.9). The tracer particles arrived at point F first due to the shortest distance and the tracer concentration reached a peak value of approximately 100 ppb. Moreover, the tracer particles were transported downstream of the cross-section F-G-H more rapidly. According the calculated values of mean travel time in Table 7.2, the travel time from point C to point F, G, and H was 1409.4s,

1510.0 s and 1764.0 s, respectively.

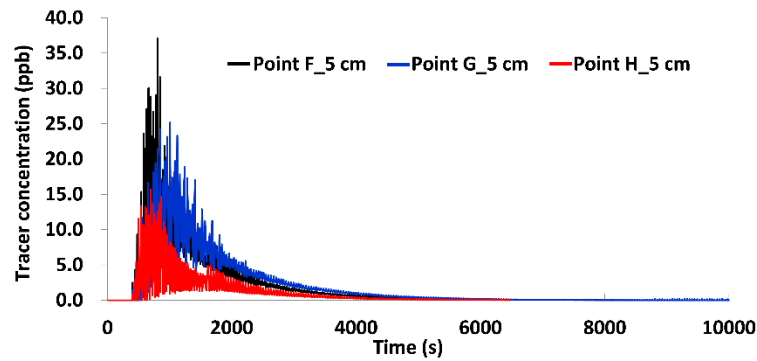


Fig. 7.9. Measured tracer concentration at points F, G, H with distance to bed of 5 cm, injected at point A.

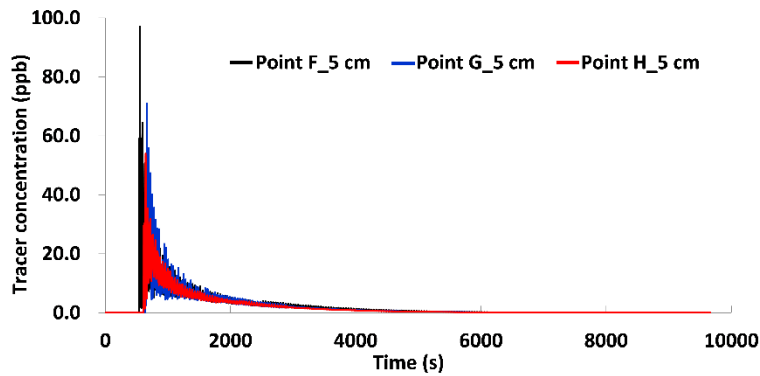


Fig. 7.10. Measured tracer concentration at points F, G, H with distance to bed of 5 cm, injected at point C.

Fig. 7.11 presents the measured tracer curves at different depths of point G, with the tracer being injected at point A. It can be observed that the tracer peak concentration with a distance of 1 cm to the bed was approximately 25 ppb, which was 10 ppb higher than that at 10 cm to the bed. It indicates that the vertical tracer distribution in this physical model was relatively homogenous: a little more tracer was transported downstream in the lower layers.

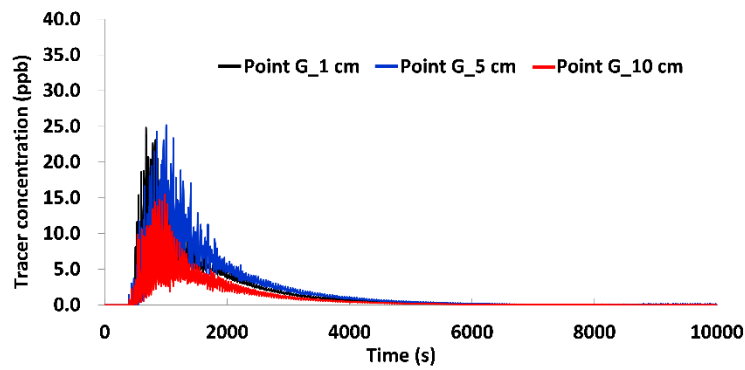


Fig. 7.11. Measured tracer concentration at point G with distances to bed of 1cm, 5 cm and 10 cm, injected at point A.

#### 7.2.2.3.3 Monitoring at the same points

Fig. 7.12 and Fig. 7.13 present the measured tracer curves monitored at points G and J with a distance of 5 cm to the bed, by injecting at different points., The monitored peak tracer values at point G varied from 80 ppb to 100 ppb for most of the injection points expect point A and D. Because point A was located at the upstream end, the injected tracer was diffused to relatively low concentration when it arrived at point G, also shown in Fig. 7.11. The tracer injected at point D has a peak value less than 20 ppb when passing point G. Point D, located near Cardiff, was very close to the cross-section F-G-H. It was due to the fact that more tracer particles were transported on the north side of the estuary. Thus, when the tracer was injected at the points along the north coastal line, most of the tracer was transported to downstream from the north side.



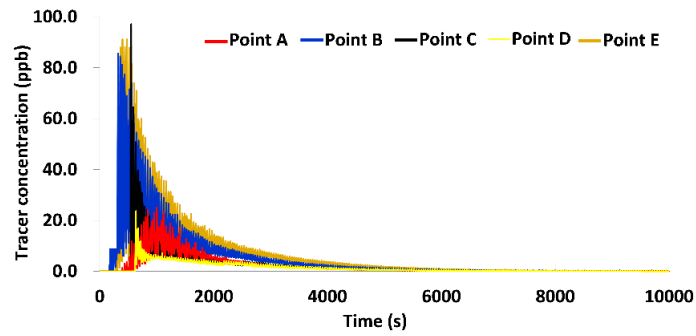


Fig. 7.12. Measured tracer concentration at point G with a distance to bed of 5 cm, injected at point A, B, C, D, and E.

Fig. 7.13 shows the measurements at point J, which was situated along the main axis in the Bristol Channel. It can be seen that by injecting at point A, the tracer was diffused to very low values at point J. By comparison with the curves with the tracer being injected points C and E, i.e. at the middle Severn Estuary, the peak values for these two tests were similar, being approximately 8 ppb. However, the tracer injected at point C arrived at point J earlier than injected at point E. From Table 7.2, the mean travel time between points C and J was 42.07 minutes, while it was 55.76 minutes between points E and J. It further indicated that strong water exchange process occurred on the north side of the estuary.

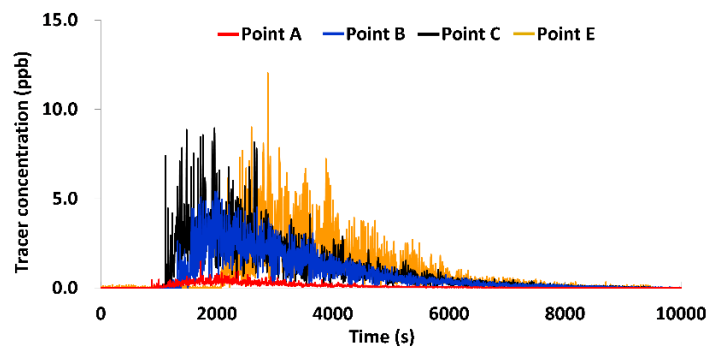


Fig. 7.13. Measured tracer concentration at point J with a distance to the bed of 5 cm, being injected at point A, B, C, and E, respectively.

#### 7.2.2.4 Tracer Flux

The tracer fluxes at cross-sections B and F-G-H were analysed in the current study, with calculations based on the measurements of water level, velocity and tracer concentration.

##### *7.2.2.4.1 Cross-section B*

Fig. 7.14 shows the water flux through cross-section B over a tidal cycle. The tracer concentration was the measurement by injecting at point A. It can be seen that at point B, the hydrodynamic phenomenon was very complex with water flux fluctuating frequently with time, ranging from 600 ml/s to 800 ml/s. By multiplying the water flux with the tracer concentration, the time series of tracer mass through the cross section was obtained, see Fig. 7.15. The maximum value of the tracer flux was around  $3 \times 10^{-2} \text{ mg/s}$  towards downstream while  $2.5 \times 10^{-2} \text{ mg/s}$  towards upstream. It indicates that when the tracer mass centre passed point B, some tracer was diffused and advected into the lower estuary, whilst a large part of tracer flowed back towards upstream with the flood tide. After 100 minutes, nearly all the tracer was transported downstream of this cross section.

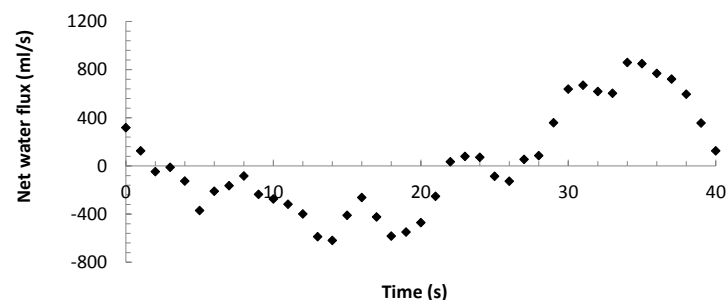


Fig. 7.14. Water flux through cross-section B over a tidal period; positive values represent velocity directed towards upstream.

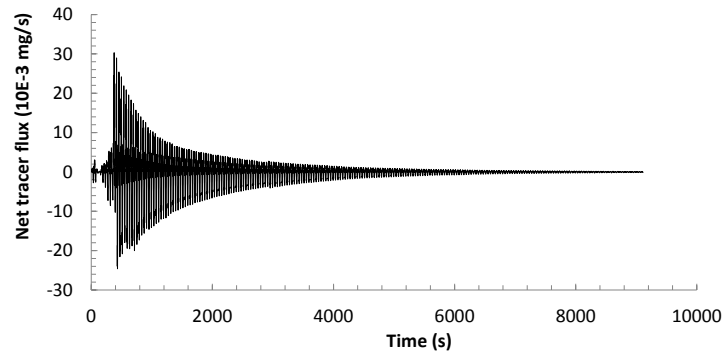


Fig. 7.15. Time series of tracer flux through cross-section B; positive values indicate towards upstream.

#### 7.2.2.4.2 Cross-section F-G-H

The water flux through cross-section F-G-H fluctuated from approximately -3 L/s to 4 L/s (see Fig. 7.16). Compared with the cross-section at B (Fig. 7.14), the hydrodynamic phenomenon was less complex. After multiplying with the tracer concentration, the time series of tracer flux was obtained, see Fig. 7.17. The peak of the net tracer flux towards upstream was approximately  $5 \times 10^{-2} \text{ mg/s}$  while it was  $4 \times 10^{-2} \text{ mg/s}$  towards downstream. Similar to the cross-section B, most of the tracer was transported downstream of this cross section after 100 minutes. However, it can be seen that the tracer mass centre passes the cross-section B more rapidly. The mean travel time is about 800 s, i.e., 400 s shorter than cross-section F-G-H.

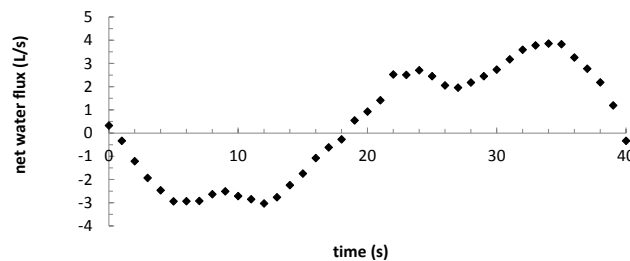


Fig. 7.16. Water flux through cross-section F-G-H over a tidal period; positive values represent towards upstream.

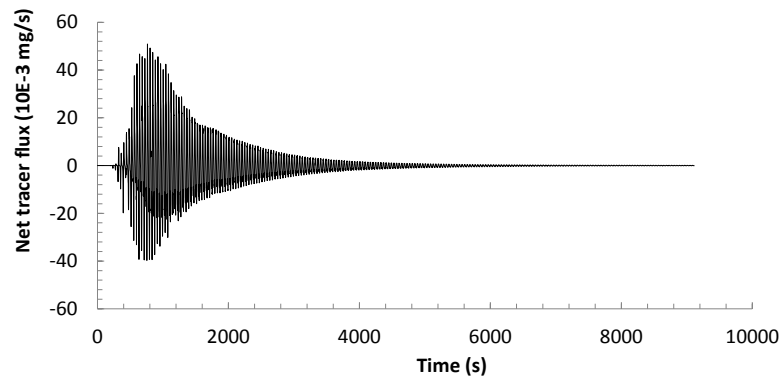


Fig. 7.17. Time series of tracer flux through cross-section F-G-H, positive values represent towards upstream while negative values represent towards downstream.

## SUMMARY

A series of physical experiments were undertaken to investigate the flow and solute transport processes in the Severn Estuary and Bristol Channel. Based on the measured velocity, water level and tracer distributions, the mean travel time and water and tracer fluxes were obtained. The main conclusions are as follows:

- 1) As tidal waves propagate towards upstream, the tidal range is amplified and the density of energy increased. The fluctuation in water level at the upstream reach during the flood is due to wave reflection from the upstream boundary.
- 2) At mean ebb water the largest speed is approximately 7 cm/s, observed at the middle layer. At mean flood water, the largest speed value is greater than 9 cm/s, observed in the surface layer. At point B near the Severn Bridge, a strong ebb current is observed. The depth-averaged velocity, perpendicular to cross-section B, varied between 0 and 2 cm/s during the flood, which was lower than at cross-section F-G-H, where the maximum velocity is 6 cm/s.
- 3) Based on the results of a series of tracer experiments, the mean travel time

between certain points is assessed. It can be seen from the tracer curves and the calculated mean travel time, the tracer injected in the upper estuary is transported to downstream mainly along the north side of the estuary.

- 4) If the tracer is injected at the upstream end, it is diffused to relatively low concentration when it arrives at downstream points, decreasing from 400ppm to less than 20 ppb at point G near Cardiff, and nearly 0 ppb in the middle of the Bristol Channel.

## **Chapter 8**

---

# **Conclusions and Recommendations for Further Research**

The water exchange process plays a critical role in controlling the chemical and biological processes in estuarine waters. When the water exchange capability decreases, the pollutants in the water body may be accumulated. This would cause environmental problems, such as eutrophication and fish kills. Thus, an improved understanding of the water exchange process is important for managing water quality. The main aim of the current study is to investigate the water exchange timescales in estuarine waters.

In this study, a three-dimensional model has been refined to predict the distribution of the age of water (AW). The AW is the time elapsed since a water parcel enters into the interested domain, which is time and location dependent, and can be used to represent the transport of individual water parcels from different sources. The AW model has been applied to two very different estuaries, namely the Pearl River Estuary (PRE), China, and the Severn Estuary and the Bristol Channel (SEBC), UK. The PRE is stratified during the wet season due to a large volume of river discharge. The density gradient creates a vertical circulation, leading to apparent three-dimensional characteristics. It becomes partially mixed during the dry season due to a decrease in discharge. In contrast, due to the high tidal range and strong tidal currents the SEBC is well-mixed, with the vertical salinity distribution being homogenous.

Based on the predicted AW distributions, the water exchange processes in the above two estuaries are investigated. By running numerical simulations for each estuary for both the barotropic mode and the baroclinic mode, the influences of density-induced circulation on the water exchange process in these two estuaries are assessed and compared.

In the PRE, a number of forcing mechanisms – including the bottom topography, tide and coastal currents, wind and freshwater discharge – operate jointly to control the hydrodynamic process. Thus, the influences of river discharge, tides and wind on the water exchange process are also analysed.

In modelling the SEBC, a turbine module is adopted to investigate the impact of turbine arrays on the surrounding estuarine water exchange process. Based on the predicted AW distributions, the site selection and turbine array design could be optimised to reduce environmental impact.

Following the numerical modelling study, a physical model investigation has been conducted in a fibreglass model of the SEBC through a series of tracer experiments. Based on the measurements of hydrodynamic parameters and estimation of mean travel time between sampling points, the water exchange process in this estuary is investigated.

## **8.1 CONCLUSIONS**

The main conclusions drawn from the current study can be summarised as the followings:

- 1) The AW distribution varies with time and space. In the PRE, a relatively low AW is at the upper layers near the water surface and a higher value is at the lower layers near the bed, leading to a landward tongue-shaped contour line near the bed. A more obvious stratification of AW can be observed in the wet season. In the SEBC, a strong water exchange process is observed on the south side of the lower



estuary.

- 2) In the PRE, the density-induced circulation increases the estuarine stratification, while it also generally shortens the retention time and enhances the estuarine water exchange process, especially in the surface layers. The density-induced circulation plays a more significant role in a micro-tidal estuary than a macro-tidal estuary.
- 3) A regression analysis reveals that the AW value decreases exponentially with an increasing discharge. The AW difference between the high and low waters is large during spring tides due to the increase in tidal range, while the tidally averaged mean AW value remains nearly constant over a spring-neap tidal cycle. AW stratification is enhanced during neap tides when the impact of the tidal mixing process becomes weaker. The wind effect is also important, it increases the vertical mixing inside the estuary and reduces the AW stratification.
- 4) The predicted average residence time (ARTM) and average exposure time (AETM) in the PRE indicate that the AETM value decreases exponentially with the increasing discharge. While the ARTM value is mainly affected by the tidal currents at the sea boundary. Under a high discharge, if the tracer is released at low water, the AETM for the entire estuary is greater than twice of that released at high water.
- 5) If turbine arrays are installed in the SEBC, the high water level increases in a large part of the estuary. However, the magnitude of water level change due to the turbines is relatively small. The peak tidal ebb current in the vicinity of turbines decreases by approximately 0.4 m/s, while the current speed increases on both sides of the turbines. The AW values downstream of the turbines decrease over tidal cycles. The AW values upstream of the turbines increase during the flood tides, but they decrease during the ebb tides.

- 6) In the physical model study of the SEBC, the mean travel times between selected points are estimated based on a series of tracer experiments. The tracer solution injected in the upper estuary is transported downstream mainly along the north side of the estuary. Higher tracer concentration is observed at the lower layers of water column.

## **8.2 RECOMMENDATIONS FOR FURTHER RESEARCH**

In this study, a three-dimensional model is refined to predict the age distribution in estuarine waters. A conservative tracer is used as the surrogate. The model has been successfully used to analyse the spatio-temporal hydrodynamic processes in both micro-tidal and macro-tidal estuaries. Further studies can be carried in the following aspects:

- 1) It would be very useful if the water age concept can be applied to describe the sediment transport process in estuarine waters. Since the distribution of sediment concentration in an estuary is influenced by fluvial and tidal dynamics. River flow may intensify stratification and upstream bottom flow (trapping particles), but also shortens the estuary, reducing the volume in which the particles may be trapped. Strong tides have a similarly ambiguous role—they may reduce stratification by erosion, decreasing the ability of a system to trap suspended material (David et al., 2007). These make the sediment deposition and possible dispersal patterns are relative to the water exchange process. Therefore, an investigation into the sedimentary environment in estuarine waters based on water age distribution is recommended in further study.
- 2) An excess of nutrients in estuaries can bring several environmental problems, such as algal bloom and hypoxia. The transport and mixing processes are critical to the concentrations of nutrients in estuarine waters. Therefore, it is very useful if the

age distribution of key water quality parameters, such as nutrients, can be directly predicted. Nutrients are transported in two forms, one of them is dissolved and the other is attached to suspended particles. The attached nutrients undergo both erosion and deposition processes with the particles, which makes the prediction of their age distributions more challenging. Further research is recommended to develop improved methods for simulating the transport and mixing processes of nutrients based on the age concept.

- 3) Although numerical models are available for calculating hydraulics and water exchange timescales, physical model experiments remain a powerful tool for investigating the fundamental physical processes in estuarine waters. In the current study, the measured travel time between selected points in the Severn Estuary and Bristol Channel is used to study the water exchange process in the basin. However, there is a large difference between the measured and model predicted water age values. This is likely due to the large scale difference between the physical and prototype models. In the future, the physical model needs be updated to allow it to be better up-scaled.

# Appendix A

## HYDRODYNAMIC AND TRANSPORT MODULES OF MIKE 3

### 1. Turbulence model

The turbulence is modelled using an eddy viscosity concept. The eddy viscosity is often described separately for the vertical and the horizontal transport. Here several turbulence models can be applied: a constant viscosity distribution, a vertically parabolic viscosity distribution and a standard  $k - \varepsilon$  model (Rodi, 1984). In many numerical simulations the small-scale turbulence could not be resolved with the chosen spatial resolution. This kind of turbulence can be approximated using sub-grid scale models.

#### 1.1 Vertical eddy viscosity

In MIKE3 FM model system, the vertical eddy viscosity could be derived from the log-law or  $k - \varepsilon$  model. In our study, the eddy-viscosity is derived from turbulence parameters  $k$  and  $\varepsilon$  as

$$v_t = c_\mu \frac{k^2}{\varepsilon} \quad (\text{A.1})$$

where  $c_\mu$  is an empirical constant,  $k$  is the turbulent kinetic energy per unit mass (TKE),  $\varepsilon$  is the dissipation rate of TKE which is obtained from the following transport equations.

$$\frac{\partial k}{\partial t} + \frac{\partial uk}{\partial x} + \frac{\partial vk}{\partial y} + \frac{\partial wk}{\partial z} = F_k + \frac{\partial}{\partial z} \left( \frac{v_t}{\sigma_k} \frac{\partial k}{\partial z} \right) + P + B - \varepsilon \quad (\text{A.2})$$

$$\frac{\partial \varepsilon}{\partial t} + \frac{\partial u\varepsilon}{\partial x} + \frac{\partial v\varepsilon}{\partial y} + \frac{\partial w\varepsilon}{\partial z} = F_\varepsilon + \frac{\partial}{\partial z} \left( \frac{v_t}{\sigma_\varepsilon} \frac{\partial \varepsilon}{\partial z} \right) + \frac{\varepsilon}{k} (c_{1\varepsilon} P + c_{3\varepsilon} B - c_{2\varepsilon} \varepsilon) \quad (\text{A.3})$$

where the shear production term,  $P$ , and the buoyancy production term,  $B$ , are given as

$$P = \frac{\tau_{xz}}{\rho_0} \frac{\partial u}{\partial z} + \frac{\tau_{yz}}{\rho_0} \frac{\partial v}{\partial z} \approx v_t \left( \left( \frac{\partial u}{\partial z} \right)^2 + \left( \frac{\partial v}{\partial z} \right)^2 \right) \quad (\text{A.4})$$

$$B = -\frac{v_t}{\sigma_t} N^2 \quad (\text{A.5})$$

with the Brunt-Väisälä frequency,  $N_B$ , defined by

$$N_B^2 = -\frac{g}{\rho_0} \frac{\partial \rho}{\partial z} \quad (\text{A.6})$$

$\sigma_t$  is the turbulent Prandtl number and  $\sigma_k$ ,  $\sigma_\varepsilon$ ,  $c_{1\varepsilon}$ ,  $c_{2\varepsilon}$  and  $c_{3\varepsilon}$  are empirical constants.  $F$  is the horizontal diffusion terms defined by

$$(F_k, F_\varepsilon) = \left[ \frac{\partial}{\partial x} \left( D_h \frac{\partial}{\partial x} \right) + \frac{\partial}{\partial y} \left( D_h \frac{\partial}{\partial y} \right) \right] (k, \varepsilon) \quad (\text{A.7})$$

The horizontal diffusion coefficients are given by  $D_h = A/\sigma_k$  and  $D_h = A/\sigma_\varepsilon$ , respectively.

Several carefully calibrated empirical coefficients enter the turbulence model. The empirical constants are listed in Table A.1 (Rodi, 1984).

**Table A.1 Empirical constants in the  $k - \varepsilon$  model.**

$c_\mu$	$c_{1\varepsilon}$	$c_{2\varepsilon}$	$c_{3\varepsilon}$	$\sigma_t$	$\sigma_k$	$\sigma_\varepsilon$
0.09	1.44	1.92	0	0.9	1.0	1.3

At the surface the boundary conditions for the turbulent kinetic energy and its rate of

dissipation depend on the wind shear,  $U_{\tau s}$ .

At  $z = \eta$ :

$$k = \frac{1}{\sqrt{c_\mu}} U_{\tau s}^2, \varepsilon = \frac{U_{\tau s}^3}{\kappa \Delta z_b}, \quad \text{for } U_{\tau s} > 0 \quad (\text{A.8})$$

$$\frac{\partial k}{\partial z} = 0, = \frac{(k\sqrt{c_\mu})^{3/2}}{\alpha \kappa h}, \quad \text{for } U_{\tau s} = 0 \quad (\text{A.9})$$

where  $\kappa = 0.4$  is the von Kármán constant,  $\alpha = 0.07$  is an empirical constant and  $\Delta z_s$  is the distance from the surface where the boundary condition is imposed. At the seabed, the boundary conditions are

At  $z = -d$ :

$$k = \frac{1}{\sqrt{c_\mu}} U_{\tau b}^2 \quad (\text{A.10})$$

$$\varepsilon = \frac{U_{\tau s}^3}{\kappa \Delta z_b} \quad (\text{A.11})$$

where  $\Delta z_b$  is the distance from the bottom where the boundary condition is imposed.

### 1.2 Horizontal eddy viscosity

In many applications a constant eddy viscosity can be used for the horizontal eddy viscosity. Alternatively, Smagorinsky (1963) proposed to express sub-grid scale transports by an effective eddy viscosity related to a characteristic length scale. The sub-grid scale eddy viscosity is given by:

$$A = c_s^2 l^2 \sqrt{2S_{ij}S_{ij}} \quad (\text{A.12})$$

where  $c_s$  is a constant,  $l$  is a characteristic length and the deformation rate  $S_{ij}$  is given by:

$$S_{ij} = \frac{1}{2} \left( \frac{\partial u_i}{\partial x_j} + \frac{\partial u_j}{\partial x_i} \right) \quad (i, j = 1, 2) \quad (\text{A.13})$$

## 2. Governing equations in Cartesian and sigma-co-ordinates

The equations are solved using a vertical  $\sigma$ -transformation

$$\sigma = \frac{z - z_b}{h}; \quad x' = x, \quad y' = y \quad (\text{A.14})$$

where  $\sigma$  varies between 0 at the bottom and 1 at the surface. The co-ordinate transformation implies the following relationships

$$\frac{\partial}{\partial z} = \frac{1}{h} \frac{\partial}{\partial \sigma} \quad (\text{A.15})$$

$$\left( \frac{\partial}{\partial x}, \frac{\partial}{\partial y} \right) = \left( \frac{\partial}{\partial x'} - \frac{1}{h} \left( -\frac{\partial d}{\partial x} + \sigma \frac{\partial h}{\partial x} \right) \frac{\partial}{\partial \sigma}, \frac{\partial}{\partial y'} - \frac{1}{h} \left( -\frac{\partial d}{\partial y} + \sigma \frac{\partial h}{\partial y} \right) \frac{\partial}{\partial \sigma} \right) \quad (\text{A.16})$$

In this new co-ordinate system the governing equations are given as

$$\frac{\partial h}{\partial t} + \frac{\partial hu}{\partial x'} + \frac{\partial hv}{\partial y'} + \frac{\partial hw}{\partial \sigma} = hS \quad (\text{A.17})$$

$$\begin{aligned} \frac{\partial hu}{\partial t} + \frac{\partial hu^2}{\partial x'} + \frac{\partial hvu}{\partial y'} + \frac{\partial hwu}{\partial \sigma} &= fvh - gh \frac{\partial \eta}{\partial x'} - \frac{h}{\rho_0} \frac{\partial p_a}{\partial x'} - \frac{hg}{\rho_0} \int_z^\eta \frac{\partial \rho}{\partial x} dz - \\ \frac{1}{\rho_0} \left( \frac{\partial s_{xx}}{\partial x} + \frac{\partial s_{xy}}{\partial y} \right) + hF_u + \frac{\partial}{\partial \sigma} \left( \frac{v_v}{h} \frac{\partial u}{\partial \sigma} \right) + hu_s S \end{aligned} \quad (\text{A.18})$$

$$\begin{aligned} \frac{\partial hv}{\partial t} + \frac{\partial huv}{\partial x'} + \frac{\partial hv^2}{\partial y'} + \frac{\partial h wv}{\partial \sigma} &= -fuh - gh \frac{\partial \eta}{\partial y'} - \frac{h}{\rho_0} \frac{\partial p_a}{\partial y'} - \frac{hg}{\rho_0} \int_z^\eta \frac{\partial \rho}{\partial y} dz - \\ \frac{1}{\rho_0} \left( \frac{\partial s_{yx}}{\partial x} + \frac{\partial s_{yy}}{\partial y} \right) + hF_v + \frac{\partial}{\partial \sigma} \left( \frac{v_v}{h} \frac{\partial v}{\partial \sigma} \right) + hv_s S \end{aligned} \quad (\text{A.19})$$

$$\frac{\partial hs}{\partial t} + \frac{\partial hus}{\partial x'} + \frac{\partial hvs}{\partial y'} + \frac{\partial hws}{\partial \sigma} = hF_s + \frac{\partial}{\partial \sigma} \left( \frac{D_v}{h} \frac{\partial s}{\partial \sigma} \right) + hS_s S \quad (\text{A.20})$$

Vertical eddy viscosity equations:

$$\frac{\partial hk}{\partial t} + \frac{\partial huk}{\partial x'} + \frac{\partial hvk}{\partial y'} + \frac{\partial hwk}{\partial \sigma} = hF_k + \frac{1}{h} \frac{\partial}{\partial \sigma} \left( \frac{v_t}{\sigma_k} \frac{\partial k}{\partial \sigma} \right) + h(P + B - \varepsilon) \quad (\text{A.21})$$

$$\frac{\partial h\varepsilon}{\partial t} + \frac{\partial hu\varepsilon}{\partial x'} + \frac{\partial hv\varepsilon}{\partial y'} + \frac{\partial hw\varepsilon}{\partial \sigma} = hF_\varepsilon + \frac{1}{h} \frac{\partial}{\partial \sigma} \left( \frac{v_t}{\sigma_\varepsilon} \frac{\partial \varepsilon}{\partial \sigma} \right) + h \frac{\varepsilon}{k} (c_{1\varepsilon}P + c_{3\varepsilon}B - c_{2\varepsilon}\varepsilon) \quad (\text{A.22})$$

$$\frac{\partial hC}{\partial t} + \frac{\partial huC}{\partial x'} + \frac{\partial hvC}{\partial y'} + \frac{\partial hWC}{\partial \sigma} = hF_C + \frac{\partial}{\partial \sigma} \left( \frac{D_v}{h} \frac{\partial C}{\partial \sigma} \right) - hk_p C + hC_s S \quad (\text{A.23})$$

The modified vertical velocity is defined by

$$w = \frac{1}{h} \left[ w + u \frac{\partial d}{\partial x'} + v \frac{\partial d}{\partial y'} - \sigma \left( \frac{\partial h}{\partial t} + u \frac{\partial h}{\partial x'} + v \frac{\partial h}{\partial y'} \right) \right] \quad (\text{A.24})$$

The modified vertical velocity is the velocity across a level of constant  $\sigma$ . The horizontal diffusion terms are defined as

$$hF_u \approx \frac{\partial}{\partial x} \left( 2hA \frac{\partial u}{\partial x} \right) + \frac{\partial}{\partial y} \left( hA \left( \frac{\partial u}{\partial y} + \frac{\partial v}{\partial x} \right) \right) \quad (\text{A.25})$$

$$hF_v \approx \frac{\partial}{\partial x} \left( hA \left( \frac{\partial u}{\partial y} + \frac{\partial v}{\partial x} \right) \right) + \frac{\partial}{\partial y} \left( 2hA \frac{\partial v}{\partial y} \right) \quad (\text{A.26})$$

$$h(F_s, F_k, F_\varepsilon, F_C) \approx \left[ \frac{\partial}{\partial x} \left( hD_h \frac{\partial}{\partial x} \right) + \frac{\partial}{\partial y} \left( hD_h \frac{\partial}{\partial y} \right) \right] (s, k, \varepsilon, C) \quad (\text{A.27})$$

The boundary condition at the free surface and at the bottom are given as follows

At  $\sigma = 1$ :

$$w = 0, \left( \frac{\partial u}{\partial \sigma}, \frac{\partial v}{\partial \sigma} \right) = \frac{h}{\rho_0 v_t} (\tau_{sx}, \tau_{sy}) \quad (\text{A.28})$$

At  $\sigma = 0$ :

$$w = 0, \left( \frac{\partial u}{\partial \sigma}, \frac{\partial v}{\partial \sigma} \right) = \frac{h}{\rho_0 v_t} (\tau_{bx}, \tau_{by}) \quad (\text{A.29})$$

The equation for determination of the water depth is not changed by the co-ordinate transformation. Hence, it is identical to Equation 3.6.



### 3. Bottom Stress

The bottom stress,  $\vec{\tau}_b = (\tau_{bx}, \tau_{by})$ , is determined by a quadratic friction law.

$$\frac{\vec{\tau}_b}{\rho_0} = C_d \vec{u}_b |\vec{u}_b| \quad (\text{A.30})$$

where  $C_d$  is the drag coefficient and  $\vec{u}_b = (u_b, v_b)$  is the flow velocity above the bottom. The friction velocity associated with the bottom stress is given by

$$U_{\tau b} = \sqrt{c_f |\vec{u}_b|^2} \quad (\text{A.31})$$

For three-dimensional calculations,  $\vec{u}_b$  is the velocity at a distance  $\Delta z_b$  above the sea bed and the drag coefficient is determined by assuming a logarithmic profile between the sea bed and a point  $\Delta z_b$  above the sea bed.

$$c_f = \frac{1}{\left( \frac{1}{\kappa} \ln \left( \frac{\Delta z_b}{z_0} \right) \right)^2} \quad (\text{A.32})$$

where  $\kappa = 0.4$  is the von Kármán constant and  $z_0$  is the bed roughness length scale. When the boundary surface is rough,  $z_0$ , depends on the roughness height,  $k_s$

$$z_0 = k_s/30 \quad (\text{A.33})$$

The Manning number can be estimated from the bed roughness length using the following

$$M = 25.4/k_s^{1/6} \quad (\text{A.34})$$

#### 4. Wind Stress

In areas not covered by ice the surface stress,  $\vec{\tau}_s = (\tau_{sx}, \tau_{sy})$ , is determined by the winds above the surface. The stress is given by the following empirical relation

$$\vec{\tau}_s = \rho_a c_d |\vec{u}_w| \vec{u}_w \quad (\text{A.35})$$

where  $\rho_a$  is the density of air,  $c_d$  is the drag coefficient of air, and  $\vec{u}_w = (u_w, v_w)$  is the wind speed 10 m above the sea surface. The friction velocity associated with the surface stress is given by

$$U_{\tau s} = \sqrt{\frac{\rho_a c_d |\vec{u}_w|^2}{\rho_0}} \quad (\text{A.36})$$

The drag coefficient can either be a constant value or depend on the wind speed. The following empirical formula proposed by Wu (1980, 1994) is used for the parameterisation of the drag coefficient.

$$c_f = \begin{cases} c_a & w_{10} \leq w_a \\ c_a + \frac{c_b - c_a}{w_b - w_a} (w_{10} - w_a) & w_a \leq w_{10} \leq w_b \\ c_b & w_{10} \geq w_b \end{cases} \quad (\text{A.37})$$

where  $c_a$ ,  $c_b$ ,  $w_a$  and  $w_b$  are empirical factors and  $w_{10}$  is the wind velocity 10 m above the sea surface. The default values for the empirical factors are  $c_a = 1.255 \times 10^{-3}$ ,  $c_b = 2.425 \times 10^{-3}$ ,  $w_a = 7 \text{ m/s}$  and  $w_b = 25 \text{ m/s}$ . These give generally good results for open sea applications. Field measurements of the drag coefficient collected over lakes indicate that the drag coefficient is larger than that obtained from open ocean data (Geernaert and Plan, 1990).

## 5. Tidal Potential

The tidal potential is a force, generated by the variations in gravity due to the relative motion of the earth, the moon and the sun that act throughout the computational domain. The forcing is expanded in frequency space and the potential considered as the sum of a number of terms each representing different tidal constituents. The forcing is implemented as a so-called equilibrium tide, which can be seen as the elevation that theoretically would occur, provided the earth was covered with water. The forcing enters the momentum equations as an additional term representing the gradient of the equilibrium tidal elevations, such that the elevation  $\eta$  can be seen as the sum of the actual elevation and the equilibrium tidal potential.

$$\eta = \eta_{ACTUAL} + \eta_T \quad (A.38)$$

The equilibrium tidal potential  $\eta_T$  is given as

$$\eta_T = \sum_i e_i H_i f_i L_i \cos(2\pi \frac{t}{T_i} + b_i + i_0 x) \quad (A.39)$$

where  $\eta_T$  is the equilibrium tidal potential,  $i$  refers to constituent number (note that the constituents here are numbered sequentially),  $e_i$  is a correction for earth tides based on Love numbers,  $H_i$  is the amplitude,  $f_i$  is a nodal factor,  $L_i$  is given below,  $t$  is time,  $T_i$  is the period of the constituent,  $b_i$  is the phase and  $x$  is the longitude of the actual position.

The phase  $b$  is based on the motion of the moon and the sun relative to the earth can be given by

$$b_i = (i_1 - i_0)s + (i_2 + i_0)h + i_3p + i_4N + i_5p_s + u_i \sin(N) \quad (A.40)$$

where  $i_0$  is the species,  $i_1$  to  $i_5$  are Doodson numbers,  $u$  is a nodal modulation factor

(see Table A.3) and the astronomical arguments  $s$ ,  $h$ ,  $p$ ,  $N$  and  $p_s$  are given in Table A.2.

**Table A.2 Astronomical arguments (Pugh, 1987)**

Mean longitude of the moon	$s$	$277.02 + 481267.89T + 0.0011T^2$
Mean longitude of the sun	$h$	$280.19 + 36000.77T + 0.0003T^2$
Longitude of lunar perigee	$p$	$334.39 + 4069.04T + 0.0103T^2$
Longitude of lunar ascending node	$N$	$259.16 + 1934.14T + 0.0021T^2$
Longitude of perihelion	$p_s$	$281.22 + 1.72T + 0.0005T^2$

In Table A.2, the time  $T$ , is in Julian century from January 1 1900 UTC, thus  $T = (365(y - 1900) + (d - 1) + i)/36525$  and  $i = \text{int}(y - 1901)/4$ ,  $y$  is year and  $d$  is day number.

$L$  depends on species number  $i_0$  and latitude  $y$  as

$$i_0 = 0, L = 3\sin^2 y - 1 \quad (\text{A.41})$$

$$i_0 = 1, L = \sin(2y) \quad (\text{A.42})$$

$$i_0 = 2, L = \cos^2 y \quad (\text{A.43})$$

**Table A.3 Nodal modulation terms (Pugh, 1987)**

	$f_i$	$u_i$
$M_m$	$1.000 - 0.130\cos(N)$	0
$M_f$	$1.043 + 0.414\cos(N)$	$-23.7\sin(N)$
$Q_1, O_1$	$1.009 + 0.187\cos(N)$	$10.8\sin(N)$
$K_1$	$1.006 + 0.115\cos(N)$	$-8.9\sin(N)$
$2N_2, \mu_2, \nu_2, N_2, M_2$	$1.000 + 0.037\cos(N)$	$-2.1\sin(N)$
$K_2$	$1.024 + 0.286\cos(N)$	$-17.7\sin(N)$

The nodal factor  $f_i$  represents modulations to the harmonic analysis and can for some constituents be given as shown in Table A.3.

# Appendix B

## NUMERICAL SOLUTION OF MIKE3

### 1. Spatial Discretization

The discretization in solution domain is performed using a finite volume method. The spatial domain is discretized by subdivision of the continuum into non-overlapping elements. In this study, a layered mesh was used: an unstructured mesh based on Cartesian coordinate in the horizontal domain while a mesh based on sigma coordinate in the vertical domain. The horizontal faces are either triangles or quadrilateral element. Thus the elements in the sigma domain can be prisms with either a 3-sided or 4-sided polygonal base.

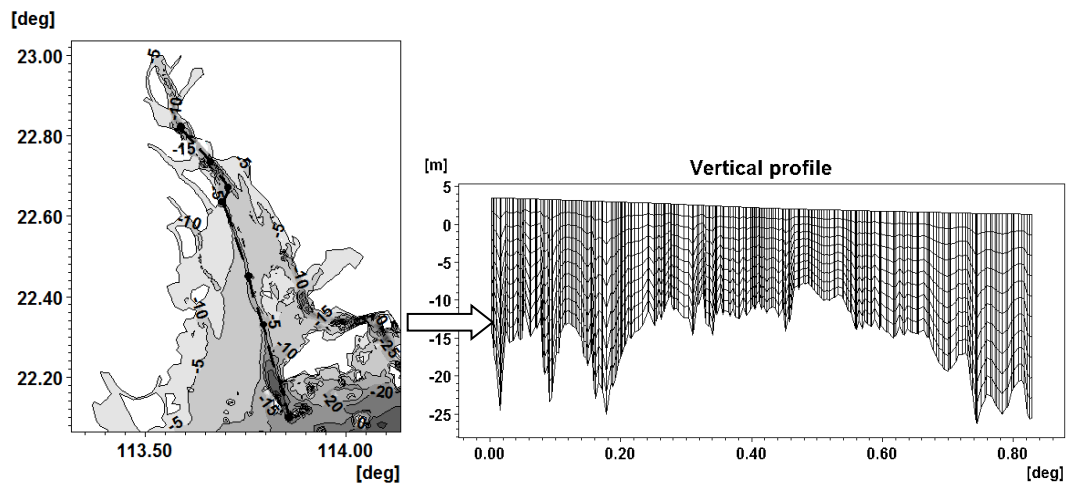


Fig. B.1. Bathymetry of the Pearl River Estuary (left); Illustration of the vertical 10-level sigma layers of along-channel section (left dash line) in the modelling (right).

Compared with the inaccuracy in representing the bathymetry and the unrealistic flow velocities brought by the stair-step bathymetry, the most important advantage using a sigma coordinate is its ability to accurately represent the bathymetry and provide

consistent resolution near the bed (see Fig. 3.3). However, the sigma coordinate can suffer from significant errors in the horizontal pressure gradients, advection and mixing terms in areas with sharp topographic changes (steep slopes).

### 1.1 Sigma Vertical Mesh

In the sigma domain a constant number of layers,  $N_\sigma$ , are used and each sigma layer is a fixed fraction of the total depth of the sigma layer,  $h_\sigma$ , where  $h_\sigma = \eta - \max(z_b, z_\sigma)$ . The discretization in the sigma domain is given by a number of discrete  $\sigma_i$  levels ( $i = 1, (N_\sigma + 1)$ ). Here  $\sigma$  varies from  $\sigma_1 = 0$  at the bottom interface of the lowest sigma layer to  $\sigma_{N_\sigma+1} = 1$  at the free surface.

Variable sigma coordinates can be obtained using a discrete formulation of the general vertical coordinate ( $s$ -coordinate) system proposed by Song and Haidvogel (1994). First an equidistant discretization in an  $s$ -coordinate system ( $-1 \leq s \leq 0$ ) is defined.

$$s_i = -\frac{N_\sigma+1-i}{N_\sigma}, i = 1, (N_\sigma + 1) \quad (\text{B.1})$$

The discrete sigma coordinates can then be determined by

$$\sigma_i = 1 + \sigma_c s_i + (1 - \sigma_c) c(s_i), i = 1, (N_\sigma + 1) \quad (\text{B.2})$$

where

$$c(s) = (1 - b) \frac{\sinh(\theta s)}{\sinh(\theta)} + b \frac{\tanh\left(\theta\left(s+\frac{1}{2}\right)\right) - \tanh\left(\frac{\theta}{2}\right)}{2 \tanh\left(\frac{\theta}{2}\right)} \quad (\text{B.3})$$

Here  $\sigma_c$  is a weighting factor between the equidistant distribution and the stretch distribution,  $\theta$  is the surface control parameter and  $b$  is the bottom control parameter. The range for the weighting factor is  $0 < \sigma_c \leq 1$  where the value 1 corresponds to

equidistant distribution and 0 corresponds to stretched distribution. A small value of  $\sigma_c$  can result in linear instability. The range of the surface control parameter is  $0 < \theta \leq 20$  and the range of the bottom control parameter is  $0 \leq b \leq 1$ . If  $\theta \ll 1$  and  $b = 0$  an equidistant vertical resolution is obtained. By increasing the value of the  $\theta$ , the highest resolution is achieved near the surface. If  $\theta \geq 0$  and  $b = 1$  a high resolution is obtained both near the surface and near the bed.

### 1.2 Shallow water equations

The integral form of the system of shallow water equations can be written as

$$\frac{\partial \vec{U}}{\partial t} = \Delta \cdot \vec{F}(\vec{U}) = \vec{S}(\vec{U}) \quad (\text{B.4})$$

where  $\vec{U}$  is the vector of conserved variables,  $\vec{F}$  is the flux vector function and  $\vec{S}$  is the vector of source terms.

In Cartesian co-ordinates the system of three-dimensional shallow water equations can be written as

$$\begin{aligned} U &= \begin{bmatrix} h \\ hu \\ hv \end{bmatrix}, \\ F_x^I &= \begin{bmatrix} h\bar{u} \\ hu^2 + \frac{1}{2}g(h^2 - d^2) \\ huv \end{bmatrix}, F_x^V = \begin{bmatrix} 0 \\ hA(2\frac{\partial u}{\partial x}) \\ hA(\frac{\partial u}{\partial y} + \frac{\partial v}{\partial x}) \end{bmatrix} \\ F_y^I &= \begin{bmatrix} h\bar{v} \\ hvu \\ hv^2 + \frac{1}{2}g(h^2 - d^2) \end{bmatrix}, F_y^V = \begin{bmatrix} 0 \\ hA(\frac{\partial u}{\partial y} + \frac{\partial v}{\partial x}) \\ hA(2\frac{\partial v}{\partial x}) \end{bmatrix} \\ F_\sigma^I &= \begin{bmatrix} hw \\ hwu \\ h w v \end{bmatrix}, F_\sigma^V = \begin{bmatrix} 0 \\ \frac{v_t}{h} \frac{\partial u}{\partial \sigma} \\ \frac{v_t}{h} \frac{\partial v}{\partial \sigma} \end{bmatrix} \end{aligned} \quad (\text{B.5})$$

$$S = \begin{bmatrix} g\eta \frac{\partial d}{\partial x} + fvh - \frac{h}{\rho_0} \frac{\partial p_a}{\partial x'} - \frac{hg}{\rho_0} \int_z^\eta \frac{\partial \rho}{\partial x} dz - \frac{1}{\rho_0} \left( \frac{\partial s_{xx}}{\partial x} + \frac{\partial s_{xy}}{\partial y} \right) \\ g\eta \frac{\partial d}{\partial y} - fuh - \frac{h}{\rho_0} \frac{\partial p_a}{\partial y'} - \frac{hg}{\rho_0} \int_z^\eta \frac{\partial \rho}{\partial y} dz - \frac{1}{\rho_0} \left( \frac{\partial s_{yx}}{\partial x} + \frac{\partial s_{yy}}{\partial y} \right) \end{bmatrix}$$

Integrating Equation B.4 over the  $i^{th}$  cell and using the Gauss theorem to rewrite the flux integral gives

$$\int_{A_i} \frac{\partial \vec{U}}{\partial t} d\Omega + \int_{\Gamma_i} (\vec{F} \cdot \vec{n}) ds = \int_{A_i} \vec{S}(\vec{U}) d\Omega \quad (\text{B.6})$$

where  $A_i$  is the volume of the cell,  $\Omega$  is the integration variable defined on  $A_i$ ,  $\Gamma_i$  is the boundary of the  $i$ th cell and  $ds$  is the integration variable along the boundary.  $\vec{n}$  is the unit outward normal vector along the boundary. Evaluating the area/volume integrals by a one-point quadrature rule, the quadrature point being the centroid of the cell, and evaluating the boundary integral using a mid-point quadrature rule, Equation B.6 can be written

$$\frac{\partial U_i}{\partial t} + \frac{1}{A_i} \sum_j^{NS} \vec{F} \cdot \vec{n} \Delta \Gamma_j = S_i \quad (\text{B.7})$$

Here  $U_i$  and  $S_i$ , respectively, are average values of  $U$  and  $S$  over the  $i^{th}$  cell and stored at the cell centre,  $NS$  is the number of sides of the cell,  $n_j$  is the unit outward normal vector at the  $j^{th}$  side and  $\Delta \Gamma_j$  the length/area of the  $j^{th}$  interface.

Both a first order and a second order scheme can be applied for the spatial discretization. For the three-dimensional case, an approximate Riemann solver (Roe, 1981) is used to calculate the convective fluxes at the vertical interface of the cells ( $x'$   $y'$ -plane). Using the Roe's scheme the dependent variables to the left and to the right of an interface have to be estimated. Second-order spatial accuracy is achieved by employing a linear gradient-reconstruction technique. The average gradients are estimated using the approach by Jawahar and Kamath (2000). To avoid numerical



oscillations a second order TVD slope limiter (Hirsch, 1990; Darwish, 2003) is used. The convective fluxes at the horizontal interfaces (vertical line) are derived using first order upwinding for the low order scheme. For the higher order scheme the fluxes are approximated by the mean value of the fluxes calculated based on the cell values above and below the interface for the higher order scheme.

### 1.3 Transport equations

The transport equations arise in the salt and temperature model, the turbulence model and the generic transport model. They all share the form of Equation 3.16 in Cartesian coordinates. For the three-dimensional case the integral form of the transport equation can be given by Equation B.4 where

$$\begin{aligned}
 \vec{U} &= hC \\
 F^I &= [huC, hvC, hwC] \\
 F^V &= \left[ hD_h \partial \frac{\partial C}{\partial x}, hD_h \partial \frac{\partial C}{\partial y}, h \frac{D_h}{h} \partial \frac{\partial C}{\partial \sigma} \right] \\
 \vec{S} &= -hk_p C + hC_s S
 \end{aligned} \tag{B.8}$$

The discrete finite volume form of the transport equation is given by Equation B.7. As for the shallow water equations both a first order and a second order scheme can be applied for the spatial discretization.

In three-dimensional the low order version uses simple first order upwinding. The higher order version approximates horizontal gradients to obtain second order accurate values at the horizontal boundaries. Values in the upwinding direction are used. To provide stability and minimize oscillatory effects, an ENO (Essentially Non-Oscillatory) type procedure is applied to limit the horizontal gradients. In the vertical direction, the 3<sup>rd</sup> order ENO procedure is used to obtain the vertical face values (Shu, 1997).

## 2 Time Integration

Consider the general form of the equations

$$\frac{\partial \vec{U}}{\partial t} = \vec{G}(\vec{U}) \quad (\text{B.9})$$

For three-dimensional simulations the time integration is semi-implicit. The horizontal terms are treated implicitly and the vertical terms are treated implicitly or partly explicitly and partly implicitly. Consider the equations in the general semi-implicit form.

$$\frac{\partial \vec{U}}{\partial t} = \vec{G}_h(\vec{U}) + \vec{G}_v(B\vec{U}) = \vec{G}_h(\vec{U}) + \vec{G}_v^I(\vec{U}) + \vec{G}_v^V(\vec{U}) \quad (\text{B.10})$$

where the  $h$  and  $v$  subscripts refer to horizontal and vertical terms, respectively, and the superscripts refer to inviscid and viscous terms, respectively.

The low order method used for the three-dimensional shallow water equations can be written as

$$U_{n+1} - \frac{1}{2}\Delta t(G_v(U_{n+1}) + G_v(U_n)) = U_n + \Delta t G_h(U_n) \quad (\text{B.11})$$

The horizontal terms are integrated using a first order explicit Euler method and the vertical terms using a second order implicit trapezoidal rule. The higher order method can be written as

$$U_{n+1/2} - \frac{1}{4}\Delta t(G_v(U_{n+1/2}) + G_v(U_n)) = U_n + \frac{1}{2}\Delta t G_h(U_n) \quad (\text{B.12})$$

$$U_{n+1} - \frac{1}{2}\Delta t(G_v(U_{n+1}) + G_v(U_n)) = U_n + \Delta t G_h(U_{n+1/2}) \quad (\text{B.13})$$

The horizontal terms are integrated using a second order Runge Kutta method and the vertical terms using a second order implicit trapezoidal rule.

The low order method used for the three-dimensional transport equation can be written as

$$U_{n+1} - \frac{1}{2}\Delta t(G_v^V(U_{n+1}) + G_v^V(U_n)) = U_n + \Delta t G_h(U_n) + \Delta t G_v^I(U_n) \quad (\text{B.14})$$

The horizontal terms and the vertical convective terms are integrated using a first order explicit Euler method and the vertical viscous terms are integrated using a second order implicit trapezoidal rule. The higher order method can be written

$$U_{n+1/2} - \frac{1}{4}\Delta t(G_v^V(U_{n+\frac{1}{2}}) + G_v^V(U_n)) = U_n + \frac{1}{2}\Delta t G_h(U_n) + \frac{1}{2}\Delta t G_v^I(U_n) \quad (\text{B.15})$$

$$U_{n+1} - \frac{1}{2}\Delta t(G_v^V(U_{n+1}) + G_v^V(U_n)) = U_n + \Delta t G_h(U_{n+\frac{1}{2}}) + \Delta t G_v^I(U_{n+1/2}) \quad (\text{B.16})$$

The horizontal terms and the vertical convective terms are integrated using a second order Runge Kutta method and the vertical terms are integrated using a second order implicit trapezoidal rule for the vertical terms.

### 3 Boundary Conditions

#### 3.1 Closed boundaries

Along closed boundaries (land boundaries) normal fluxes are forced to zero for all variables. For the momentum equations, this leads to full slip along land boundaries.

#### 3.2 Open boundaries

The open boundary conditions can be specified either in the form of a unit discharge or as the surface elevation for the hydrodynamic equations. For transport equations either a specified value or a specified gradient can be given.

### 3.3 Flooding and drying

The approach for treatment of the moving boundaries problem (flooding and drying fronts) is based on the work by Zhao et al. (1994) and Sleigh et al. (1998). When the depths are small the problem is reformulated and only when the depths are very small the elements/cells are removed from the calculation. The reformulation is made by setting the momentum fluxes to zero and only taking the mass fluxes into consideration.

The depth in each element/cell is monitored and the elements are classified as dry, partially dry or wet. Also, the element faces are monitored to identify flooded boundaries. An element face is considered as flooded if the following two criteria are satisfied: Firstly, the water depth at one side of face must be less than a tolerance depth, dry  $h_{dry}$  and the water depth at the other side of the face larger than a tolerance depth, flood  $h_{flood}$ . Secondly, the sum of the still water depth at the side for which the water depth is less than dry  $h_{dry}$  and the surface elevation at the other side must be larger than zero. An element is dry if the water depth is less than a tolerance depth, dry  $h_{dry}$ , and no of the element faces are flooded boundaries. The element is removed from the calculation.

An element is considered as partially dry if the water depth is larger than dry  $h_{dry}$  and less than a tolerance depth, wet  $h_{wet}$ , or when the depth is less than the dry  $h_{dry}$  and one of the element faces is a flooded boundary. The momentum fluxes are set to zero and only the mass fluxes are calculated. An element is considered as wet if the water depth is greater than wet  $h_{wet}$ . Both the mass fluxes and the momentum fluxes are calculated.

The wetting depth, wet  $h_{wet}$ , must be larger than the drying depth, dry  $h_{dry}$ , and flooding depth, flood  $h_{flood}$ , must satisfy

$$h_{dry} \leq h_{flood} \leq h_{wet} \quad (\text{B.17})$$

The default values are  $h_{dry}=0.005\text{m}$ ,  $h_{flood}=0.05\text{m}$  and  $h_{wet}=0.1\text{m}$ .

For very small values of the tolerance depth,  $h_{wet}$ , unrealistically high flow velocities can occur in the simulation and give cause to stability problems.

# Appendix C

## THE TRADITIONAL CENTRAL REGIME THEORY

Assuming an estuary has a rectangular cross-section, with a constant cross sectional area and depth, one can divide the velocity  $u(x, z)$  and salinity  $s(x, z)$  into depth-averaged and depth-varying components, i.e.,

$$u = \bar{u}(x) + u'(x, z) \quad (C.1)$$

$$s = \bar{s}(x) + s'(x, z) \quad (C.2)$$

where  $\bar{u}$  and  $\bar{s}$  are depth-averaged parts and  $u'$  and  $s'$  are depth varying parts,  $x$  and  $z$  are horizontal and vertical coordinates. The along channel momentum balance can be written as (Dyer, 1997)

$$0 = -\frac{1}{\rho_0} p_x + (K_M u_z)_z \quad (C.3)$$

where  $p$  is pressure along the channel,  $\rho_0$  is a constant background density, and  $K_M$  is vertical eddy viscosity. The equation of state is approximated as  $\rho = \rho_0(1 + ks)$  and  $k = 7.7 \times 10^{-4}$ . Assuming that the pressure distribution is hydrostatic and the horizontal salinity gradient  $s'_x \ll \bar{s}_x$  (Pritchard, 1952), the pressure gradient can be written as

$$-\frac{1}{\rho_0} p_x = -g\eta_x + gk\bar{s}_x z \quad (C.4)$$

Using Equations C.3 and C.4, the velocity profile can be written as

$$u_{zzz} = -\frac{gk\bar{s}_x}{K_M} \quad (\text{C.5})$$

Using boundary conditions  $u(z = -H) = 0$  and  $u_z(z = 0) = 0$ , and  $H^{-1} \int_{-H}^0 u dz = \bar{u} = Q_R/A$ , where  $Q_R$  is the river volume flux,  $H$  is depth,  $A$  is the cross-sectional area. Integrating Equation C.5 (Hansen and Rattray, 1965; Officer, 1976; MacCready, 2004; Shen and Lin, 2006) yields

$$u' = \bar{u}P_1 + u_E P_2 \quad (\text{C.6})$$

$$P_1 = \frac{1}{2} - \frac{3}{2}\varpi\xi^2 \quad (\text{C.7})$$

$$P_2 = 1 - 9\xi^2 - 8\xi^3 \quad (\text{C.8})$$

Where

$$\xi = z/H \quad (\text{C.9})$$

$$u_E = gk\bar{s}_x H^3 / (48K_M) \quad (\text{C.10})$$

Salt conservation can be written as:

$$s_t = \frac{1}{A}(usA)_x + (ws)_z = \frac{1}{A}(K_H s_x A)_x + (K_S s_z)_z \quad (\text{C.11})$$

Where  $K_H$  and  $K_S$  are horizontal diffusion coefficient and vertical eddy diffusivity.

The vertically averaged salt balance equation can be expressed as:

$$\bar{s}_t + \frac{1}{A}(\bar{u}\bar{s}A)_x + \frac{1}{A}(\overline{u's'}A)_x = \frac{1}{A}(K_H \bar{s}_x A)_x \quad (\text{C.12})$$

Subtracting Equation C.12 from Equation C.11 and assuming  $s'_x \ll \bar{s}_x$ , the dominant steady-state balance for  $s'$  can be written as (Pritchard, 1954)

$$u' \bar{s}_x \cong K_S s'_{zz} \quad (\text{C.13})$$

Integrating Equation C.13 with the use of boundary conditions, i.e., vertical salt flux vanishes at the surface and the bottom, one can obtain the vertical salinity profile as follows (Hansen and Rattray, 1965; Officer, 1976; MacCready, 2004; Shen and Lin, 2006)

$$s' = \frac{H^2}{K_S} \bar{s}_x (\bar{u}P_3 + u_E P_4) \quad (C.14)$$

$$P_3 = -\frac{7}{120} + \frac{1}{4}\xi^2 - \frac{1}{8}\xi^4 \quad (C.15)$$

$$P_4 = -\frac{1}{12} + \frac{1}{2}\xi^2 - \frac{3}{4}\xi^4 - \frac{2}{5}\xi^5 \quad (C.16)$$

This shows that the vertical salinity profile depends on estuarine gravitational circulation (the second term of Equation C.14) and mean flow due to discharge (the first term of Equation C.14). By considering a tracer being released continuously at the upper stream of an estuary, the dominant steady-state balance of the depth-varying tracer concentration  $c'$  is similar to the salinity, which can be expressed as:

$$u' \bar{c}_x = K_S c'_{zz} \quad (C.17)$$

Where  $\bar{c}$  and  $c'$  are the vertical mean tracer concentration and the depth-varying part. Integrating Equation C.17 with the use of boundary conditions similar the salinity, the vertical profile of the tracer can be written as

$$c' = \frac{H^2}{K_S} \bar{c}_x (\bar{u}P_3 + u_E P_4) \quad (C.18)$$

Equation C.18 shows that the vertical tracer distribution is similar to salinity that can be described by  $P_3$  and  $P_4$  functions. The vertically averaged age concentration can be written as

$$\bar{\alpha}'_t + \frac{1}{A} (\bar{u} \bar{\alpha} A) + \frac{1}{A} (\overline{u' \alpha' A})_x = \frac{1}{A} (K_H \bar{\alpha}_x A)_x + \bar{c} \quad (C.19)$$

The dominant steady-state balance for  $\alpha'$  can be written as



$$u' \overline{\alpha_x} \cong K_S \alpha'_{zz} + c' \quad (\text{C.20})$$

Using Equation C.6 and Equation C.20 and integrating Equation C.18 using non-flux boundary conditions at the surface and the bottom, and  $\int_{-1}^0 \alpha' d\xi = 0$ , one obtains

$$\alpha' = \frac{H^2}{K_S} \overline{\alpha_x} (\bar{u} P_3 + u_E P_4) - \frac{H^4}{K_S} \bar{c_x} (\bar{u} P_5 + u_E P_6) \quad (\text{C.21})$$

where

$$P_5 = \frac{31}{5040} - \frac{7}{240} \xi^2 + \frac{1}{48} \xi^4 - \frac{1}{240} \xi^6 \quad (\text{C.22})$$

$$P_6 = \frac{1}{126} - \frac{1}{24} \xi^2 + \frac{1}{24} \xi^4 - \frac{1}{40} \xi^6 - \frac{1}{105} \xi^7 \quad (\text{C.23})$$

$$\alpha' = \frac{H^2}{K_S} \overline{\alpha_x} u_E P_4 \quad (\text{C.24})$$

$$c' = \frac{H^2}{K_S} \bar{c_x} u_E P_4 \quad (\text{C.25})$$

The age of water (AW)  $a$  can be calculated as

$$a = \frac{\alpha}{c} = \frac{\bar{\alpha} + \alpha'}{\bar{c} + c'} \cong (\bar{\alpha} + \alpha') \left( \frac{1}{\bar{c}} - \frac{c'}{\bar{c}^2} \right) \quad (\text{C.26})$$

The depth-varying part of age concentration  $\alpha'$  can be written as

$$\alpha' = \frac{1}{\bar{c}^2} (\bar{c} \alpha' - \bar{\alpha} c' - \alpha' c') \cong \frac{1}{\bar{c}^2} (\bar{c} \alpha' - \bar{\alpha} c') \quad (\text{C.27})$$

$$\alpha' = \frac{H^2 u_E}{K_S \bar{c}^2} P_4 (\bar{c} \overline{\alpha_x} - \overline{\alpha c_x}) \quad (\text{C.28})$$

Here, it is assumed that  $c' \ll \bar{c}$  and only keep the first term of Taylor series expansion of tracer concentration  $c$  in Equation C.26. In Equation C.27,  $\alpha' c'$ , which is proportional to the product of  $c_x$  and  $\alpha_x$ , is of smaller order than the other terms. Therefore, it is neglected. Equation C.28 suggests that the vertical structure of the AW profile can be described by  $P_4$ . Note that the two terms  $\bar{c} \overline{\alpha_x}$  and  $\overline{\alpha c_x}$  are on the same order. However, it has been proven that  $\bar{c} \overline{\alpha_x}$  is larger than  $\overline{\alpha c_x}$  (Beckers et al., 2001;

Shen and Lin, 2006). Therefore, the vertical AW distribution can be described by the  $P_4$  function, indicating a small AW near the surface and a large AW at the bottom when stratification exists.

The solution also shows that the vertical AW deviation depends on estuarine circulation where stratification exists. The stronger the estuarine circulation is, the larger the AW difference between the surface and the bottom waters.

# Appendix D

## NUMERICAL MODEL PARAMETERS AND SENSITIVITY TEST

### 1. Pearl River Estuary

Table D.1 shows the main parameters of the Pearl River Estuary three-dimensional model. The bottom roughness height was selected by sensitivity tests.

**Table D.1. A summary of the model set up attributes of Pearl River Estuary**

Pearl River Estuary	
Horizontal plane	Unstructured mesh
	8511 elements
	400m-3000m
Vertical direction	A structured mesh based on a sigma-coordinate transformation
	10 sigma layers with thicknesses equally distributed
Time step	30s
Horizontal eddy viscosity	Smagorinsky coefficient
Vertical eddy viscosity	k- $\epsilon$ model
Bottom roughness height	0.3m

Fig. D.1 and Fig. D.2 show the sensitivity test of bottom roughness height at sampling station S16 which is located near the estuary mouth in July and October, 2006, respectively. It can be seen that comparing with other bottom roughness height, the model with 0.3m bottom roughness height agrees with the measured data better. The test shows that the error of phase-lag is not mainly caused by the bed friction. By adjusting the eddy viscosity coefficient range, the predicted water level and current speed correctly reflected the hydrodynamic variation of the salinity trend throughout the tidal cycles which can be seen in Fig. 4.11 and Fig. 4.12.

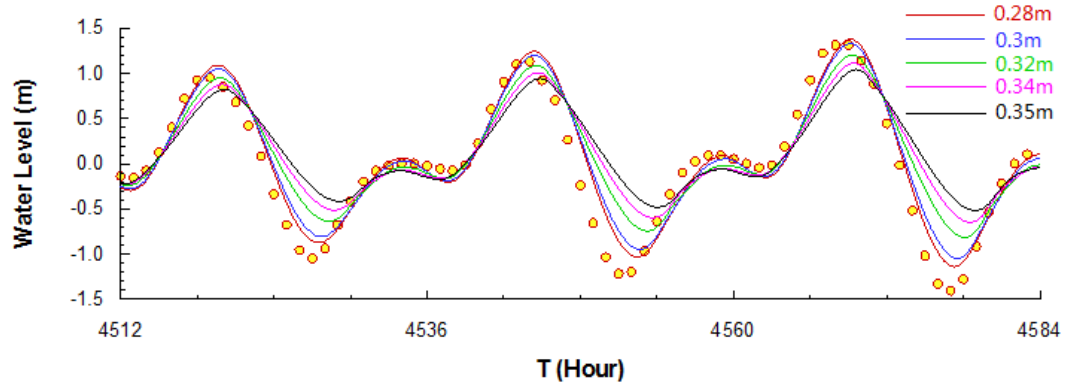


Fig. D.1. Sensitivity test of roughness height at S16 in Jun, 2006. Points: measured data; Line: predicted data.

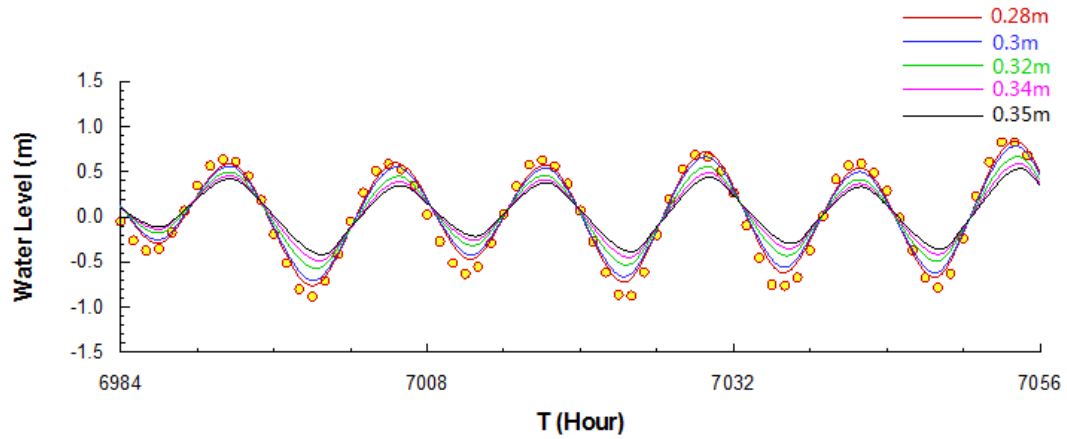


Fig. D.2. Sensitivity test of roughness height at S16 in Oct, 2006. Points: measured data; Line: predicted data.

## 2. Severn Estuary and Bristol Channel

Table D.2 shows the main parameters of the three-dimensional model of the Severn Estuary and Bristol Channel. The bottom roughness height was selected by sensitivity tests.

**Table D.2. A summary of the model set up attributes of the Severn Estuary and Bristol Channel.**

<b>Severn Estuary and Bristol Channel</b>	
<b>Horizontal plane</b>	Unstructured mesh
	11681 elements
	200m-1500m
<b>Vertical direction</b>	A structured mesh based on a sigma-coordinate transformation
	10 sigma layers with thicknesses equally distributed
<b>Time step</b>	5s
<b>Horizontal eddy viscosity</b>	Smagorinsky coefficient
<b>Vertical eddy viscosity</b>	k- $\epsilon$ model
<b>Bottom roughness height</b>	0.1m

---

## Reference

Abdelrhman, M.A., 2005. Simplified modeling of flushing and residence times in 42 embayments in New England, USA, with special attention to Greenwich Bay, Rhode Island. *Estuarine, Coastal and Shelf Science* 62(1-2), 339-351.

Adkins, J.F., Boyle, E.A., 1997. Changing atmospheric  $\delta^{14}\text{C}$  and the record of deep water paleoventilation ages. *Paleoceanography* 12(3), 337-344.

Ahmadian, R., Falconer, R.A., 2012a. Assessment of array shape of tidal stream turbines on hydro-environmental impacts and power output. *Renewable Energy* 44, 318-327.

Ahmadian, R., Falconer, R.A., Bockelmann-Evans, B., 2012b. Far-field modelling of the hydro-environmental impact of tidal stream turbines. *Renewable Energy* 38(1), 107-116.

Arega, F., Armstong, S., Badr, A.W., 2008. Modeling of residence time in the East Scott Creek Estuary, South Carolina, USA. *Journal of Hydro-environment Research* 2, 99-108.

Barber, R.W., Scott, R.J., 2000. Numerical modeling of tidal propagation in the Severn Estuary using a depth-adapted non-orthogonal grid. In: Rodriguez, G.R., ed. *Environmental Coastal Regions III*. WIT Press, 126-136.

Beckers, J.M., Delhez, E., Deleersnijder, E., 2001. Some properties of generalized age-distribution equations in fluid dynamics. *Journal of Applied Mathematics* 61(5), 1526-1544.

Bolin, B., Rodhe, H., 1973. A note on the concepts of age distribution and age distribution and transit time in natural reservoirs. *Tellus* 25, 58-62.

Burchard, H., Petersen, O., Rippeth, T.P., 1998. Comparing the performance of the Mellor–Yamada and the  $k-\epsilon$  two-equation turbulence models. *Journal of Geophysical Research* 10388(C5), 10543-10554.

Burwell, D., Vincent, M., Luther, M., Galperin, B., 2000. Modeling residence times; Eulerian vs. Lagrangian. In *Proceedings of the 6th International Conference on Estuarine and Coastal Modeling*. American Society of Civil Engineers, New Orleans, Louisiana. 995-1009.

Chen, S.T., Ruan, W.Q., 1994. The biogeochemical research of phosphorus in Jiulong River estuary and West Sea. *Acta Oceanologica Sinica* 16(2), 63-71.

Chen, X.J., 2007. A laterally averaged two-dimensional trajectory model for estimating transport time scale in the Alafia River estuary, Florida. *Estuarine Coastal and Shelf Science* 75(3), 357-370.

Crump, B.C., Hopkinson, C.S., Sogin, M.L., Hobbie, J.E., 2004. Microbial Biogeography along an Estuarine Salinity Gradient: Combined Influences of Bacterial Growth and Residence Time. *Applied and Environmental Microbiology* 70(3), 1494-1505.

Dai, M.H., Guo, X.H., Zhai, W.D., Yuan, L., Wang, B., Wang, L., Cai, P., Tang, T., Cai, W.-J., 2006. Oxygen depletion in the upper reach of the Pearl River Estuary during a



very drought dry season. *Marine Chemistry* 102, 159-169.

Dai, M.H., Zhai, W.D., Cai, W.-J., Callanhan, J., Huang, B.Q., Shang, S.L., Huang, T., Li, X.L., Lu, Z.M., Chen, W.F., Chen, Z.Z., 2008. Effects of an estuarine plume-associated bloom on the carbonate system in the lower reaches of the Pearl River estuary and the coastal zone of the northern South China Sea. *Continental Shelf Research* 28, 1416-1423.

David A.J., Philip M.O., Thomas C., Douglas J.W., Annika M.V.F., 2007. Particle Trapping in Stratified Estuary: Application to Observations. *Estuaries and Coasts* 30 (6), 1106-1125.

de Brauwere, A., de Brye, B., Blaise, S., Deleersnijder, E., Residence time, exposure time and connectivity in the Scheldt Estuary, 2011. *Journal of Marine Systems* 84(3-4), 85-95.

de Brye, B., de Brauwere, A., Gourgue, O., Delhez, E.J.M., Deleersnijder, E., 2012. Water renewal timescales in the Scheldt Estuary. *Journal of Marine Systems*, 74-86.

Deleersnijder, E., Campin, J.-M., Delhez, E.J.M., 2001. The concept of age in marine modelling I. Theory and preliminary model results. *Journal of Marine System* 28, 229-267.

Deleersnijder, E., Mouchet, A., Delhez, E.J.M., Beckers, J.-M., 2002. Transient behaviour of water ages in the World Ocean. *Mathematical and Computer Modelling* 36(1-2), 121-127.

Delesalle, B., Sournia, A., 1992. Residence time of water and phytoplankton biomass in coral reef lagoons. *Continental Shelf Research* 12(7-8), 939-949.

Delhez, E.J.M., Campin, J.-M., Hirst, A.C., Deleersnijder, E., 1999. Toward a general theory of the age in ocean modelling. *Ocean Modelling* 1(1), 17-27.

Delhez, É.J.M., Deleersnijder, É., Mouchet, A., Beckers, J.-M., 2003. A note on the age of radioactive tracers. *Journal of Marine Systems* 38(3-4), 277-286.

Delhez, E.J.M., Deleersnijder, E., 2008. Age and the time lag method. *Continental Shelf Research* 28(8), 1057-1067.

Delhez, E.J.M., Heemink, A.W., Deleersnijder, E., 2004a. Residence time in a semi-enclosed domain from the solution of an adjoint problem. *Estuarine, Coastal and Shelf Science* 61, 691-702.

Delhez, E.J.M., Lacroix, G., Deleersnijder, E., 2004b. The age as a diagnostic of the dynamics of marine ecosystem models. *Ocean Dynamics* 54(2), 221-231.

Dias, J.M., Sousa, M.C., Fortunato, A.B., Oliveira, A., 2009. Numerical modelling of the impact of the Ancao Inlet relocation(Ria Formosa, Portugal). *Environmental Modelling and Software* 24(6), 711-725.

Dong, L., Su, J., Wong, L.A., Cao, Z., Chen, J.-C., 2004. Seasonal variation and dynamics of the Pearl River plume. *Continental Shelf Research* 24(16), 1761-1777.

Dronkers, J., Zimmerman, J.T.F., 1982. Some principles of mixing in tidal lagoons. In: Lasserre, P. et al. eds. Coastal lagoons: Proceedings of the international symposium on coastal lagoons, Bordeaux, France, 8-14 September 1981. *Oceanologica Acta*, 107-117.

Dyer K.R., 1973. Estuaries: a physical introduction. London: John Wiley & Sons.

Falconer, R.A., Xia, J., Lin, B., Ahmadian, R., 2009. The Severn Barrage and other tidal energy options: Hydrodynamic and power output modeling. *Science in China, Series E: Technological Sciences* 52(11), 3413-3424.

Fukumoto, T., Kobayashi, N., 2005. Bottom stratification and water exchange in enclosed bay with narrow entrance. *Journal of Coastal Research* 21(1), 135-145.

Uncles, R.J., Jordan, M.B., 1994. Measurements of tidal currents and estimated energy fluxes in the Bristol Channel. In: Beven K J, ed. *Mixing and Transport in the Environment*. Chichester: John Wiley, 221-245.

Geyer, W.R., 1997. Influence of wind on dynamics and flushing of shallow estuaries. *Estuarine, Coastal and Shelf Science* 44: 713-722.

Gong, W., Shen, J., Hong, B., 2009. The influence of wind on the water age in the tidal Rappahannock River. *Marine Environmental Research* 68(4), 203-216.

Gourgue, O., Deleersnijder, E., White, L., 2007. Toward a generic method for studying water renewal, with application to the epilimnion of Lake Tanganyika. *Estuarine, Coastal and Shelf Science* 74(4), 628–640.

Hansell, D.A., Kadko, D., Bates, N.R., 2004. Degradation of Terrigenous Dissolved Organic Carbon in the Western Arctic Ocean. *Science* 304(5672), 858-861.

Hansen, D.V., Rattray, M., 1965. Gravitational circulation in straits and estuaries. *Journal of Marine Research* 23, 104-122.

Hare, J.A., Thorrold, S., Walsh, H., Reiss, C., Valle-Levinson, A., Jones, C., 2005. Biophysical mechanisms of larval fish ingress into Chesapeake Bay. *Marine Ecology Progress Series* 303, 295-310.

Harrison, P.J., Yin, K., Lee, J.H.W., Gan, J., Liu, H., 2008. Physical-biological coupling in the Pearl River Estuary. *Continental Shelf Research* 28(12), 1405-1415.

Holton, J.R., 1992. *An Introduction to Dynamic Meteorology*, 3rd edition, Academic Press, 77.

James, E.J., Sreedharan, K.E., 1983. Exchange of fresh and salt waters in the beypore estuary on the Malabar Coast. *Journal of the Institution of Engineers(India): Civil Engineering Division* 64, 81-87.

Ji, X., Sheng, J., Tang, L., Liu, D., Yang, X., 2011. Process study of circulation in the Pearl River Estuary and adjacent coastal waters in the wet season using a triply-nested circulation model, *Ocean Modelling* 38(1-2), 138-160.

Josefson, A.B., Rasmussen, B., 2000. Nutrient retention by benthic macrofaunal biomass of Danish estuaries: Importance of nutrient load and residence time.

Estuarine, Coastal and Shelf Science 50(2), 205-216.

Kemp, W.M., Boynton, W.R., Adolf, J.E., Boesch, D.F., Boicourt, W.C., Brush, G., Cornwell, J.C., Fisher, T.R., Gilbert, P.M., Hagy, J.D., Harding, L.W., Houde, E.D., Kimmel, D.G., Miller, W.D., Newell, R.I.E., Roman, M.R., Smith, E.M., Stevenson, J.C., 2005. Eutrophication of Chesapeake Bay: historical trends and ecological interactions. *Marine Ecology Progress Series* 303(21), 1-29.

Kheiasy, K.E.L., Mccorquodale, J., Georgiou, I., Meselhe, E., 2010. Three dimensional hydrodynamic modeling over bed forms in open channels. *International Journal of Sediment Research* 25(4), 431-440.

Kirby, R., Shaw, T.L., 2005. Severn Barrage, UK - environmental reappraisal. *Proceedings of the Institution of Civil Engineers: Engineering Sustainability* 158(1), 31-39.

Kong, J., Song, Z.-Y., Xia, Y.-F., Zhang, W.-S., 2007. Characteristics of water and sediment exchange between Yangtze Estuary and Hangzhou Bay. *China Ocean Engineering* 21 (2), 255-266.

Kot, S.C., Hu, S.L., 1995. Water flows and sediment transport in Pearl River Estuary and waves in South China near Hong Kong. *Coastal infrastructure development in Hong Kong - A review*, HongKong Government, Hong Kong, 13-32.

Lane, A., 2004. Bathymetric evolution of the Mersey Estuary, UK, 1906-1997: causes and effects. *Estuarine, Coastal and Shelf Science* 59, 249-263.

Larson, M., Bellanca, R., Jönsson, L., Chen, C., Shi, P., 2005. A model of the 3D circulation, salinity distribution, and transport pattern in the Pearl River Estuary, China. *Journal of Coastal Research* 21(5), 896-908.

Lasserre, P. et al. eds. Coastal lagoons: Proceedings of the international symposium on coastal lagoons, Bordeaux, France, 8-14 September 1981. *Oceanologica Acta*, 107-117.

Legović, T., 1991. Exchange of water in a stratified estuary with an application to Krka(Adriatic Sea). *Marine Chemistry* 32(2-4), 121-135.

Li, J., Yao, Y.M., Li, X.Y., Zhang, H.W., 2008. Numerical analysis on water exchange and its response to the coastal engineering in the Yueqing Bay in China. *Acta Oceanologia Sinica* 27, 60-73.

Lin, H.Y., Han, W.Y., 1990. Preliminary investigation into water exchange change in the Pearl River Estuary. *Chinese Science Bulletin* 35(5), 366-369.(in Chinese).

Lin, Z.H., Liang, S.H., 1996. A study on the tidal currents in the waters of the Pearl River mouth. *Marine Science Bulletin* 15(2), 11-15.(in Chinese)

Liu, W.-C., Chen, W.-B., Kuo, J.-T., Wu, C., 2008. Numerical determination of residence time and age in a partially mixed estuary using three-dimensional hydrodynamic model. *Continental Shelf Research* 28(8), 1068-1088.

Liu, W.-C., Chen, W.-B., Hsu, M.-H., 2011. Using a three-dimensional

particle-tracking model to estimate the residence time and age of water in a tidal estuary. *Computers & Geosciences* 37, 1148-1161.

Liu, Z., Wang, H., Guo, X., Wang, Q., Gao, H., 2012. The age of Yellow River water in the Bohai Sea. *Journal of Geophysical Research C: Oceans* 117(11), art. no. C11006.

Lowery, T.A., 1988. Difference equation-based estuarine flushing model application to U.S. Gulf of Mexico estuaries. *J. Coast. Res.* 14, 185-195.

Lucas, L.V., Koseff, J.R., Cloern, J.E., Monismith, S.G., Thompson, J.K., 1999a. Processes governing phytoplankton blooms in estuaries. I: The local production-loss balance. *Marine Ecology Progress Series* 187, 1-15.

Lucas, L.V., Koseff, J.R., Monismith, S.G., Cloern, J.E., Thompson, J.K., 1999b. Processes governing phytoplankton blooms in estuaries. II: The role of horizontal transport. *Marine Ecology Progress Series* 187, 17-30.

Luther, K.H., Haitjema, H.M., 1998. Numerical experiments on the residence time distributions of heterogeneous groundwatersheds. *Journal of Hydrology* 207(1-2), 1-17.

MacDonald, D.G., 2006. Estimating an estuarine mixing and exchange ratio from boundary data with application to Mt. Hope Bay(Massachusetts/Rhode Island). *Estuarine, Coastal and Shelf Science* 70(1-2), 326-332.

Marshall, J., Plumb, R.A., 2007. Atmosphere, Ocean, and Climate Dynamics. Academic Press.

Mao, Q.W., Shi, P., Yin, K.D., Gan, J.P., Qi, Y.Q., 2004. Tides and tidal currents in the Pearl River Estuary. Continental Shelf Research 24, 1797-1808.

Miller, S.D., Luther, M.E., 2008. A numerical simulation of residual circulation in Tampa Bay. part II: Lagrangian residence time. Estuaries and Coasts 31, 815-827.

Monsen, N.E., Cloern, J.E., Lucas, L.V., Monismith, S.G., 2002. A comment on the use of flushing time, residence time, and age as transport time scales. Limnology and Oceanography 47, 1545-1553.

Muyllaert, K., Sabbe, K., Vyverman, W., 2000. Spatial and temporal dynamics of phytoplankton communities in a freshwater tidal estuary(Schelde, Belgium). Estuarine, Coastal and Shelf Science 50(5), 673-687.

Neller, R.J., Lam, K.C., 1998. The environment. In: Yeung, Y.M., Chu, D.K.Y.(Eds.), Guangdong: Survey of a Province Undergoing Rapid Change. Chinese University Press, Hong Kong, 435-464.

Nortek-AS, 1997a. ADV Operation Manual.

Nortek-AS, 1997b. ADV Software Manual.

Oliveira, A., Fortunato, A.B., Rego, J.R.L., 2006. Effect of morphological changes on



the hydrodynamics and flushing properties of the Obidos lagoon(Portugal). Continental Shelf Research 26(8), 917-942.

Osborne R., 1895. Philosophical Transactions of the Royal Society of London. A, Vol. 186, 123- 164.

Owen A., 1980. A three-dimensional model of the Bristol Channel. Journal of Physical Oceanography 10, 1290-1302.

Pandoe, W.W., Edge, B.L., 2004. Cohesive sediment transport in the 3D-hydrodynamic-baroclinic circulation model, study case for idealized tidal inlet. Ocean Engineering 31(17-18), 2227-2252.

Pejrup, M., Bartholdy, J., Jensen, A., 1993. Supply and Exchange of Water and Nutrients in the Gr ådyb Tidal Area, Denmark. Estuarine, Coastal and Shelf Science 36, 221-234.

Pond, S., Pickard, G.L., 1983. Introductory Dynamical Oceanography. Pergamon Press, New York.

Primo, A.L., Azeiteiro, U.M., Marques, S.C., Martinho, F., Baptista, J., Pardal, M.A., 2012. Colonization and nursery habitat use patterns of larval and juvenile flatfish species in a small temperate estuary. Journal of Sea Research 76, 126-134.

Pritchard, D.W., 1952. Salinity distribution and circulation in the Chesapeake Bay estuarine system. Journal Marine Research 11, 106-123.

Rabalais, N.N., Gilbert, D., 2009. Distribution and consequences of hypoxia. In: Urban, E., Sundby, B., Malanotte-Rizzoli, P., Melillo, J.M. eds., *Watersheds, Bays and Bounded Seas*. Island Press, Washington, DC, 209-226.

Rasmussen, E. B., 1993. Three-dimensional hydrodynamic models. Section 3.1 hydrodynamic models. *Coastal, Estuarial and Harbour Engineer's Reference Book*, 109-116.

Rasmussen, E. B., Pietrzak, J., Brandt, R., 1999. A coupled iceocean model for the Greenland, Iceland and Norwegian Seas. *Deep-Sea Research, Part II* 46, 1169-1198.

Ribbe, J., Wolff, J.-O., Staneva, J., Gräwe, U., 2008. Assessing water renewal time scales for marine environments from three-dimensional modelling: A case study for Hervey Bay, Australia *Environmental Modelling and Software* 23(10-11), 1217-1228.

Rodi, W., 1984. *Turbulence models and their applications in hydraulics: A State of the Art Review*. IAHR, Delft, the Netherlands, Ashgate Pub Co.

Schlichting, H., 1979. *Boundary-Layer Theory*. 7th ed., McGraw-Hill, New York.

Scully, M.E., Friedrichs, C.T., Brubaker, J.M., 2005. Control of estuarine stratification and mixing by wind-induced straining of the estuarine density field. *Estuaries* 28, 321-326.

Sheldon, J.E., Alber, M., 2002. A comparison of residence time calculations using simple compartment models of the Altamaha River estuary, Georgia. *Estuaries* 25(6B),

1304-1317.

Shen, J., Haas, L., 2004. Calculating age and residence time in the tidal York River using three-dimensional model experiments. *Estuarine, Coastal and Shelf Science* 61, 449-461.

Shen, J., Lin, J., 2006. Modeling study of the influences of tide and stratification on age of water in the tidal James River. *Estuarine, Coastal and Shelf Science* 68(1), 101-112.

Shen, J., Wang, H. V., 2007. Determining the AW and long-term transport timescale of the Chesapeake Bay. *Estuarine, Coastal and Shelf Science* 74, 585-598.

Simons, R.D., Monismith, S.G., Johnson, L.E., Winkler, G., Saucier, F.J., 2006. Zooplankton retention in the estuarine transition zone of the St. Lawrence Estuary. *Limnology and Oceanography* 51(6), 2621-2631.

Simpson, J.H., Brown, J., Matthews, J., Allen, G., 1990. Tidal straining, density currents, and stirring in the control of estuarine stratification. *Estuaries* 13(2), 125-132.

Smart, P. L., Laidlaw, I. M. S., 1977. An Evaluation of Some Fluorescent Dyes for Water Tracing. *Water Resources Research* 13(1), 15-33.

Stephens, C. V., 1986. A three-dimensional model for tides and salinity in the Bristol Channel. *Continental Shelf Research* 6(4), 531-560.

Stoschek, O., Zimmermann, C., 2006. Water exchange and sedimentation in an estuarine tidal harbor using three-dimensional simulation. *Journal of Waterway, Port, Coastal and Ocean Engineering* 132(5), 410-414.

Spivakovskaya, B., Deleersnijder, E., Rancher, J., 1997. The water residence time in the Mururoa atoll lagoon: sensitivity analysis of a three-dimensional model. *Coral Reefs* 16(3), 193-203.

Spivakovskaya, D., Heemink, A.W., Deleersnijder, E., 2007. The backward Ñ method for the Lagrangian simulation of transport processes with large space variations of the diffusivity. *Ocean Science* 3(4), 525-535.

Takeoka, H., 1984. Fundamental concepts of exchange and transport time scales in a coastal sea. *Continental Shelf Research* 3(3), 311-326.

Tartinville B., E. Deleersnijder and J. Rancher, 1997. The water residence time in the Mururoa atoll lagoon: a three-dimensional model sensitivity analysis, *Coral Reefs*, 16, 193-203

Turner Designs, 1998. Digital Fluorometer AU-10 Manual.

UNESCO, 1981. The practical salinity scale 1978 and the international equation of state of seawater 1980, UNESCO technical papers in marine science, 36, 1981.

Wang, -P.D., 1979. Wind - driven circulation in the Chesapeake Bay, winter 1975. *Journal of Physical Oceanography* 9(3), 564-572.

Wan, Y., Ji, Z.-G., Shen, J., Hu, G., Sun, D., 2012. Three dimensional water quality modeling of a shallow subtropical estuary. *Marine Environmental Research* 82, 76-86.

Wang, B., Wei, Q., Chen, J., Xie, L., 2012. Annual cycle of hypoxia off the Changjiang(Yangtze River) Estuary. *Marine Environmental Research* 77, 1-5.

Williams, J., Hindell, J.S., Swearer, S.E., Jenkins, G.P., 2012. Influence of freshwater flows on the distribution of eggs and larvae of black bream *Acanthopagrus butcheri* within a drought-affected estuary. *Journal of Fish Biology* 80(6), 2281-2301.

Wong, L.A., Chen, J.C., Xue, H., Dong, L.X., Su, J.L., Heinke, G., 2003a. A model study of the circulation in the Pearl River Estuary(PRE) and its adjacent coastal waters: 1. Simulations and comparison with observations. *Journal of Geophysical Research* 108(C5)25, 1-17.

Wong, L. A., Chen, J. C., Xue, H., Dong, L. X., Guan, W. B., Su, J. L., 2003b. A model study of the circulation in the Pearl River Estuary(PRE) and its adjacent coastal waters: 2. Sensitivity experiments. *Journal of Geophysical Research* 108(C5) 26, 1-12.

Wong, L.A., Chen, J.C., Dong, L.X., 2004. A model of the plume front of the Pearl River Estuary, China and adjacent coastal waters in the winter dry season. *Continental Shelf Research* 24(16), 1779-1795.

Wu, J., 1980. Wind-stress Coefficients over sea surface and near neutral conditions- A revisit. *Journal of Physical, Oceanography* 10, 727-740.

Wu, J., 1994. The sea surface is aerodynamically rough even under light winds, *Boundary layer Meteorology* 69, 149-158.

Xia, J., Falconer, R.A., Lin, B., 2010a. Hydrodynamic impact of a tidal barrage in the Severn Estuary, UK. *Renewable Energy* 35(7), 1455-1468.

Xia, J., Falconer, R.A., Lin, B., 2010b. Impact of different tidal renewable energy projects on the hydrodynamic processes in the Severn Estuary, UK. *Ocean Modelling* 32(1-2), 86-104.

Xu, J.L., 1985. Shoal Growth and Evolution of Lingdingyang of the Pearl River Mouth. China Ocean Press, Beijing.(in Chinese)

Yanagi, T., Hinata, H., 2004. Water exchange between Tokyo Bay and the Pacific Ocean during winter. *Ocean Dynamics* 54(3-4), 452-459.

Yang, Y.H., Sheng, G.Y., Fu, J.Y., Fu, J.N., 1995. Organic micropollutants in water environment of the Pearl River Delta, Guangdong, China. Water-rock interaction. Proc. symposium, Vladivostok, 281-285.

Yuan, D., Lin, B., Falconer, R.A., 2007. A modelling study of residence time in a macro-tidal estuary. *Estuarine Coastal and Shelf Science* 71, 401-411.

Zhao, H., 1990. The Evolution of the Pearl River Estuary. China Ocean Press, Beijing, 1-357. (in Chinese)

Zhang, Q.Y., 2006. Comparison of two three-dimensional hydrodynamic modeling systems for coastal tidal motion. *Ocean Engineering* 33(2), 137-151.

Zheng, J., Yan, Y., Zhu, Y., 2002. Three dimensional baroclinic numerical model for simulating fresh and salt water mixing in the Yangtze Estuary. *China Ocean Engineering* 16(2), 227-238.

Zheng, B.H., Zhu, Y.L., Yu, D.S., Zheng, Z., Chen, C.H., 2010. Dynamic process effected commonly by runoff and tide at the eight main entrances to the Pearl River Estuary, *Advances in Marine Science* 28, 1-7.(in Chinese)

Zimmerman, J. T. F., 1976. Mixing and flushing of tidal embayments in the western Dutch Wadden Sea. Part I: Distribution of salinity and calculation of mixing time scales. *Netherlands Journal of Sea Research* 10(2), 149-191.